ULTRAFAST STRUCTURAL DYNAMICS IN ELECTRONICALLY EXCITED MANY-BODY SYSTEMS

THÈSE N^O 3148 (2004)

PRÉSENTÉE À LA FACULTÉ SCIENCES DE BASE

Institut des sciences et ingénierie chimiques

SECTION DE PHYSIQUE

ÉCOLE POLYTECHNIQUE FÉDÉRALE DE LAUSANNE

POUR L'OBTENTION DU GRADE DE DOCTEUR ÈS SCIENCES TECHNIQUES

PAR

Luigi BONACINA

laurea in fisica, Università degli Studi di Milano, Italie
et de nationalité italienne

acceptée sur proposition du jury:

Prof. M. Chergui, directeur de thèse
Dr M. Drabbels, rapporteur
Prof. O. Martin, rapporteur
Prof. G. Scoles, rapporteur
Prof. F. Vallée, rapporteur

Lausanne, EPFL
2004

Ultrafast structural dynamics in electronically excited many-body systems

Ph.D Thesis

Luigi Bonacina
Laboratoire de Spectroscopie Ultrarapide
Institut des Sciences et Ingénierie Chimiques
Faculté des Sciences de Base - EPFL-BSP CH-1015 Dorigny-Lausanne

Abstract

This thesis reports on results of three different experiments of photo-induced structural dynamics in the condensed phase, investigated by time-resolved pump-probe spectroscopy with femtosecond time-resolution.

In the first part, we address the ultrafast dynamics of a *quantum solid*: crystalline hydrogen. This is accomplished by optical excitation of a dopant molecule, Nitric Oxide (NO), to a large orbital Rydberg state, which leads to a bubble-like expansion of the species surrounding the impurity. The dynamics is directly inferred from the time-resolved data, and compared with the results of molecular dynamics simulations. We report the presence of three time-scales in the structural relaxation mechanism: the first 200 fs are associated with the ultrafast inertial expansion of the first shell of lattice neighbors of NO. During the successive 0.6 ps, as the interactions between the molecules of the first and of the successive shells increase, we observe a progressive slowing-down of the bubble expansion. The third timescale ($\sim$ 10 ps) is interpreted as a slow structural re-organization around the impurity center. No differences were observed between the dynamics of normal- and para-hydrogen crystals, justifying the simplified model we use to interpret the data, which ignores all internal degrees of freedom of the host molecules. The molecular dynamics simulations reproduce fairly well the static and dynamic features of the experiment. In line with the measurements, they indicate that the quantum nature of the host medium plays no role in the initial ultrafast expansion of the bubble.

In the second part, we present the results of our study on the photo-physics of *triangular-shaped silver nanoparticles* upon intraband excitation of the conduction electrons. The picosecond dynamics is dominated by periodic shifts of the surface plasmon resonance, associated with the size oscillations of the particles, triggered by impulsive lattice heating by the laser pulse. The oscillation period compares very well with the lowest totally symmetric vibrational frequency of a triangular-plate, which we calculated improving an existing elastodynamic model. We propose an explanation for the unusual phase behavior of the oscillations, based upon the non-spherical shape, and size-inhomogeneity of the sample. Taking into account these effects, we are able to reproduce spectrally

and temporally our data.

In the last part, we present a comparative study of the ligand dynamics in *heme proteins*. We studied the photo-induced spectroscopic changes in the *ferric* CN complexes of Myoglobin and Hemoglobin I upon photo-excitation of the porphyrin ring to a low-lying electronic state (*Soret*), monitoring the UV-visible region of the Soret band, and the mid-infrared region of the fundamental C≡N vibrational stretch.

The transient response in the UV-visible spectral region does not depend on the heme pocket environment, and is very similar to that known for *ferrous* proteins. The infrared data on the MbC≡N stretch vibration provides a direct measure for the return of population to the ligated electronic (and vibrational) ground state with a 3 ps time constant. In addition, the CN stretch frequency is sensitive to the excitation of low frequency heme modes, and yields independent information about vibrational cooling, which occurs on the same timescale. The similarity between ferrous and ferric hemes rules out the charge transfer processes commonly invoked to explain the ligand dissociation in the former.

Etude de la

dynamique structurale ultrarapide

de systèmes multicorps

électroniquement excités

Thèse de doctorat

Luigi Bonacina
Laboratoire de Spectroscopie Ultrarapide
Institut des Sciences et Ingénierie Chimiques
Faculté des Sciences de Base - EPFL-BSP CH-1015 Dorigny-Lausanne

Version abrégée

Cette thèse présente les résultats de trois expériences de dynamique structurelle photo-induites dans la phase condensée, étudiés par spectroscopie pompe-sonde avec une résolution femtoseconde.

La première partie se consacre à l'étude de la dynamique ultrarapide d'un *solide quantique* : l'hydrogène cristallin. Pour ce faire un dopant moléculaire (oxyde d'azote, NO) est excitée à un état de Rydberg, qui se caractérise par une orbitale spacialement étendue. Cette excitation déclenche une expansion radiale des molécules d'hydrogène adjacentes à NO. La dynamique se déduit directement des mesures temporelles, et est ainsi comparées aux simulations de dynamique moléculaire. Les mécanismes de relaxation structurelle apparaissent avec trois échelles de temps. Les premières 200 fs sont associés à l'expansion inertielle ultrarapide de la première couche. Durant les 0.6 ps suivantes, les interactions entre la première couche et les suivantes se traduisent par une diminution de la vitesse d'expansion. Une troisième échelle de temps de 10 ps est interprétée comme réorganisation structurelle autour de l'impureté. Aucune différence n'a été observée entre la dynamique des cristaux d'hydrogène normaux et para. Ceci justifie notre modèle d'interprétation, negligeant tout degré de liberté interne des molécules du cristal. Les simulations de dynamique moléculaire reproduisent bien les aspects statique et dynamique de l'expérience. Ils indiquent que la nature quantique du milieu ne joue pas un rôle dans l'expansion ultrarapide initiale.

Dans la deuxième partie nous présentons les résultats de notre étude sur la photo-physique de *nanoparticules d'argent de forme triangulaires*, déclenchée par excitation des électrons de conduction. La dynamique picoseconde est dominée par un dèplacement périodique de la résonance de plasmon de surface. Cette dynamique, associée à l'oscillation de la taille des particules, est initiée

par l'augmentation thermique impulsive de la maille, causée par l'impulsion laser. La période d'oscillation correspond au mode fondamental totalement symétrique d'une plaque triangulaire, calculé en utilisant un modèle théorique. En prenant en compte la distribution de taille de l'échantillon et son aspect non sphérique, nous proposons une explication pour le comportement atypique de la phase des oscillations. Dans ce cadre, il est possible de reproduire l'intégralité des données à la fois en fréquence et en temps.

La troisième partie présente une étude comparative de la dynamique des ligands dans les *protéines d'hème*. Nous avons étudié les changements spectroscopiques photoinduits dans les complexes *ferrique* de la Myoglobine et l'Hemoglobine liés à CN, après excitation de la bande de Soret. Leurs évolution à été suivie en observant la région UV-visible de la bande de Soret ainsi que la région infrarouge autour de la vibration de C=N. La réponse transitoire dans le visible ne dépend pas de l'environnement protéique et est très similaire à la réponse observée dans les protéines ferreuses. Les données infrarouges concernant les vibrations de MbC=N fournissent une mesure directe du retour de population au niveau électronique (et vibrationnel) fondamental avec une constante de 3 ps. La fréquence d'élongation CN est sensible à l'excitation des modes de basses fréquences de l'hème et fournit une information indépendante concernant le refroidissement vibrationnel, caractérisé par la même échelle de temps. La similarité entre protéines d'heme ferreux et ferrique exclut le processus de transfert de charge, souvent énvoqué pour expliquer la dissociation du ligand dans l'hème ferreux.

Contents

viii

Introduction

Understanding many-body systems is one of the primary issues of condensed matter science. In particular, the study of *dynamics* in solids, liquids and proteins can bring new insights for a deeper comprehension of many fundamental processes in physics, chemistry and biology. To mention a few examples, the topics of structural-phase transitions [1], photo-induced defect formation [2–5], and radiation damage [6] have received growing attention from the physics community in the last decade. The Nobel Prize in chemistry awarded to Prof. Ahmed H. Zewail in 1999 testifies the significance and the wide-reaching interest of his research on transition states in chemical reactions [7]. Finally, the study of dynamics in biology shines a different light on the classical paradigm associating structure to function. Indeed, if we consider that function is a sequence of events characterized by structural changes, the time-resolved study of these changes becomes a privileged approach to understand the basic mechanisms of biological activity [8, 9].

Obviously for studying ultrafast dynamics one needs to apply a very fast perturbation, which can only be obtained by using optical pump-probe techniques. Norman and Porter, with their pioneering work on flash photolysis, first exploited this idea observing spectroscopically the evolution of a chemical reaction on a millisecond timescale [10]. Ever since the advent of laser in the 60's, sources with progressively shorter pulses have been developed till the realization of the first femtosecond [1] laser in 1982 [11]. Considering that the typical speed of atomic motion is 1 Km/s, a time-resolution of the order of tens of femtoseconds, which nowadays tabletop ultrafast laser systems can provide, is suited to investigate processes associated to length-scales of just few Ångstroms [12]. In this respect, the conventional distinction between physics, chemistry and biology becomes less meaningful: a femtosecond measurement in the condensed phase is sensitive to the ultrafast dynamics of the molecular species localized around a center selectively activated by a light pulse. The specific macroscopic character of the environment (solid, liquid, protein,...) plays a minor role.

This work reports on results obtained in the real-time spectroscopic investigation of the picosecond and sub-picosecond dynamics of three fairly different systems, driven out of equilibrium by an impulsive light-induced *electronic excitation*. Specifically, we studied:

---

[1]One femtosecond corresponds to 10^{-15} seconds, one picosecond to 10^{-12} seconds.

1. the structural dynamics of a quantum solid (solid H_2) around a dopant molecule excited to a large orbital Rydberg state;

2. the photophysics of a sample of triangular-shaped silver nano-plates dispersed in water upon intraband excitation of the conduction electrons;

3. the ligand binding and dissociation dynamics in heme proteins upon photo-excitation of the porphyrin ring to a low-lying electronic state.

In what follows, we present a general overview on each of these studies, together with a short outline of the corresponding section of the thesis.

Structural dynamics in solid hydrogen. The dynamics of lattice re-arrangement upon a charge redistribution on a molecular impurity is an issue of general interest, because such a process is expected to accompany any chemical reaction in the condensed phase. To characterize this mechanism we need first to provide a chemically inert non-polar medium with well defined properties. Rare gas and hydrogens crystals meet these requirements, being structurally stable matrices, well characterized in terms of their elastic and thermodynamic properties [13–17]. Additionally, they are easy to grow by direct gas deposition on a cold substrate in high vacuum. It is worth remarking that the cryogenic temperature of these samples reduces the density of states accessible to the guest molecules that are trapped therein, minimizing the complexity of the system under study.

Hydrogen presents an additional appeal with respect to other van der Waals crystals, arising from the extremely light mass of its constituents. It is an example of quantum solid, as it is characterized by major zero-point amplitude motions of the molecules around their lattice sites [15]. Thus it provides a soft, *quasi-liquid*, environment around the impurity centers, without presenting many of the drawbacks associated with real liquids, in particular the presence of multiple solute-solvent configurations.

The main motivation for the present experiment is the investigation of hydrogen as a quantum crystal. To our knowledge, *dynamical* time-resolved studies in quantum hosts are very scarce in literature, limited to the work of Stienke-meier *et al.*, who studied adatoms coherence phenomena on the surface of large He clusters [18], the study of Benderski *et al.* about the formation of bubble state around Rydberg excited He_2^* dimers in liquid helium [19], and, finally, the work of our group on the structural relaxation in solid normal-hydrogen [2] [20]. These works are accompanied by a much larger body of frequency-resolved spectroscopic [21–27] and computational [28–32] studies that address the issue of dynamical couplings between an impurity and its environment in quantum crystals and clusters. Some of these works are motivated by the possible utilization of solid doped-hydrogen as a rocket propellant or fuel [26, 33].

The large amplitude motions of molecules, and the low temperature regime make solid hydrogen also a fascinating system to investigate fundamental

---

[2]Normal-hydrogen: sample which presents the room temperature concentration of 25% of para-H_2 molecules and 75% of ortho-H_2 molecules.

mechanisms in low temperature chemistry, in particular solvation dynamics. In our experiment, the investigation of the structural re-arrangement that follows the electronic excitation of an impurity is achieved using a molecular probe, which possesses three fundamental characteristics: (1) it does not affect the equilibrium properties of the solid when it is in the electronic ground state, (2) it interacts strongly with the surrounding crystal environment when it is electronically excited, and (3) it provides an experimental observable which is intrinsically highly sensitive to the environment, such that the medium response is *directly observed*, and not *indirectly inferred* by some intramolecular properties [3]. Nitric oxide (NO) presents all these characteristics as: (1) it fits comfortably in substitutional sites of hydrogen [35], (2) when photo-excited to the first Rydberg state, A, its electronic cloud overlaps spatially with the closed shell orbitals of the nearest lattice neighbors, triggering a major radial displacement of the H_2 molecules, and finally (3) the fluorescence of the A state allows a direct, background free, measurement of the strength of the interaction between the crystal species and the impurity [35].

The present study continues a work started a few years ago to investigate lattice dynamics in solid normal-hydrogen [20]. We modified the original experiment introducing the possibility to work on para-hydrogen crystals, and a novel excitation scheme. The latter was necessary to improve the time-resolution of the measurement, in order to investigate the very early dynamics of the system.

After an introduction about the properties of solid hydrogen (Chap. 1), in Chap. 2 we present some basic concepts essential for the interpretation of the spectroscopic features of molecular impurities trapped in solid hosts. In Chap. 3, we provide a review of the main results of the steady-state spectroscopy of NO embedded in solid normal-hydrogen, and derive a set of harmonic potentials that describe the interactions between the impurity and the surrounding matrix in the ground and the lowest three Rydberg states. In Chap. 4, we present an experimental scheme capable of following the dynamics of the system in real-time. We then discuss the technical aspects of the experiment, pointing out the most significant ones: the two-photon excitation scheme, and the technique applied to determine the absolute position of time-zero in the experimental signals. Finally, we describe the apparatus used to convert normal- into para-hydrogen, and the details of the sample preparation. The characterization of the sample is discussed in Chap. 5, which contains the spectroscopy of doped para-hydrogen including Raman, absorption, fluorescence, and photostability measurements. The results of the time-resolved experiment are presented in Chap. 6. Chapter 7 describes the molecular dynamics calculations that were performed to simulate the structural relaxation of the system, and which reproduce the actual pump-probe signals. In these two chapters the fundamental timescales of the lattice dynamics are extracted and related to specific physical mechanisms, involving the molecules which surround the impurity center in the crystal. Last, in Chap. 8, we discuss the possibility of applying a continuum model to describe the dynamics, and we

---

[3]See, for example, the work of Zadoyan *et al.* on the vibrations of I_2 in rare gas solids [34]

present a comparison with the results obtained performing similar measurements in different host matrices (argon and neon).

Dynamical properties of triangular-shaped silver nanoparticles. The optical properties of metal nanoparticles arise from quantum confinement, and from the interplay between bulk and surface effects. In particular, the resonant excitation of the conduction band electrons determine the presence of an extinction band, the *surface plasmon band*, which is absent in the spectrum of bulk metals. Its spectral character is sensitive to the size and shape of the particles, and to the dielectric properties of the surrounding medium [36]. Consequently, many works have envisaged a widespread body of possible applications that take advantage of these unique spectroscopic features. To cite a few examples, the sensitivity of the local surface plasmon band to the dielectric constant of the environment was exploited to provide optical sensors with zeptomole sensitivity [37]. Following the same principle, properly activated silver nano-triangles were used as highly efficient bio-sensors to probe antigen-antibody interactions on their surface [38]. Another fascinating possibility relies on the capability of noble-metal nanoparticles, in particular of ellipsoidal and triangular shape, to provide dramatic enhancement of local electromagnetic fields [39–41]: this property can be used to provide very efficient localized light sources for applications in near-field microscopy [42, 43].

Callegari *et al.* have developed an original technique to drive the photochemical growth of a colloidal solution of spherical nanoparticles by changing the conditions of illumination at which the preparation is exposed [44]. They demonstrated that light can be used to control the final shape and size of the nanoparticles, with a high degree of homogeneity. This approach has been applied to prepare the samples of silver triangular nano-plates that have been studied in the present work.

We have explored the fundamental photophysics of these particles monitoring, on a timescale of picoseconds, the transient absorption changes in the region of the surface plasmon resonance upon direct photo-excitation of the conduction electrons. The principal results of this study, reported in Chap. 9, follow a general description of the different physical mechanisms that are triggered by the photo-excitation of a solution of metallic nanoparticles. The laser pulse initially interacts with the conduction electrons creating a transient, short-lived, non-thermal distribution [45]. Successively, the hot electrons thermalize with the lattice on a timescale of a few picoseconds [46, 47]. This causes rapid heating of the particles which, due to the anharmonicity of the crystal, impulsively excites low-frequency vibrational modes [48–50]. The ensuing periodic changes in dimension affect the position of the plasmon band, because of its sensitivity to the size and shape of the particles. Consequently, they can be easily followed spectroscopically by monitoring transient changes in the absorption properties of the sample.

The measurements were performed using broad-band probe and detection, therefore we were able to accumulate detailed information about the dynamics of the system throughout the spectral region of the surface plasmon band.

The results were successively analyzed applying different techniques of global analysis as explained in § 9.5. In particular, we investigated the influence of an inhomogeneous distribution of sizes in a sample composed by particles of *non-spherical* symmetry. In this context, we present the outcome of a simple simulation that is able to reproduce with fairly good agreement the principal spectral and temporal features observed in the experimental signals. Finally, we report the results of a numerical calculation based on elastic theory of continuum bodies [51], that we performed to derive the theoretical symmetries and frequencies of the free vibrations of a triangular plate with the dimensions of the nanoparticles studied. The outcomes of the procedure are compared with the results of the time-resolved experiment at the end of the section.

Comparative study of ligand dissociation and rebinding in heme proteins. In the last section of the thesis we report the results of an experiment on ligand dynamics in heme proteins [52].

The essential motivation of this work resides in the study of the fundamental interactions between a ligand and its protein environment. To this end we decided to perform a comparative study of the ultrafast dynamics of ligand dissociation and rebinding in two similar globins (Myoglobin and Hemoglobin I), which present substantial differences in the distribution of the aromatic residues which surround the heme [53]. To enforce the validity of the comparison, we chose CN as a ligand molecule, which binds to the heme central iron in the ferric oxidation state *in both proteins*.

It is remarkable that, even though there exists a large body of time-resolved studies about ligand dissociation in globins [54–61], all these works are essentially limited to systems with the heme iron in the ferrous state [4]. In this respect, the present experiment provides an additional insight. Considering that charge transfer processes are typically invoked to explain ligand photolysis upon photo-excitation of the heme porphyrin [60, 62], the possibility to study the same mechanism in a different oxidation state of iron could help clarifying the consistency of the interpretations proposed so far.

The results, presented in Chap. 10, include two complementary sets of measurements, one probing in the infrared, the other in the UV-visible. The comparison of the dynamics observed through these two approaches, turns out to be essential for understanding the evolution of these complex systems. Indeed, the infrared bands, providing precious information on both vibrational cooling, and relaxation of the electronic excitation of the heme, help to interpret the transient features observed in the visible region. Their assignment is generally an extremely complicated task, because of the simultaneous presence of several spectrally overlapping contributions.

---

[4]This is the oxidation state in which vertebrate myoglobin binds O_2, and carries on its biological function.

Chapter 1

Solid Hydrogen

Molecular solid hydrogen presents a series of fascinating and unique properties deriving from its light mass and weak intermolecular interactions. In the following, the principal characteristics of this molecular solid will be reviewed, mainly focusing on the issues of interest for this work: the quantum character and the rotational properties.

1.1   Intermolecular forces and structure

Hydrogen molecules are closed-shell species ($1s\sigma^2$). In the solid, the attractive long range forces that keep the molecules together include dispersion (van der Waals) and direct multipole forces. The lowest multipole interaction is the electric quadrupole-quadrupole, which is associated uniquely with molecules with non-zero rotational states, as discussed in § 1.2. Dispersion forces are, by far, the strongest interactions in the solid. For short time intervals of the order of 10^{-13} s [17], a hydrogen molecule can show a dipole moment of about 10^{-29} C·m, due to the fluctuations of its electron cloud. This transient dipole induces a similar moment, proportional to

Common core

h.c.p.   f.c.c.

Figure 1.1: Derivation of the basic crystal structures of solid hydrogen from the common core.

the polarizability, in a neighboring molecule. The cohesive energy that is then exerted between the two molecules is very weak (about 1% of the ionization potential [63]), and, therefore, the nearly spherical electronic distribution of the

gas-phase is conserved. This fact has an influence on the crystalline structure of the solid: hydrogen adopts both face-centered cubic (f.c.c.) and hexagonal closed-packed (h.c.p.) structures, which happen to be the two most probable packing schemes for identically sized spheres. The structure is generally h.c.p. [64], the f.c.c. phase occurs only at low temperature, and with high content of $J = 1$ molecules (J stands for the rotational quantum number). Under particular conditions the appearance of the f.c.c. arrangement in unexpected region of the phase diagram is observed. The epitaxy, for instance, can influence the structure. Diffraction studies showed that films of H_2 grow from vapor in the f.c.c. phase [14]. On the other hand, samples with high $J = 1$ concentration were reported to solidify in the h.c.p. phase on an h.c.p. substrate, even at very low temperature [65].

1.1.1   Quantum nature and anharmonicity
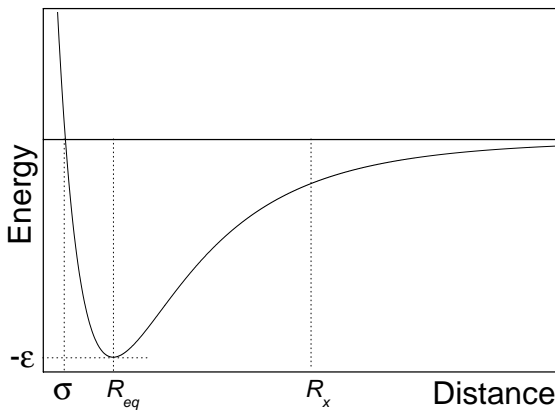
Figure 1.2: Lennard - Jones pair potential.

Solid hydrogen and its isotopes are quantum crystals. This definition relies on the fact that the amplitude of the zero-point lattice vibrations is an appreciable fraction of the lattice constant, as a result of the small mass of the molecules, and the relatively weak intermolecular forces. However, contrary to liquid helium and solid helium in the b.c.c. phase [66], bulk liquid and solid hydrogen are normally not affected by quantum exchange statistics [1,2] [68].

We can define the quantum character of the system with respect to the Lennard-Jones potential, that is typically used to described the intermolecular interactions in van der Waals solids. This isotropic pair potential can be written in the form:

$$V_{LJ} = 4\epsilon \left[\left(\frac{\sigma}{R} \right)^{12} - \left(\frac{\sigma}{R} \right)^{6} \right] \, , \qquad (1.1)$$

which is characterized by the length and energy parameters σ and ϵ defined by $V(\sigma) = 0$ and $V(R_{eq}) = -\epsilon$, where R_{eq} corresponds to the minimum of the potential, $V'(R_{eq}) = 0$. Following these definitions, the Hamiltonian that

---

[1]The absence of quantum exchange in hydrogen seems surprising, considering that its molecular mass is half that of helium. The difference is explained by the weaker pair interaction in helium (well depth 10 K and 30 K in He and H_2 respectively).

[2]Quantum exchange statistics may become relevant in interfacial systems. For example, evidence of superfluid behavior of hydrogen has been reported for a system of 14-16 p-H_2 molecules surrounding a linear carbonyl sulfide molecule inside an He-4 droplet [67].

describes the solid takes the form:

$$H^* = -\frac{1}{2}\lambda^{*2}\sum_i \nabla_i^{*2} + \sum_{i>j} V^*(R_{ij}^*) \ , \qquad (1.2)$$

where the superscript * indicates that the parameters are expressed in units of ϵ and σ: $H^* = H/\epsilon$, $R_{ij}^* = R_{ij}/\sigma$ [3]. The parameter $\lambda^* = \left[\hbar/\sigma(M\epsilon)^{\frac{1}{2}}\right]$, or *de Boer quantum parameter*, yields a quantitative measure of the quantum nature of the system. For a given structure (f.c.c. or h.c.p.), this is the only crystal-dependant parameter in Eq. 1.2: it ranges from 0.01 (solid Xe) to 0.5 (solid He). For H_2 it corresponds to 0.274 [64]. The reduced properties of the solid, like - for instance - the lattice parameter R_0, are continuous functions of λ^*. For $\lambda^* \ll 1$, the crystal behaves classically and $R_0 \sim R_{eq}$. But, as λ^* increases for lighter atoms or molecules, the crystal lattice constant augments as well to minimize the total energy of the solid. If R_0 exceeds the value corresponding to the inflexion point of potential ($R_0 > R_x$ where $V_{LJ}''(R_x) = 0$, see Fig. 1.2), the frequencies of some harmonic modes can become imaginary [4] and the results of the decomposition in normal modes are not longer adequate to describe the properties of the solid.

The presence of normal modes with imaginary frequencies implies that *the configuration of the molecules in the lattice sites is unstable in the harmonic approximation.* This property can be taken as a definition for quantum crystal [15].

The existence of a stable ground state of solid hydrogen, even at zero external pressure, can be understood considering that the instability of the molecules around R_0 is *overcompensated* by the repulsive part of the pair potentials V_{LJ}, as the displacement from the central position increases, and the electronic clouds of neighboring molecules start to penetrate into each other. The ground state can be regarded as an arrangement of relatively large *single molecule* zero-point distributions around the sites of the regular lattice. The low-lying excitations of the crystal are associated to collective oscillations of these distributions around their equilibrium positions.

Figure 1.3 shows the density of one-phonon states in rare gas crystals and in solid Hydrogen.

Figure 1.3: Phonon density of states of van der Waals solids from incoherent neutron scattering experiments. **Top.** Rare gas solids [13]. **Bottom.** Solid H_2 [64]. **Continuous line.** Experimental data. **Dashed line.** Result of harmonic calculation.

The result of the harmonic calculation for H_2 (dashed line in the lower panel) presents a sharp peak just before the cutoff frequency (analogous to the one present in the rare gas spectra in the upper panel), which has no experi-

---

[3]This formulation of the Hamiltonian of the solid is sometimes referred to as *quantum extension of the law of corresponding states.*

[4]In the harmonic approximation, the frequencies ω of the normal modes of a solid are found solving the secular equation $(D - I\omega^2)\vec{u} = 0$, where $\vec{u}$ is the eigenvector associated to a given normal mode and D is the dynamical matrix, which is proportional to $\frac{\partial^2 V}{\partial r_i \partial r_j}$.

mental correspondence. The data points measured beyond the classical Debye frequency (86 cm^{-1}) are a clear indication of the presence of pronounced anharmonic contributions related to the quantum character of the system.

1.2   Rotational states in solid hydrogen

The solution of the Hamiltonian describing the solid in the approximation of *pairwise* and *isotropic* interactions shows that solid hydrogens can be regarded as an assembly of free rotors localized at lattice sites within the translational zero-point motion of the molecules [14]. The wavefunction that solves the Hamiltonian is separable, and the solution of the angular part bears the well known rotational eigenvalues in the form $E = BJ(J + 1)$, where $B = \hbar^2/2I$, and J is the rotational quantum number. The corresponding wavefunction is the spherical harmonic Y_{JM}. For the lowest $J = 0$, the rotational wavefunction of the solid is simply a product of constant terms Y_{00}'s and, therefore, the angular distribution results spherically symmetric. For a generic Y_{JM}, all the $(2J + 1)$ levels of each M sublevel are equally populated, and thus the molecules are not angularly localized. To analyze how the *anisotropic* contribution modifies this picture, we can limit ourselves to the dominant electric quadrupole-quadrupole interaction, and disregard the remaining anisotropic contributions coming from dispersion-induction forces, overlap and exchange interactions. Maintaining even for the anisotropic potential the approximation of pure two-body interactions, it was calculated by a first-order perturbative correction of the two-particle wavefunction that the fraction of rotationally mixed states in the solid should not exceed 1% [14]. The validity of this estimate was first verified measuring the ratio of forbidden to allowed Raman transitions [69]. In the following, therefore, we will assume that J is a good quantum number in the solid.

1.2.1   Normal hydrogen

The thermodynamical equilibrium concentration of odd and even rotational states varies as a function of temperature. At room temperature, for example, the even-J/odd-J ratio is 0.2507/0.7493, and samples with this composition are commonly referred to as *normal*-Hydrogen (n-H$_2$).
This ratio is retained when the gas is cooled down: for n-H$_2$ the residual rotational energy associated with the $J = 1$ molecules at 4 K is as high as 1062 J/mol. This is the reason why, for specific technical applications, samples with exclusively even rotational states (para-H$_2$) are strongly preferred. Liquid p-H$_2$ samples are, for example, economically more convenient to be stored. The heat of conversion is 670 J g^{-1}, which is to be compared with the heat of evaporation of 440 J g^{-1}. The loss of n-H$_2$ from a vessel as a result of this internal heating corresponds to 50% after 170 h [70].
Table 1.1 reports a comparison of the values assumed by a series physical parameters in solid normal- and para-hydrogen under the typical experimental

Crystal	Molar volume $[\mu(\mathrm{m}^3/\mathrm{mol})]$	Lattice parameter [Å]	Sound velocity [m/s]
n-H_2	22.820 [a],[1]	3.76 [b],[2] (h.c.p.)	long. 2190 transv. 1160 [c],[1]
p-H_2	23.064 [a],[1]	3.783 [b],[2] (h.c.p.)	long. 2100 transv. 1140 [c],[1]

Crystal	Thermal conductivity [W/m·K]	Young modulus [MPa]	Shear modulus [MPa]
n-H_2	$\sim 10^{-1}$ [a],[1]	284 [c],[1]	108 [c],[1]
p-H_2	$\sim 10^{2}$ [a],[1]	281 [c],[1]	108 [c],[1]

Table 1.1: [a] Ref. 17; [b] Ref. 64; [c] Ref. 16; [1] at 4 K; [2] from neutron scattering (T=0, P=0).

conditions of this work. We note that the molar volume of solid p-H_2 is slightly greater than that of solid n-H_2. This difference is explained by the presence of the electric quadrupole-quadrupole interactions that pull the molecules closer together when the concentration of the J=1 molecules become important. Conversely, J=0 molecules, because of their high symmetry, do not interact via multipole forces.

1.2.2 Intrinsic conversion

Because of the quantum symmetry and interactions with nuclear magnetic moments, we can not observe $\Delta J = -1$ transitions during the thermal de-excitation process of a homonuclear molecule. This concept relies on the antisymmetric nature of the overall wavefunction under nuclear exchange: in a parallel nuclear spin configuration (ortho-H_2), only the odd rotational levels are present, while the even rotational levels are present only for anti-parallel nuclear spin configuration (para-H_2). If we cool down an H_2 sample to 4 K, the rotational state of an even-J molecule drops down in stages of $\Delta J = -2$ to $J = 0$. Conversely, for an odd-J molecule, J drops down to 1. The low-temperature $J = 1$ molecules remain in a *rotationally metastable* state.

The interaction between J and the total nuclear spin I is expected to slowly allow the transition to $J = 0$ (*conversion*). For a hypothetical isolated H_2 molecule, such a process is absolutely negligible: its time constant corresponds to 10^{12} years! In solid or liquid H_2, the $\Delta J = -1$ de-excitation is favored by the interaction with the magnetic moments of all the neighboring molecules (*intrinsic conversion*). It is remarkable that the asymmetric force that can un-couple the nuclear spins and cause the conversion results much smaller than the

interaction within the nuclear spins of the molecule itself [17]. The transition is, therefore, not expected in a strictly thermodynamic sense, but it is purely quantum mechanical. An additional factor limiting the rate constant of the process is related to the fact that the rotational energy gap in H_2 corresponds to 170 K, well above the Debye cut-off temperature of the solid [64]. The lattice can not take this extra energy in one shot: a 10 times slower two-phonon process is needed for de-excitation. Intrinsic conversion towards equilibrium for H_2 in the solid state at zero pressure takes place with a rate constant as low as 0.019 h^{-1} [64].

Chapter 2

Impurity spectra and phonon coupling

In the following chapter we briefly review a few fundamental aspects of the theory of molecular impurities in solids. In particular, in § 2.2, we introduce the concept of configuration coordinate, that will be extensively used throughout this work. The technique of the moment analysis, which permits to derive effective intermolecular potentials to describe the interactions between an impurity and the surrounding environment, is discussed in § 2.3. The chapter is concluded by an overview on the non-radiative processes that can mediate intramolecular electronic relaxation via phonons.

2.1 The lineshape function

Broadening of the lineshapes in the condensed phase is commonly dominated by the *inhomogeneous* contributions due to the co-existence of multiple sites [1] that lead to different energy shifts of the intermolecular potential energy surfaces. In rare gas and hydrogens solids at very low temperature, only few trapping sites are encountered for small dopant molecules like NO [71]. The line broadening is mainly determined by the coupling of the vibronic transition of the dopant molecule to the excitations of phonons in the matrix (electron-phonon coupling). In general, matrix-isolated molecules have intramolecular vibrational energies much larger than the Debye cut-off of the environment and, consequently, these modes can be treated independently from low-frequency modes of the lattice vibrations (adiabatic approximation). We can associate each vibronic state of the molecule to an intermolecular potential energy surface, which describes the equilibrium positions and the motion of the lattice species when the dopant is in this state. These intermolecular potential sur-

---

[1]Molecule-environment configurations.

faces determine the lineshapes of any vibronic transition of the system.

The normalized lineshape function for the transition from an electronic state $|a\rangle$ to an electronic state $|b\rangle$ is given by [72, 73]:

$$I_{|a\rangle \to |b\rangle}(E) = \left\langle \sum_{\beta} |\langle a\alpha|b\beta\rangle|^2 \delta\left(\epsilon_{|b\beta\rangle} - \epsilon_{|a\alpha\rangle} - E\right) \right\rangle_{T,|\alpha\rangle} . \qquad (2.1)$$

In the expression, $|\alpha\rangle$ and $|\beta\rangle$ represent the phonon levels in the states $|a\rangle$ and $|b\rangle$, respectively. The brackets $\langle \ldots \rangle_{T,|\alpha\rangle}$ indicate that the thermal average on the initial state $|\alpha\rangle$ has to be taken. It is worth nothing that the expected dependence of $I_{|a\rangle \to |b\rangle}$ on the transition dipole moment $\overrightarrow{\mu}$ is absorbed in the normalization factor. In fact, in the Condon approximation, $\overrightarrow{\mu}$ does not depend on the intramolecular separation of the nuclei, and $\langle a\alpha|\overrightarrow{\mu}|b\beta\rangle = \overrightarrow{\mu}_0\langle a\alpha|b\beta\rangle$. Consequently, $|\langle a\alpha|b\beta\rangle|^2$ are intermolecular Franck-Condon factors describing the overlap of the phonon wavefunctions involved in the transition.

The lineshape function just defined consists of a number of δ functions, centered at different energies. The average spacing between adjacent δ functions becomes usually smaller than the spectrometer bandwidth as the number of available phonon states $|\beta\rangle$ increases. Moreover, the fact that these phonon levels are associated to finite lifetimes, and hence widths, explains why the observed spectra are usually not discrete.

The energies $\epsilon_{a\alpha(b\beta)}$ in Eq. 2.1 satisfy the condition:

$$\left[T_N + E_{|a\rangle(|b\rangle)}(\overrightarrow{x})\right] \psi_{a\alpha(b\beta)}(\overrightarrow{x}) = \epsilon_{a\alpha(b\beta)}\psi_{a\alpha\ (b\beta)}(\overrightarrow{x}) , \qquad (2.2)$$

where T_N represents the nuclear kinetic energy operator, $\overrightarrow{x}$ the nuclear coordinates and, finally, $E_{|a\rangle(|b\rangle)}(\overrightarrow{x})$ describes the adiabatic potential in which the nuclei move [2]. This latter can be expanded in a Taylor series in the displacements of the nuclei about their equilibrium position. Performing a normal-mode transformation, the ground-state potential can be written as a function of the normal coordinates q_i, normal masses m_i, and normal frequencies $\omega_{|a\rangle i}$ as:

$$E_{|a\rangle}(\overrightarrow{x}) = \frac{1}{2} \sum_i m_i \omega_{|a\rangle i}^2 q_i^2 . \qquad (2.3)$$

Assuming now the *same* normal coordinates [3] q_i for the excited vibronic state $|\beta\rangle$, we can write

$$E_{|b\rangle}(\overrightarrow{x}) = E^0_{|a\rangle \to |b\rangle} + \sum_i A_i q_i + \frac{1}{2} \sum_i m_i \omega_{|b\rangle i}^2 q_i^2 + \frac{1}{2} \sum_{j>i} B_{ij} q_j q_i . \qquad (2.4)$$

In this expression, the adiabatic energy $E^0_{|a\rangle \to |b\rangle}$ represents the energy difference between the minima of the two potential surfaces (zero-phonon energy). Under specific circumstances, we can further simplify the expression, and neglect the crossed term $\frac{1}{2} \sum_{j>i} B_{ij} q_j q_i$ [73].

---

[2]$E_{|a\rangle(|b\rangle)}(\overrightarrow{x})$ on its turn is the energy eigenvalue of the electronic part of the adiabatic Hamiltonian for state $|a\rangle(|b\rangle)$.

[3]In general, a normal-mode transformation of the excited state $|\beta\rangle$ will yield different normal coordinates q_i, since its symmetry , and hence the adiabatic potential, differs from that of the ground state.

2.2 Configuration coordinate model

The number of normal modes in expressions 2.3 and 2.4 is of the order of $3N$, where N is the number of molecules in the medium. To simplify the analysis of the spectral lineshapes, we can reduce this multi-dimensional surface to a *single harmonic potential*, which represents the equilibrium position and vibration of the solvent species for a given vibronic state of the dopant molecule. The curvature of the harmonic intermolecular potential corresponds to an *effective* phonon frequency. The presence of a relative displacement between the upper and lower curve along the configuration coordinate q reflects a rearrangement of the solvent upon electronic excitation of the dopant. Several different situations can arise, depending on the strength of the interaction between the impurity and the surrounding lattice. We can, in general, distinguish between:

1. *linear coupling*: the frequencies in the ground and excited state are the same $\omega_{|a\rangle} = \omega_{|b\rangle}$, but $E_{|b\rangle}$ contains a term linear in the normal mode displacement;

2. *quadratic coupling*: the two frequencies differ ($\omega_{|a\rangle} \neq \omega_{|b\rangle}$), but the equilibrium configurations are identical;

3. the general case, where both linear and quadratic couplings are present.

Typically, if the impurity-lattice coupling is weak, the rearrangement is minor, and intermolecular potentials result almost parallel. In this situation, the absorption and emission spectra show a narrow zero-phonon line at low temperature. On the other hand, a strong interaction will lead to strongly shifted intermolecular potentials. The absorption spectrum results severely broadened, and an important Stokes shift [4] is observed. These two extreme situations are illustrated in Fig. 2.1.

The configuration coordinate q should be generally regarded an abstract quantity: an *effective* combination of different parameters. However, in few specific cases, it can be directly connected to a *physically meaningful* quantity. In the case of polar solvents, for instance, it can represent the angle of rotation of an ensemble of solvent molecules, responding to a change in the dipole moment of the impurity. For the purpose of this work, as we will see in the following chapters, it can be simply associated to the radial motion of the H_2 molecules surrounding the dopant. Evidently, the assumption that a uni-dimensional cut through the N-dimensional intermolecular potential surface is able to describe the dynamics of a complex system is very crude. However, a justification of its validity can be found *a posteriori*, considering the good agreement among the experimental absorption-emission lineshapes, and those calculated considering exclusively two displaced harmonic potentials and a single configuration coordinate.

---

[4]Energy difference between absorption and emission.
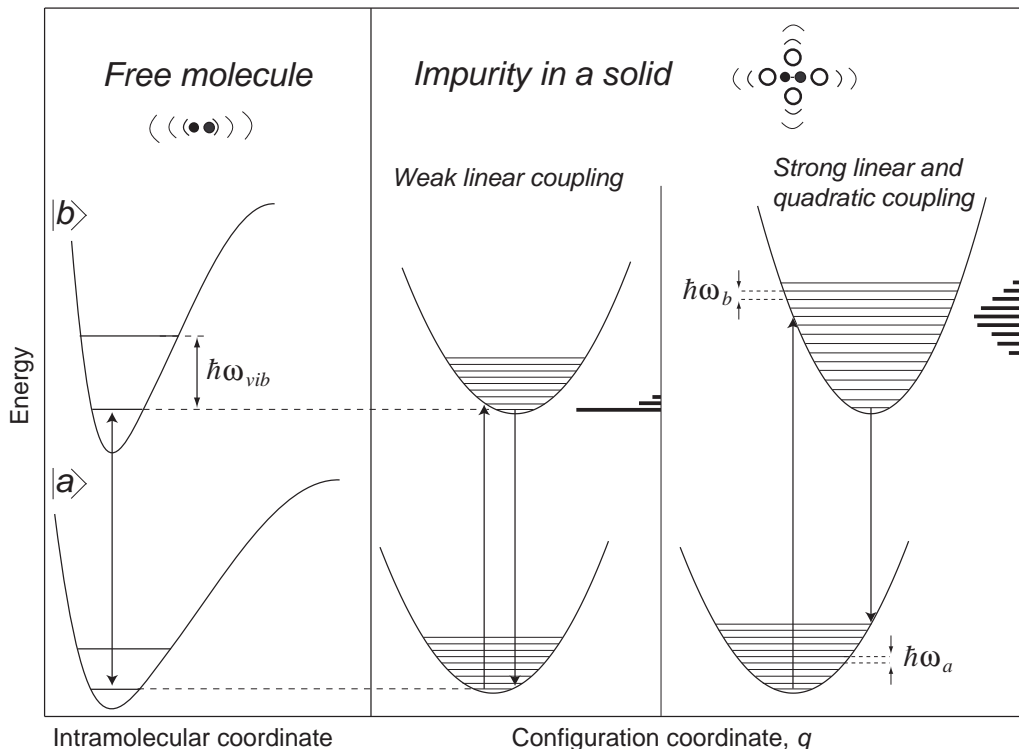
Figure 2.1: Configuration coordinate model. The absorption lineshapes corresponding to the transitions indicated by the arrows are plotted on the right vertical axes.

2.3   The moment analysis

An apposite procedure to derive the effective intermolecular potentials of a system from the experimental lineshapes was first proposed by Lax [72], and successively simplified by O'Rourke [74]. The method results particulary suited for strongly interacting systems, characterized by important absorption-emission Stokes-shifts. The application of this analytical tool to the system of interest for this work will be shortly described in § 3.3, additional details can be found in references 75 and 76.

Briefly, the nth moment associated to the lineshape of a generic $|a\rangle \rightarrow |b\rangle$ transition is defined as

$$M_n = \int_{-\infty}^{\infty} E^n I_{|a\rangle \rightarrow |b\rangle}(E) dE \ , \qquad (2.5)$$

higher moments are usually re-scaled on the area of the lineshape,

$$M_0 = \int_{-\infty}^{\infty} I_{|a\rangle \rightarrow |b\rangle}(E) dE \ , \qquad (2.6)$$

and centered on the first moment, which, in fact, yields the center of gravity of the lineshape. With these definitions, M_2 is essentially proportional to the square width of the band, and M_3 can be considered as a measure of its asymmetry.

We proceed re-writing the expressions 2.3 and 2.4 for a single effective coordinate in the compact form:

$$V_a(q) = \frac{1}{2}m\omega_a^2 q^2$$

$$V_b(q) = E_{ab}^0 + \frac{1}{2}m\omega_b^2(q - \Delta q)^2 \;, \tag{2.7}$$

where E_{ab}^0 is the zero-phonon energy, and Δq indicates the change in the equilibrium configuration among the ground and the excited state. If now we define the following set of substitutions and definitions:

$$\begin{cases} S_b = \Delta q^2 \frac{\omega_b^2}{2\hbar\omega_a} & \text{\textit{Huang-Rhys} factor for emission} \\[2ex] B_b = \frac{\omega_b^2 - \omega_a^2}{\omega_a^2} & \text{\textit{quadratic coupling strength} - emission} \\[2ex] S_a = \Delta q^2 \frac{\omega_a^2}{2\hbar\omega_b} & \text{\textit{Huang-Rhys} factor for absorption} \\[2ex] B_a = \frac{\omega_a^2 - \omega_b^2}{\omega_b^2} & \text{\textit{quadratic coupling strength} - absorption} \;, \end{cases} \tag{2.8}$$

the first two moments for emission (ems) and absorption (abs) satisfy the following *closed* system of equations:

$$\begin{cases} M_1^{\text{ems}} = E_{ab}^0 - S_a\hbar\omega_b - \frac{B_a}{4}\hbar\omega_b \\[2ex] M_2^{\text{ems}} = S_a(\hbar\omega_a)^2 \\[2ex] M_1^{\text{abs}} = E_{ab}^0 + S_b\hbar\omega_a + \frac{B_b}{4}\hbar\omega_a \\[2ex] M_2^{\text{abs}} = S_b(\hbar\omega_b)^2 \;. \end{cases} \tag{2.9}$$

With these figures and interdependent coupling constants, the relaxation energies in the excited and ground states result $E_b^{\text{rel}} = S_b\hbar\omega_a$ and $E_a^{\text{rel}} = S_a\hbar\omega_b$, respectively.

2.3.1 Semi-classical projection method

The projection method is a simple procedure directly derived from the semi-classical version of the Franck-Condon principle. It can be readily applied to obtain the transition lineshapes of impurities, which are homogenously broadened by electron-phonon interaction. Basically, it allows to compute the lineshape function given in Eq. 2.1, without explicitly calculating the intermolecular Franck-Condon factors. The procedure can be used to calculate both

absorbtion and emission lineshapes [77].

In the $T = 0$ limit, we can assume that the initial state of the system is the $n = 0$ gaussian-shaped wavefunction of an harmonic oscillator, with effective frequency $\omega_{a(b)}$ [78]:

$$\psi_{a(b)}(q) \sim \exp\left[-\frac{\omega_{a(b)}}{2\hbar}(q - q_{a(b)}^{eq})^2\right] \ . \tag{2.10}$$

In the equation, $q_{a(b)}^{eq}$ represents the equilibrium configuration of the state $a(b)$. For any given value of the configurational coordinate q, we can calculate the corresponding potential energy difference $\Delta E(q) = V_b(q) - V_a(q)$ from the potentials of Eq. 2.7.

The lineshape, at the end, corresponds simply to

$$I(\Delta E(q)) = |\psi_{a(b)}(q)|^2 \ . \tag{2.11}$$

This procedure is particulary adequate for calculating the lineshapes of the transitions considered in this work. In fact, Rydberg states of NO are characterized by major displacements in the equilibrium positions with respect to the ground state (see chapter 3). Therefore, any vertical transition from the ground state or from the well of an excited state, will realize the excitation of fairly high n levels. It can be shown that the good correspondence between the fully quantum calculation of Eq. 2.1, and the semiclassical approach of Eq. 2.11 depends critically on the values n of the final vibrational states [77]. The method works best for $10 \leq n \leq 20$.

In § 3.3.1 the procedure will be applied extensively to the specific case of an NO impurity embedded in solid hydrogen. The iterative application of the projection method for fitting all the available experimental data (absorption, fluorescence, depletion of fluorescence) will permit to determine a complete set of parameters and describe all the electronic states of interest in the experiment with harmonic potentials in the form of Eq. 2.7.

2.4   Non radiative relaxation processes

Non radiative relaxation pathways can mediate intramolecular electronic relaxation via phonons. If the molecular frequencies considerably exceed the lattice Debye frequency, these medium-induced vibrational relaxation phenomena can be handled in terms of multi-phonon processes of higher order, averaging out the detailed properties of each phonon mode involved. Studies of multi-phonon relaxations of guest molecules embedded in several different solid hosts have shown that the rate W of such processes exhibits approximately an exponential dependence on the energy gap, ΔE, to the next lower level (Fig. 2.2):

$$W(\Delta E) = W(0)e^{-\alpha\Delta E} \ . \tag{2.12}$$

The constants α and $W(0)$ depend generally on the host crystal properties, on the molecule-lattice coupling and, to less extent, on the specific electronic
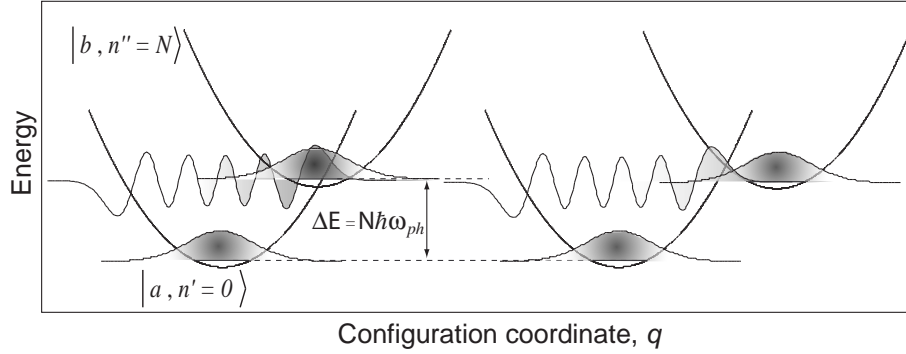
Figure 2.2: The intramolecular non-radiative relaxation between two electronic states of the impurity depends on the relative displacement between the harmonic potentials which represent the two states in the configuration coordinate model.

state of the impurity [79]. The energy gap ΔE is proportional to the number of phonons N, of *mean weighted* frequency ω_{ph}, that have to be created in the lattice to bridge the energy gap. Formula 2.12 holds for $\Delta E = N\hbar\omega_{ph} \gg \hbar\omega_{ph}$, but it must eventually break down for small energy gaps, where the relaxation by one or two phonon processes becomes possible. In this regime, in fact, the statistical averaging that occurs for higher order processes is no longer valid, and relaxation rates become strongly dependent on the phonon density of states and coupling at given frequencies. In Ref. 80, a general expression for Eq. 2.12 is derived under the conditions of $T \to 0$, weak coupling, large N and validity of the mean frequency approximation for the medium phonon spectrum:

$$W_{ba} \sim C \frac{1}{\sqrt{N}} e^{-S} e^{-\gamma N} \ . \tag{2.13}$$

The illustration in Fig. 2.2 visualizes, in the configuration coordinate picture, the two electronic states $|a\rangle$ and $|b\rangle$ interested by the resonant intramolecular relaxation process. The multiplicative term C in Eq. 2.13 accounts for the *intramolecular* Franck-Condon factors and electronic coupling, S is the Huang-Rhys factor defined by Eq. 2.8, and $\gamma = \ln\left(\frac{N}{S}\right) - 1$. In references 81 and 82 non radiative rates of Rydberg and valence states of NO impurities in rare gas hosts are explicitly calculated. Expression 2.13 is thereby re-casted in the explicit form

$$W_{ba} = \frac{2\pi}{\hbar^2\omega_{ph}} |A\langle v''|v'\rangle_R \langle n'' = N|n' = 0\rangle_q|^2 \ , \tag{2.14}$$

where A accounts for the electronic coupling (spin-orbit, Coriolis), while $\langle v''|v'\rangle_R$ is the *intramolecular* Franck-Condon factor calculated at a given intramolecular distance R. The actual values of these first two terms should not differ from the correspondent gas-phase ones. On the other hand, the q dependence of the *intermolecular* Franck-Condon terms $\langle n'' = N|n' = 0\rangle_q$ shows that the overlap of the phonon wavefunctions critically depends on the relative displacement of the potentials of states $|a\rangle$ and $|b\rangle$ along the configurational coordinate (Fig. 2.2). If the harmonic approximation holds, these factors can be expressed as explicit functions of the Huang-Rhys coefficients S, and of the

number of phonons needed to overcome the gap N:

$$|\langle n'' = N | n' = 0 \rangle_q|^2 = e^{-S}\frac{S^N}{N!} \quad .$$

$$(2.15)$$

Chapter 3

Steady state spectroscopy of NO in solid hydrogen

This chapter provides an overview of the UV and visible spectroscopy of NO in solid normal-hydrogen. After a concise review of the spectroscopic properties of isolated NO molecules, the excited states of interest for the time-resolved experiment are characterized both in absorption and in emission in § 3.2. On the ground of these results, we propose a first simple physical model for describing the structural rearrangement which follows the electronic excitation of the NO impurity to a Rydberg state (§ 3.3). In Chap. 5, the spectroscopic results discussed here will be integrated with the characterization of *para*-hydrogen samples, along with a comparison between one- and two-photon excited fluorescence.

3.1   Isolated NO molecule

Nitrogen oxide is a highly reactive open shell molecule. Its gas phase spectroscopy has been reviewed extensively by Miescher and Huber [83]: the $A^2\Sigma \leftrightarrow X^2\Pi$, $B^2\Pi \leftrightarrow X^2\Pi$ and $C^2\Pi \leftrightarrow X^2\Pi$ are the strongest spectroscopic transitions. These bright emission systems can be observed in the aurora spectrum of upper atmosphere of earth [84].
The electronic structure of the molecule corresponds to: [85]

$$(1s_O\sigma)^2(1s_N\sigma)^2(2s_O\sigma)^2(2s_N\sigma)^2(2p_O\sigma)^2(2p_O\pi)^4(2p_N\pi) \ . \qquad (3.1)$$

Its high reactivity is determined by the single un-paired electron in the $2p_N\pi$ nitrogen antibonding orbital. The molecular ground state X is split into $^2\Pi_{\frac{1}{2}}$ and $^2\Pi_{\frac{3}{2}}$ components, separated by 121.1 cm^{-1}. Excited states of valence nature are formed in case an inner electron is excited to a $2p_N$ state. These states (a,b,B) span the energy region between 5 and 9 eV, and are characterized by an intramolecular distance larger than in the ground state, resulting from the occupancy of an antibonding orbital (see Fig. 3.1).
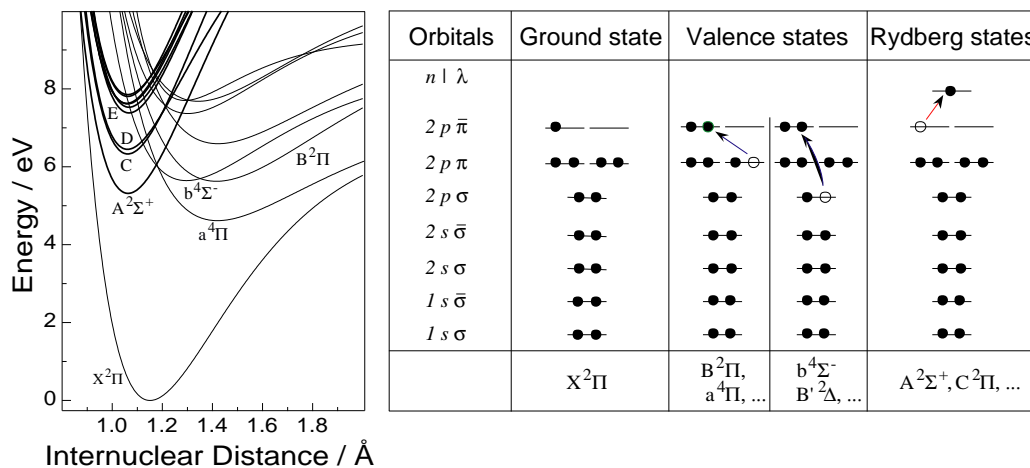
Figure 3.1: **Plot.** Potential energy curves of isolated NO, evaluated by the Morse potential parameters of Ref. 85 **Thick lines.** Rydberg states. **Table.** Electronic structure of the molecular orbitals. The notation $n\ell\bar{\lambda}$ indicates the antibonding orbitals.

Due to its low ionization energy, NO possesses a rich manyfold of Rydberg states from the lowest $A^2\Sigma^+$ at 5.3 eV to superexcited states above the ionization limit. The internuclear distance, in this case, is smaller than for the X state, as an antibonding orbital is emptied. On the other hand, the size of the electronic cloud of the molecule increases, given the change in the main quantum number n. All Rydberg states of NO have nearly parallel potential energy curves, converging to the NO$^+$ ion. This characteristic implies that these states exhibit similar frequencies and posses almost identical equilibrium separation of the nuclei. As a consequence, $\Delta v = 0$ Rydberg to Rydberg transitions are associated with near-unity Franck-Condon factors, resulting from an appreciable overlap of the vibrational wavefunctions. The characteristic vibrational frequencies of the Rydberg progression are generally twice as large as those of the valence states (see Tab. 3.1).

The energy of the nth state of the series, E_n, can be expressed as a function of the ionization potential E_{ion} (9.26 eV) and of the Rydberg constant R (13.6 eV). It corresponds to $E_n = E_{ion} - \frac{R}{(n-\delta_n)^2}$. The quantum defect δ measures the extent of penetration of the Rydberg electron into the core. The more important the penetration (larger δ_n values), the stronger the attraction on the electron exerted by the positive core. The average radius of the orbital

$\langle r_{\text{elctr}}\rangle$ can be calculated as [86]:

$$\langle r_{\text{elctr}}\rangle = \frac{1}{2}\left[[3(n-\delta_n)^2 - \ell(\ell-1)]\right] a_0 \ , \tag{3.2}$$

where a_0 is the Bohr-radius.

Table 3.1 lists the values of δ for the lowest electronic states and the corresponding size $\langle r_{elctr.}\rangle$ [87]. Note that the quantum defect correction represents an important fraction of the main quantum number n for the states of interest in this work (A,C,D).

State	$n\ell\lambda$	E_{00} [eV]	ω_e [cm^{-1}]	$\omega_e x_e$ [cm^{-1}]	B_e [cm^{-1}]	R_e [Å]	δ	$\langle r_{electr.}\rangle$ [Å]
$X^2\Pi$	$2p\pi$	-	1904	14	1.7	1.151	0.786	0.7
$A^2\Sigma^+$	$3s\sigma$	5.465	2374	16	2.0	1.063	1.104	2.9
$C^2\Pi$	$3p\pi$	6.478	2395	15	2.0	1.062	0.782	-
$D^2\Sigma^+$	$3p\sigma$	6.593	2324	23	2.0	1.061	0.735	-
$E^2\Sigma^+$	$4s\sigma$	7.531	2375	16	1.986	1.067	1.186	6.4
$B^2\Pi^+$	$2p$	5.692	1037	7.7	1.092	1.416	-	-
$b^4\Sigma^-$	$2p$	5.72	1206	15	-	-	-	-
$a^4\Pi$	$2p$	4.68	1017	11	-	1.415	-	-

Table 3.1: Molecular constants of NO in the gas phase. E_{00} energy difference with the ground state; ω_e harmonic constant; $\omega_e x_e$ anharmonic constant; B_e rotational constant; R_e equilibrium internuclear separation; δ quantum defect and $\langle r_{electr.}\rangle$ average radius of the orbital.

3.2 NO in solid hydrogen

The spectroscopy of NO isolated in rare gas matrices has been characterized in several previous works [75,82,88–90]. In the following, we will briefly review the main results for solid hydrogens [35,76,91].

3.2.1 Fluorescence spectroscopy

Figure 3.2 shows the **fluorescence spectrum** obtained upon laser excitation of the $A \leftarrow X$ transition at two distinct wavelengths . The lower plot corresponds to laser excitation at 210.10 nm. It shows exclusively the $A(0,v'')$ progression. The fluorescence spectrum in the upper inset, on the other hand, corresponds to the $A(1,v'')$ series, obtained exciting at 193.3 nm by an ArF laser. Weaker peaks, corresponding to $A(0,v'')$, show up even at this laser
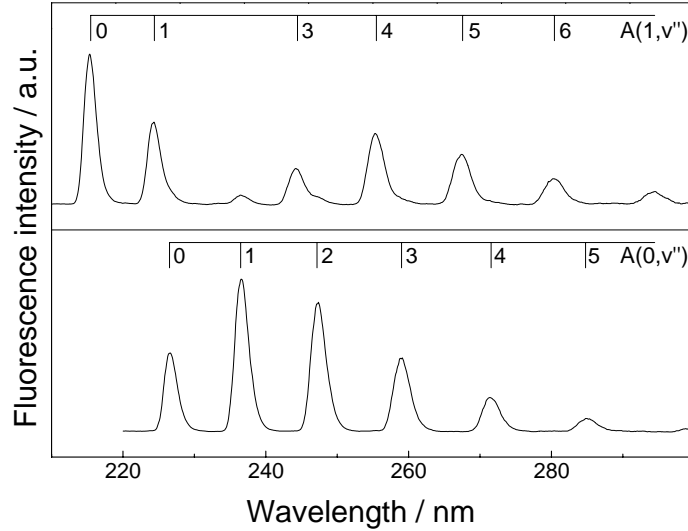
Figure 3.2: *A* state emission spectrum in solid hydrogen [76]. **Top**. Laser excitation at 193 nm. **Bottom**. Laser excitation at 210 nm.

energy. Their presence is due to the excitation of the blue tail of the $A(v' = 0)$ absorption band which overlaps the $A(v' = 1)$ at this wavelength [1]. The origin bands $A(1, 0)$ and $A(0, 0)$ peak slight to the red of the corresponding gas phase energy (about 15 meV for the $A(1, 0)$). The bands of both progressions are asymmetric and show a red wing. Their full width half maximum corresponds to about 350 cm^{-1}. No further details of the structure are revealed improving the resolution to 0.1 nm. The fluorescence decays monoexponentially from both vibrational states with lifetimes of 185 ± 15 ns ($A(0, v'')$) and 65 ± 5 ($A(1, v'')$). The quantum efficiencies can be calculated in the order of 1 and 0.3 respectively, given that the gas phase lifetime corresponds to 200 ns [92]. The lower efficiency of the $A(1, v'')$ progression points to depopulation via non-radiative channels, but no valence emission band is observed in the region above 300 nm upon excitation at 193 and 210 nm (see also § 3.2.3).

Fluorescence-excitation spectroscopy.   The $A(v' = 0)$ excitation spectrum presented in Fig. 3.3 was measured using synchrotron radiation [35]. It reveals a broad $A(0, 0)$ absorption band (FWHM 1900 cm^{-1}) at 6 eV with large asymmetry on the high energy side. The small shoulder appearing on the rise of the large feature is identified as the red wing of the $A(2, 0)$ absorption band, on the basis of its width, and of the vibrational spacings of the A state [35]. The large peak at 6.9 eV can be decomposed into two contributions associated with the ground-state absorption of the Rydberg C and D states. In fact, it can be fitted by two gaussians with $C - D$ energy separation taken from the gas phase, assuming for both the same width of the A band.
Valence transitions, recognized as progression of the B, B' and G states, appear as sharp negative dips up to 9 eV.

---

[1]The existence of an $A(v' = 1) \rightarrow A(v' = 0)$ non-radiative channel can be ruled out simply considering that the observed rise-time of the $A(v' = 0)$ band results shorter than the laser pulse-width (15 ns), while the decay of the $A(v' = 1)$ band corresponds to 65 ns.
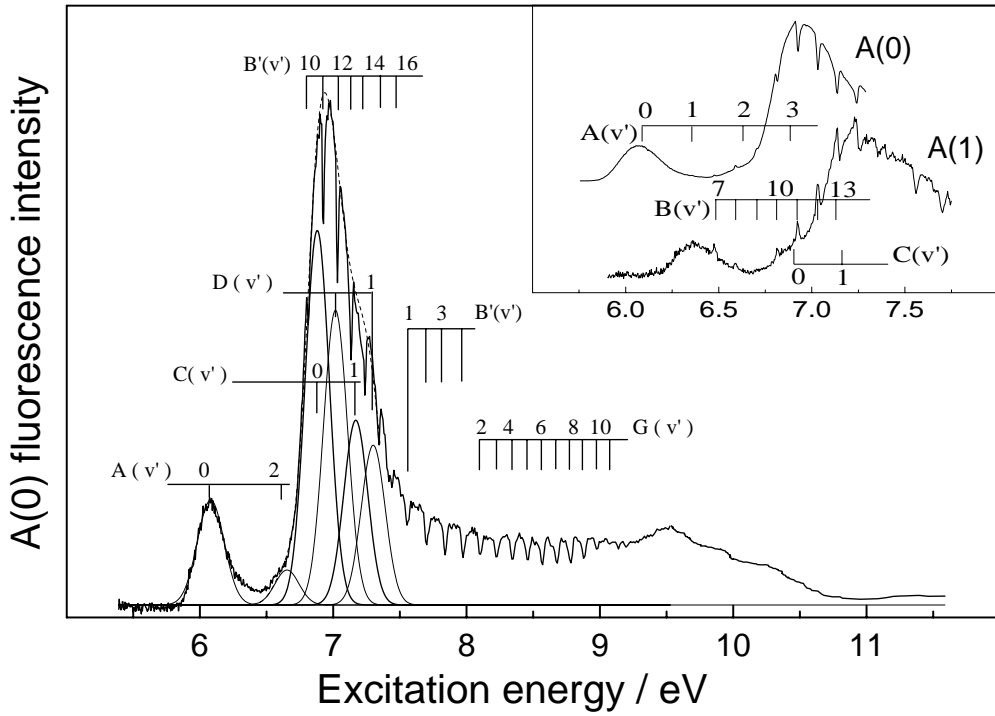
Figure 3.3: $A(0)$ fluorescence excitation spectrum [35]. **Inset**. Comparison between the $A(0)$ and $A(1)$ excitation spectra.

In the inset, the low energy range of the $A(v' = 0)$ excitation spectrum is compared with the corresponding region of the $A(v' = 1)$ spectrum. The $A(1,0)$ band shows up with the expected vibrational shift, and it is followed by a large structure identified with the red wing of $C(1,0)$. This feature is preceded by a shoulder on the red side at 6.9 eV, corresponding to the A(3,0) absorption band. The origin of positive peaks in the same spectral positions of the $A(v' = 0)$ dips will be discussed in § 3.2.3. We note that the $A(0,0)$ and $A(1,0)$ bands present a non negligible overlap in the energy region between 6.2 and 6.35 eV.

3.2.2 Excited state absorption

The excited A state absorption spectrum in solid n-H$_2$ measured by pump-probe two-color nanosecond spectroscopy is shown in Fig. 3.4 [91].
One can observe a broad band peaking around 1.03 eV, which is identified with the absorption of the C and D states. The assignment of this feature to two distinct components is made in light of the results in rare gas matrices, where the $A \rightarrow C$ and $A \rightarrow D$ bands are always the narrowest structures present in the depletion spectrum. The additional band around 1.1 eV is tentatively assigned to a transition to the next higher Rydberg state, $E^2\Sigma^+(4s\sigma)$. This identification, however, needs to be confirmed. It is very likely that it is associated to more than a single component, given that its width is significantly

larger than that of C and D. Finally, a weak but reproducible shoulder, labelled S in the figure, can be observed at 0.96 eV.
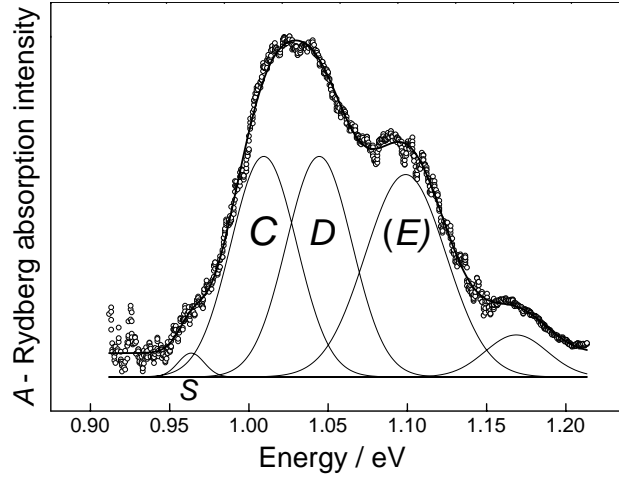
Figure 3.4: A state fluorescence depletion spectrum [91].

Transitions	E_{gas}	E	Γ	ΔE
$X \rightarrow A^2\Sigma^+$	5.48	6.08	0.240	0.60
$X \rightarrow C^2\Pi$	6.50	6.88	0.215	0.38
$X \rightarrow D^2\Sigma^+$	6.60	7.02	0.215	0.42
$A^2\Sigma^+ \rightarrow X$	5.48	5.47	0.053	-0.01
$A^2\Sigma^+ \rightarrow S$	-	0.096	0.039	-
$A^2\Sigma^+ \rightarrow C^2\Pi$	1.02	1.01	0.097	-0.01
$A^2\Sigma^+ \rightarrow D^2\Sigma^+$	1.13	1.05	0.097	-0.08
$A^2\Sigma^+ \rightarrow E^2\Sigma^+$	2.07	1.10	0.120	-0.97
M_1^{abs}	-	-	6.097	-
M_1^{em}	-	-	5.467	-
$M_1^{\text{abs}} - M_1^{\text{em}}$	-	-	0.630	-

Table 3.2: Energies (E), FWHM (Γ) and gas to matrix shifts (ΔE) of the ground and A state absorption and emission bands of NO in solid H_2. The first moments M_1 of the $A \leftrightarrow X$ bands and their differences are also reported. S stands for the shoulder structure at 0.96 eV. All entries are in eV.

3.2.3 Non radiative processes

A **state** $\leftrightarrow$ **valence states.** The reduced quantum efficiency of the $A(1)$ state is ascribed to non radiative relaxation processes from Rydberg to valence states [35]. Using Eq. 2.14, the non radiative rates were computed for all the
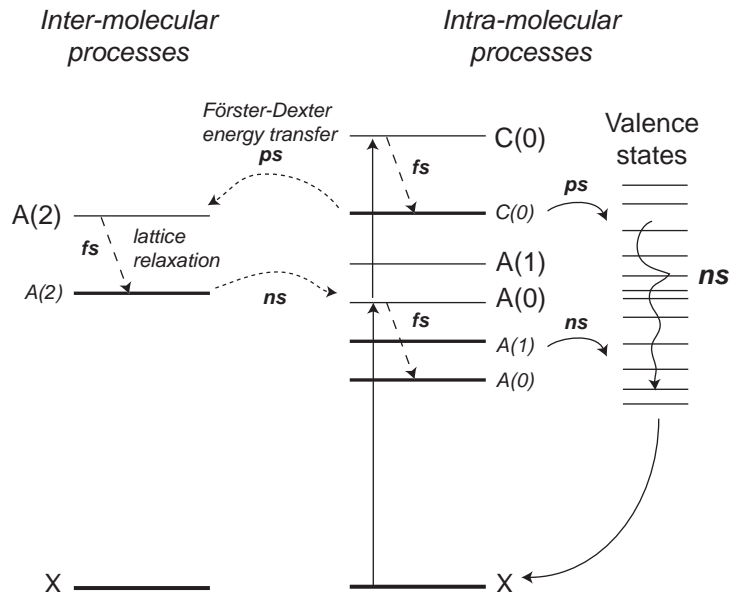
Figure 3.5: Schematic diagram of non-radiative relaxation mechanisms of NO in H_2 by intramolecular and energy transfer processes. The typical timescales associated to the different processes are reported. The dashed arrows indicate the sub-picosecond lattice relaxation processes associated to the absorption-emission Stokes-shift shown in Fig. 3.6 [35].

possible pairs of near-resonant Rydberg-valence levels involving the $A(v' = 0)$ and $A(v' = 1)$ levels [35]. It was found that the $A(1) \rightarrow b(1)$ pathway is the best candidate to account for the 10^{-7} measured rate.

On the other hand, the existence of a valence to Rydberg relaxation channel is observed in the excitation spectrum of $A(v' = 1)$, where the vibrational levels of the B states appear as positive peaks (see inset in Fig. 3.3). This is not the case for $A(v' = 0)$, all the features associated to valence states, in fact, appear as dips in the spectrum.

Higher Rydberg states $\rightarrow A$. As the strong contribution of the C state to the fluorescence of the A state, indicated by the presence of the big structure at ~ 7 eV in Fig. 3.3, can not be mediated by valence states, it is most likely associated to a Förster-Dexter type energy transfer via the pathways: $C(0) \rightarrow A(2) \rightarrow A(0)$ and $C(1) \rightarrow A(3) \rightarrow A(1)$. This mechanism, illustrated in Fig. 3.5, accounts as well for the presence of negative B bands in the excitation spectrum of $A(v' = 0)$: they happen to be in resonance with the $A(2)$ band. The depopulation towards these levels compete with the Förster-Dexter transfer to $A(0)$, quenching the fluorescence.

The hypothesis of Förster-Dexter mechanism is qualitatively confirmed by the NO concentration dependence of the C state contribution to the excitation spectrum. Larger concentration corresponds to shorter statistical separations among donor and acceptor molecules, and to an increased efficiency of the transfer [2]. *This relaxation process can easily be suppressed by lowering the*

---

[2]The rate associated with the Förster-Dexter energy transfer implies a r^{-6} dependence on the donor-acceptor distance.

dopant concentration.

Considering now exclusively *intramolecular* relaxation processes, the possibility of a $C(0) \rightarrow A(0)$ radiative de-excitation can be ruled out, because there is no observation of such a process in the IR region. Moreover, if it was taking place, an analogous transition from the C to the X state would be observable, given that the oscillator strength of this transition is 6 times larger than the one from C to A [93]. The lack of radiative de-activation of the C state is not surprising, as it is strongly electronically coupled with the valence B state [94]. Table 3.3 summarizes the population decay rates from B to A.

Initial state	Final state	Rate [s^{-1}]
$C(1)$	$B(11)$	10^{10}
$B(6)$	$A(1)$	$10^6 - 10^7$
$C(0)$	$B(9)$	10^{12}
$B(4)$	$A(0)$	$10^3 - 10^4$

Table 3.3: Rates for the intramolecular $C \rightarrow A$ relaxation via B in solid H_2 [35].

To conclude, if we consider that:

1. at the low dopant concentration used in the present work (0.05%) the Förster-Dexter mechanism is negligible;

2. the $C \rightarrow B$ rate corresponds to $\sim 10^{10}$ s^{-1};

3. no infrared $C \rightarrow A$ emission has been observed;

4. there is not a $C \rightarrow A$ non-radiative channel;

we can safely neglect any mechanism feeding population from higher Rydberg states back into the A state in the analysis of the results of the time-resolved experiment presented in the next chapters.

3.3   The bubble model

In the upper panel of Fig. 3.6 are reported the $A \leftrightarrow X$ transition in absorption (from the excitation spectrum) and emission of NO embedded in solid hydrogen. The large blue gas-to-matrix shift of absorption, the broadening, and the Stokes-shifted emission point to a strong electron-phonon coupling, as illustrated in Fig. 2.1. Indeed, the bands are broad and lack a zero-phonon line. The absorption-emission Stokes-shift reflects a severe medium rearrangement around the excited molecule. The blue shifted absorption, in fact, can be explained by the repulsive interaction exerted among the electron, promoted to an orbital characterized by an average radius comparable to the nearest
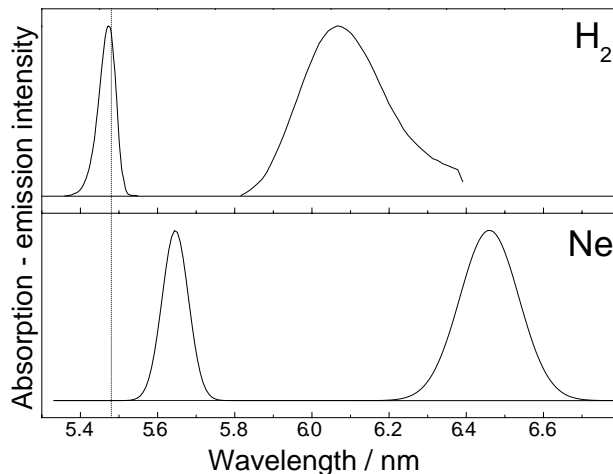
Figure 3.6: Absorption and emission bands of NO embedded in cryogenic crystals [76, 95]. **Dotted line:** gas-phase transition. **Top.** Hydrogen matrix. **Bottom.** Neon matrix.
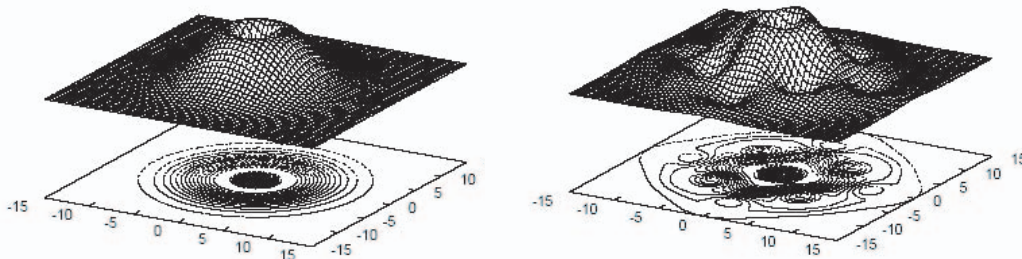
Figure 3.7: Amplitude of the A orbital in a plane perpendicular to the molecular axis, distances in bohr units [96]. **Left.** Free NO. **Right.** NO embedded in Ar matrix.

neighbor distance in the crystal, and the molecules belonging to the first shell of lattice neighbors.

To better visualize this scenario, Fig. 3.7 presents a result obtained by Groß and Spiegelmann, who calculated the matrix induced modifications on the A state of NO embedded in Ar matrix [96]. The orbital in the crystal is strongly perturbed, and exhibits avoidance at the sites occupied by the matrix atoms.

On the other hand, the emission energy (slight to the red of the gas-phase value), and its bandwidth (53 meV) suggest a very loose environment around the molecule after the structural re-organization.

There is a close analogy between these features and those reported in the case of neutral atoms (metastable helium, alkaline-earth-metal atoms, alkali metal atoms) in liquid [97–106] and solid helium [107, 108], and in the case of atoms or molecules excited to Rydberg states in rare-gas matrices [75, 109], which have been all interpreted in terms of formation of a spherical cavity around the excited solute. The assumption of a simple radial displacement of the matrix species is reasonable, since the $3s\sigma$ orbital of the A state nearly conserves

its spherical symmetry [110].

The mechanism of bubble formation is schematically depicted in Fig. 3.8. Excitation of NO promotes the sole unpaired electron of the ground state to the *A* Rydberg orbital. Pauli repulsion moves the first shell away from the impurity, leading the formation of the spherical bubble. Once a new equilibrium is reached in the expanded cage, fluorescence with a lifetime of several hundreds of nanoseconds brings the system back to the ground state. Finally, immediately following fluorescence, cage contraction drives the system back to its initial configuration.

This model has been successfully applied to the study of structural relaxation processes triggered by the *A* state excitation of NO impurities in rare gas matrices like argon [111], neon [112, 113], hydrogen and deuterium [20]. Even if the results of the steady state spectroscopy on all these systems share similar features, solid hydrogens present peculiarities associated with their quantum nature.
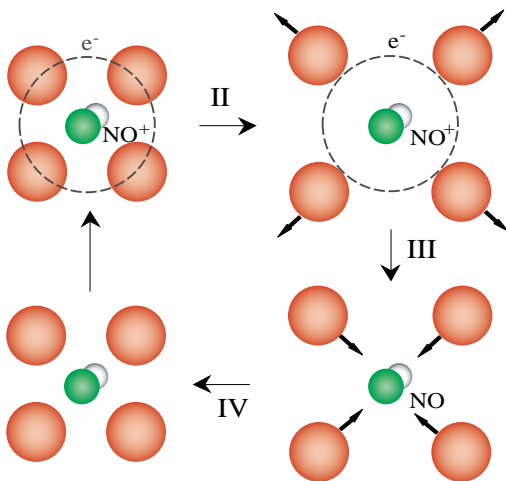
Figure 3.8: Schematic representation of the bubble formation and dynamics

In rare-gas matrices, the observation that the bandwidth of absorption and its shift with respect to the gas-phase value increase, going down in mass from solid xenon to solid neon [75], is explained in terms of increasing repulsion with decreasing cage size [114]. Although this trend is reproduced going from deuterium to hydrogen, the observed blue shift is weaker than expected when compared to the rare gas series. This effect is explained invoking the delocalized character of the ground-state wavefunction [35, 91].

Briefly, the long range region of the two-body potential that describes the NO *A* - H_2 interaction is the less steep (i.e. repulsive), thus a very broad wavefunction samples more efficiently than a localized one the softer part of the potential, and this, in turn, results in a weaker shift of the absorption. On the other hand, the absorption bandwidth in hydrogen (240 meV) is the largest of all the series, and, together with the one measured in deuterium, bears a clear asymmetry on the high energy side (Fig. 3.6 upper panel). For comparison, the bandwidth in neon, which is the broadest observed in rare gas hosts, is 180 meV, and has a perfectly gaussian shape (Fig. 3.6 lower panel). The quantum nature of solid hydrogen is again at the origin of the broadening, and the asymmetry of this feature: the increased bandwidth can be accounted considering that the ground state wavefunction spans a much larger range of the ground state potential, because of the zero-point energy. Following the semiclassical approach introduced § 2.3.1, the calculated absorption spectrum results non-zero only if the energy difference

between the two potentials is sampled by the ground state wavefunction. In other words, when the wavefunction is projected to the excited state potential, the energy region that gives contribution to the spectrum is proportional to the delocalization of the ground state wavefunction.

3.3.1 Derivation of the intermolecular potentials

The description of the structural re-arrangement in terms of radial expansion of a microcavity around the solute defines a *natural* configuration coordinate to model the process: the radius of the bubble delimited by the first shell of lattice neighbors [3]. The scheme shown in Fig. 3.8 can, therefore, be immediately associated to a set of uni-dimensional parabolic potentials, equivalent to the ones introduced by Eq. 2.7. The parameters describing these potentials can be extracted applying the procedure discussed in chapter 2. The moment analysis is applied on the absorption and emission band of the $A(0)$ state to extract potential curves for the ground state, and the first Rydberg states in the configuration coordinate model [35, 75]. Then, *assuming* the reduced mass of the system to be correspondent to the first shell of lattice neighbors around the impurity, the bubble radius r can be expressed as a function of the configuration coordinate through the equivalence:

Figure 3.9: Harmonic intermolecular potentials associated to the ground and first three Rydberg states of NO corresponding to the parameters reported in Tab. 3.4.

$$\Delta r = \frac{\Delta q}{\sqrt{M}} \ , \tag{3.3}$$

where M corresponds to the mass of 12 hydrogen molecules.
The $n = 0$ phonon wavefunctions of the ground (X) and excited state (A) are now explicit expressions of r and M (see Eq. 2.10),

$$\psi_{X,A}(r) = \sqrt[4]{\frac{M\omega_{X,A}}{\pi\hbar}} \exp\left[-\frac{M\omega_{X,A}}{2\hbar}(r - r_{X,A}^{eq})^2\right] \ . \tag{3.4}$$

The wavefunction of the ground state is projected onto the A potential to fit the absorption profile, both in energy and shape, whereas the emission lineshape is reproduced projecting the A state wavefunction on the ground state

---

[3]As a first approximation, the initial cage radius can be taken as the nearest neighbor distance in the pure solid. However, given that the pair potential for the NO-H_2 complex is slightly deeper than the corresponding H_2 -H_2 pair potential, the bubble radius may be smaller than 3.8 Å.

(Eq. 2.11). The parameters of the parabolic potentials are adjusted by consecutive iterations of this procedure. When the harmonic potentials of the states X and A are established, the same principle can be iteratively applied to fit the higher Rydberg levels C and D, optimizing their parameters for fitting the absorption to these states both from the well of the ground and A state. For X and A, since the number of adjustable parameters (adiabatic energy, curvature, spatial displacement) matches the number of constrains (absolute energies of the transitions and spectral profiles), it results always possible to solve the system and find the correct set of parabolic potentials. For higher Rydberg states, on the contrary, the situation is complicated because the spectroscopic characterization is not complete (i.e. emission bands are not observed). In the case of argon and neon matrices, it is not possible to find a unique harmonic potential describing C and D capable to reproduce the ground state absorption, and A state depletion bands at the same time. Remarkably, in the case of solid hydrogen, a unique parabolic curve satisfactorily interpolates both lineshapes. Table 3.4 contains the parameters obtained with the projection method corresponding to the curves in Fig. 3.9. The comparison between measurements and fits is shown in Fig. 3.10.

	$X^2\Pi$	$A^2\Sigma^+$	$C^2\Pi$	$D^2\Sigma^+$
ω [cm^{-1}]	60	111	116	126.5
Δr [Å]	-	0.93	0.71	0.75
E_{ZP} [eV]	-	5.60	6.585	6.625

Table 3.4: NO-H$_2$ intermolecular potential parameters extracted from the moment analysis in the configuration coordinate model. ω is the effective phonon frequency associated with each state; Δr is the cage radius increment with respect to the ground-state equilibrium configuration; E_{ZP} is the zero-phonon transition energy.

The final dimension of the bubble after structural relaxation, in the emission configuration, can be calculated from the equilibrium position of the A state: $r = 4.73$ Å. The bubble increment associated with structural relaxation corresponds to about 30% of the initial cage radius. This value compares well with analogous estimates found in literature. Poll and co-workers, for instance, associated the broad absorption observed in solid deuterium samples irradiated with proton-beams with electrons localized in cavity-like states [115,116]. They calculated a cavity radius of 4.75 Å, which would correspond to an increment of about 1.2 Å of the initial cage in our experiment. Molecular dynamics simulations, based on independently extracted pair potentials, give very similar estimates for the radius increment, as discussed in chapter 7.

The effective frequency of the phonon state associated to the ground electronic level of the impurity, X, falls well inside the experimental one-phonon density of states of solid hydrogen, shown in Fig. 1.3. This point enforces the assumption that the environment is not perturbed when the impurity is in its ground state. On the other hand, the A state frequency lies at the edge of the phonon spectrum, even if it is not easy to determine the exact cut-off value due to the sparse experimental data in the high frequency region.

A final remark should be made about the radius increment of the states C and D reported in Tab. 3.4. We remind that both these states stem from p-type atomic orbitals (Tab. 3.1). The Δr value, consequently, should be considered as an averaged cage radius increment. The fact that it bears values shorter than the equilibrium position of the A state can be related to the smaller electronic density at the nodal plane, which favors the attraction of the lattice species around the impurity, diminishing the mean radius [117].
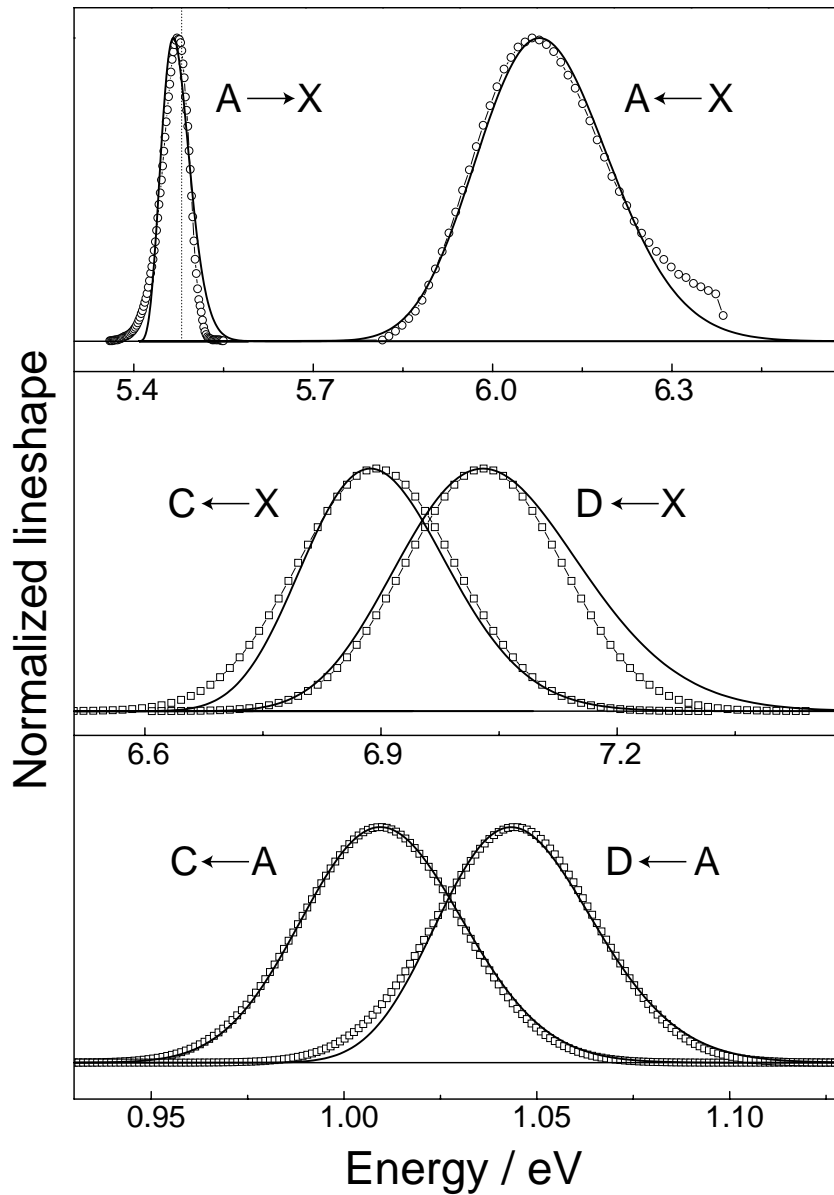
Figure 3.10: Results of the lineshape analysis. **Circles.** Experimental data. **Squares.** Gaussian fits to experimental data from Fig. 3.3 and 3.4. **Lines.** Simulated lineshapes.

Chapter 4

Experimental

The first section of the chapter contains an overview of the set-ups used for the steady-state characterization of the samples: Raman, absorption and fluorescence. In § 4.2, we discuss the scheme applied to probe in real time the structural dynamics in hydrogen, and we motivate the choice to excite the Rydberg A state of NO by two photons. The details of the set-up for the time-resolved experiment are successively presented in § 4.3, with particular focus on the detection scheme. The chapter is concluded by the description of the vacuum system, and of the sample preparation.

4.1 Set-ups for the steady state spectroscopy

Different spectroscopic techniques were used to characterize the samples and to derive the parameters for the intermolecular potentials. In particular, *Raman scattering* was employed to determine the exact ortho/para concentration of pure hydrogen crystals, as discussed in § 5.1.1. *Absorption* measurements of NO embedded in para- and normal-hydrogen were performed to complete the comparison between the two hosts (the fluorescence excitation spectrum measured at synchrotron presented Fig. 3.3 was taken exclusively for normal hydrogen).

The NO *fluorescence* spectrum upon laser excitation was routinely measured using the same set-up employed for the time-resolved experiment, described in details in § 4.3.2.

4.1.1 Raman

A YLF laser (SPECTRA PHYSICS, MILLENIA) at 532 nm was used as light source. The laser light was dispersed in a monochromator (JOBIN-YVON, 270M) equipped with a 300 grooves/mm grating, and detected by a nitrogen cooled CCD camera (JOBIN-YVON, SPECTRUM ONE). The intensity of the laser scattered light was reduced using a long-wave-pass edge-filter (SEMROCK). In order to increase the strength of the Raman signal, the samples were prepared depositing on the substrate up to 5 times more hydrogen than normally (see § 4.4.3).

4.1.2 Absorption

A stabilized deuterium lamp (HAMAMTSU) was employed for the absorption measurements. The light of the lamp was collimated with a system of two diaphagrams of 2 mm aperture and two quartz lenses. The light spot on the sample was about 1 cm diameter. The light was successively focussed by a third fused silica lens onto the entrance of a monochromator (ACTON, ARC) equipped with 600 grooves/mm grating blazed at 150 nm and, finally, detected by an UV-enhanced nitrogen cooled CCD camera (PRINCETON APPLIED RESEARCH, OMA VISION). The NO absorption spectra in para- and normal-hydrogen (Fig. 5.3) were calculated using as baselines the spectra measured on neat hydrogen crystals of equivalent thickness.

4.2 Methodology of the ultrafast experiment

The easiest approach to follow spectroscopically the structural-relaxation in the A state (i.e. the bubble expansion) would be a fluorescence experiment in the femtosecond domain. However, this method is not easy to implement. An experimentally simple (and background-free) approach resides in the possibility, schematically illustrated in Fig. 4.1, to induce transitions to higher Rydberg states. Following this approach:

1. the experimental observable is the depletion of the A state fluorescence, which can be detected in a time-integrated fashion as a function of the pump-probe delay;

2. transitions from the A to the C and D states lie in the near infrared energy region (~ 1 eV), and pulses in this spectral range can be easily produced and tuned by an optical parametric amplifier (OPA);

3. $A - C$ and $A - D$ transitions are characterized by near unity Franck-Condon factors (see § 3.1) and, consequently, the depopulation of the A state is expected to occur only to distinct Rydberg states;

4. as discussed in § 3.2.3, A is not re-populated from the C and D states.

The main drawback of the approach resides in the necessity to provide the exact topology of the accessible Rydberg states above A. As detailed in § 3.3.1, this task has been accomplished applying the moment analysis to the lineshapes of the C and D absorptions from the ground state and from A. The lack of any emission from these states, necessary to close the system of equations 2.8, can be overcome since the potentials of the states X and A are *fully* and *independently* determined.
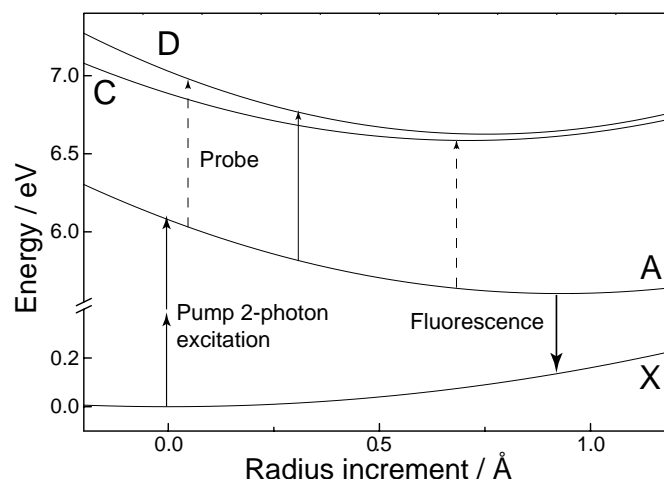
Figure 4.1: Schematics of the time-resolved experiment. The excess energy above the potential minimum after the excitation corresponds to 0.47 eV. Note that different probe wavelengths open different observation windows, and that different configurations can be associated to the same probe energy (**dashed arrows**).

The energy of the probe pulse can be tuned in order to match the $A - C$ and $A - D$ energy difference corresponding to different cage configurations. It should be noted that *one* or *several* configurations of the cage can correspond to a given probe energy, as indicated by the dashed arrows in Fig. 4.1.
As suggested by the scheme, at first, a pulse in the hard UV region (*or centered around 400 nm*) excites (*by two-photons*) the NO impurity to the A state, creating a wavepacket of intermolecular modes, which starts evolving along the potential. Successively, the probe pulse arrives on the sample, retarded with a continuously adjustable time delay. If the wavepacket is passing through the observation window associated to the energy of the probe as the latter reaches the sample, it is resonantly transferred to the C or D state. The resulting decrease in the A state population determines a depletion of the fluorescence signal, which is experimentally detected as a function of the pump-probe time delay (Eq. 4.3).
The actual observation windows are calculated projecting the spectral shape of the probe pulse on the $A - C$ and $A - D$ difference potentials (Eq. 7.10). Evidently, the spectral bandwidth of the probe limits the resolution of the experiment in the configuration-coordinate space: a typical width of 15 nm (HWHM) around 1200 nm corresponds to a radius uncertainty of 0.08 Å for
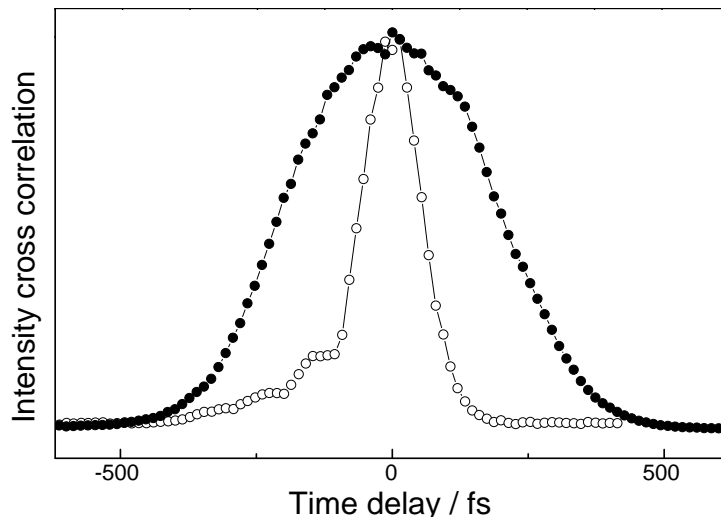
Figure 4.2: Experimental pump-probe cross correlations measured by frequency sum in a BBO crystal. **Open circles:** 400 nm and infrared. **Filled circles:** 200 nm and infrared.

measurements in the linear regime of probe intensity (see also Fig. 6.4).

4.2.1   Choice of the excitation scheme

The motivation for adopting a two-photon excitation scheme in the experiment is principally related to the improvement of the time-resolution. The latter is limited predominantly by the time broadening of hard UV pump pulses (200 nm) when passing through all the refractive optical elements, and, in particular, through the thick quartz window of the vacuum chamber. Considering that the group velocity dispersion parameter for fused silica is 17 times bigger at 200 nm than at 400 nm [118], exciting the $X \rightarrow A$ transition by a two-photon process is the easiest way to minimize the pulse broadening. In addition, contrary to VUV pulses, the broadening of 400 nm light can be pre-compensated by adding a negative chirp using a double-prism compressor (see Fig. 4.3). The actual experimental pump-probe cross correlations obtained in the one- and the two-photon experiment are shown in Fig. 4.2. The main disadvantage when pumping the system at 400 nm is associated to the reduced excitation efficiency, intrinsic to any multiphoton process. The resulting decrease in the number of emitted fluorescence photons can greatly affect the signal to noise ratio of the time-resolved measurements. However, by improving the detection scheme we overcome this limitation (§ 4.3.2).

Two-photon absorption.   In 1931 Maria Göppert-Mayer (Nobel prize laureate in 1963) theoretically predicted that a molecule could absorb two photons in a single quantized event [119]. This possibility represented a formerly unrecognized solution of Dirac's dispersion equation. The experimental verification of this prediction was postponed until the development of the laser in the early

60's.

The Lambert-Beer expression for absorption can be extended to include two-photon processes in the form:

$$\frac{\mathrm{d}I}{\mathrm{d}z} = -\left[\alpha + \beta I G^{(2)}\right] I \; . \tag{4.1}$$

In this expression, I indicates the source intensity, α and β the one- and two-photon absorption coefficients respectively, and $G^{(2)}$ a second order coherence function measuring the intensity correlation at two different space-time points. The I^2 and $G^{(2)}$ dependence in Eq. 4.1 suggests that the two-photon absorption process can be strongly enhanced in the case of femtosecond laser sources, which can provide strong space-time correlations between photons in the same pulse, and, moreover, high peak power at relatively low energy.

Indeed, the molecular two-photon absorption rate ϕ, calculated for pulsed excitation at a given average power P, is proportional to

$$\phi \sim 0.56 \frac{1}{\tau f} \sigma_2 \frac{P^2}{(\hbar\omega A)^2} \; , \tag{4.2}$$

where τ is the pulse width, f denotes the repetition rate, σ_2 represents the two-photon cross section, $\hbar\omega$ is the photon energy, and A the focal area. The factor 0.56 holds for hyperbolic-secant-squared shaped pulses [120]. The relationship between the two-photon absorption coefficient β of Eq. 4.1 and σ_2 is given by $\beta = 2N\sigma_2/\hbar\omega$, where N represents the molecular number density.

The gas-phase two-photon absorption cross section for the $A^2\Sigma^+(v' = 0) \leftarrow X^2\Pi(v'' = 0)$ transition of NO corresponds to $(1.5\pm1.8)\cdot10^{-49}$ cm^4 s [121,122].

4.3 The pump-probe set-up

4.3.1 Laser system

Ultrashort laser pulses are generated by a commercial femtosecond laser system from SPECTRA PHYSICS (SP), equipped with a regenerative amplifier.

Titanium:Sapphire oscillator. The laser oscillator (SP, TSUNAMI) is pumped by a continuous diode-pumped, intercavity-doubled Nd:YVO$_4$-laser (SP, MILLENIA), operated at an output power of 3.4 W. Pulsed operation of the oscillator is achieved by passive mode-locking via Kerr lensing in the 4 mm Ti:Sapphire crystal, and compensation for group velocity dispersion in a prism compressor. A radio-frequency driven acousto-optical modulator facilitates the initiation of the mode-locking and suppresses cw-lasing. The system can be tuned between 770 and 820 nm, without loss of mode locking, acting on a broad slit placed in the symmetry plane of the intercavity prism compressor. The oscillator typically delivers pulses of 3-4 nJ at a repetition rate of 80 MHz.

Regenerative amplifier.   The pulses obtained by the oscillator are too weak for most of non-linear processes. During this work, a commercial regenerative amplifier (SP, SPITFIRE) was used to increase the pulse energy and dispose of enough power to generate the different colors required by each experiment. The gain in intensity is accompanied by a severe reduction in the repetition rate, which is limited to 1 KHz. The pulses from the oscillator are first stretched in time to a few hundred picoseconds, in order to reduce their peak power and avoid optical damages (*chirped pulse amplification*). Every millisecond, a single pulse from the mode-locked train is confined, by polarization, inside the Ti:Sapphire cavity of the amplifier. The injection and ejection of the pulses is controlled by a couple of Pockels cell synchronized to the RF signal generated by the mode-locker of the seed laser. The cavity crystal is optically pumped by a Nd:YLF laser, typically operated at ~ 9 W. The seed pulse is amplified at each passage through the Ti:Sapphire rod. After about 20 consecutive passages, it is coupled out from the cavity and re-compressed in time. The typical output power of the system corresponds to 500-800 μJ/pulse. The intensity autocorrelation signal, measured using a commercial autocorrelator (APE PULSE SCOPE), is 60-70 fs, indicating an actual pulse duration of 40-50 fs. The spectrum is $\sim$30 nm wide (FWHM 470 cm^{-1}).

4.3.2   Set-up for the ultrafast fluorescence-depletion experiment

Pulse generation.   The 400 nm pump pulse was produced generating the second harmonic of the amplifier fundamental frequency in a 500 μm thick BBO crystal. The remaining 800 nm light was filtered out by a blue glass filter (SCHOTT). As indicated in Fig. 4.3, the beam was successively passed through a double prism pulse compressor to pre-compensate for the positive group velocity dispersion induced mostly by the thick (6.3 mm) fused silica window of the vacuum chamber. The distance between the two prisms was optimized minimizing the temporal profile of the sum-frequency signal obtained focussing pump and probe beam on the surface of a BBO crystal placed in the exact position of the sample. During this procedure, a window, completely equivalent to the one mounted on the spectroscopic chamber, was set in the optical paths of the beams to reproduce the experimental conditions.

The tunable infrared (IR) probe pulses were generated using a commercial OPA (SP, OPA-800) pumped by 30% of the output of the regenerative amplifier. The IR generation takes place in two successive stages. In a first pre-amplification stage, the continuum, generated focussing 10% of the beam on a Sapphire plate, undergoes parametric down conversion in a BBO crystal as it interacts with a small fraction of the 800 nm light. The idler beam produced after this first passage, is used as seed pulse in a second power amplification stage, as it is pumped by the remaining 800 nm beam. Wavelength tuning is
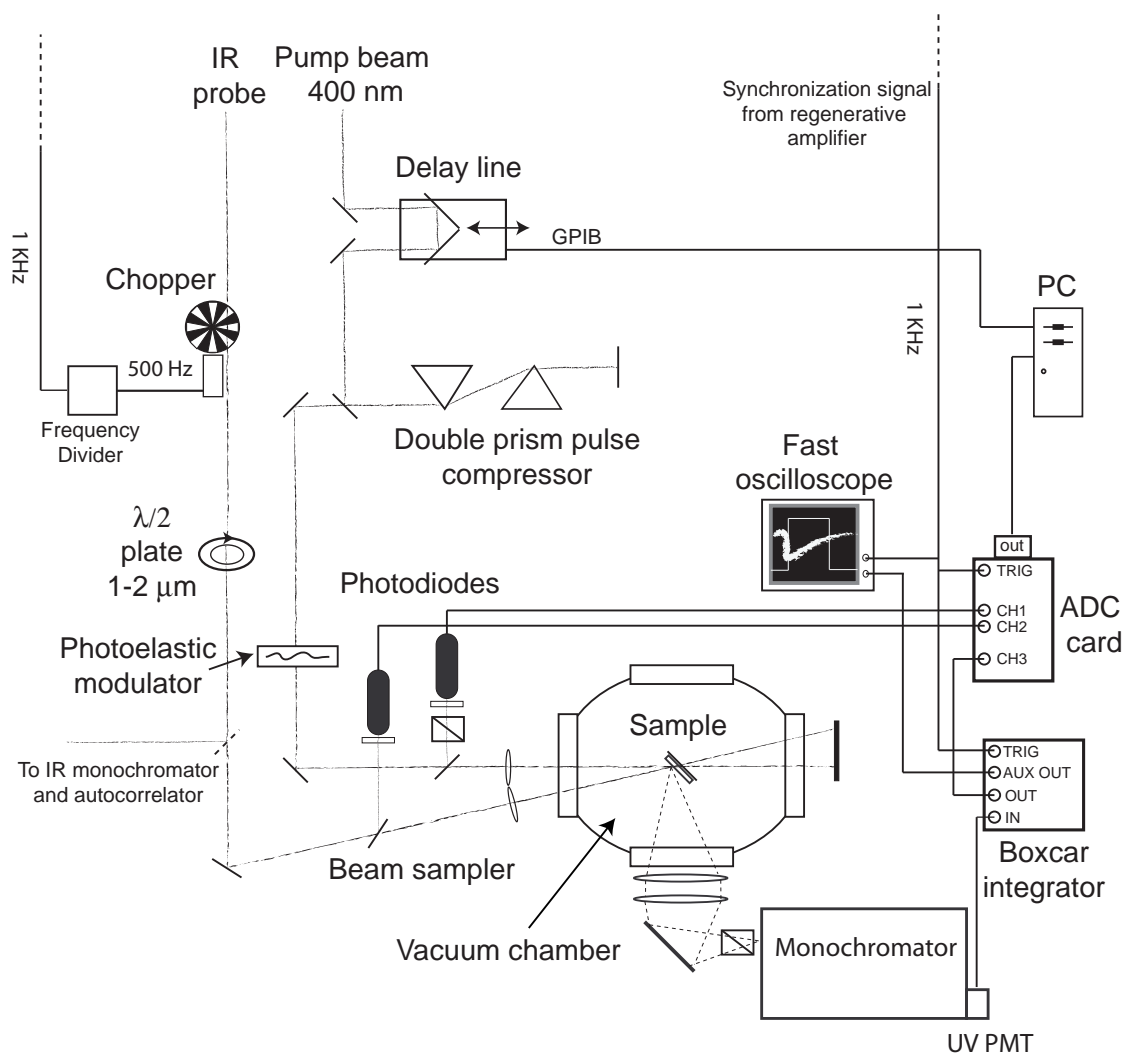
Figure 4.3: Schematic view of the essential elements of the fluorescence depletion set-up.

accomplished by changing the phase matching angle of the BBO crystal. The energies of the signal beam ranged typically between 10 and 30 μJ. Idler was not used during this work. The autocorrelation was measured by an home-built autocorrelator, and it was typically of the order of 130 fs. Incidentally, we note that the final cross-correlation of the experiment was limited by this value and not by the duration of the 400 nm pulse.
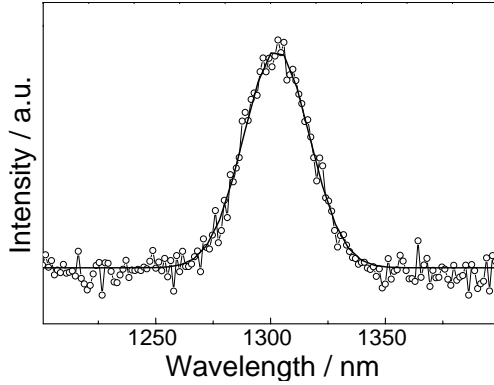
Figure 4.4: Typical probe pulse spectrum. The gaussian fit to the data indicates a FWHM of 33 nm.

During the frequency-tuning procedure, the output spectrum was monitored in real-time to get immediate feedback. The pulse was dispersed through a monochromator built with photo-camera optics (HANIMEX (f=135 mm), and NIKON (f=50 mm)) and detected using a InGaAs diode array (HAMAMATSU, G9201-256R). Pulses in the 1.05 μm and 1.3 μm region, with spectral widths of 28-35 nm (FWHM), were easily obtained (see Fig. 4.4). Contrary to the specifications of the system, major problems were encountered when trying to tune to wavelengths above 1.35 μm: in this case pulses were spectrally much broader and asymmetric. This severe limitation has motivated the relatively narrow range of wavelengths used in the experiment.

Central Wavelength	Spectral width	Duration	Typical pulse energy	Generation
800 nm	30 nm	55 fs	500 μJ	Ti:Sapphire amplifier
400 nm	3.3 nm	80 - 100 fs	0.5 μJ	Frequency doubling 800 nm
1150 - 1350 nm	28 - 35 nm	110 - 130 fs	< 0.1 μJ	OPA

Table 4.1: Principal characteristics of the laser pulses used in the experiment.

Detection scheme and signal calculation. After the pump excitation, the NO fluorescence was collected at right angle by an f=250 mm fused silica lens placed at the exit of the spectroscopic chamber, as illustrated in Fig. 4.3, and then focussed by a second f=300 mm lens mounted on a 3-axis stage onto the entrance slit of a 0.5 m monochromator (ACTON, SPECTRA PRO 500). A grating with 300 grooves/mm blazed at 300 nm was normally employed for the time-resolved measurements. When higher spectral resolution

was required (i.e. steady-state fluorescence scans), a holographic grating with 1200 grooves/mm was preferred. Fluorescence photons were detected by a solar-blind side-on type photomultiplier (HAMAMATSU, R166UH) characterized by a rise time of the order of 2 ns. The photocurrent signal was fed into a boxcar integrator (STANFORD RESEARCH SYSTEMS, SR250) triggered at 1 KHz by the Pockels cells signal of the Ti:Sapphire amplifier. Every millisecond, the fluorescence signal was time-integrated over a ~ 100 ns wide interval. The photomultiplier signal, and the boxcar gate were monitored using a fast oscilloscope (TEKTRONIX, TDS3052B - 500 MHz). The opening of the time-integration window of the boxcar was normally delayed by a few nanoseconds after the trigger signal, in order to exclude from the sampling procedure the scattered light of the laser. The boxcar output was then digitally converted and recorded on computer. Likewise, the intensity of every pump and probe shot was detected by photodiodes (HAMAMTSU, S1336-8BQ with interference filter at 400 nm and HAMAMTSU, G3476-05 with GaAs filter), digitized using the same data acquisition card (NATIONAL INSTRUMENTS, SC2040), and recorded on computer.

During the depletion measurements, a phase-locked chopper (HMS, LIGHT BEAM CHOPPER 221), synchronized to half of the laser repetition rate, was set in the optical path of the probe beam to block every second pulse.

The depletion signal at a given time-delay τ was calculated in a single-shot fashion, as the difference between the number of fluorescence counts detected in presence (F_{depl}) and in absence (F_{undepl}) of the probe beam on the sample, normalized by the instantaneous value of the unperturbed fluorescence:

$$S_\tau = \frac{F_{\text{depl}} - F_{\text{undepl}}}{F_{\text{undepl}}} \ . \tag{4.3}$$

This approach presents several advantages in comparison to the detection with a lock-in amplifier. Slow photo-degradation of the sample and sudden losses in the fluorescence intensity can be corrected by the instantaneous value of the fluorescence (see also Fig. 5.7). This possibility is particulary advantageous when two-photon excitation scheme is applied: in this case the number of fluorescence photons is much scarcer, and the quality of signal statistics results strongly affected. Moreover, the possibility to monitor in real-time the dispersion of the intensities of pump and probe shots represents a very useful diagnostic tool during data acquisition, and a sound criterion for data rejection during the successive analysis.

Polarization measurements Different polarization settings were used during the experiment. The polarizations of the pump and probe beams could be rotated by adjusting the angle of standard $\lambda/2$ plates tailored for their respective wavelengths. A UV-transmitting Glan-Thompson polarizer (FOCTEK, GMP6012) was set before the monochromator, in the collimated fluorescence beam. Moreover, the polarization of the pump pulse could be continuously rotated at a fixed frequency (50 KHz) by means of a photo-elastic modula-
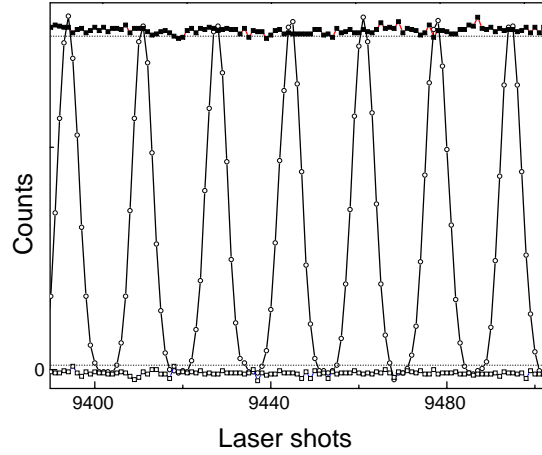
Figure 4.5: Pump photodiode counts for different polarization settings. **Empty squares.** Detection polarizer crossed to the pump polarization. **Filled squares.** Detection polarizer parallel to the pump polarization. **Empty circles.** Detection polarizer parallel to the pump polarization and photo elastic modulator operating. **Dotted lines.** Threshold values used for calculating the signal associated to the different polarization settings.

tor [1] (HINDS, FS3). Considering that the modulator could not be directly synchronized with the laser, the instantaneous polarization of each shot was detected setting in front of the pump photodiode a polarizer parallel to the polarization of the beam before the modulator (Fig. 4.3): high intensity counts corresponded to the original polarization, low counts to $\pi/2$ flipped polarization, as illustrated in Fig. 4.5.

The depletion signals associated to the two different settings were calculated accounting exclusively for the fluorescence shots corresponding to the two possible perpendicular polarizations of the pump (values above and below the thresholds indicated in Fig. 4.5).

***In situ* determination of time zero.** The possibility to change continuously the polarization of the beams and of the detection was exploited to determine the absolute time-zero in the time-resolved scans. Indeed, the necessity to work in a vacuum chamber prevents measuring the experimental cross correlation at the exact position of the sample. The procedure of removing the chamber and measuring the sum-frequency signal in a non linear crystal set in the position of the sample substrate, even with the accuracy to put in the optical path of the beams a quartz window equivalent to the one of the vacuum chamber, does not give a precision higher than 200 fs in the determination of time zero [76, 123].

The cross-correlation could be measured *in-situ* recording, along with the fluorescence signal, a weak sum-frequency signal generated by pump and probe overlapping on the sample. This was achieved subtracting from the signal recorded with vertically polarized pump, the signal obtained with horizontally polarized pump, keeping fixed the polarization of the probe (vertical) and that

---

[1]The operation of the device is based on the photo-elastic effect: a transparent solid material exhibits birefringence when it is mechanically stressed by compression or stretching.
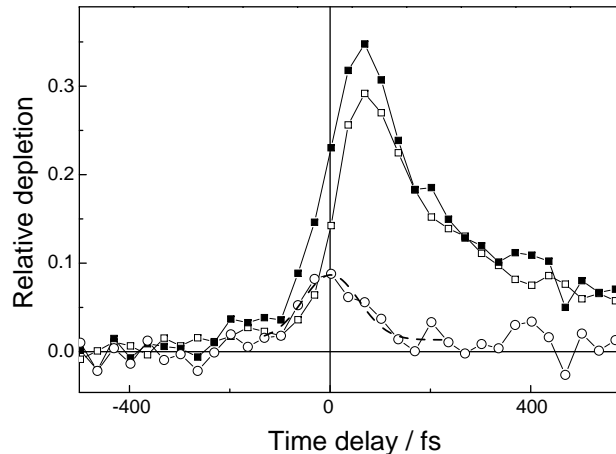
Figure 4.6: Absolute determination of time-zero at the sample position measured along with the fluorescence depletion signal. **Filled squares.** Signal correspondent to vertically polarized pump, probe and detection. **Empty squares.** Signal correspondent to vertically polarized probe and detection and horizontally polarized pump. **Empty circles.** Difference of the two signals. **Dashed lines.** Gaussian fit to the difference signal.

of the detection (vertical). Figure 4.6 shows the result of this procedure directly on a typical fluorescence-depletion scan calculated using Eq. 4.3.

During this type of measurements, the starting position of the boxcar time-window was anticipated of a few nanoseconds, in order to include in the signal the photons associated with the sum-frequency of the beams, which posses the same time-structure of the laser scattered light.

4.4   Sample preparation

4.4.1   Catalytic conversion of hydrogen

The intrinsic conversion process described in § 1.2.2 can be greatly accelerated in order to dispose of pure $J = 0$ hydrogen samples (or equivalently $J = 1$ deuterium samples). Conversion requires a simultaneous change of rotational angular momentum of unity, and a change from parallel state of nuclear spin to anti-parallel state. This entails the presence of an inhomogeneous magnetic field. At atmospheric pressure, and temperature between 14 and 21 K, a mixture of ortho- and para-H_2 self converts itself by collisions, but, given the very slow rate, it requires several weeks to obtain an equilibrium p-H_2 concentration approaching 99%. This rate can be greatly increased by the use of a suitable catalyst, which provides an external source of inhomogeneous magnetic field. This condition can be met bringing liquid H_2 in contact with the strong magnetic field gradients present at the surface of a *paramagnetic salt.*

During last years, many catalysts have been used with success to this goal: all large hydrogen liquefiers use iron oxide or ferric oxide, but in literature

neodymium oxide, Fe-Ni alloys, chromic anhydride, ferric hydroxide gel appear as well [124]. Probably the most cited one is a highly porous nickel silica gel (commercial name APACHI-I by Houdry Inc.) indicated as the most efficient in the review paper by Silvera [14]. Our preference for nickel sulfate ($NiSO_4$) as a catalyst relies exclusively on its availability, being synthesized directly in our chemistry department.

Design. A schematic diagram of the conversion apparatus, built following the indications of Juarez *et al.* [125], is displayed in Fig. 4.7. The converter is designed to be inserted in a helium dewar through is neck. Research grade n-H_2 (99.9999% purity) enters into the body of the converter through a 1 mm thick inox tube of 4 mm internal diameter. The catalytic reaction takes place in the concentric cylindrical copper container of 22 mm diameter, 96 mm depth and 1 mm thickness, which surrounds the inox tube. The outer tube is filled up by catalyst powder (granules of nickel sulfate esa-hydrate, average diameter 0.5 mm, 98% purity), and it is split into smaller compartments by 5 equidistant copper disks welded directly to the inner tube. Hydrogen passes from one compartment to the other via semicircular apertures of 6 mm diameter located at the edges of the disks. The design is meant to enhance the contact of hydrogen with the catalyst along its way up to the brass mesh, which avoids that the catalyst granules get into the gas system. The inox output tube has an internal diameter of 12.8 mm, and a wall thickness of 0.6 mm. The conical part at the end of the output tube is screwed to the copper body with indium wire as a seal.

To keep the temperature of the container in the required range, the reaction chamber is screwed to a 150 mm long copper tube which is immersed in liquid helium. A indium foil is compressed in the contact area between this helium finger and the converter's body to assure, a better contact. The depth of the finger in the liquid helium can be adjusted to achieve the desired working temperature loosening a split collar at the neck of dewar, and sliding up or down the converter.

The temperature is monitored by a silicon diode attached to the side. A four-lead, phosphore-bronze cable is used to pass the current, and read the voltage difference across the diode using a temperature controller (Lakeshore, 330). Given that hydrogen is an explosive gas, major consideration has been given to safety. The gas line consists entirely of copper and stainless steel, and is assembled using exclusively Swagelock all metal sears.

Operation. A preliminary test was conducted to ensure the system was airtight, monitoring any eventual pressure drop over a period of many hours, after pressurizing the apparatus with 4 bar of helium gas.

The converter had to be conditioned before use, in order to remove water from the catalyst. The system was evacuated by mechanical pumping for 24 h, while the temperature was kept at 100º C using standard baking stripes. During this operation, particular care is required not to exceed the melting point of indium-wire gaskets (156º C). In order to activate the catalyst, and

Catalytic converter

NiSO$_4$ powder

p-H$_2$

n-H$_2$

temp.diode

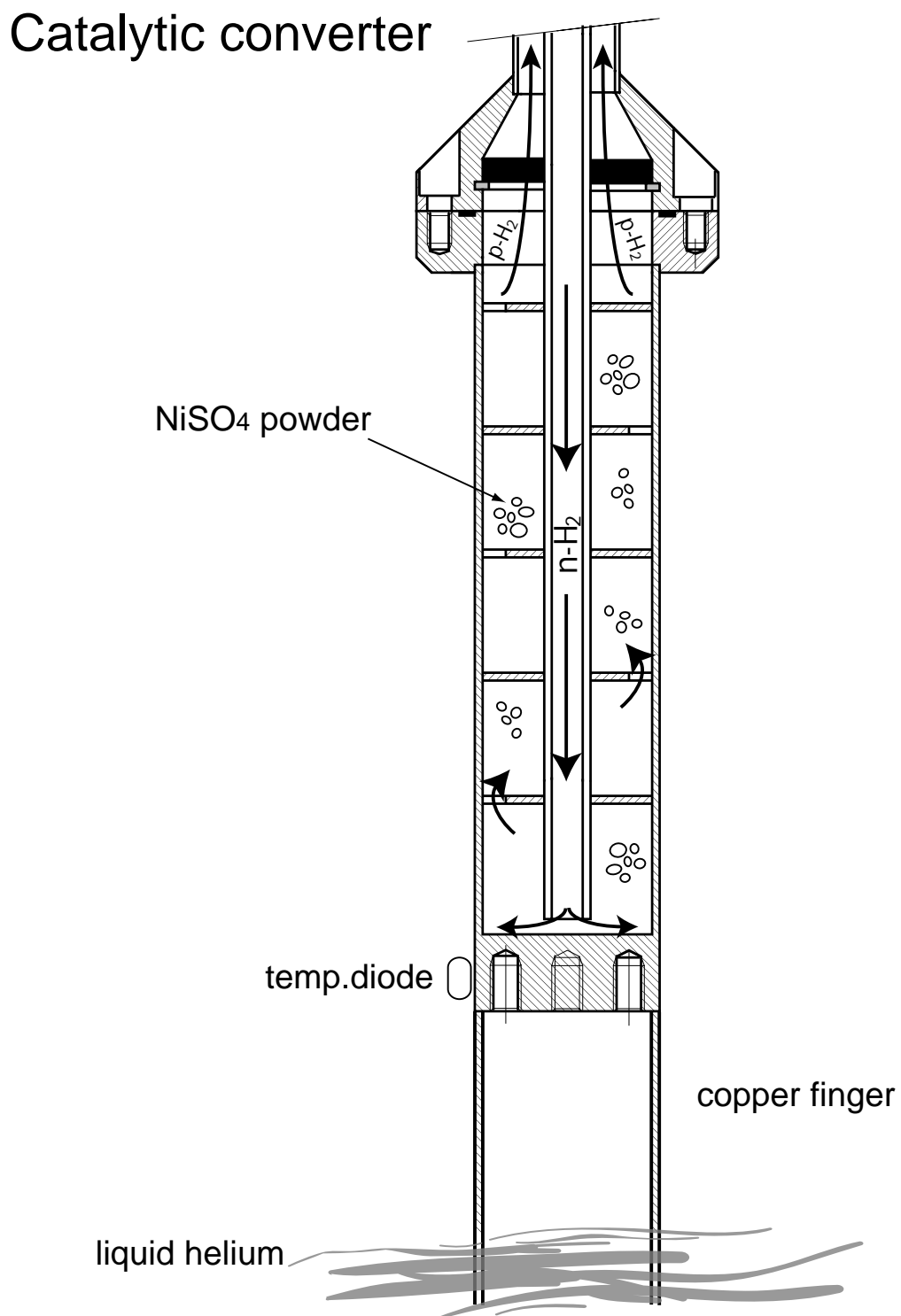copper finger

liquid helium

Figure 4.7: Design of the catalytic converter used during this work.

adsorb hydrogen on its surface, the converter was filled up at intervals of a few hours with 2 bar of hydrogen, which was pumped away again after a few minutes. At the end of this conditioning process, the converter was filled up with 2 bar of hydrogen and cooled down to liquid nitrogen temperature before being finally inserted in the helium dewar.

Standard safety valves at the neck of the helium dewar relieve any excess pressure produced by the evaporation of liquid helium. As the temperature decreased, hydrogen pressure inside the converter was kept constant at 2 bar. When the working temperature of 14 K was stabilized, the gas inside the converter line out was evacuated by mechanical pumping, and hydrogen was *slowly* inserted in the tube maintaining the temperature of the converter body below 16 K. For safety reason, the temperature of the system was monitored very closely, in particular when the helium in the dewar was about to finish: the volume occupied by one liter of liquid hydrogen increases by a factor 788 at 1 bar when evaporated.

When not filled up with hydrogen, the converter was kept under vacuum (10^{-6} mbar) via the turbo and the primary pumping system of the mixing chamber (see Fig. 4.8).

4.4.2 Vacuum systems and cryogenics

A schematic representation of the high-vacuum system used for the sample preparation is shown in Fig. 4.8.

Gas mixing unit. A first small stainless-steel chamber is connected to the output of the catalytic converter and to the NO bottle via all inox SWAGE-LOCK flexible tubing and valves. When not used to prepare the gas mixture, the chamber was evacuated by a turbo molecular pump (PFEIFFER VACUUM, TC600) down to a pressure of about 10^{-7} mbar read by a cold cathode gauge (BALZERS, IKR020). During the sample preparation, the chamber was isolated from the pumping system, and the gas pressure was detected by means of a capacitance diaphragm pressure gauge (CCM INSTRUMENTS). Any unused portion of gas mixture, remaining in the chamber after sample preparation, was evacuated directly by the rotary pump (ALCATEL, 2015), bypassing the turbo pump, until the pressure dropped below 10^{-3} mbar. The same pumping line was used to empty the residual hydrogen present in the catalytic converter for safety reason.

Spectroscopic chamber. The main vacuum chamber consists of a six-sided cross made of stainless steel, connected to the mixing unit via an inox tubing ending 1.5 cm in front of the sample holder. A needle valve allows a fine control of the gas flow from the mixing to the spectroscopic chamber during the crystal growth. The chamber is *permanently* evacuated by a turbo-molecular pump, the pressure is typically below the detection limit of the cold cathode gauge
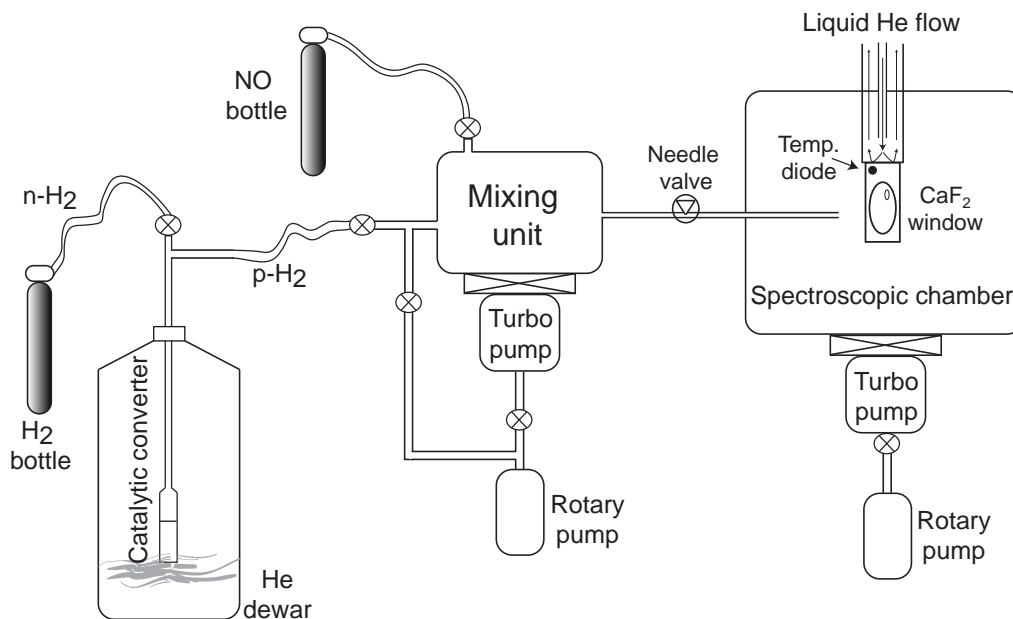
Figure 4.8: Schematic view of the mixing and spectroscopic chamber and of the catalytic conversion apparatus.

($5 \cdot 10^{-9}$ mbar), even at room temperature.

The sample holder consists of a 5 cm long block of highly pure copper attached at the top to the cooling finger of a continuous flow cryostat (JANIS, ST400) connected to a liquid helium dewar by a flexible transfer line. A CaF_2 window (2.5 cm diameter) is mounted on the sample holder at an angle of 45° with the chamber axis, in order to allow optical access from all four sides (see Fig. 4.3). Sample holder and cryostat can be moved in all three directions with the help of a high-vacuum manipulator.

4.4.3 Sample growth

A gas mixture of NO (99.95 %) and H_2 (99.9999%) was prepared in the mixing unit, with partial pressures ratio of 0.05% and global pressure of 0.5 bar. The mixture was then allowed inside the spectroscopic chamber by opening the needle valve and was sprayed on the cold substrate ($\sim$ 2 K).

The optical and structural properties of the samples depended strongly on the conditions during the deposition of the gas mixture onto the cold CaF_2 substrate: a slow and controlled growth resulted in samples which were less scattering and presented more stable fluorescence.

The sample growth usually consisted of two stages: the first 10 mbar of gas mixture were deposited at a background pressure in the spectroscopic chamber of 10^{-7} mbar, then the needle valve was opened until a stable pressure of 10^{-6}
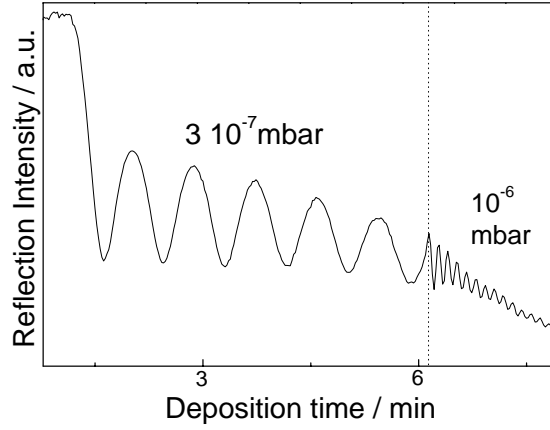
Figure 4.9: Interference pattern in the reflected intensity of a He-Ne laser produced by a n-H$_2$ sample. The vertical line indicates the moment when the background pressure in the chamber is increased.

mbar was reached. The preparation was completed after the pressure in the mixing chamber was dropped by 100-150 mbar.

Determination of the crystal thickness.   By a simple interferometric experiment we could monitor the thickness of the crystal during the growth, and characterize the speed of deposition as a function of the background pressure in the spectroscopic chamber. The light of a He-Ne laser was shone on the sample holder, the beam reflected at right angle was measured by a photodiode as a function of the pressure decrease in the mixing chamber. The intensity of the reflected light was modulated by the interference of the laser beam at the vacuum-matrix, and matrix-substrate interface. The thickness d of the crystal could be calculated from the interference pattern using the following expression [126]:

$$d = \frac{N\lambda}{2\sqrt{n_{H_2}^2 - n_0^2 \sin^2 \alpha}}, \tag{4.4}$$

where λ represents the laser wavelength, N the number of interference fringes, α the incidence angle, n_{H_2} and n_0 the refractive indices of solid hydrogen and vacuum respectively.

The two typical background pressure regimes of growth, 10^{-7} mbar and 10^{-6} mbar, correspond to a flux of 0.83 mbar/min and 4.8 mbar/min respectively. The frequency of the interference pattern in Fig. 4.9 shows clearly the change in the speed of deposition from 0.5 μm/min to 2.6 μm/min associated to the increase in the background pressure after 6 minutes of deposition. Typically the samples were grown depositing up to 100 mbar, corresponding to a final thickness of $\sim$50 μm .

Chapter 5

Spectroscopic characterization and photostability of the sample

This section describes a series of procedures, we applied to fully characterize the samples prior to performing the time-resolved measurements. In particular, rotational Raman spectroscopy confirms the catalytic conversion. A direct comparison among the absorption spectra of NO in para- and normal-hydrogen reveals that the impurity, when excited to a Rydberg level, feels a slightly different environment in the two hosts. On the contrary, the two fluorescence spectra show no difference, indicating that the relaxed configurations are very similar.

5.1 Pure solid hydrogen

5.1.1 Raman characterization

Raman scattering allows a direct determination of the ortho/para ratio [14]. The para concentration can be measured from the relative intensities of the rotational Raman lines I_{02} and I_{13} (I_{if} indicates the Raman intensity of the $J = i \rightarrow f$ transition).
The Raman selection rules for the transitions of rotationally *unmixed* states (see § 1.2) correspond to $\Delta J = 0, \pm 2$. We note that the lack of $\Delta J = \pm 1$ transitions holds only for homonuclear hydrogens (H_2, D_2 and T_2) [17], where we expect to see intense $J = 0 \rightarrow 2$ and $J = 1 \rightarrow 3$ transitions at cryogenic temperature. Their ratio is proportional to the square modulus of the matrix elements of the anisotropic polarizability $|\langle f|\alpha_{anis}|i\rangle|^2$ between the initial and final states, and to the probability of occupation of the initial state $|i\rangle$.

The evaluation of these matrix elements yields the expression:

$$\frac{I_{02}}{I_{13}} \sim \frac{5}{3} \left(\frac{c_e}{1 - c_e} \right) \left(\frac{\omega - \omega_{02}}{\omega - \omega_{13}} \right)^3 \left\{ \frac{1 + 7/3 e^{-10B/kT} + ...}{1 + 5 e^{-6B/kT} + ...} \right\} \ , \qquad (5.1)$$

where c_e represents the concentration of molecules with even rotational state, ω the frequency of the laser, and ω_{if} the frequency shift associated to a rotational transition. Considering that $B/k = 85.4$ K, then $kT \ll 6B$, and we can set the quantity in curly brackets equal to one. We can further simplify the expression neglecting the cubic ratio of the frequency differences. The rotational shifts, in fact, are much smaller than the laser frequency: $6B, 10B \ll \hbar\omega$. Extracting c_e, we finally obtain:

$$c_e = 1 - \frac{5}{3} \left(I_{02}/I_{13} + 5/3 \right)^{-1} \ , \qquad (5.2)$$

that we can directly apply to evaluate the para concentration of the sample substituting the integrated intensities of the Raman lines [127].
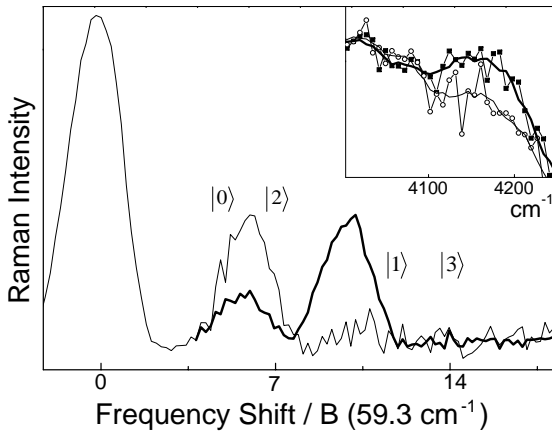
Figure 5.1: Raman scattering intensity as a function of the rotational constant B. **Thick line.** Solid n-H_2. **Thin line** Solid p-H_2. **Inset.** Raman signal associated to the $v = 0 \rightarrow 1$ vibrational transition.

The plot in Fig. 5.1 shows the Raman scattering intensity measured on an H_2 crystal prepared using normal hydrogen (thick line), compared with the one obtained growing the crystal with hydrogen processed by the catalytic conversion apparatus (thin line). The relative concentration of the two rotational species can be determined applying Eq. 5.2. Even if the measurement has been taken a few hours after the deposition, the Raman signal shows that normal hydrogen sample retains the high-temperature even-J/odd-J ratio at low temperature. On the contrary, the odd-J transition has disappeared in the sample prepared with hydrogen processed by converter, and we can safely estimate a para concentration superior to 98%.

The inset shows the intensity of the vibrational $v = 0 \rightarrow 1$ transitions observed in both samples. The lines are superimposed to a fluorescence background caused by the sample substrate. The n-H_2 sample exhibits a stronger line, as the Raman scattering cross section for the vibrational transitions in the solid state are not independent of the initial rotational states. The ratio between the two cross sections depends on the concentration of the $J = 1$ states, and can vary between 2 and 4. In gaseous H_2 this coupling effect is very weak and can be neglected [15].

5.1.2 Crystallite light scattering

During the growth of the crystal, $J = 1$ molecules act like impurities that perturb the crystallization process favoring the presence of smaller distinct crystalline domains [17]. The determination of the light scattering properties of a crystal can give an estimate of the structural quality of the sample.
The intensity of a light beam passed through a crystal cracked into adhering crystallites of length L is given by

$$I = I_0 e^{-\pi a^2 Q n_c L} \ , \tag{5.3}$$

where I_0 stands for the initial intensity, a for the radius of the crystallites, Q for the extinction coefficient, and n_c for the number of scattering centers per unit volume. The extinction coefficient Q can be calculated as the ratio between the scattering cross section and the geometric cross section of the scattering centers πa^3. For many purposes, the value of Q can be determined considering the values assumed by the dimensionless ratio $k = \frac{2\pi a}{\lambda}$ and the phase shift $k(n-1)$. For k and $k(n-1) > 1$, Q assumes a limiting value of 2 [17].
The inherent scattering power is very low for hydrogen, because its refractive index is very close to 1 at all wavelengths [1], which explains why good hydrogen crystals are usually hard to see by eye.

In Fig. 5.2 the transmission of a deuterium lamp at 250 nm is plotted as function of the crystal thickness calculated from Eq. 4.4. The n-H_2 sample (filled squares) shows an immediate and abrupt drop of the light intensity already for a relatively thin crystal. To estimate the dimensions of the crystal domains, we can suppose that the crystallites that compose the sample are tightly packed spheres of radius a. Therefore, we can calculate an

Figure 5.2: Transmitted intensity at 250 nm as a function of crystal thickness. **Squares.** n-H_2 sample. **Circles.** p-H_2 sample. **Lines.** Results of the fits obtained using expression 5.3.

average number of scattering centers n_c to substitute in Eq. 5.3, in the form: $n_c = \left(\frac{4}{3}\pi a^3\right)^{-1}$. We can successively fit the data through Eq. 5.3, letting the average radius a free to vary.
The value obtained corresponds to $a \simeq 9 \ \mu m$ for n-H_2 . In the case of p-H_2 , the fit is not significant, because the calculated radius a results actually bigger than the crystal thickness! Qualitatively this comparison is an additional confirmation that the $J = 1$ molecules strongly perturb the crystallization process and, consequently, the macroscopic structural properties of H_2 crystals. It should be noted that the presence of NO impurities, even at low relative concentrations (10^{-4}), affect as well the scattering properties of the sample,

---

[1]The refractive index of H_2 can be calculated using the empirical expression $(n-1) \simeq 4.73 \cdot 10^{-6} \lambda^{-0.062} \rho$, λ being the wavelength in nm and ρ the density in mol/m^3.

indicating a perturbation of the lattice structure. Nevertheless, several observations showed that doped para-hydrogen samples still scatter much less than normal ones.

5.2   NO-doped solid hydrogen

5.2.1   Absorption spectrum
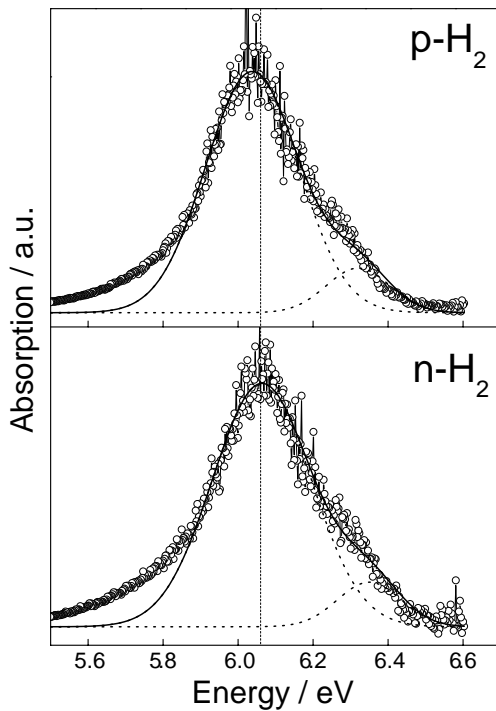
Figure 5.3: Comparison of the $A \leftarrow X$ absorption of NO embedded in para- and normal-hydrogen. **Dotted curves.** Gaussians representing the contributions of the $A(v' = 0)$ and $A(v' = 1)$ vibrational levels to the total absorption band. **Vertical dotted line.** Eye guide centered on the $A(0) \leftarrow X$ transition in normal-hydrogen. Note that the transition in para hydrogen is red-shifted of about 0.03 eV.

The excitation spectrum of Fig. 3.3, measured monitoring the $A(0)$ fluorescence of normal hydrogen was recorded using synchrotron radiation. The feature around 6 eV is analogous to the $A(0) \leftarrow X$ absorption band. Given that an equivalent measurement does not exist for para hydrogen, we measured the absorption spectra of NO embedded in the two different crystals, using a standard deuterium lamp as a source.

Different experimental limitations have affected the quality of the measurements shown in Fig. 5.3. In particular, the reduced sensitivity of the CCD camera in this spectral region, the fact that these wavelengths are close to the transmission cut-off of the atmosphere and, finally, the different scattering properties of doped and un-doped samples, which complicate the determination of the correct baseline for the spectra.

From the comparison in Fig. 5.3 we observe that the para hydrogen band is shifted by $\sim$0.03 eV to the red of the normal hydrogen band, which can be explained by looser cage environment for the pure $J = 0$ solid, in line with the discussion presented in § 3.3. Indeed, the quadrupolar interactions, exerted among the 75% of $J = 1$ molecules present in n-H_2, amount to about 10 J/mol. This extra energy pulls the molecules closer together, so that n-H_2 is denser than p-H_2 (see Tab. 1.1). Such a difference may qualitatively explain the shift observed in the absorption spectra. In addition, in doped

n-H_2 , the presence of multipolar interactions between the ortho-H_2 molecules and the NO impurity (quadrupole-dipole, quadrupole-quadrupole) can further tighten the local environment around the guest molecule.

Both samples present a shoulder around 6.3 eV, which is associated with the $A(1) \leftarrow X$ vibronic transition (see inset in Fig. 3.3). The long tail extending towards lower energies below 5.85 eV is an artefact due to the baseline used for the calculation.

5.2.2 Two-photon fluorescence

The progression of the $A \rightarrow X$ fluorescence bands obtained upon two-photon excitation of NO in normal hydrogen corresponds to the one obtained exciting the A state by a direct one-photon transition.

The comparison between the emission spectra of NO embedded in para- and normal-hydrogen (Fig. 5.4) yields no shifts in the positions of the bands. This finding indicates that the relaxed configuration of the lattice around the impurity is the same in the two hosts. This is not surprising, considering the large amount of excess energy given to the system with respect to the minor shift measured in the absorption spectra [2]. On the other hand, the relative intensities of the two overlapping vibronic progressions present some differences. This is reasonable, as the vibronic excitation of $A(v = 1)$ at 6.2 eV (by two photons) is enhanced in para-hydrogen with respect to normal-hydrogen, due to the red-shifted absorption (Fig. 5.3).
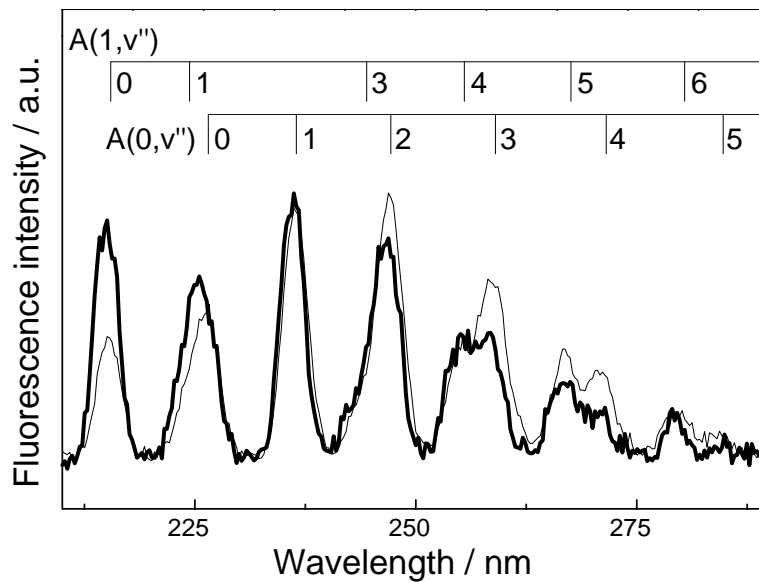
Figure 5.4: Fluorescence emission spectra of NO embedded in para- (**thick line**) and normal- (**thin line**) hydrogen. The differences in the relative intensities of the band are due to the different spectral positions of the absorption bands.

---

[2]The emission of the A state of NO in solid deuterium lies as well at the gas phase value. The width of the band differs from the hydrogen case: it corresponds to 70 meV instead of 53 meV [91].

The two-photon character of the excitation is illustrated in Fig. 5.5, where the intensity of the fluorescence, plotted against the laser power at 400 nm, is fitted by a square power law (see Eq. 4.2).

The interplay between the number of fluorescence counts and the sample photostability is a key-point to obtain data with a good signal to noise ratio. In this respect, the dimensions of the pump beam spot-size on the sample are a critical parameter that is worth investigating. In Fig. 5.6, the two-photon excited fluorescence is plotted as a function of the distance between the sample and the focal spot, modified changing the position of the focussing lens. Even if the $1/A^2$ dependence of Eq. 4.2 is not exactly reproduced, the strong sensitivity to the focal spot size is a clear signature of the multi-photonic character of the process.
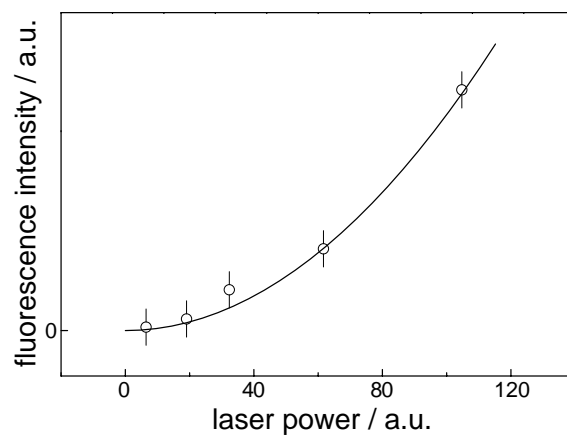
Figure 5.5: NO $X^2\Pi \leftarrow A^2\Sigma^+$ fluorescence intensity as a function of laser power at 400 nm. The **continuous line** represents the $const \cdot P^2$ fit to the datapoints.
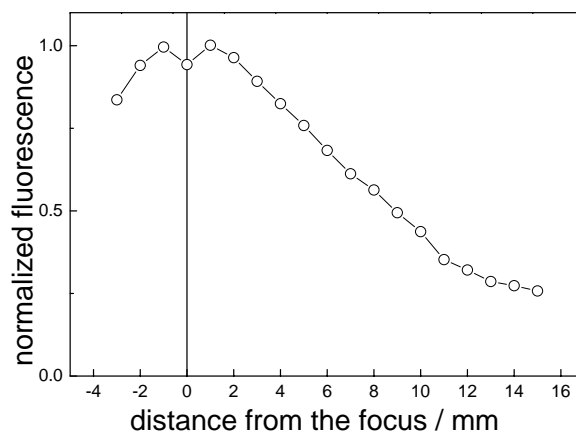
Figure 5.6: Normalized fluorescence intensity as a function of the distance of the sample from the focus.

5.2.3 Photo-stability

The stability upon laser irradiation of the fluorescence of NO embedded in solid hydrogen represented one of the major challenge during this work. The intensity of the laser excited fluorescence (by one- or two-photon excitation) presents a much less stable behavior in hydrogen and deuterium than in other rare gas matrices (Kr,Ar,Ne) prepared with the same technique, and similar concentration of the dopant. In the upper plot of Fig. 5.7, the intensity of the two-photon excited fluorescence is plotted against the number of laser shots (at the typical repetition rate of 1 Khz). The loss of the signal intensity follows an exponential behavior, which was observed to be strongly dependent on the laser power and spot size. It is possible to find regimes where the fluorescence signal results more stable, at the expense of the number of emitted photons, which depends quadratically on the power.

This exponential loss of the fluorescence is not the unique form of instability reported during the experiment. Particulary when the substrate temperature was around 3 - 4 K, instead of the typical growing temperature of 1.5 - 2 K, after a few minutes of irradiation, starting off with a fresh sample, we observed a drastic loss of intensity of the fluorescence, followed by a partial recovery (10-20 % of the initial value) on the timescale of minutes. The fluorescence intensity remained then constants for a few minutes before undergoing sudden but less drastic drops, always followed by partial recoveries. The noteworthy feature of this behavior is the fact that the sudden intensity losses necessitate a few minutes of irradiation to occur. In the lower plot of Fig. 5.7, it is remarkable that the number of laser shots before the sudden drop is very similar for different irradiated spots of the crystal. Likewise the recovery is also slow, but immediately follows the drastic intensity drops.

The details of these instabilities are unclear: they are probably due to a macroscopic destruction of parts of the sample by the laser. During the experiment with nanosecond lasers at 193 nm [91] or with femtosecond excitation at 195 nm [76, 123], this behavior was *always* reported and associated to even more drastic losses (up to 1 order of magnitude).

Most probably local heating (whose mechanism remains to be found) accompanied by dimerization and/or clustering of NO would explain the drops of fluorescence, as dimers and larger aggregates of NO do not fluoresce [128]. The partial recovery may be due to subsequent dissociation of the dimers and clusters.

It is worth noting that the adoption of the single shot detection scheme described in § 4.3.2, which permits to calculate the signal with the correct value of fluorescence at every laser shot, has been motivated principally by the instabilities and losses observed in the sample fluorescence. Simply lowering the pumping power to attain steady regimes of fluorescence is, in fact, not a solution, considered that a low number of fluorescence counts strongly limits the signal statistics.
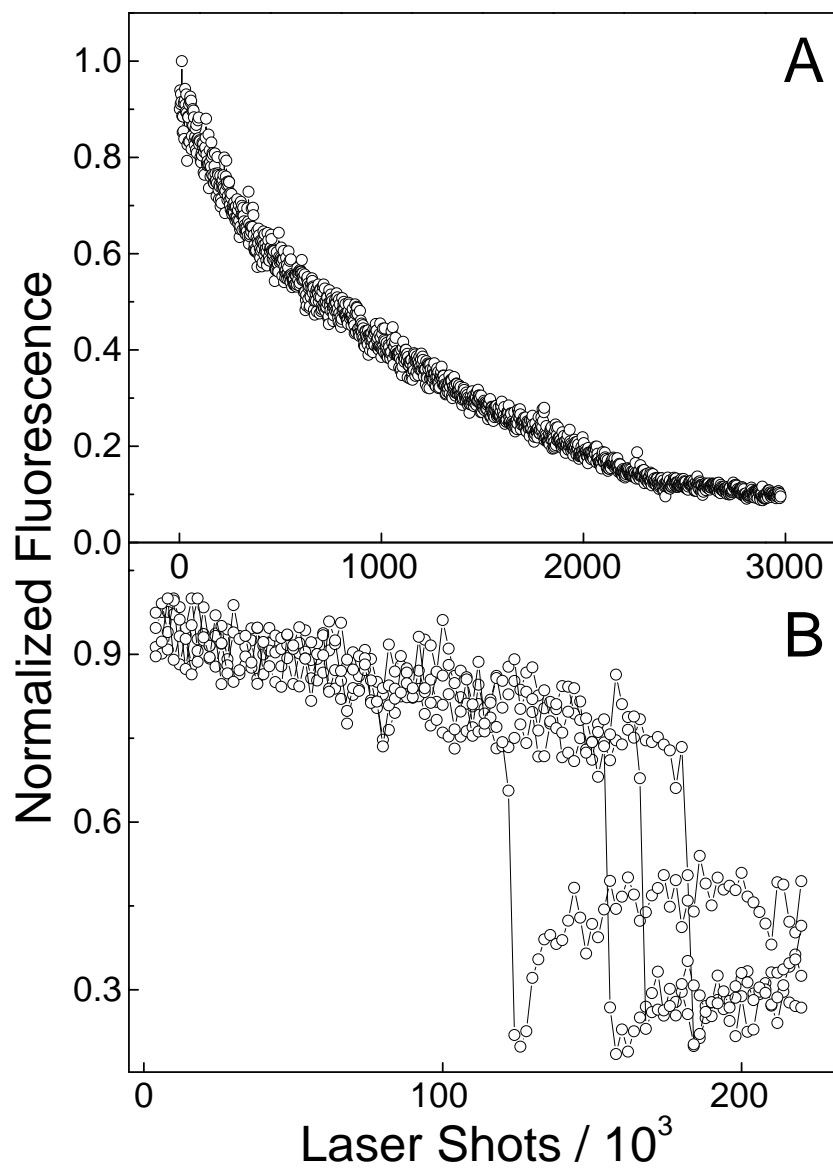
Figure 5.7: Fluorescence decay upon laser irradiation as a function of laser shots. **A.** Exponential decay behavior. **B.** Fluorescence drop and partial recovery measured at different spots of the sample.

Chapter 6

Results of the time-resolved experiment

The results of the time-resolved experiment are presented and interpreted on the basis of the configuration coordinate model introduced in § 3.3. Transients at different probe wavelengths show the existence of three timescales in the lattice relaxation dynamics: a first expansion of $\sim$ 200 fs is followed by a slower expansion continuing up to 0.8 ps. Finally, at longer time delays, we report an increase of the depletion signal, which lasts for several picoseconds. The assignment of this feature to a specific structural process of the lattice around the impurity is more problematic, and calls for discussion in Chap. 8. A comparison of the time-resolved results for NO in para- and normal-hydrogen shows that, in the two hosts, the local ultrafast dynamics does not present significant differences.

Note about the measurements. *Except if differently stated, the excitation of the Rydberg A state is achieved by 2-photon pumping at $\sim$ 404 nm, and the host matrix is para-hydrogen. The fluorescence is recorded setting the monochromator on the $A(0,2)$ transition (Fig. 5.4), and allowing a broad spectral range (up to several nanometers) to be detected, in order to improve the signal statistics. The transients represent typically the average of 4-5 consecutive scans on the same sample spot, with an integration time of 1 s per data point at the repetition rate of 1KHz.*

6.1   Short time dynamics

Figure 6.1 contains a series of transients corresponding to probe wavelengths ranging from 1370 nm to 1185 nm. The linearity with respect to the probe beam intensity has been checked independently for each wavelength (see appendix A). The transient corresponding to the probe at 1370 nm consists of a peak followed by a weak decreasing tail. We included in the plot the cross-correlation signal measured by sum-frequency in a non linear crystal for the very same probe wavelength. The two peaks compare quite well, indicating that the dynamics probed at this wavelength is faster than the time-resolution of the experiment ($\sim$130 fs). Gaussian fits to the rise of the successive signals show that the two transients at 1300 and 1280 nm are characterized by dynamics around time-zero faster than the ones probed by shorter wavelengths. The steep rise of the signals, in fact, ranges from $\sim$ 130 fs at 1300 nm to more than 230 fs at 1185 nm. The contrast between the intensity of the initial peak and the signal at longer times decreases going towards the bluer probes, and, in the extreme case of the scan at 1185 nm, the signal intensity around 200 fs is smaller than at later times. A general feature shared by all the signals is the presence of two distinct timescales, one associated with the initial rise (130 - 230 fs), and a second one that leads to the levelling off of the signal around 800 fs (vertical dashed line). This second timescale corresponds to the slow decrease of the signals associated with the red probes, and with the parallel increase of the signal at 1185 nm.

A crucial information for the interpretation of the time-resolved signals comes from the determination of the absolute time-zero. The plots in Fig. 6.2 display the cross correlation measured *in situ* (§ 4.3.2) along with two fluorescence depletion signals corresponding to probe at 1300 nm and at 1200 nm. From this direct and *absolute* comparison, we derive that the peak structure at the 1300 nm probe takes place during the rise of the signal at 1200 nm. Afterwards, around 150 fs, a slower process sets in, and governs the dynamic evolution of the system. We remark that, in the case of the signal at 1300 nm, the width of the experimental cross-correlation is comparable to the rise time of the transient. Hence, the timescale observed in the dynamics of the system fully justifies the adoption of the two-photon excitation scheme.

To show the improvement gained from the latter, one- and two-photon excited signals are compared in Fig. 6.3 for different probe wavelengths. It is evident that the time resolution associated with the two-photon experiment is more suited to investigate the early stages of the dynamics. In particular, in the one-photon experiment, it is not possible to distinguish between the two timescales mentioned above, i.e. the initial fast rise associated to the first 200 fs, and the second one, that lasts up to 800 fs. Incidentally, it is worth noting that the slow growing behavior of the 1185 nm transient is reproduced between the two experiments and, somehow, better captured by the one-photon transient, which presents, in this case, less dispersion of the experimental data points.
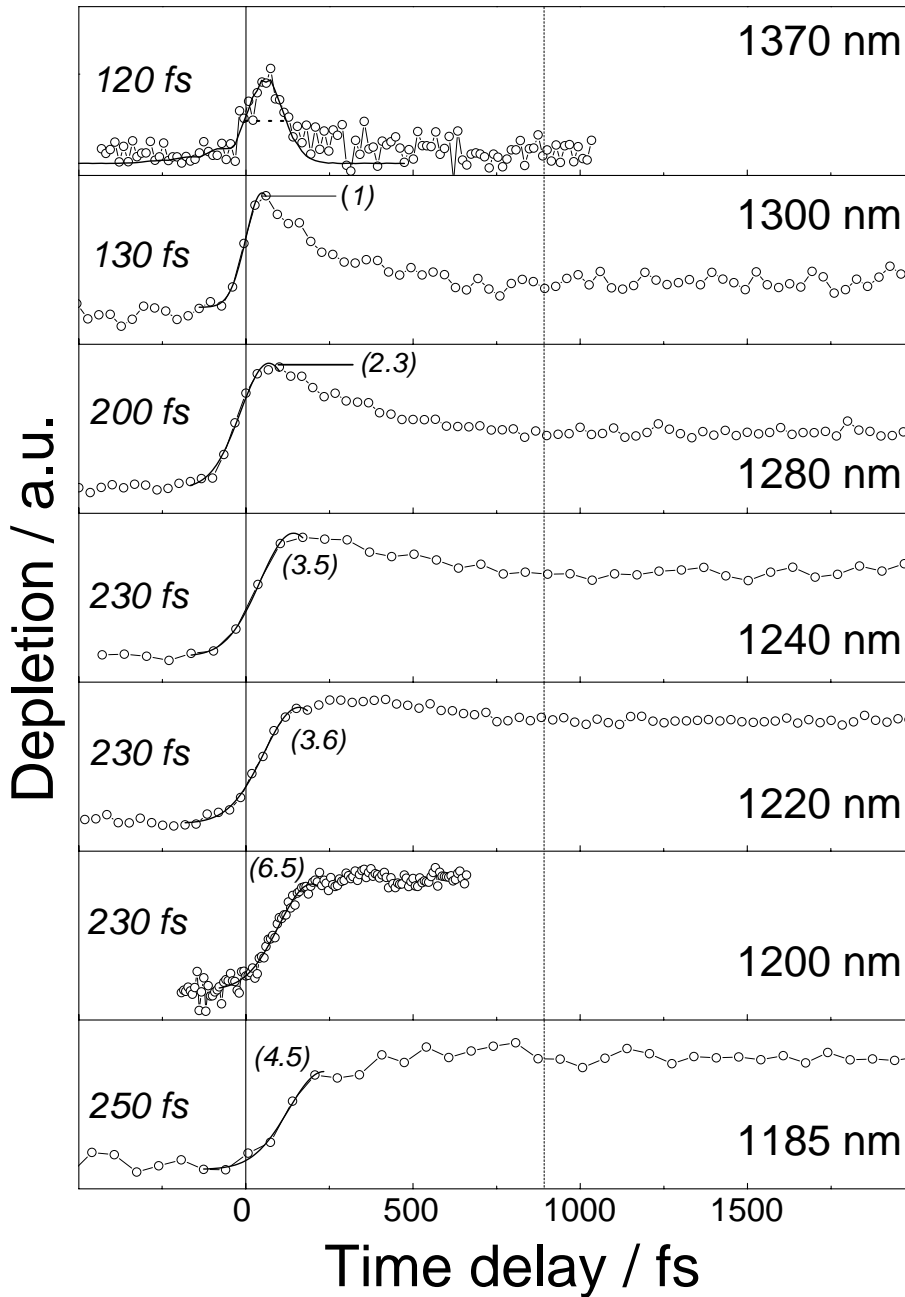
Figure 6.1: Short time depletion scans for different probe wavelengths. The excitation of the NO A state is achieved by 2-photon pumping at 404 nm, with a typical pump power of 0.7 μJ. The fluorescence detection is set at the maximum of the $A(0,2)$ band. The probe power is not constant for the different signals presented ($\leq$0.1 μJ). The linearity of the signals in the probe power is verified independently for each transient in the plot. The quantities in brackets indicate the relative signal intensities at fixed probe power (see also Fig. A.3). The values shown on the left indicate the rise time of the signals (from gaussian fit). In the transient corresponding to 1370 nm, the pump-probe cross-correlation signal (fitted by a gaussian of 120 fs FWHM) is superimposed to the fluorescence depletion signal. The **dotted vertical line** indicates the end of the slow expansion process (see text for details).
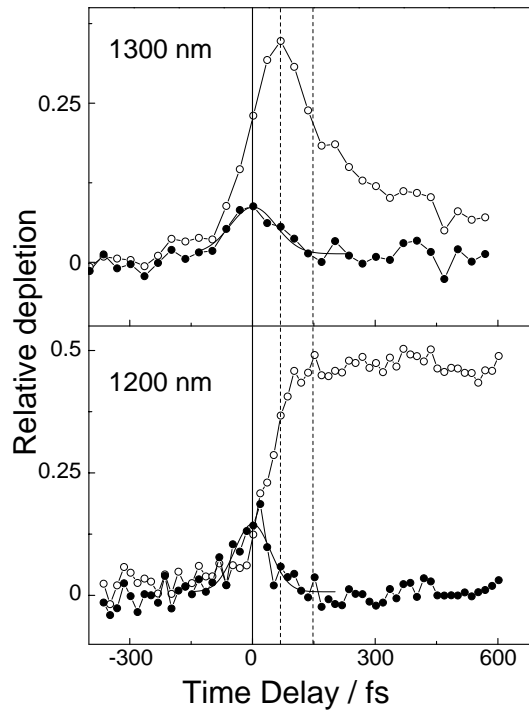
Figure 6.2: Depletion signal (**open circles**) and *in situ* cross-correlation (**filled circles**) measured along with the signal for two selected transients. See § 4.3.2 for details.

Interpretation of the transients.   The probe windows associated with the different scans of Fig. 6.1 are plotted in Fig. 6.4, along with the harmonic potentials describing the NO-lattice interaction in the A, C and D states of the impurity, obtained by the moment analysis (§ 3.3.1). In the plot, the independent variable corresponds to the cage radius increment, calculated via the substitution 3.3. Within the approximation of a constant displaced mass of 12 hydrogen molecules, the A state potential well is shifted by 0.93 Å from the ground-state equilibrium distance, indicated by the vertical line at 0 in Fig. 6.4.

At this point, we can interpret the signals presented in Fig. 6.5 considering the evolution of a wavepacket of intermolecular modes, created by the pump-pulse, rapidly moving on the A state potential (§ 4.2). According to Fig. 6.4, the probe at 1370 nm opens a single observation window centered at a radius increment of ~ 0.5 Å, nearly half of the total expansion. The corresponding signal, represented by a narrow peak with the same FWHM of the pump-probe cross-correlation, can be associated with the initial fast dynamics of the cage expansion. The wavepacket reaches the configuration probed by this wavelength on a time much shorter than the time-resolution of the experiment. The narrow width of the signal suggests that, up to this point, the expansion is fundamentally a coherent process, as the time structure of the excitation pulse is conserved in the signal.

The probes at 1300 and 1280 nm sample the beginning of the dynamics on the $A - D$ transitions, opening broad observation windows between 0 and 0.5
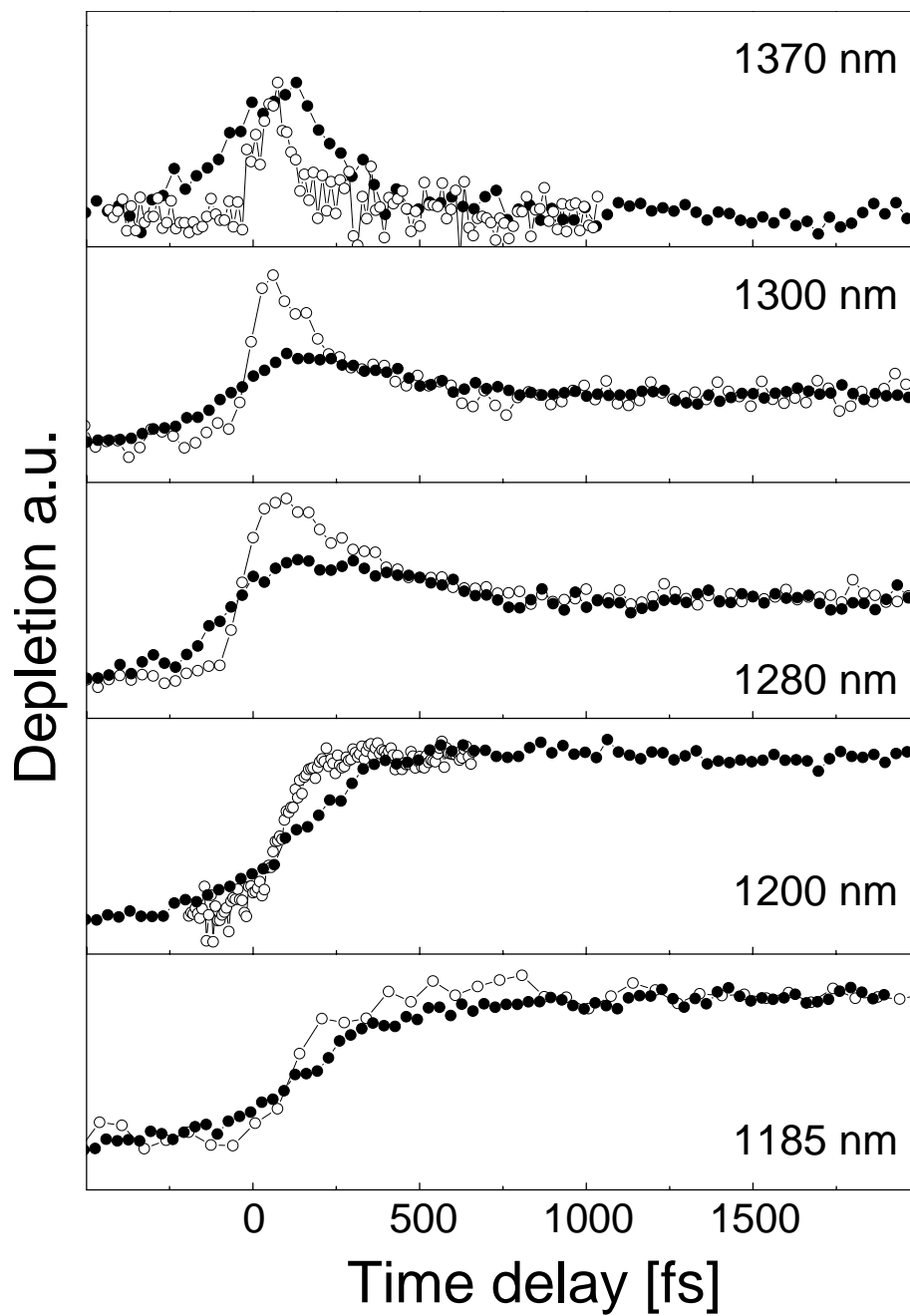
Figure 6.3: Comparison between one- and two-photon excited transients at different probe wavelengths. Refer to Fig. 4.2 for the corresponding experimental cross-correlations. **Open circles:** two-photon excitation. **Filled circles:** one-photon excitation [76].
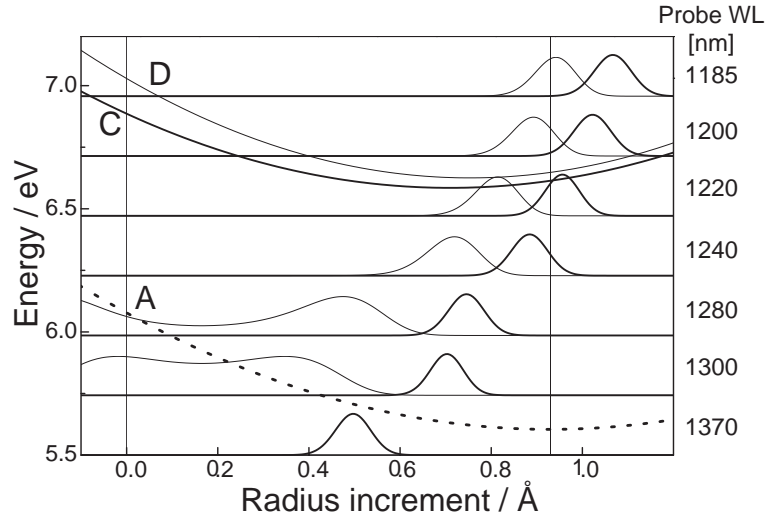
Figure 6.4: Probe windows calculated in the configuration coordinate model associated to different wavelengths (see also § 4.2). **Thick lines.** Transitions to the C state. **Thin lines.** Transition to the D state.

Å increment (Fig. 6.4). On the contrary, the narrow windows centered around 0.7 Å arise from the $A - C$ transition. The fast rise observed in Fig. 6.5 for these two transients, therefore, is consistent with the creation and ultrafast departure of a wavepacket, in line with the interpretation of the signal at 1370 nm. Given that the first structure in the 1300 nm transient is larger than the experimental cross-correlation, it can be decomposed into the sum of two gaussians with the width of this latter. Such a procedure suggests that this feature can be related to the overlapping signals arising from the two distinct transitions opened by the probe to the D and C states. The difference in amplitude of the two gaussians, reflects the importance of the relative contributions of the windows to the depletion, which is also related to their widths along the configuration coordinate.

The dotted lines in Fig. 6.5 represent a visual guide to follow the subsequent procedure, which establishes a *direct* link between the depletion transients and the time-evolution of the cage radius increment.

The second peak in the scan at 1280 nm is almost coincident with the corresponding one at 1300 nm, as expected from the relative positions of the windows to the C state opened by these two wavelengths. The peak shown by the transient at 1370 nm, according to Fig. 6.4 and to the fact that it corresponds to a dynamics faster than the time-resolution, reasonably takes place between the maxima of the two gaussians used to fit the signals at 1300 and 1280 nm. The rise of the signal at 1240 nm reaches its maximum in correspondence to the second window at 1300 nm, which sits at the same configuration of the first probe window of this transient (Fig. 6.4). The scans obtained at shorter wavelengths (1185 nm), on the other hand, clearly keep on growing after the time delay associated to the second window at 1300 nm (160 fs), as the wavepacket, at this stage, has still not reached the configuration sampled by these probes.
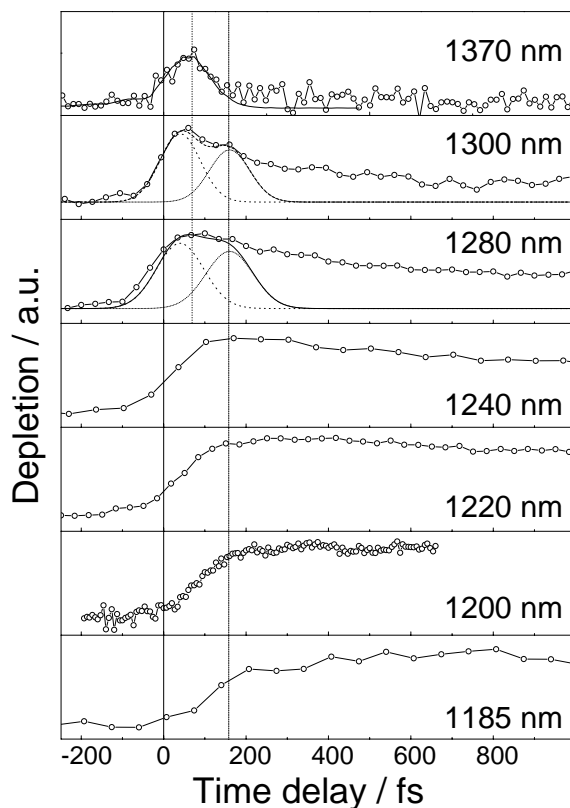
Figure 6.5: Internal clocking procedure from the decomposition of the two redmost transients using the probe windows of Fig. 6.4.

The intensities of the depletion signals increase as the probe wavelengths decrease. In fact, the efficiency of the depletion process depends on the dwell time of the wavepacket in the configuration sampled by a given probe. Therefore, it is not surprising that the most intense signals are associated to wavelengths which sample the final stage of the dynamics, at the bottom of the A state potential, where the system settles down, after the ultrafast initial expansion.

6.2   Long time dynamics

The relaxation process is not completed after 1-2 ps. Indeed, the series of depletion scans measured for longer time delays presented in Fig. 6.6, unambiguously reveals that dynamical processes are still taking place on the time scale of several picoseconds.

The scans in the figure are measured with the same pump power and at different probe wavelengths. All the transients chosen for the comparison are characterized by the same relative depletion level (~ 0.4). The relative intensities of the different probes used to achieve this depletion level are given as a function of the intensity of the bluemost probe, I_0. This depletion is relatively

7cm
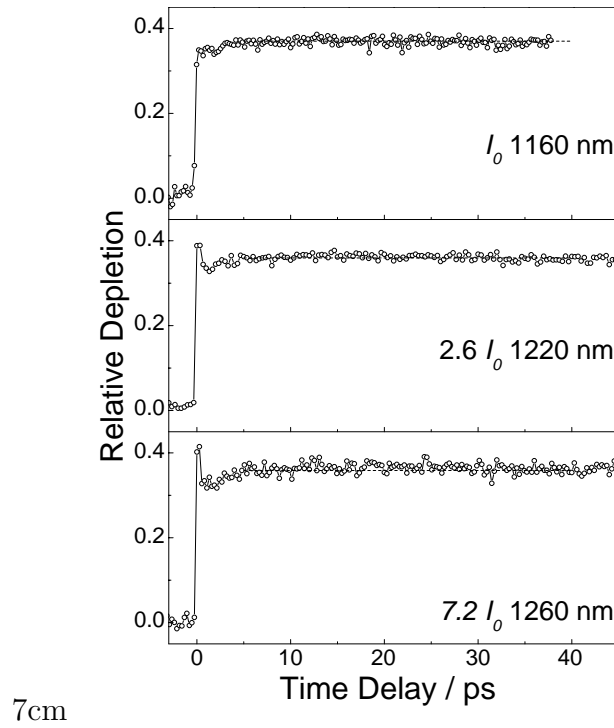
Figure 6.6: Long time depletion scans at different probe wavelengths. The depletion level is the same in all the transients (~ 0.4). The intensity of the probe beams are relative to the intensity at 1160 nm, I_0.
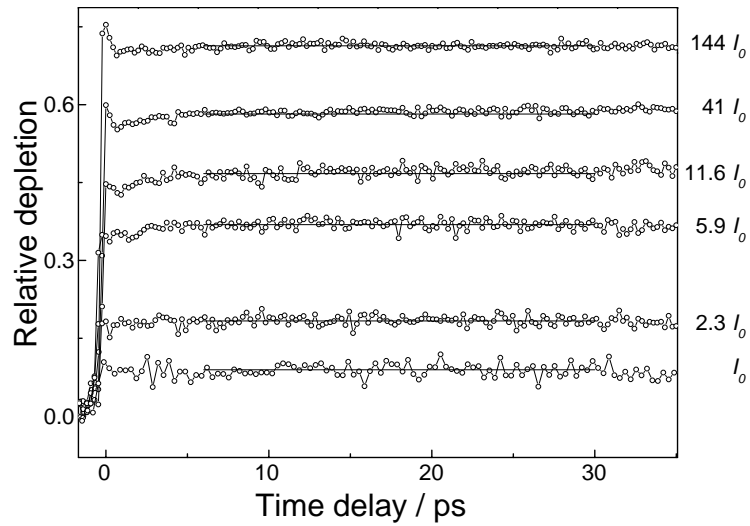
Figure 6.7: Probe power series at 1160 nm. On the right side the probe intensities relative to the weakest probe I_0.

high, and the corresponding transients are saturated in the probe power (see appendix A). The effect we are interested in, namely the rise in the depletion signal during the first 5 ps, is a 5-7% effect, and it is clearly above the noise exclusively for measurements at high-depletion level (see also Fig. 6.7). As a general observation, we can state that this increase in the depletion level takes place in 5-10 ps and is common to all probe wavelengths.
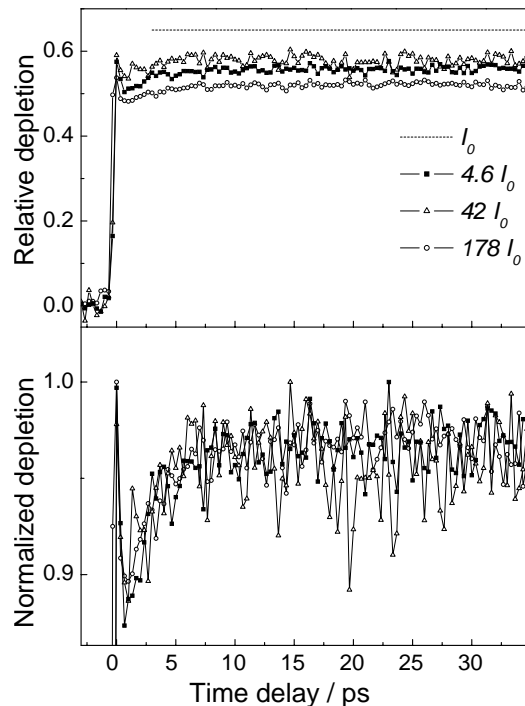
Figure 6.8: **Upper panel.** Pump power dependence at 1160 nm. The difference traces correspond to different pump intensities. The number of fluorescence counts associated to each curve is expressed as a multiple of the weakest fluorescence, I_0 . The dotted line represents the average level of depletion obtained for I_0. **Lower panel.** Depletion curves of the upper panel normalized.

Figure 6.8 shows the depletion transients at 1200 nm, obtained varying the pump intensity over a wide range of values, and keeping fixed the probe intensity. Even in presence of variation of a factor 40 in the number of fluorescence photons, the different transients show the same time dependence, when normalized to the first peak (Fig. 6.8 bottom), and we clearly distinguish the rise time on a time scale of 5-10 ps.

To understand the origin of this feature, we have performed a series of polarization measurements on this long timescale (see § 4.3.2), looking for any signature of time-dependent anisotropy. The transients associated to different pump, probe and detection polarizations are equivalent: this observation allows us to exclude that this effect is related to the rotational re-orientation of the impurity in the matrix cage.

For a few measurements at high probe-power, characterized by a particulary good signal-to-noise ratio (namely better laser shot-to-shot stability and more constant behavior of the fluorescence) a structure after 10 ps is observed in the long time signal (Fig. 6.9). The presence of such a feature, which is probably a recurrence, suggests an analogy with similar results in NO-doped rare gas solids [95, 112, 129]. In these cases, analogous structures were related to breathing modes of the cage. A sort of elastic response of the bulk perturbed by the sudden expansion of the first shell of molecules around the impurity, which determines a contraction of the cage around the dopant, and results
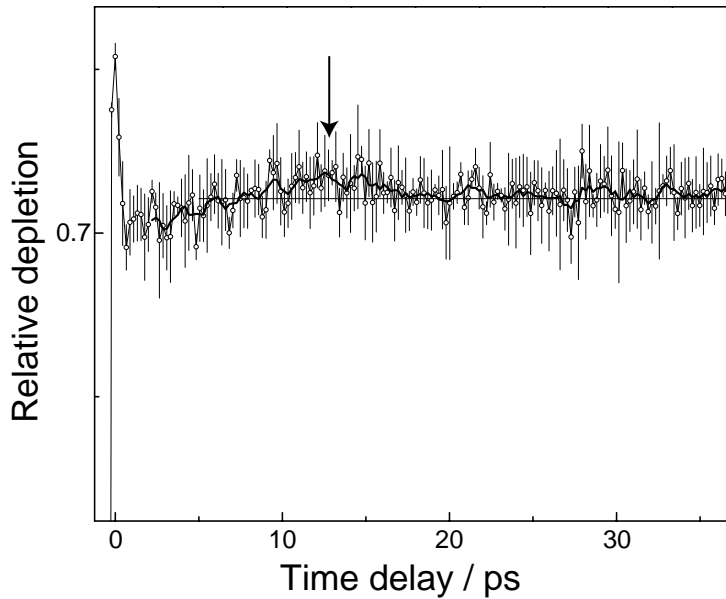
Figure 6.9: Particular of the depletion signal at 1160 nm obtain at very high probe intensity. The error bars represent the dispersion of the experimental data points. The transient is the average of four successive scans at 1000 shots per data point. The **arrow** indicates the position of the recurrence at 12 ps. **Thick line:** smoothing of the experimental data points. **Thin line:** guideline to the eye.

in an increase in the depletion signal. This *mechanical* interpretation is very tempting for its simplicity. The difference in the timescales observed in hydrogen, neon and argon will be further discussed in terms of the macroscopic bulk properties of the different hosts in chapter 8.
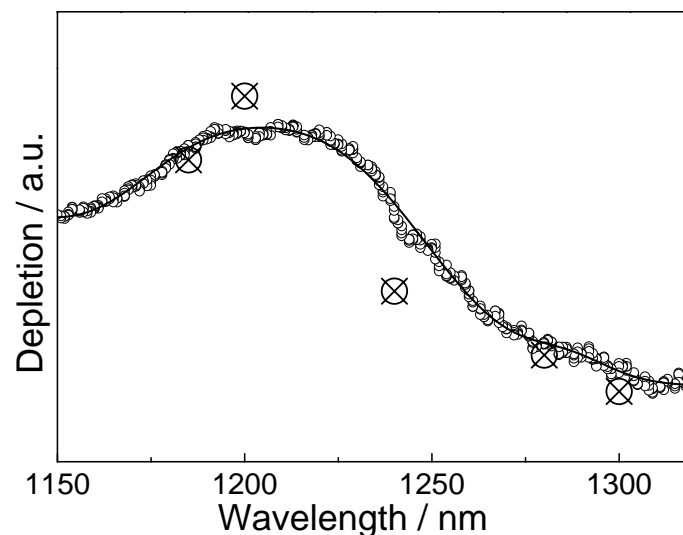
Figure 6.10: Signal at long delays (**crossed circles**) and nanosecond profile of the Rydberg *A* - Rydberg *C* and *D* states (**open circles**). See also Fig. 3.4

As a final remark, we note that the dynamics of the system is completely over on the timescale investigated by the experiment. This evidence is provided

by the agreement among the final levels of depletion (> 10 ps) measured for various probe wavelengths, and the spectral profile of the A state *nanosecond* depletion, as reported in Fig. 6.10 [20]. The depletion levels shown by the different transients, in the limit of very low probe intensities, span more than one order of magnitude going from 1300 to 1200 nm.

6.3 Excitation energy dependence

The time-resolved transients presented in this chapter have been obtained measuring the depletion of the fluorescence stemming from the $v' = 0$ level of the A state, setting the fluorescence detection at the maximum of the $A(0, 2)$ band. In § 5.2.2, we observed that, upon laser excitation at 404 nm, we measure two distinct vibronic progressions associated to the $v' = 0$ and $v' = 1$ vibrational levels of the A state. The time-resolved transients corresponding to the depletion of these two distinct progressions are *a priori* not equivalent. The schematic diagram shown in Fig. 6.11 indicates that, in the configuration coordinate model, the NO vibrational states $A(v' = 0)$ and $A(v' = 1)$ are represented by two parallel harmonic potentials shifted by one vibrational quantum, which corresponds to 2307 cm^{-1}, as calculated from the energy difference between the positions of the $A(0, 0)$ and $A(1, 0)$ bands shown Fig. 5.4. From the scheme, it is evident that, after the vertical transition induced by the pump beam, the system is left with a different amount of excess energy with respect to the well of the potential: 4305 cm^{-1} and 2004 cm^{-1} for the $A(0)$ and $A(1)$ state, respectively. The two transients plotted in Fig. 6.12 are measured using a narrow spectral detection centered selectively at the maximum of the $A(1, 0)$ (filled circles) and $A(0, 1)$ (empty circles) fluorescence bands. The probe wavelength (1200 nm) samples the end of the dynamics according to the windows of Fig. 6.4.

The two transients do not show any difference. This observation can be interpreted in terms of an adiabatic evolution of the system during the first 200 fs, as it expands along the A state intermolecular potential. In other terms, the system behaves as a pure isolated harmonic oscillator during the initial stages of the cage expansion: *the time elapsed to reach the minimum of the potential does not depend on the starting position on the potential curve.*

This interpretation is consistent with the time-profile measured for the signal corresponding to 1370 nm probe (Fig. 6.1). In fact, as we observed in § 6.1, the fluorescence depletion signal probed by this wavelength conserves the time-structure of the pump pulse, pointing to a highly coherent evolution of the wavepacket up to this stage of the dynamics (70 fs, 0.5 Å of radius increment and more than 50% of the initial potential excess energy lost). This scenario, which describes the initial step of the structural relaxation as the *free expansion* of the first shell of H_2 molecules around the impurity, not interacting with the rest of the solid, is also independently confirmed by the results of the molecular dynamics simulations presented in the following chapter.
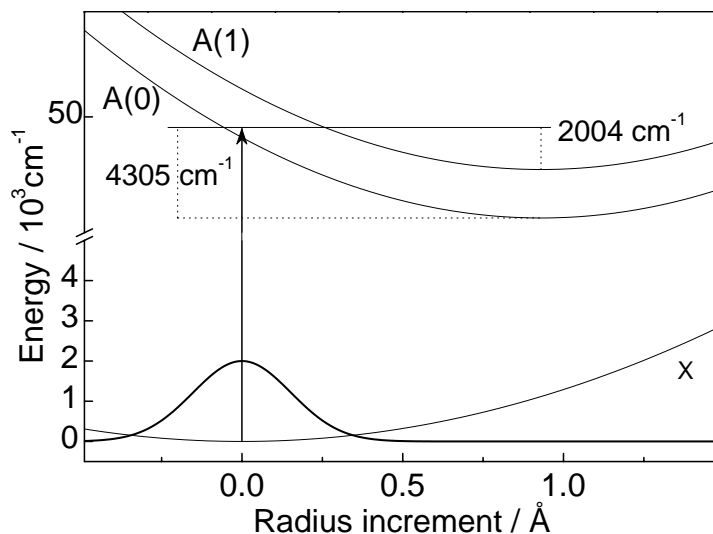
Figure 6.11: Illustration in the configuration coordinate model of the $A(0)$ and $A(1)$ vibronic levels of NO. The excitation process (**vertical arrow**) is associated to an energy of 49504 cm^{-1} (corresponding to $404/2 = 202$ nm). The excess energies above the well of the respective potentials correspond to 4305 cm^{-1} for $A(0)$, and 2004 cm^{-1} for $A(1)$. The ground state wavefunction is calculated substituting in Eq. 2.10 the parameters for the X state given in Tab. 3.4.
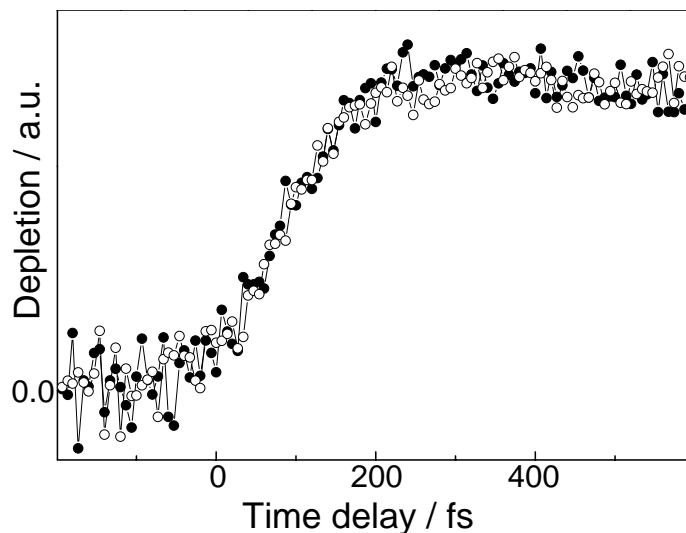
Figure 6.12: Comparison of the time-resolved scans measured detecting the fluorescence of the $A(1,0)$ (**filled circles**) and $A(0,1)$ (**empty circles**) fluorescence bands. The dynamics associated to the two distinct vibrational levels of the A state presents no difference within the time resolution and the noise dispersion of the experiment.

6.4 Comparison between normal- and para-hydrogen

We have carefully looked into the time-resolved dynamics measured with NO-doped para and normal hydrogen samples, searching for the presence of any eventual discrepancy in the fluorescence-depletion transients.

Figure 6.13 presents a comparison between three selected time-resolved transients measured in p-H_2 (open circles) and n-H_2 (filled circles) probed at different wavelengths. Within the noise, no clear differences can be observed. The two scans at short times (upper panels) sample the region mainly associated to the initial expansion (1300 nm) and to the well of the A state potential (1200 nm), as illustrated by the corresponding windows in Fig. 6.4. For the probe corresponding to 1300 nm, the two signals show no significant differences in the rise or in the ratio between the depletion peak at short time, and the long time depletion level. In the case of the 1200 nm probe, the rising-edges of the two signals result very well overlapped. This behavior indicates that the timescales of the expansion process are equivalent for the two hosts.

We observe that the discrepancy in the excess energy left to the system after the pump pulse excitation, arising from the shift in the absorption bands (Fig. 5.3), *does not influence the dynamics* in light of the discussion of § 6.3. In fact, in this context, the time-resolved scans did not show any noticeable difference, even in presence of discrepancies in the excess energy much more important than the present one ($\sim$2000 cm^{-1} between $A(1)$ and $A(0)$ vibronic states).

The lack of any major difference between para- and normal-hydrogen leads also to the conclusion that *the rotational states of the host do not contribute to energy dissipation.* As a matter of fact, even if the energy transfer to the rotational degrees of freedom is energetically favorable [1], it is unlikely to occur. It would not release the repulsion exerted by the Rydberg cloud on the crystal molecules, and, therefore, it would not explain why the emission band occurs slightly red of the gas-phase position of the $A \rightarrow X$ transition (Fig. 3.6). We remind that this fact was considered a clear indication that the host lattice is not strongly interacting with the impurity at the end of the relaxation process. Incidentally, such an observation is in agreement with the scenario proposed in § 3.3, where we related the structural dynamics of the system *exclusively* to the translational (radial) motion of the host molecules around the impurity center.

 The good overlap of the signals obtained for the long time scans (lower panel in Fig. 6.13) indicates that also the third timescale observed in the dynamics,

---

[1]From the rotational Raman measurement in Fig. 5.1, we note that the excess energy given to the system after the pump excitation (Fig. 6.11) would be *largely sufficient* to excite the ΔJ=2 rotational transitions observed in solid hydrogen, corresponding to $6 \cdot B$=356 cm^{-1} ($|0\rangle \rightarrow |2\rangle$) and $9 \cdot B$=534 cm^{-1} ($|1\rangle \rightarrow |3\rangle$). We remind that the absence of excitations of a single rotational quantum is related to the very weak probability to induce a para $\leftrightarrow$ ortho conversion process in the crystal.
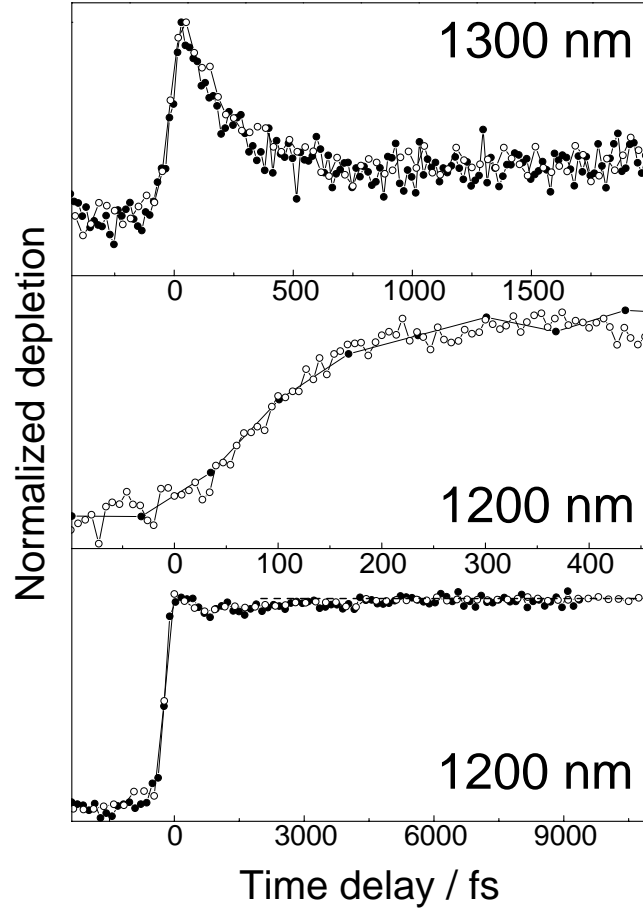
Figure 6.13: Comparison between depletion scans in normal (**filled squares**) and para (**open circles**) hydrogen probing at 1300 and 1200 nm. Note that the time axis in the plots are different.

corresponding to the 5-10 ps rise of the signals discussed in § 6.2, presents no differences in the two hosts. The longitudinal sound velocity is ∼4% greater in normal- with respect to para-hydrogen (Tab. 1.1). Considering that this value is of the order of $2 \cdot 10^3$ m/s, such a difference should become significant on a time scale of 10 ps, and its effects should be evident within the temporal resolution of the experiment. Nevertheless, considering that almost the total amount of energy transferred to the excited center leaves the impurity site on a sub-picosecond timescale, we hardly expect to see a 4% difference in the residual signal associated with the energy which is still localized within a few lattice shells around the impurity.

Another argument, which seems to exclude the presence of discrepancies in the two hosts connected to the different sound velocities, comes from the observation that the perturbation induced by the femtosecond pump laser pulse in the crystal lies out of the response spectrum of the solid. Therefore, we do not expect to see a lattice response characterized by the *static macroscopic properties* of the system.

The results of the molecular dynamics simulations, that will be presented in

the next chapter, seem to confirm this interpretation.

6.5   Summary of results

- Structural relaxation in solid hydrogen is characterized by three timescales: 200 fs, 0.8 ps, 10 ps.

- The first two (200 fs and 0.8 ps) are interpreted, in the framework of the configuration coordinate model, as different regimes of the impurity cage expansion.

- The third timescale is associated with a slow rise of the depletion signal largely independent from the specific probe wavelengths. The bluemost transient presents a very weak recurrence at 12 ps. Similar features observed in NO-doped rare gas crystals have been assigned to breathing modes of the cage surrounding the impurity.

- The comparison between the time-resolved signals at long time delays ($>$10 ps) and the nanosecond profile of the $A - C$ and $A - D$ depletion indicates that the dynamics is over on the timescale investigated by the experiment.

- The excess energy measurements and the transient at 1370 nm point to a coherent character of the very early expansion of the bubble.

- The equivalence in the dynamics of normal- and para-hydrogen indicates that the internal degrees of freedom of the host molecules do not participate to the structural relaxation.

Chapter 7

Molecular dynamics simulations of structural relaxation in NO-doped solid p-H_2

The results of the steady-state and time-resolved spectroscopy indicate that the structural relaxation process is mainly associated with an extensive radial re-arrangement of the lattice species surrounding the site occupied by the excited impurity. In order to confirm this dynamical scenario and get some new insights, we have run a series of computer simulations analogous to the ones carried out on lattice relaxation around NO in solid argon and neon [113, 129]. Simulations of solid hydrogen, however, represent a formidable challenge because of the difficulty of reproducing the zero-point energy effects. When the de Broglie thermal wavelength becomes sizeable with respect to the hard core diameter of the particle, a quantum treatment of the system is required.

While classical simulations of many particles are straightforward, dynamical treatment of many quantum degrees of freedom poses serious difficulties: solving the Schrödinger equation for many-body systems in the interaction field generated by their neighbors is an extremely hard task, much more demanding, from the computational point of view, than simulating the Newtonian dynamics of a large, but finite, number of classical particles. Several approximate methods, usually tailored to specific applications, have been proposed in recent years. The comparison with the experimental results, even if fairly good in a few cases, remains on the average at a semi-quantitative level.

7.1 Computer simulations of quantum solids

The most common approaches adopted for simulating quantum many-body systems are based on the *path integral* formulation of quantum statistical mechanics developed by Feynman [130]. These Monte Carlo (MC) methods, however, are inherently *equilibrium* calculations. This technique was applied in several studies to investigate the nature of lithium trapping sites in para-hydrogen and ortho-deuterium crystals [28, 31, 32].

Scharf *et al.* found that the lattice easily deforms to admit the presence of the dopant molecule, and the distortions heal quickly as one moves away from the impurity site [32]. The high compressibility of the solid is directly attributed to the zero-point motions, and the results show a fairly good agreement with the outcome of similar calculations based on a variational approach derived from the Einstein model [131], as well as with the spectroscopic measurements by Fajardo and co-workers [26]. It is worth noting that the minimum of the p-H_2 - Li pair potential occurs at 5.22 Å and, therefore, it is comparable to the size of the relaxed bubble in our work, as deduced from the moment analysis presented in § 3.3.1.

Very recently, Saito *et al.* calculated fundamental static properties of solid para-hydrogen including the isothermal compressibility and the phonon density of states, using a novel development of the Feynman path integral approach, known as *centroid molecular dynamics* [132]. With this approach, one can obtain the time correlation function in the quantum Boltzmann statistical regime from semiclassical trajectories [133]. In perspective, this technique could be applied to simulate dynamical properties of quantum systems, being a semiclassical extension of the classical molecular dynamics (MD) approach [1]. The point-like molecules are substituted by ring polymers of interacting classical quasi-particles (the *centroids*), whose time evolution is determined by hybrid MD-MC algorithm [135].

Still, even these recent quantum-based approaches do not fully capture the nature of solid hydrogen. In the work of Saito *et al.*, for example, the comparison of the simulated phonon spectrum with the most recent inelastic neutron scattering measurements is not completely satisfactory [68]. In particular, while any computational method applied so far shows the correct typical Debye-type rise on the low energy side of the phonon density distribution ($\sim \omega^2$), the high energy region results always poorly reproduced.

Simulations of *dynamical* processes in quantum crystals are, at present, even more scarce and less established. Sterling and Apkarian suggested a conceptually simple approach to the problem: they proposed to represent each particle of the system by a spatial Gaussian distribution and to simulate *classically* the time evolution of the centers of the Gaussians in a field of additive pairwise forces [136]. They formally demonstrated that this approach is equivalent to running a classical MD simulation convoluting the potential that governs

---

[1]The method has been finally justified in a rigorous mathematical sense in 1999 by Jang and Voth [134], for various years it was applied because it was intuitively considered correct, or - to quote Voth - because it *"feels right"* [133].

the two-particles interaction with a Gaussian function. The width of the latter should be determined in a self-consistent manner, namely it is required that the minimization of the lattice sum of the convoluted potentials yields the experimental lattice constant. However, applying this requirement of self-consistency, the simulations of the static properties of the crystal do not produce satisfactory results. In particular, the simulated radial distribution function and the phonon distribution do not compare well with those calculated using quantum Monte Carlo approaches. In a successive publication [30], the same authors apply the model to study the rotation of molecular oxygen in solid hydrogens. In this case, the Gaussian is optimized in order *to reproduce* the phonon density of states and the radial distribution function, and therefore its width is not determined independently from the model. The results reproduce the experimental evidence of absence of free rotations of oxygen when excited to the A' state [27], in contrast with the predictions of the classical MD simulations [2]. These results are in line with the image that, in quantum hosts, the cavity surrounding the solute is a dynamic structure which tends to conform to the impurity, and the rotations are quenched into coupled molecule-cage librations.

In conclusion, to our knowledge, just few computational method are able to simulate the properties of condensed phase quantum media, taking into account their nature in a fully rigorous way. Moreover, these methods can provide only limited information about *excited states* and dynamical processes [137], and they are still not suited to study systems *strongly driven out of equilibrium*, as in the case of the present experiment. In addition, calculations based on these recent computational techniques generally require to be performed on large computer clusters [137].

7.2 Classical molecular dynamics simulations

We have chosen to implement *classical MD simulations with an effective temperature correction to mimic the quantum fluctuations of the system.*
Our choice is based on the following considerations:

1. the specific physical properties of the process, in particular its energetics;

2. the requirement to compare with simulations both static and dynamic features (static spectroscopy and time-resolved fluorescence depletion);

3. the observation that the internal degrees of freedom (rotational states) of the host solid are not involved in the dynamics, as assumed in the bubble model of § 3.3 and discussed in light of the experimental results in § 6.13.

---

[2]In this work, the effective temperature in the classical MD simulations was set to 50 K, using the correction shown in Eq. 7.7.

7.2.1 Methodology

MD simulation were implemented using a standard procedure [138]. A hexagonal closed packed cell lattice (lattice constant $a = 3.78$ Å, see Fig. 1.1) composed by 800 hydrogen molecules was created, and periodic boundary conditions were applied in order to simulate an infinite crystal. The primitive box resulted almost cubic, with dimensions $L_x = 30.32$ Å, $L_y = 32.83$ Å, $L_z = 30.95$ Å.

The dynamics of the system of H_2 molecules was simulated via the numerical integration of the classical equations of motion of an ensemble of $N=800$ interacting point-like particles described by the Hamiltonian:

$$H(\overrightarrow{r}, \overrightarrow{p}) = \sum_{i=1}^{N} \frac{p_i^2}{2m_i} + V(\overrightarrow{r}_1, ..., \overrightarrow{r}_n) \; , \qquad (7.1)$$

where the potential $V(\overrightarrow{r}_1, ..., \overrightarrow{r}_n)$ can be decomposed into a sum of pair interactions $V_{ij}(R_{ij})$, depending on the distance R_{ij} between the ith and j^{th} particle:

$$V(\overrightarrow{r}_1, ..., \overrightarrow{r}_n) = \frac{1}{2} \sum_{i}^{N} \sum_{j \neq i}^{N} V_{ij}(R_{ij}) \; . \qquad (7.2)$$

The integration of the equations was achieved using the velocity-Verlet algorithm [139] with a time-step of 5 fs. The forces acting on each particle were calculated using the minimum image convention, and the interaction potentials were truncated by a radial cutoff corresponding to half of the shortest box length. Equilibrium simulation were run in the microcanonical ensemble [3] for 500 ps after a typical equilibration period of 50 ps in the canonical ensemble [4]. For this equilibration step, the velocities of molecules were scaled to reach the desired temperature and adjusted to yield a system with zero total angular momentum.

7.2.2 Intermolecular potentials

Hydrogen-Hydrogen. The interactions between hydrogen molecules were approximated by the Silvera-Goldman (SG) pair potential [140]. This semi-empirical potential, which was developed to reproduce bulk properties of solid H_2 and D_2 , implicitly incorporates many-body corrections. It can be written, in fact, as the sum of a pair, $\phi_{pair}(R_{ij})$, and a many-body, $\Phi_{mb}(\overrightarrow{r}_1, ..., \overrightarrow{r}_n)$, contribution. The latter is approximated as a sum of *effective* pair interactions

---

[3]At constant energy.
[4]At constant temperature.

$\phi_{mb}(R_{ij})$ proportional to R_{ij}^{-9}. The complete analytical expression is given by:

$$V_{H_2-H_2}(R_{ij}) = [\phi_{pair}(R_{ij})] + [\phi_{mb}(R_{ij})] =$$
$$= \left[\exp(-\alpha - \beta R_{ij} - \gamma R_{ij}^2) - \left(\frac{C_6}{R_{ij}^6} + \frac{C_8}{R_{ij}^8} + \frac{C_{10}}{R_{ij}^{10}}\right) f(R_{ij})\right] +$$
$$+ \left[\frac{C_9}{R_{ij}^9} f(R_{ij})\right] ,$$

$$(7.3)$$

where the function $f(R_{ij})$, which is introduced to join the short and long range asymptotic behavior, cutting off the terms which diverge to infinity at the origin, is defined as:

$$f(R_{ij}) = \begin{cases} \exp\left[-(1.28R_{min}/R_{ij} - 1)^2\right] & R_{ij} < 1.28 \ R_{min} \\ 1 & R_{ij} > 1.28 \ R_{min} \ . \end{cases} \qquad (7.4)$$

In the expression, R_{min} represents the position of the well minimum of the pure pair interaction potential $\phi_{pair}(R_{ij})$.

With the parameters given in Tab. 7.1, the well depth corresponds to $\epsilon_{H_2-H_2} = 32.2$ K, and the potential minimum occurs at 3.44 Å.

α	β	γ	C_6	C_8	C_{10}	C_9
1.713	1.5671	$9.93\cdot10^{-3}$	12.14	215.2	4813.9	143.1

Table 7.1: Values for the Silvera-Goldman potential from Ref. 140. All entries in atomic units.

Ground state NO - Hydrogen The interaction between the NO impurity in its ground state X, and the hydrogen molecules of the host crystal was described by a Lennard-Jones pair potential:

$$V_{NO(X)-H_2}(R_{ij}) = 4\epsilon \left[\left(\frac{\sigma}{R_{ij}}\right)^{12} - \left(\frac{\sigma}{R_{ij}}\right)^6\right] , \qquad (7.5)$$

with $\epsilon = 6.2\cdot10^{-3}$ eV (71.9 K) and $\sigma = 3.11$ Å. The potential corresponds to the one proposed by Thuis *et al.* for describing the NO X - Ne interaction on the basis of inelastic scattering data in molecular beams [141].

The choice was motivated by the fact that an equivalent *experimental* potential for NO-H$_2$ does not exist [35]. Alternatively, we could have adopted a *combination* of the NO-NO and H$_2$ -H$_2$ pair potentials. According to the rule suggested in Ref.142, the depth of the NO-H$_2$ pair interaction corresponds to $\epsilon_{NO-H_2} = \sqrt{\epsilon_{NO-NO} \cdot \epsilon_{H_2-H_2}} \simeq 65.3$ K. Considering the approximations involved in both the alternatives, and the relative small discrepancy (10%), we decided to retain the experimental potential for the simulations.
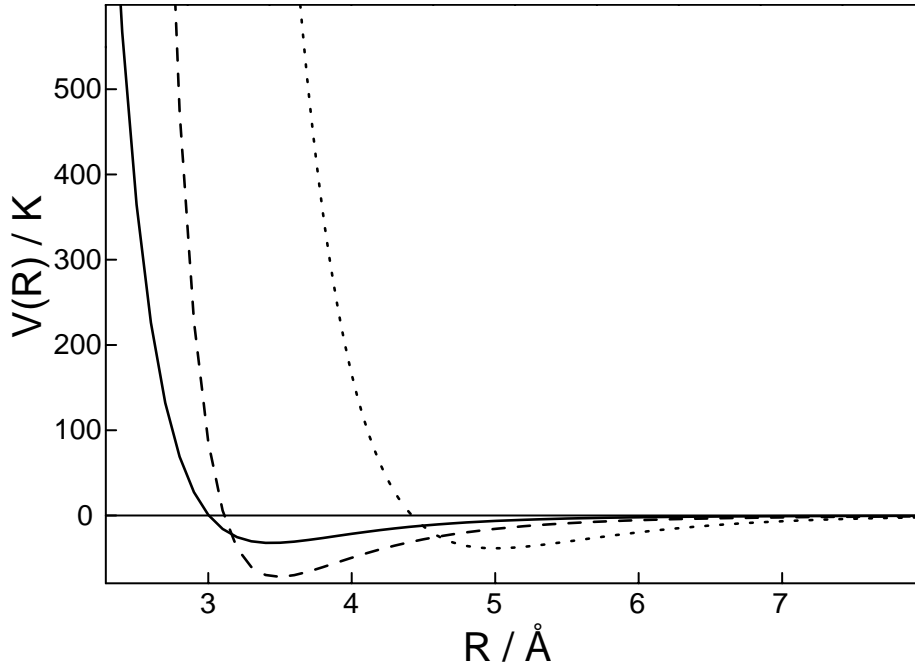
Figure 7.1: Potential curves used for the simulations. **Continuous line.** Silvera-Goldman potential to describe the H_2 - H_2 interaction, from Ref. 140. **Dashed line.** NO X - Ne Lennard-Jones potential. **Dotted line.** NO A - H_2 Morse potential.

Excited state NO - Hydrogen   We chose a Morse potential in the form:

$$V(r) = D_0 \left[1 - e^{-\beta(r-r_e)}\right]^2 - D_0 \ , \qquad (7.6)$$

to describe the interaction between the impurity in the excited A state and the hydrogen molecules. The various parameters entering in the formula were *iteratively* adjusted so as to reproduce the experimental steady-state absorption and emission lineshapes. The details of this procedure are discussed in § 7.3.2. We observe that the choice of a Morse potential was motivated exclusively by the better agreement found over other possible analytical expressions, and it is not justified by any specific physical reason. The final set of parameters, corresponding to $D_0 = 2.3 \cdot 10^{-3}$ eV, $\beta = 1.195$ Å^{-1} and $r_e = 5$ Å, yields a fairly good agreement with the experimental spectra, as shown in Fig. 7.3.

7.3   Results of the MD simulations

7.3.1   Simulation of the neat H_2 solid

Classical MD simulations are unable to reproduce the structure of solid hydrogen, because they do not capture its quantum character.
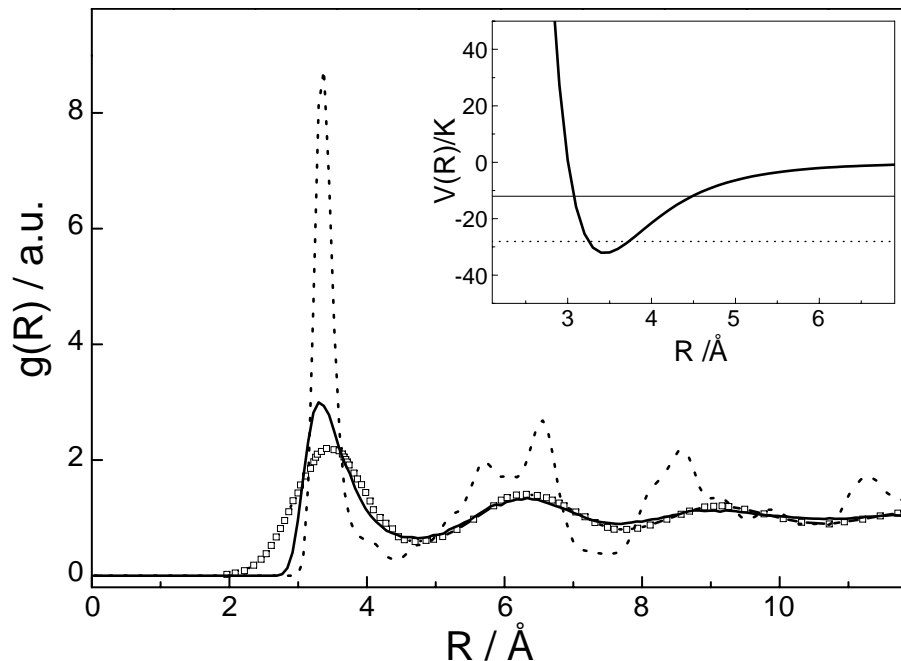
Figure 7.2: Radial distribution functions. **Empty squares.** Result of PIMC simulations from Ref. 32. **Dotted line.** Result of MD simulations run at 4 K. **Continuous line.** Result of MD simulations run at 20 K. **Inset.** Region of the well of the SG potential compared with the temperatures of the classical MD simulations represented as lines at 4 K (**dotted line**) and 20 K (**continuous line**) above the potential minimum.

Figure 7.2 displays the H_2 - H_2 radial distribution functions [5], $g(R)$, calculated at 4K using MD simulation (dotted line) and at 3K using Path Integral Monte Carlo (PIMC) simulations (empty squares) [32]. Since PIMC simulations were found very good at reproducing this structural quantity, inferred from inelastic neutron scattering [143], the latter is considered in the following as a reference. As expected, because of the quantum delocalization effect, it results much less structured than the distribution simulated by the classical MD approach at 4 K. The "exact" $g(R)$ bears the shape typically observed for classical liquids. As we are interested in investigating the dynamical response of the medium to an impulsive local excitation, it is mandatory to reproduce the structure as close as possible.

In order to include in MD simulations the effect of quantum fluctuations in the particles positions, Bergsma *et al.* proposed the so-called thermal harmonic quantum correction [144]: the nuclear motions are assumed to be harmonic oscillations of angular frequency ω, and the classical limit ($\frac{\hbar}{2} \to 0$) is applied to approximate the diagonal elements of the density matrix at temperature T. The classical result can be corrected to include the quantum effects in the position of the molecules, simply multiplying the temperature T, at which the

---

[5]This function gives the probability of finding a pair of atoms at a distance R apart, relative to the probability expected for a completely random distribution at the same density [138].

classical calculations are performed, by the factor C defined as:

$$C = \frac{f}{\tanh(f)} \ ; \ f = \frac{\hbar\omega}{2K_BT} \ . \tag{7.7}$$

This correction has already been applied for simulating rare gas crystals, assuming ω to coincide with the Debye frequency of the solid [113].

In the case of hydrogen, however, the Debye frequency lies between 80-100 cm^{-1} (Fig. 1.3) and, according to correction 7.7, the scaled temperature would exceed 50 K for the simulation of a solid at 4 K. Accordingly, the *effective* kinetic energy of the particles would rise beyond the pair-binding energy (32 K), and therefore the simulations would correspond to that of a lattice gas. This is not surprising, as in solid hydrogen the anharmonicities of the potential are expected to be important even close to equilibrium [15], and the correction may not apply.

We decided to anyway keep the idea of a thermal correction, and we proceeded to adjust the temperature in order to reproduce as close as possible the quantum fluctuations in the particles positions via the radial distribution function. The best agreement between the $g(R)$ calculated using the PIMC technique and the result of the classical MD simulations was found for an effective temperature of 20 K (continuous line in Fig. 7.2). In the inset of the figure, the region around the well of the H_2 - H_2 pair potential is compared with the temperature of the MD simulations: we note that at 20 K the contribution of the anharmonic part of the potential to the dynamics is much more significative than at 4 K. The overall agreement between the two radial distribution functions is fairly good. In the following sections, we will justify the assumption that the details of the structure at short distances from the excited center (i.e. the molecules starting to participate very early to the dynamics of the system) are not supposed to be strongly affected by the discrepancies among the two curves. The artificial introduction of kinetic energy implies also that some dynamical properties, such as self diffusion, are not reproduced. Again, the influence of this inconsistency on the medium response, at least at short times, is not expected to be very significant, as the amount of energy introduced in the system by the cavitation exceeds by far the average kinetic energy of the lattice molecules [6].

7.3.2   Simulation of the steady state spectra

The methodology applied to simulate the *doped crystal* is similar to the one described for the neat solid hydrogen, with the difference that one H_2 molecule is now replaced by a NO molecule. The equilibrium MD simulations are run at an effective temperature of 20 K to reproduce the correct structure of the solid surrounding the impurity, as discussed in the preceding section. The NO A - H_2 Morse potential was iteratively optimized in order to reproduce the

---

[6]The observed Stokes shift of 0.6 eV corresponds to about 7000 K: for comparison this temperature coincides with the kinetic energy of 230 particles at 20 K.
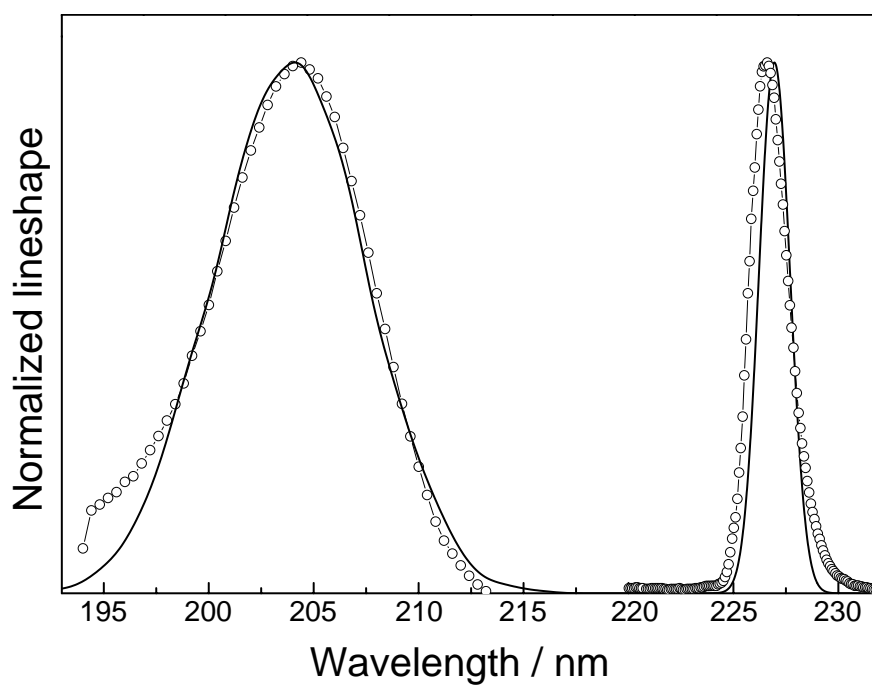
Figure 7.3: Experimental (**empty circles**) and simulated (**lines**) absorption and emission lineshapes.
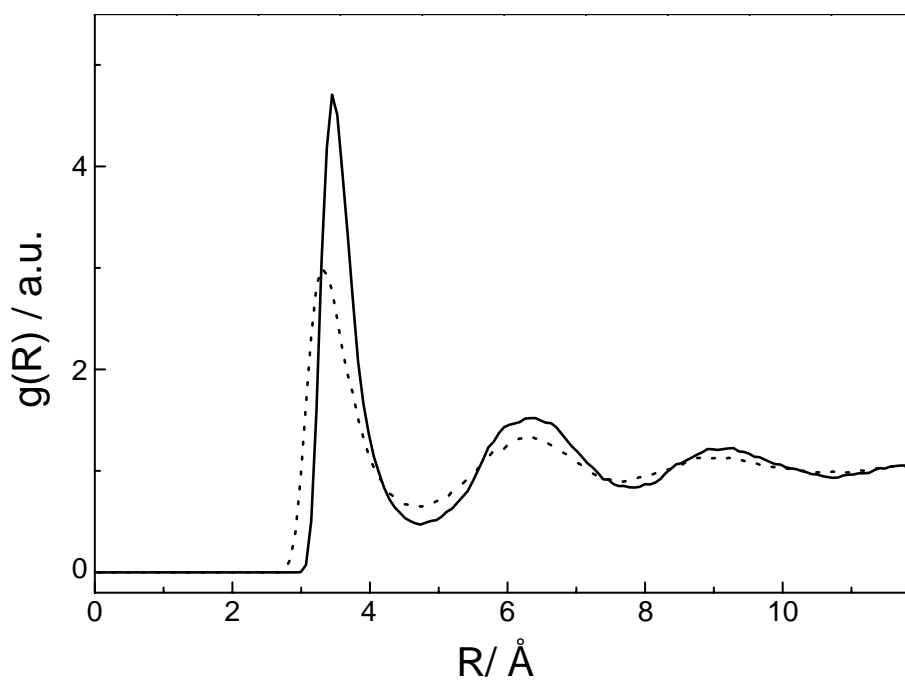
Figure 7.4: Comparison between the simulated radial distribution function $g(R)$ around the NO impurity (**line**) and in the neat solid (**dots**). Note that the presence of the impurity tends to structure more the coordination shells.

experimental absorption and emission lineshapes shown in Fig. 7.3.

In the MD calculations, the lineshapes were approximated by the histogram of transition energies randomly selected during a long equilibrated trajectory (500 ps) for NO respectively in the ground (absorption) and in the excited state (fluorescence). To reproduce correctly the fluorescence band, the spin-orbit splitting of the NO electronic ground state ($\Delta E \sim 15$ meV) was taken into account. The two components of this band were accurately simulated by assuming a branching ratio of 0.8 among the $A^2\Sigma^+ \rightarrow X^2\Pi_{\frac{1}{2}}$ and the $A^2\Sigma^+ \rightarrow X^2\Pi_{\frac{3}{2}}$ transition [145]. For absorption measurements at 4 K, the population of the $X^2\Pi_{\frac{1}{2}}$ state is negligible, so that only the $A^2\Sigma^+ \leftarrow X^2\Pi_{\frac{3}{2}}$ doublet component needed to be computed. The simulated bands were finally convoluted with a gaussian representing the instrumental response function (FWHM 1.5 nm).

From the quality of the agreement in Fig. 7.3, we extract the interaction potentials presented in § 7.2.2.

Figure 7.4 compares the radial distribution function around the ground state NO impurity, and that of the neat solid. The distance to the nearest neighbors does not change appreciably (~ 3.8 Å), as NO in its electronic ground state does not perturb significatively the environment, and fits well in a substitutional site of the crystal [35]. We note, however, that the presence of the guest molecule tends to structure the shells around the impurity, decreasing the probability to find H_2 molecules in the region between two successive maxima of the radial distribution function. This effect is related to the difference in the depth and shape of the H_2 - H_2 (32 K) and NO X - H_2 (72 K) potentials, in the latter the spatial distribution of an NO - H_2 pair allowed at 20 K is considerably less extended.

7.3.3   Simulation of the structural relaxation dynamics

The medium response to the impulsive Rydberg transition of NO have been investigated through non equilibrium MD simulations. To start, uncorrelated initial configurations are taken from an equilibrium trajectory of NO in the electronic ground state. The electronic excitation is successively simulated by switching to the excited state potential, and following the numerical integration of the equations of motion on this energy surface. As a matter of fact, the sample is supposed to be excited by a *broad band, infinitely short laser pulse.* The number of initial configurations taken into account (typically 2000) and the time of numerical integration in the excited state (~ 5 ps) were chosen to reproduce correctly the equilibrium absorption and emission spectra. In particular, the radius of the first shell (or "bubble"), in the configuration of the emission at the end of the dynamics, corresponds to ~ 4.95 Å, and it compares quite well with the value extracted from the moment analysis in § 3.3.1. As mentioned previously, this value of the final bubble radius is in fairly good agreement with a series of experimental works on electron localized in cavity-like states in H_2 and D_2 [115, 116], and with the quantum calculations on the
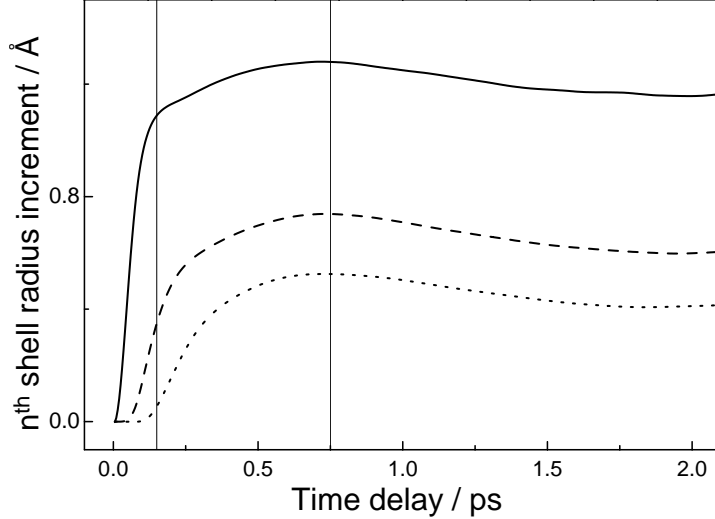
Figure 7.5: Radius increment of the first three lattice shells around the impurity. **Continuous line.** 1st shell. **Dashed line.** 2nd shell. **Dotted line.** 3^{d} shell. The **vertical lines** indicate the instants when the character of the expansion of the 1st shell changes and they are meant to ease the comparison with the depletion signals in Fig. 7.6.

trapping sites of alkali atoms in para-hydrogen [31, 32].

Figure 7.5 shows the radial increments of the first three lattice shells surrounding the impurity as a function of time delay after the excitation. These quantities are calculated as the mean distance between the impurity and the N_i hydrogen molecules composing the ith shell, minus the equilibrium distance R_i^{eq} of the shell calculated for NO in the ground state:

$$R_i(t) = \left[\frac{1}{N_i} \sum_{j=1}^{N_i} |\vec{r}_{ij}(t) - \vec{r}_{NO}(t)| \right] - R_i^{eq} , \quad i = 1, 2, 3 . \quad (7.8)$$

The number of molecules associated to each shell, N_i, is derived directly from the equilibrium distribution function of Fig. 7.4, calculating the integral

$$N_i = \int_{R_i^{min}}^{R_i^{max}} 4\pi r^2 g(r)\rho \, \mathrm{d}r \quad (7.9)$$

between the positions R_i^{min} and R_i^{max} of two successive minima in the function $g(R)$, which defines the spatial extension of the ith shell.

With this procedure, the first shell corresponds to the 14 H_2 molecules nearest to NO, the second to the successive 45, and the third to the following 87.

Early dynamics. Figure 7.5 clearly indicates the presence of two timescales in the expansion of the first shell. 80% of the total expansion distance is associated to a sudden increase of the radius, during the first 150 fs. Later, the dynamics slows down, but the bubble continues to expand until 0.8 ps. The presence of two timescales can be related to the analogous behavior observed in the experimental transients. For simplicity, the changes in regime indicated by the MD simulations are compared directly to the experimental signals by
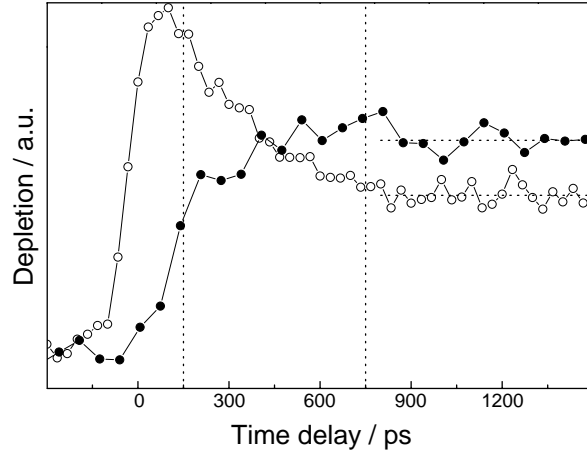
Figure 7.6: Time-resolved depletion signals measured at 1280 nm (**empty circles**) and 1185 nm (**filled circles**) probe wavelengths. The **vertical lines** correspond to the changes in the first shell dynamics derived from the MD simulations (Fig. 7.5). The **horizontal lines** indicate the levelling off of the signals after 0.8 ps. The relative intensities of the plots are re-scaled to facilitate the comparison.

the vertical lines in Fig. 7.6. The initial fast timescale, corresponding to the rising edge of the depletion signals, can be associated to the ultrafast expansion of the bubble up to 0.9 Å increment, shown in Fig. 7.5. We note that the MD simulations indicate that the 2nd and 3^{d} shells are not set in motion during this initial time interval, in agreement with the scenario proposed in § 6.3, which associates the first 150 fs of the structural relaxation to a free expanding bubble, defined uniquely by the 1st shell of lattice neighbors of the impurity. More precisely, the second shell starts to respond to the perturbation 50 fs after the excitation, and the third after ~120 fs. In Fig. 7.6, in agreement with the slowing-down of the bubble dynamics predicted by the calculations, we note a change in the slope of the experimental signals. Indeed, in the 1300 nm transient, at a delay of 150 fs, the system has already passed through the configuration probed by the spectroscopic window (Fig. 6.4), and the intensity of the depletion signal diminishes accordingly. On the contrary, the radius of the bubble has not reached yet the maximum of the observation window opened by the 1185 nm probe, and, in fact, the experimental data indicate a slow growth of the signal of the latter parallel to the decrease at 1300 nm. Finally, we note that the levelling off of the signal around 850 fs, indicated by the vertical line, matches up very well with the end of the expansion in the scenario predicted by the simulations.

The radial increment plots presented in Fig. 7.5, however, represent an approach which is not completely satisfactory to follow the evolution of the system. Indeed, given the liquid-like shape of the $g(R)$, which resembles that of a Lennard-Jones liquid close to the triple point, and taking into account the strength of the perturbation, it is unlikely that the number of molecules in each shell stays constant during all the stages of the lattice response to the perturbation.

To verify the validity of this argument, we have calculated a complete series of *time-dependent radial distribution functions* and derived directly the struc-
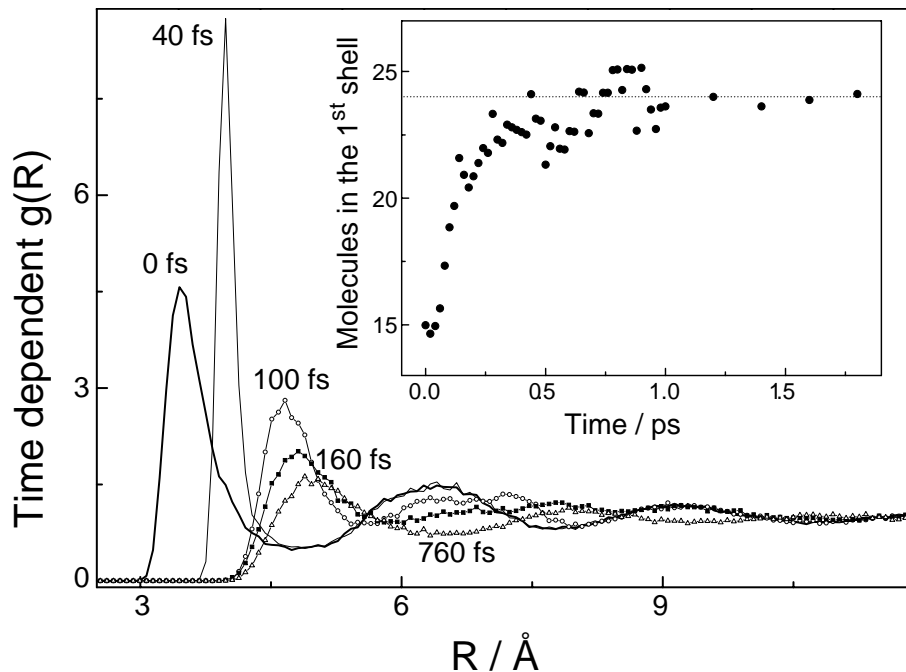
Figure 7.7: Time dependent radial distribution functions at the instant of the transition (**thick line**), and at delays of 40 fs (**thin line**), 100 fs (**open circles**), 160 fs (**squares**), 760 fs (**open triangles**). **Inset.** Number of atoms in the first shell as a function of time.

tural properties of the system, without assuming any given structure. The main results of this calculation are shown in Fig. 7.7. For the analysis which follows, we define a shell at time $\bar{t}$ as the area between the positions $R_i^{min}(\bar{t})$ and $R_i^{max}(\bar{t})$ of two successive minima in the time-dependent radial distribution function, $g(r, \bar{t})$. The significant physical quantities (position, number of constituent molecules,...) associated to each shell are calculated integrating within these boundary limits the appropriate expression of $g(r, \bar{t})$, as indicated, for example, in Eq. 7.9 for calculating the number of molecules in a shell.

At the moment of the excitation, the first shell around the impurity (thick line in Fig. 7.7) contains ∼14 molecules, as indicated in the inset of the figure. During the first 60 fs following the excitation, the structural relaxation involves exclusively this shell. The distribution narrows down as the molecules move away from the impurity site (thin line). This spatial focussing corresponds to a transient increase in the density of the spherical layer, which defines the boundary of the expanding bubble, by about 30% [7]. Correspondingly, the expansion velocity of the molecules of the first shell, $\dot{R}_1(t)$, reaches its maximum (1450 m/s) after 60 fs.

---

[7]Incidentally, we note that the reduction of the zero-point delocalization in presence of a density increase in the solid can be related directly to the expression of the de Broglie thermal wavelength Λ_{dB} of a molecule. Briefly, for a free particle of mass m at a temperature T, the thermal wavelength corresponds to $\Lambda_{dB} = h/(\sqrt{2\pi m k_B T})$. If now we substitute in this equation the expression describing the mean kinetic energy of a free particle, $\langle E_k \rangle = (3/2)k_B T$, we obtain $\Lambda_{dB} = h/(\sqrt{4\pi/3 m K_B T \langle E_k \rangle})$. Considering that the mean kinetic energy increases with the density, we expect the zero-point fluctuations and, more generally, the quantum effects, which are proportional to Λ_{dB}, to be reduced as the local density augments [68].

The "bubble" scenario discussed in § 3.3 results an extremely good approximation to describe this initial period of the structural dynamics, characterized by the free expansion of the first shell of lattice molecules around the impurity. After 100 fs (open circles in Fig. 7.7), this description starts to become inadequate: the number of molecules in the first shell is increased by 25% and the second shell has been set in motion. In the successive 100 fs, the third shell starts too move as well (filled squares), and it results more and more difficult to define the exact structure of the higher shells. As a matter of fact, the environment is perturbed at distances beyond 10 Å from the impurity, while the energy in excess is re-distributed within several hundreds molecules by successive collisions. Moreover, the number of molecules in the first shell is increased by 60%, hence the constant mass assumption made in § 3.3.1 can not yield an accurate description of the dynamics at this stage. The overall slowing-down of the expansion dynamics, associated to the increased mass set in motion during this second regime of the structural relaxation, is recognizable in all the experimental transients shown in Fig. 6.1 by the comparison between the slope of the rising edge at short time delays, and that characterizing the decrease in the depletion signal between 150 and 850 fs (increase in the case of the 1185 nm probe). After the first 150 fs, the assumption of an adiabatic radial expansion of a quasi-isolated harmonic system with the mass of the first shell of lattice neighbors becomes uncorrect. The excess energy left to the system after the electronic excitation of NO is rapidly dissipated throughout the crystal.

In addition, the MD calculations point to *a very rapid randomization of the energy*, contrary to what observed in the case of NO in solid argon [147]. For that host crystal, in fact, the directionality of the perturbation was conserved during the dynamical evolution of the system. In particular, the delays in the response of the higher shells were strongly depending on the crystallographic axes where the Ar atoms were located. For example, it was observed that the 2nd shell was basically silent during all the dynamics, while the atoms of the 9th shell were responding almost immediately to the perturbation, because they were positioned on a linear chain defined by the impurity and the atoms of the 1st and the 4th shells [147].

Propagation of the perturbation.   The MD simulations indicate that the propagation velocity of the perturbation among the various shells exceeds the velocity of the longitudinal sound waves in solid p-H_2 , which corresponds to 2100 m/s (Tab. 1.1). In fact, the calculations yield a value of $\sim$4000 m/s for the propagation velocity of a wave of increased local density between the 1st and the 2nd shell, and a value of $\sim$3350 m/s among the 2nd and 3^{d} shell.

Dynamics at longer time delays (2-5 ps).   The radial distribution functions corresponding to 760 fs and 5 ps are given in Fig. 7.8. The comparison between the two traces indicates that the lattice shells re-organize and become
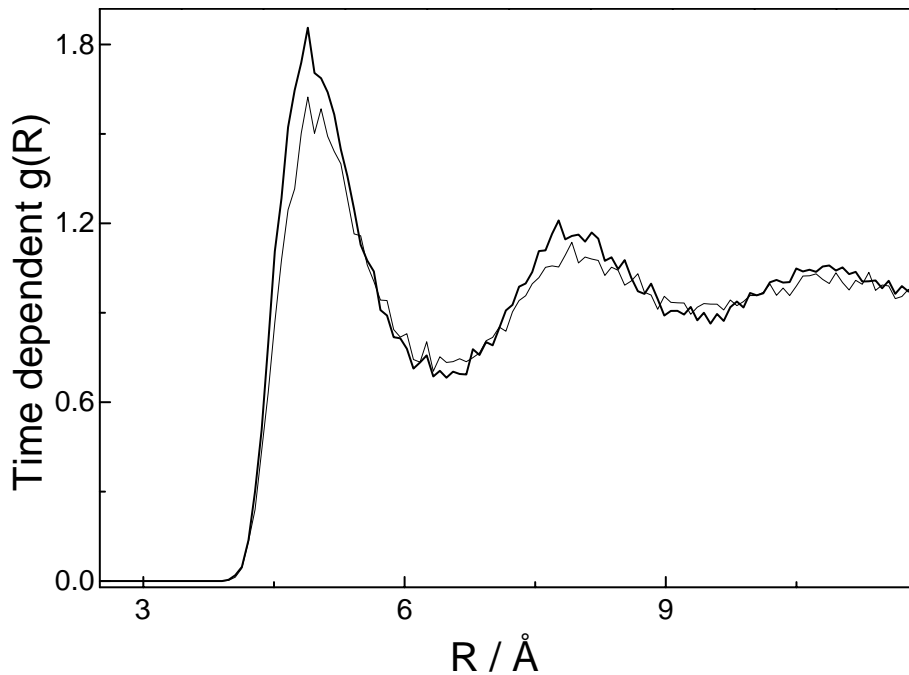
Figure 7.8: Time dependent radial distribution functions at 760 fs (**thin line**) and at 5 ps (**thick line**).

more structured during this interval of time, as indicated by the increased contrast between the maxima and the minima shown by the radial distribution function at 5 ps. More specifically, the simulations suggest an increase of the molecular density around the impurity taking place on a timescale slower than the expansion, as illustrated also by the time evolution of the radius of the first shell in Fig. 7.5. Such a scenario is compatible with the slow-rise observed in the experimental transients at long time delays (see Fig. 6.6). Nevertheless, it should be noted that the re-organization shown by the simulations is over after $\sim$2 ps, while the experimental depletion signals show a growth lasting more than 5 ps. Moreover, various tests indicated that the simulations at long time exhibit a stronger dependence on the effective temperature chosen for simulating the system. Conversely, the sub-picosecond expansion process shows only minor differences when this parameter is varied. This observation may indicate that, on a 5-10 picoseconds timescale, properties like self-diffusion, which we remarked to depend very critically on the effective temperature of the simulations, start to play a fundamental role.

The simulations do not suggest the presence of the recurrence (anyway, very weak: $\sim$1 % of the total depletion signal) at long time delays observed in the experiment (Fig. 6.9).

It should be remarked that, as time goes and an important fraction of the molecules in the simulation box is set in motion, the thermal correction (Eq. 7.7) is not supposed to hold anymore. In fact, the energetic contribution of the excitation, divided by the number of particles participating to the dynamics, becomes comparable to the effective energy given to the system to reproduce the quantum fluctuations. Hence, it is already a remarkable result that few

essential aspects of the dynamics are qualitatively reproduced for delays longer than one picosecond.

7.3.4   Justification of the classical approximation

The classical MD simulations are based on very basic approximations regarding the nature of the environment and they do not reproduce many properties of the solid. However, for the initial few hundreds femtoseconds, we can safely suppose that the dynamics of the system is mainly influenced by the distribution of molecules around the impurity (i.e. the $g(R)$ function that the calculations reproduce with a fairly good agreement) and not by the details of the correlations between the particles or by any other property associated to longer timescales (i.e. diffusion). This assumption is somehow analogous to the *impulse approximation* applied for interpreting the results of deep inelastic neutron scattering [8] experiments [148].

Briefly, if the excitation energy is very much in excess of the maximum energy available within the response spectrum of the lattice, we can neglect the inter-particles interactions and suppose that *the molecules on a short timescale behave as if they were free.* To give a rough estimate, supposing that the excess energy left to the system after the electronic excitation is immediately transformed in kinetic energy of the nearest 15 molecules, the momentum transfer associated to this process would be of the order of 93 Å^{-1}. For comparison, Andreani *et al.* showed that the impulse approximation for their measurements on liquid para-hydrogen is a valid assumption when the momentum transfer is greater than 50 Å^{-1} [149]. In simpler terms of energetics, it is reasonable to suppose that the 7000 K associated to the excitation completely determine the dynamics and hinder the details of the inter-body interactions and the real nature of the delocalization. At least until this excess energy is re-distributed among a great number of particles.

7.4   Simulation of the pump-probe transients

In § 7.3.3, we pointed out that the simulations reproduce the two timescales observed in the experimental transients during the first picosecond of the dynamics. Previously, in § 6.1, we proposed an analysis of the time-resolved data based on the potentials extracted from the moment analysis (§ 3.3.1). At this stage, we can test the validity of these two independent approaches, and simulate the pump-probe signals using the time-dependent radius of the bubble extracted from the MD calculations as input trajectory in the procedure described in Ref. 20 and outlined below.

---

[8]Sometimes this technique is referred to as neutron Compton scattering.

7.4.1 Methodology

The potentials derived by the moment analysis, with the corresponding configurational-dependent probe windows $W_{E_{prb}}(r)$, represent the link between the time-resolved signals $S_{E_{prb}}(t)$ and the temporal evolution of the bubble radius obtained by molecular dynamics, $r_{md}(t)$ [9]. In this respect, the procedure outlined here is explicitly dependent on the assumptions of the bubble model (§ 3.3).

The absorption window associated to each probe laser wavelength is defined as [150]

$$W_{E_{prb}}(r) = \sum_{\alpha=C,D}^{2} \exp\left[-4\ln(2)\frac{(\Delta V_{\alpha-A}(r) - E_{prb})^2}{\Gamma_{prb}}\right] , \qquad (7.10)$$

where E_{prb} and Γ_{prb} represent the probe energy and spectral width respectively [10]. ΔV_{i-A} indicates the difference potential between the A state and the two higher Rydberg states included in the calculation. The key parameters for simulating the depletion signals are the time-dependent *population distribution of radii over space* $(p(t))$, and the corresponding *dwell times* at all configurations and at all times. At a delay τ after the excitation envelope maximum, the time-dependent *classical* population distribution is obtained by projecting a gaussian pulse of duration Θ_{pmp} on $r_{md}(t)$:

$$\frac{dp^c(t,\tau)}{dt} = \exp\left[-4\ln(2)\frac{(\tau - t)^2}{\Theta_{pmp}^2}\right] . \qquad (7.11)$$

The spatial dependence in this expression becomes explicit through the relation:

$$\frac{dp^c(t(r),\tau)}{dr_{md}} = \frac{dp^c(t,\tau)}{dt}\frac{dt}{dr_{md}} , \qquad (7.12)$$

which provides the distribution of radii at any time-delay. To mimic a quantum distribution, the classical distribution is convoluted in space with the gaussian function $\psi(r)$, representing the quantum-mechanical population of the $n = 0$ phonon level of the A state (see Eq. 2.10):

$$\frac{dp(r_{md},\tau)}{dr_{md}} = \int dr' \frac{dp^c(r_{md}\tau)}{dr_{md}}|\psi(r - r')|^2 . \qquad (7.13)$$

In the procedure, we require that the population is conserved at any time after the complete excitation of the system. The dwell time of the population at all configurations, and the finite duration of the probe pulse, are included by means of the coefficients $f_{E_{prb}}$, defined as

$$f_{E_{prb}}(\Delta R) = \begin{cases} \Delta R/v & \text{if } \Delta R/v \leqslant \Theta_{prb}, \\ \Theta_{prb} & \text{otherwise.} \end{cases} \qquad (7.14)$$

---

[9]This quantity is calculated using Eq. 7.8 limiting the sum over the first $N=12$ H_2 molecules nearest to NO.

[10]For simplicity pump and probe pulses are assumed to be gaussian functions both spectrally (Γ) and temporally (Θ).

The parameter $v(r_{md})$ represents the velocity of the wavepacket in the observation window. The spatial extension of the latter depends on the probe spectral width and on the steepness of the difference potential in a given region of space Δr:

$$\Delta R_{\alpha=C,D} = \frac{\Gamma_{prb}}{\frac{\partial}{\partial r}[V_\alpha(\Delta r) - V_A(\Delta r)]} \ . \tag{7.15}$$

With these definitions, the time-dependent pump-probe signal at a given probe energy is calculated integrating the expression:

$$S_{E_{prb}}(\tau) = \int dt' e^{-4\ln 2[(t'-\tau)/\Theta_{prb}]} \int dr_{md} \frac{dp(r_{md},\tau)}{dr_{md}} W_{E_{prb}}(r) f_{E_{prb}}(r_{md}) \ . \tag{7.16}$$

7.4.2   Results

The results of the simulations are displayed in Fig. 7.9 for four different probe wavelengths, distributed in the spectral range covered by the experiment. We observe that the rising edges of the three signals are reproduced with a fairly good agreement. Moreover, the position of time-zero in the simulated traces coincide within ± 30 fs with the direct measurements shown in Fig. 6.2. In particular, the zero is correctly located just before the peak in the 1300 nm transient, and at the beginning of the rise in the 1200 nm one. A similar procedure, applied to all the remaining signals, is in agreement with the relative positions assigned to each of them as they appear in Fig. 6.5. This observation additionally confirms that the MD simulations correctly capture the character of the initial fast expansion of the bubble. Nevertheless, we remark that the simulated traces deviate from the actual signals at time-delays of the order of 200 fs. The increase of the long time offset is reproduced going from 1300 nm to 1200 nm, but the relative intensities are strongly underestimated.

Figure 7.9: **Open circles.** Experimental transients at four different probe wavelengths (1370 nm, 1300 nm, 1240 nm, 1200 nm). **Lines.** Transients reconstructed applying the procedure described in § 7.4.1 using as input the average radius of the 12 nearest neighbors of NO obtained by the MD simulations.

There are many explanations that can account for this discrepancy, some of them are associated to the approximations made to simulate the signal, others

Figure 7.10: Comparison between the X and A potentials from the moment analysis (**continuous lines**) and the ones derived from the simulations (**circles**), as discussed in the text. Note that the energy of the zero-phonon transition has been subtracted to the potentials corresponding to the A state, and therefore the energy difference between the two potentials at 0 radius increment corresponds to the Stokes-shift of the transition.

are more rooted in the assumptions that we have taken to describe the system. Therefore, it can be very insightful to investigate them.

Comparison between the potentials from the MD and from the moment analysis. In Fig. 7.10, we present a direct comparison among the potentials extracted using the configuration coordinate model, and those extracted from the MD simulations. The latter correspond to the time-dependent sum of the energies of all the possible NO-H_2 pairs plotted against the average distance of the first 12 nearest neighbors during the initial 250 fs of the dynamics. The two sets of curves are clearly different and, in particular, the potentials from the simulations lose their harmonic character at relatively short radius increments ($\sim$0.5 Å). This change happens simultaneously to the increase in the interactions between the first and the higher shells of the crystal (Fig. 7.7). This observation calls for a critical re-consideration of some of the assumptions made in § 3.3, where we supposed that the potentials were harmonic when plotted as a function of the bubble radius.

We do not reject the hypothesis that one-dimensional harmonic potentials can be a good approximation to describe the coupling between the impurity and the host crystal. Indeed, the plots in Fig. 3.10 yield a fairly good agreement with the results of the steady state spectroscopy. On the other hand, we note that the potentials of the moment analysis were derived assuming an abstract configuration coordinate q, and only *independently* and *successively* we stated the equivalence $\Delta r = \frac{\Delta q}{\sqrt{M}}$. The validity of this assumption throughout the dynamics is very doubtful in light of the results of the MD simulations.

The hypothesis that the mass of the bubble remains constant along the course of the dynamics holds *strictly* for less than 100 fs (Fig. 7.7). For longer delays, the number of molecules *effectively* associated to the first shell increases by
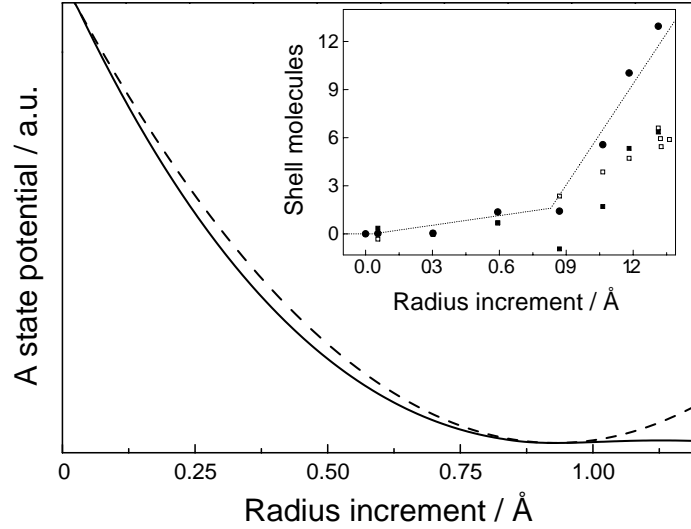
Figure 7.11: Effect of an increasing mass on the A state potential. **Dashed line.** Original potential from the moment analysis plotted against the bubble radius assuming a constant mass in the substitution. **Continuous line.** Same potential plotted assuming the increase of mass as a function of the bubble radius obtained by the MD simulations. **Inset.** Number of additional molecules as a function of the radius increment in the first (**empty squares**) and second (**filled squares**) shell. The **filled circles** represent the sum of the two contributions, the **dotted line** the $m(r)$ function used in Eq. 7.17 to recalculate the potential.

more than 60%. In addition, given the quantum nature of the environment, *there is no clear distinction among the various shells* at some stages of the dynamics.

As a matter of fact, a constant increase in the mass can lead to distortions of a harmonic potential qualitatively consistent with the outcome of the simulations. To verify this point, we proceed to re-define Eq. 3.3, which describes the dependence of the radial increment r on the abstract coordinate q, in the form:

$$r^2 = \frac{q^2}{M + m(r)} \ , \tag{7.17}$$

where M corresponds to the constant mass assumed previously, i.e. 12 H_2 molecules, while $m(r)$ is the increment derived from the simulations. The results of this substitution are illustrated in Fig. 7.11. We note that the modified A state potential (continuous line) for short radius increments is slightly steeper than the purely harmonic one (dashed line). As the bubble increases furthermore, it flattens down and becomes almost constant, exactly as observed for the simulated potential in Fig. 7.10. These observations may eventually help explaining why the simulated transients, that are derived applying the *radial dependent* probe windows to the radius from the MD simulations, deviate so early from the experimental traces.

It is worth noting that the whole timing procedure based on these probe windows conserves its validity. In fact, given the expansion velocity of the bubble at early time, most of the configurations probed by the spectral windows are visited during the ultrafast period when the A state potential conserves a

quasi-harmonic character (§ 6.1). We can suppose that the potentials of the C and D states behave similarly, and the *difference potentials* used to extract the spectral windows are not strongly modified for small radius increments. This assumption is strengthened by the consistency of the analysis of the short time transients carried out in Chap. 6. Moreover, the intensities of the simulated signals of Fig.7.9 span the same range of values exhibited by the experimental transients in the linear regime (see Fig. A.3), even if the exact details are not reproduced.

To conclude, we observe that the potentials derived from the simulations point to the fact that about 65% of the Stokes-shift energy is associated with the dynamics in the A state, while the remaining 35% with the bubble contraction in the X ground state (Fig. 7.10). This result is qualitatively in agreement with the scenario of the moment analysis, which indicates that 75% of the energy in excess is used up to expand the cage around the electronically excited impurity.

7.5 Summary of results

- Equilibrium MD simulations run at 20 K approximate with good agreement the radial distribution function of solid hydrogen.

- The experimental absorption / emission lineshapes are very well reproduced by the equilibrium simulations.

- The bubble radius compares well with the value extracted from the moment analysis and with the estimates reported in literature.

- The simulated time-dependent radial distribution functions reproduce the two regimes of bubble expansion observed in the data (200 fs and 0.8 ps).

- In agreement with the experimental findings, the initial expansion has an *inertial* character. The simulations indicate that the quantum nature of the host medium plays no role during this period of the dynamics.

- The slowing down of the dynamics after 200 fs is due to the increased interactions among the 1st and the successive lattice shells around the impurity.

- The simulations indicate that a slow structural-reorganization process takes place between 0.8 and 2.5 ps.

- The time-dependent bubble radius extracted from the simulations can be used to directly reproduce the experimental pump-probe signals at short time delays.

Chapter 8

Discussion and conclusions

The possibility to apply a continuum model for describing the structural relaxation triggered by Rydberg excitation of NO in solid hydrogen is discussed in § 8.1.1. Successively, we will compare the experimental outcomes obtained for solid hydrogen with analogous results measured with NO embedded in rare gas matrices. In this context, we will generalize the discussion on the common aspects shared by the time-resolved dynamics of these systems, and we will mention possible links with their macroscopic bulk properties.

8.1 Continuum models

In a previous study of bubble formation in solid hydrogens, the structural relaxation was modelled as a hydrodynamic process, where sound emission and friction were assumed as energy dissipation processes [76, 151]. The model applied was originally proposed by Rips to describe electron solvation in water [152], the same approach succeeded in describing the oscillations of a spherical cavity around an excited center in liquid He-II [19]. This comparison was carried out within the framework of the one-photon experiment, characterized by a time-resolution of the order of 350 fs. The model showed agreement to the data for a value of the viscosity (which was the only free parameter in the procedure) of $5 \cdot 10^{-5}$ Pa·s (close to the liquid value). This result suggested a liquid-like response of the medium surrounding the electronically excited impurity. However, the data obtained by one-photon excitation were pointing to a scenario fairly different from the one inferred by the present experiment, and from the MD simulations, as fundamental details about the sub-picosecond ex-

pansion were overlooked due to the poor time-resolution. The cavity radius, in fact, was supposed to undergo over-damped motion, i.e. without overshooting the final equilibrium position, on a timescale similar to the time-resolution.

In the present context, the hydrodynamic model seems inadequate: our data at increased resolution indicate the existence of two timescales in the bubble expansion, followed by a much slower process taking place on a few picoseconds. These observations are altogether not consistent with a hydrodynamic approach.

The presence of multiple timescales rather points to a viscoelastic response. Moreover, this approach seems to be more suited for a process triggered by an high frequency perturbation, beyond the response spectrum of the solid.

8.1.1   Viscoelastic model

Berg has adapted a model based on viscoelastic assumptions to describe analytically the response function $R(t)$ of a solute undergoing an electronic solvation process in a non-polar solvent [153–155]. The normalized time-dependent Stokes-shift $R(t)$ is defined as:

$$R(t) = 1 - \frac{S(t)}{S(\infty)} \ ,$$ (8.1)

where $S(t)$ indicates the time-dependent energy of the electronic transition between the ground and the excited state.

Unfortunately, the observable of our experiment does not allow a *direct* comparison with $R(t)$. In what follows, we will refer to the experimental data when a direct evaluation of the agreement with the viscoelastic model is possible (i.e. timescales), otherwise we will limit ourselves to compare the results of the MD simulations with the model.

The solvation process is simplified in terms of a small expansion (or contraction) of a quasi-spherical cavity within a viscoelastic continuum, as illustrated in Fig. 8.1. The intermolecular interactions of the solute with the solvent are linearized and characterized by a force constant K_s, that we derive from the potentials of the moment analysis. In fact, as this quantity is defined as

$$K_s = -V \frac{\mathrm{d}P}{\mathrm{d}V} \ ,$$ (8.2)

where P represents the outward pressure exerted by the solute on the solvent, and V corresponds to the volume of the cavity, we simply calculate P as

$$P = \frac{F}{4\pi r^2} = -\frac{1}{4\pi r^2} \frac{\mathrm{d}V_A(r)}{\mathrm{d}r} \ ,$$ (8.3)

substituting in Eq. 2.7 the appropriate values contained in Tab. 3.4, which define the harmonic potential V_A.

The solutions of the model predict the existence of two characteristic
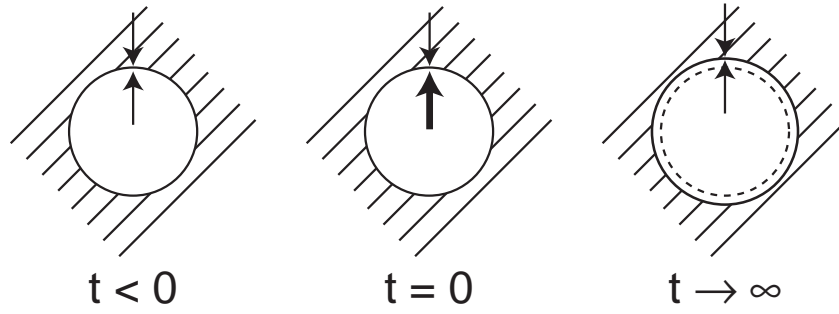
Figure 8.1: Schematic illustration of the viscoelastic model developed by Berg. The solute occupies the central cavity and it is surrounded by the viscoelastic solvent. The equilibrium size of the cavity for $t < 0$ is determined by the balance among the outward pressure of the solute and the pressure from the solvent. A $t = 0$ the solute is electronically excited, and the modulus of the outward pressure changes according to the change in the solute-solvent interaction potential. Successively, the cavity expands until a new equilibrium with the environment is reached.

timescales: τ_l, defined as the time for a high frequency longitudinal sound wave to travel a distance equal to the solute radius, and τ_s, indicating the characteristic timescale for relaxation of shear stress. Under the assumption of mono-exponential decay of the mechanical moduli [1], the latter is simply defined as the ratio of macroscopic viscosity η, and shear modulus $G_\infty : \tau_s = \frac{\eta}{G_\infty}$. The value of τ_l, instead, is calculated as a function of the final bubble size (r_b), solvent density (ρ), and of the bulk (K_∞) and shear modulus (G_∞) [153]:

$$\tau_l = r_b \left[\frac{\rho}{K_\infty + \frac{4}{3}G_\infty} \right]^{\frac{1}{2}} . \tag{8.4}$$

With these definitions, the solvation response function reduces to the sum of two components:

$$R(t) = (1 - f)R^{\text{ph}}(\frac{t}{\tau_l}) + fR^{\text{st}}(\frac{t}{\tau_s}) . \tag{8.5}$$

The faster component, R^{ph}, is due to propagation of a coherent phonon wavepacket in the solvent, which, at short times, reacts to the perturbation as a perfect elastic medium. The second component, R^{st}, accounts for the relaxation of the shear stress created by the impulsive phonon-induced expansion. The weighting parameter f assumes the role of a "Debye-Waller" factor for the process. Its dependence on the solute-solvent force constant K_s is given by

$$f = \frac{\frac{4}{3}G_\infty}{K_s + \frac{4}{3}G_\infty} . \tag{8.6}$$

Comparison with MD simulations. In Fig. 8.2, we present the result of the viscoelastic model (continuous line) along with the response function

---
[1]This approximation is often referred to as *Maxwell model*.
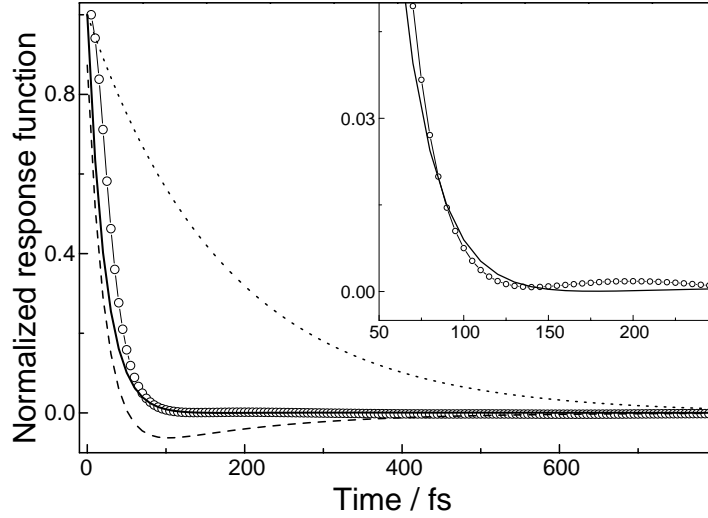
Figure 8.2: **Continuous line.** Viscoelastic response from the model. **Empty circles.** Response function extracted from the MD simulations. **Dashed line.** Phonon-induced component, R^{ph}. **Dots.** Structural contribution, R^{st}. **Inset.** Detail of the comparison at higher magnification.

extracted by the simulations (empty circles). The latter is calculated as the time-dependent energy difference between the sum of all the NO - H_2 pair-interactions in the A and in the X state of the impurity in the configurations assumed by the system during the non-equilibrium dynamics in the A state (§ 7.3.3). For completeness, the separate contributions associated to the phonon-induced R^{ph}(dashed line) and structural R^{st} (dots) relaxations are also displayed.

The input parameters of the model, given in Tab. 8.1, correspond to the macroscopic density, shear and compression moduli of solid hydrogen, and to the effective interaction modulus K_s, derived from the potentials of the moment analysis.

Bulk modulus K_∞	Shear modulus G_∞	Effective modulus K_s	Viscosity η
$2.1 \cdot 10^8$ Pa[a]	$1.08 \cdot 10^8$ Pa[b]	$9.93 \cdot 10^8$ Pa[c]	$1.65 \cdot 10^{-5}$ Pa·s

Table 8.1: [a] for $T = 5.4$ K and $P = 0$ from Ref. 64; for $T = 4.2$ K from Ref. 16; [c] from the moment analysis, A state potential.

The sole free parameter is the viscosity of solid para-hydrogen η, whose value is not known at 3 K [2]. The value of η which yields the best agreement with the response function of the MD simulations corresponds to $1.65 \cdot 10^{-5}$ Pa·s.

---

[2]The available data on plastic deformations, which could be used to extract this quantity, indicate a value of the order of 10^{11} Pa·s [64]. However, these measurements are taken with techniques which involve low-frequency perturbations, and are not expected to describe the behavior of a system driven out of equilibrium by a strong *impulsive* perturbation.

For comparison, the values of viscosity measured in *liquid* para-hydrogen at saturated vapor pressure between 14 K and 20 K range from $2.61 \cdot 10^{-5}$ Pa·s to $1.43 \cdot 10^{-5}$ Pa·s [16].

Even if the agreement between the model and the simulations is not perfect, bearing in mind that the following discussion is strongly *model-dependent*, we believe that we may capture some essential physical aspects of the process.

A first remark regards the phonon-like response of the system: the corresponding typical timescale τ_l results ~ 190 fs. This value compares very well with the fast component shown by the experimental transients. Moreover, the character of this initial expansion is consistent with a coherent process, as discussed in § 6.3.

It is worth noting that the discrepancy between the model and the simulations at very short times in Fig. 8.2 is intrinsic to any continuum approach: in the early period the response function is dominated by single-molecule effects, and the details of the molecular structure can not be averaged out as for later times. Incidentally, the simulations show the correct gaussian-shape behavior around time-zero [155].

The curve corresponding to the phonon response alone (dashed line in the figure), R^{ph}, overshoots the long time asymptote and then decays in an overdamped fashion: this behavior is typical in presence of a very strong solute-solvent interaction [153]. The model predicts that the overdamped character sets in when the value of the effective modulus K_s satisfies the expression:

$$K_s > \frac{4}{3}(K_\infty + G_\infty) \ . \tag{8.7}$$

This inequality is clearly satisfied by the parameters reported in Tab. 8.1. It reflects the fact that the frequency of the perturbation, implicitly contained in K_s via its dependence on the effective frequency of the A state potential (Eq. 8.2), lies out of the mechanical response spectrum of the system.

From all the preceding considerations, we can envisage a scenario as follows: the structural relaxation starts with the creation of a phonon wavepacket propagating away from the impurity. After the main fraction of the Stokes-shift energy has been used to expand the solute cavity, the stress left in the region surrounding the impurity relaxes via dissipative viscous flow. At this stage, the medium response is expected to be associated to modes of lower frequencies.

So far we have supposed that the decay of the mechanical moduli is purely mono-exponential (Maxwell model). This assumption is probably wrong. As a matter of fact, any direct comparison with experiments in liquid solvents from low [156] to very high viscosity [154] indicates that the functions approximating the relaxation of the mechanical properties vary from stretched exponentials to gaussians! The lack of a reliable model increases the number of unknown parameters, and reduces the possibility to extract meaningful quantities from the comparison in Fig. 8.2. However, if we limit ourselves to order of magnitudes, we can keep the Maxwell approximation and simply substitute in the expression for τ_s the duration of the second timescale observed in the experimental transients (0.8 ps). The value that we obtain corresponds

to $\sim 8 \cdot 10^{-5}$ Pa·s. This result enforces the idea that the relaxation process possesses a viscoelastic character, and that the two timescales that we observe in the cavity expansion (200 fs and 0.8 ps) are associated with an initial coherent phonon emission and a successive diffusive viscous flow, characterized by a value of the viscosity close to that of liquid hydrogen. Moreover, the assumption of a single solvent coordinate (i.e. the radius of the bubble) with a complex dynamics (i.e. the presence of multiple timescales), characteristic of the viscoelastic approach, is confirmed both by the experimental results and by the MD simulations.

Such a liquid-like response in solid hydrogen is not totally surprising, considering both the delocalized nature of the radial distribution function, and the great amount of excess energy that we use to perturb the system, which results in a transitory modification of the boundaries between the shells (Fig. 7.7).

8.2   Comparison with structural relaxation in rare gas crystals

Figure 8.3 shows a comparison of time-resolved depletion scans measured in different host matrices. Before proceeding further, we note that the data regarding rare gas crystals are measured via direct one-photon excitation of NO. The corresponding instrumental response is of the order of 350 fs, instead of 130 fs (see § 4.2.1).

We observe a clear trend going from argon to hydrogen:

1. The thermalization time, indicated by the complete levelling off of the depletion signal, gets progressively longer (1.7 ps , 2.5 ps and >10 ps in Ar, Ne, and H_2 respectively).

2. Likewise, the recurrence appears at increasingly longer delays: $\sim$0.8 ps in Ar, $\sim$1.4 ps in Ne, and $\sim$12 ps in solid H_2 .

3. The recurrence gets progressively broader, its temporal width corresponds to <0.5 ps in Ar, to $\sim$ 1 ps in Ne, and to > 5 ps in H_2 . Accordingly it becomes less pronounced with respect to the overall signal intensity.

In rare gas hosts, the presence of recurrences have been explained in terms of elastic response of the medium to the compression wave launched by the sudden expansion of the cavity around the impurity [112, 157]. Argon reacts more promptly and more strongly to this perturbation than neon or hydrogen. In line with this observation, we note that the bulk moduli of the three host crystals, reported in Tab. 8.2, progressively decrease in value going from Ar to H_2 .

This difference in the macroscopic mechanical properties is also related to the
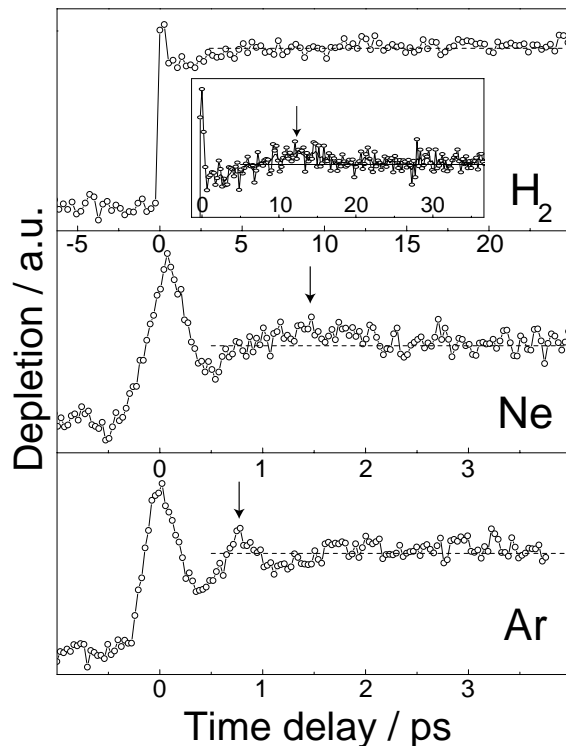
Figure 8.3: Fluorescence depletion scans of NO embedded in hydrogen, neon and argon matrices. The *A* state is excited via 2-photon in hydrogen and 1-photon in the rare gases. Note that the time-axis of the first plot is different. The **arrows** indicate the position of the recurrence.

dissimilar features observed in steady-state spectroscopy. Figure 8.4 shows the absorption and emission lineshapes of NO measured for the three crystals. The spectral position of the emission band, which peaks at the blue of the gas-phase value (vertical dotted line) in both argon and neon, points to a non complete relaxation of the lattice: the dopant molecule is still constrained by the cage when it fluoresces, as the surrounding crystal resists to any further compression. For hydrogen, the situation is the opposite: the emission band lies slight to the red of the gas-phase line, indicating a completely lose cage around the impurity.

According to the results of the MD simulations, the differences in the elastic properties of the host crystals should play a major role only during a second stage of the dynamics, as the initial ultrafast expansion is associated to a freely expanding isolated system, defined by the first shell of neighbors around the impurity. Molecular dynamics simulations in argon [147] have shown that also in this crystal the first shell expands adiabatically during a short time interval [3].

---

[3]Analogous calculations for neon indicate quite different scenario, characterized by the almost instantaneous displacement of several solvation shells [113]. This effect is related to the short lattice parameter (Tab. 8.2) of the solid, and to the potentials used to the described the inter-particles interactions. Additional simulations are currently in development to confirm these results.

Despite the fact that Ar and H_2 have a very similar nearest neighbor distance (Tab. 8.2), the duration of this *inertial* regime is shorter in H_2 , because of the lighter mass of the latter and of the non-negligible probability to find molecules between the lattice shells, due to the delocalized nature of the radial distribution function.

Matrix	Mass	Nearest neighbor	Bulk modulus	E_{max} [a]	Recurrence time	Effective mode[b]
	[a.m.u.]	[Å]	[Kbar]	[cm^{-1}]	[ps]	[cm^{-1}]
H_2	2.02	3.8	2.1[c]	86	12	111
Ne	20.18	3.16	11[d]	52	1.4	58
Ar	39.95	3.75	28.6[d]	64	0.8	47

Table 8.2: [a] upper limit of the longitudinal acoustic phonons; [b] from lineshape analysis; [c] Ref. 64; [d] Ref. 13.
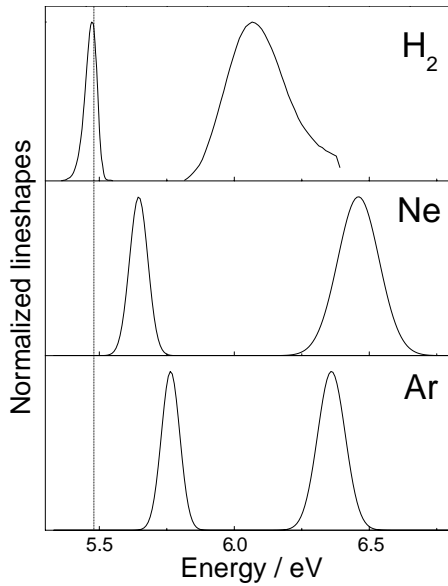
Figure 8.4: NO *A* state absorption emission Stokes-shift measured in hydrogen, neon and argon. The dotted line represents the gas-phase position of the transition. We observe that, contrary to what measured for rare gas crystals, the emission band in hydrogen is slightly at the red of the gas phase value, indicating a lose cage environment around the impurity at the end of the structural relaxation.

The frequencies of the signal recurrence (arrows in Fig. 8.3) in argon and neon correspond to 41 cm^{-1} and 24 cm^{-1} respectively. In the case of hydrogen, the peak displayed in the inset of the figure points to a value smaller than 5 cm^{-1}, which may seem hardly realistic to be associated to a local mode of the solid.

Interestingly, it has been recently observed the presence of a recurrence at long time delays in the dynamics of a 13 Å spherical bubble in bulk He-II [19]. The recursion time of the bubble and its amplitude is found to depend critically on the temperature of the sample or, more specifically, on the ratio among normal and superfluid fraction of He. The period ranges from 140 ps (1.4 K) to 200 ps (2.2 K), and its width is of the order of 30 ps.

This comparison between the dynamics in para-hydrogen and helium leads to a very intriguing subject, if one considers that it is theoretically predicted that p-H_2 should show a superfluid behavior below 6 K [158, 159]. Given that hydrogen solidifies at 13.81 K at zero external pressure [16], in order to observe any eventual

sign of superfluidity it is necessary to provide the experimental conditions for a supercooled environment. The results of the present work, which are limited to a very localized region of a few Angstroms and to a picosecond time duration, suggest that these conditions can be transiently met upon excitation of an isolated molecular impurity to an electronic state strongly interacting with the nearest crystal neighbors (see note 2, Chap. 1).

Alternative interpretations for the long time signals (5-10 ps) in hydrogen.

A different explanation for the origin of the long time signal, which is not based on the mechanical response of the lattice, is that of a *diffusion driven process*: after the impulsive expansion, H_2 molecules slowly migrate back towards the impurity center, along the density gradient left by the expansion. However, the expected mass current would be very small considering the self diffusion constant of hydrogen at this temperature [64].

Another interpretation could be related to *heterogeneity*: a small fraction of molecules, which were initially not efficiently depopulated by the probe pulse, because energetically less accessible, for example due to peculiar conformation of their crystal sites, become available for the process after a local slow rearrangement of the lattice. This scenario fits well with the observation that the slow rise in the signal is observed at all probe wavelengths, and is therefore largely independent of the configuration probed. Moreover, the instabilities in the fluorescence signals reported in § 5.2.3 can be consistent with this interpretation [160].
On the other hand, we observe that the timescale of the long-time signal was found to be independent of the pump pulse intensity (Fig. 6.8), contrary to the instabilities of the fluorescence, that were always reported to depend critically on this parameter (§ 5.2.3) [76, 91, 123].

In addition, the presence of the recurrence speaks against both these interpretations, rather pointing to an extremely weak elastic response associated to the very small fraction of excess energy, which has remained localized around the impurity center.

8.3 Conclusions

This work represents a comprehensive experimental and computational study aimed at the characterization of the structural dynamics which follows a charge redistribution on a molecular impurity in solid para- and normal-hydrogen. The dynamics of the crystal cage around the dopant center is *triggered* and *probed* by means of low-n Rydberg states of NO. This technique provides a *direct* visualization of the lattice relaxation, whereas, in general, the response of

the environment is only indirectly inferred by its effects on the intramolecular dynamics of the impurity [30, 34, 161, 162].

The experimental results show the existence of three timescales in the system dynamics. The first 150-200 fs are associated to the free expansion of the first shell of lattice neighbor surrounding the impurity. As the molecules start to interact with the rest of the crystal, the dynamics slows down, but the expansion process continues up to 800 fs. The third timescale, identified by a slow rise of the depletion signal lasting up to 10 ps, has been interpreted as a gradual re-organization of the crystal around the dopant site. We observed the presence of a weak recurrence in the signal around 12 ps, which, in analogy with similar results in rare-gas crystals, has been related to an elastic response of the medium to the perturbation.

The time-resolved dynamics in normal- and para-hydrogen presents no differences. This result enforces the assumption, underlying the bubble model, that the internal degrees of freedom of the host molecules are not participating to the dynamics.

The outcomes of the MD simulations reproduce with fairly good agreement the principal static and spectroscopic features of the experiment. In particular, they are useful to characterize the two short timescales observed in the data, and they confirm the general interpretation of the dynamics based on the intermolecular potentials from the moment analysis. The simulated time-dependent radial distribution functions indicate that the perturbation propagates at a supersonic velocity away from the impurity site, and that the first three lattice shells are transiently strongly modified during the cage expansion. Both the analysis of the experimental transients and the MD simulations suggest that the early ultrafast expansion of the impurity cage is related to the loss of almost the totality of the Stokes-shift energy. During this stage of the dynamics, the quantum nature of the host lattice plays no role.

Finally, we found a qualitative agreement between the two timescales observed in the subpicosecond dynamics, and the predictions of a viscoelastic model of solvation.

Chapter 9

Dynamical properties of triangular-shaped silver nanoparticles

Metal nanoparticles have attracted growing interest in recent years, because of their peculiar properties, arising from quantum confinement and from the interplay between bulk and surface effects. Laser spectroscopy is well-suited to investigate the physical properties of these particles, and ultrafast pump-probe spectroscopy has already been applied with success to probe the photophysics of such systems upon impulsive excitation. Transient absorption, in particular, offers the possibility to study the various mechanism of relaxation of the energy deposited by the pump laser pulse (§ 9.1). Recent works have addressed these issues in relation with the particle size (from a few to hundreds nanometers), composition (mainly noble metals), and environment (liquid solvents, glassy matrices). The influence of shape has received much less attention, mostly because of the difficulties associated with preparing non-spherical nanoparticles with uniform size and shape. Recently, various methods have been devised to produce nanoparticles of various non-spherical shapes, in large quantities and with narrow size- and shape-distribution. Measurement of the dynamics of such particles remains, at present, limited to a handful of cases: silver nano-ellipsoids [163], gold nano-rods [164], and, very recently, silver nano-prisms [165].

The contribution presented in this chapter is focussed on the photoinduced dynamics of triangular silver nano-plates in aqueous solution, from few hundreds femtoseconds to hundred picoseconds. The particles have been synthesized in our laboratory with a photochemical method that allows controlling their size and shape.

In addition to fundamental issues, characterizing the optical response of these particles is of important practical interest. The strong field enhancement localized at the tips [41] together with the possibility to tune the absorption maximum throughout the visible and near-IR spectrum [44], makes them an interesting local probe for various applications, such as scanning field optical microscopy [42], bio-labelling and bio-sensing.

The general description of the time-resolved white light absorption apparatus and detection system is given elsewhere (appendix B), and only the details specific to these measurements are given here. On the other hand, a brief description of the optical properties and of the synthesis of the particles is in order, before presenting the experimental results and their analysis.

9.1   Optical properties of metal nanoparticles

The optical properties of a diluted suspension of spherical metal nanoparticles are summarized by the effective dielectric function

$$\tilde{\epsilon}(\omega) = \epsilon_{\rm sol} + 3p\epsilon_{\rm sol}\frac{\epsilon(\omega) - \epsilon_{\rm sol}}{\epsilon(\omega) + 2\epsilon_{\rm sol}} \ , \tag{9.1}$$

which depends on the solvent dielectric constant $\epsilon_{\rm sol}$, on the dielectric function of the nanoparticles ϵ, and on the (low) particle concentration p (expressed as a fraction of the total volume). $\epsilon_{\rm sol}$ is assumed to be real and weakly dependent on frequency, while $\epsilon = \epsilon_1(\omega) + i\epsilon_2(\omega)$ is complex and, in general, strongly dependent on frequency.

The absorption coefficient of the composite particle-solvent system takes the form [1] [166] :

$$\tilde{\alpha}(\omega) = \frac{9p\epsilon_{\rm sol}^{\frac{3}{2}}}{c}\frac{\omega\epsilon_2(\omega)}{[\epsilon_1(\omega) + 2\epsilon_{\rm sol}]^2 + \epsilon_2^2(\omega)} \ . \tag{9.2}$$

The absorption is resonantly enhanced by dielectric confinement around the frequency ω_{SP}, which minimizes the denominator and defines the condition for the *surface plasmon resonance* or Mie's resonance of the system [167].

The dielectric function of an *isolated* metal particle, $\epsilon(\omega)$, can be regarded as the sum of two distinct contributions:

$$\epsilon(\omega) = \epsilon^{\rm intra}(\omega) + \epsilon^{\rm inter}(\omega) \ . \tag{9.3}$$

The first term of the sum is associated with the free electrons in the conduction band, and its real and imaginary components can be expressed within the

---

[1]Note that for small particles, of dimensions $\ll \lambda/2\pi$, the scattering contribution to the extinction coefficient, which causes spectral broadening and band red-shift, can be safely neglected [46].

Drude model by the following relations:

$$\epsilon_1^{\text{intra}} = 1 - \frac{\omega_p^2}{\omega^2 + \gamma^2} \ ; \ \epsilon_2^{\text{intra}} = \frac{\omega_p^2 \gamma}{\omega(\omega^2 + \gamma^2)} \ , \quad (9.4)$$

where γ is a damping constant describing the dephasing rate of electrons in the bulk (possibly dependent on the particle size [36]). The plasma frequency ω_p, in turn, is a function of the electron density n_e , and of the electron effective mass m_e [168]:

$$\omega_p^2 = \frac{n_e e^2}{\epsilon_0 m_e} \ . \quad (9.5)$$

The last term in Eq. 9.3, $\epsilon^{\text{inter}}(\omega)$, represents the interband contribution to the total dielectric constant. Its explicit expression as a function of the joint density of states $D(E, \omega)$ has been calculated [169], and compared with experiments [170] by Rosei and co-workers for transitions from the d-band to the Fermi surface in bulk silver. It should be noted that this term depends on the Fermi distribution function $n_f(E, T)$ through the proportionality $\epsilon^{\text{inter}}(\omega, T) \propto \int_{-\infty}^{+\infty} D(E, \omega)[1 - n_f(E, T)]$, and represents the sole temperature-dependent contribution to ϵ.

In silver, given the relatively high energy associated to the interband transition, the dielectric function of the system can be adequately described considering exclusively free-electrons contributions (see Eq. 9.4) [46]. In this approximation, the peak of the plasmon band occurs at

$$\omega_{SP} = \frac{\omega_p}{\sqrt{1 + 2\epsilon_{\text{sol}}}} \ . \quad (9.6)$$

Using definition 9.5, it follows that the maximum of the band is proportional to the square root of the free electron density, and therefore can be modulated by a change in the particles' volume.

These results are strictly valid only for particles of spherical shape. For treating non spherical-particles, numerical techniques are necessary, since only spherical and spheroidal shapes allow an analytical solution of the Laplace equation. New numerical techniques have been introduced recently. Among these, the *discrete dipole approximation* consists in modelling any object of interest by a cubic lattice of polarizable points, and then solve the electrodynamic equations for this ensemble of points. This technique was applied with success to reproduce the experimental extinction spectra of silver nano-prisms with regular and snipped tips [41]. It was found that the plasmon peak position results mostly sensitive to the particle aspect ratio: for plates of a given thickness, ω_{SP} peaks at longer wavelengths correspond to larger lateral sizes.

9.2 Photochemical synthesis

This section reports a brief description of the synthesis of the silver nano-prisms, developed in our laboratory, for the time-resolved experiment. More
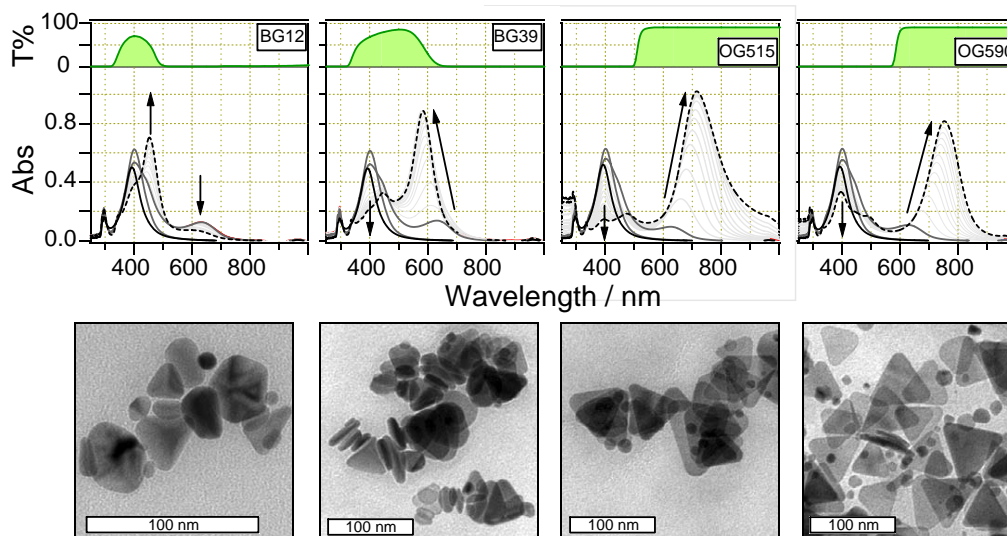
Figure 9.1: Photochemical preparation and evolution of silver nanoparticles under different illumination conditions. **Top row.** Extinction spectra taken every 30 min during the growth. **Continues black lines.** Solution before irradiation, the peak at 400 nm is associated to small spherical particles. **Dark gray lines.** First stage of growth, the samples are exposed to light from a conventional fluorescent tube. **Light gray lines.** Second stage of growth. Each sample is fitted with a specific color filter (the different transmission properties are indicated in the insets together with the commercial names from SCHOTT). **Dashed black lines.** Spectra of the solution at the end of the process. **Bottom row.** TEM pictures of the resulting silver nanoparticles corresponding to the dashed-line spectra in the top row.

details can be found in Ref. 44.

In this synthesis the nanoparticles are produced by photochemical methods. Their size and shape can be controlled by the specific wavelength used to drive the process. The preparation starts off with an aqueous solution of spherical silver nanoparticles produced by borohydrate reduction of $AgNO_3$. The solution is initially exposed to a conventional fluorescent tube (230 nm $< \lambda <$ 700 nm), and subsequently to light of selected wavelength(s). UV-visible absorption spectroscopy (Fig. 9.1) is used to monitor the growth process. After an induction time of about 1 h, a noticeable and rapid change of color of the solution from yellow to pale green

Figure 9.2: Silver nano-plates arranged in stacks on the TEM grid upon evaporation of the solvent.

occurs. At this stage, it is possible to steer the evolution of the reaction, and select its final outcome simply varying the illumination conditions. The transmission electron microscopy (TEM) images presented in the bottom row of Fig. 9.1 indicate that the exposition to different spectral windows correspond to different sizes and shapes in the resulting nanoparticles.

The extinction spectra contain important information about the size and aspect ratio of the particles in solution at the various stages of the growth process,

as mentioned in § 9.1. In particular, the peak around 400 nm corresponds to the plasmon resonance of the small spherical particles present in the original solution. The shoulder at 450 nm is interpreted as small particles or aggregates with low aspect ratio, while the species peaking at 630 nm are associated with plates of high aspect ratio that can eventually grow larger shifting the band maximum to the red. The thickness of the particle ($\sim$ 8 nm) can be inferred from the picture in Fig. 9.2, which shows the silver nano-plates arranged in stacks. All the samples analyzed show a high degree of *shape homogeneity*, this fact constitutes a great advantage for the interpretation of the time-resolved data presented in § 9.4. In particular, there is no evidence of co-existence of triangles with other shapes, contrary to what was recently reported by Okada *et al.*, who observed the presence of $\sim$12% of rods in their sample of thick silver nano-prisms [165].

9.3 Review of the literature

Measurements of the time-dependent changes in the optical absorption induced by a short laser pulse on a large ensemble of metal nanoparticles have been used to follow the underlying dynamics. Many metallic systems, in solution, or embedded in a matrix, have been investigated in recent years, including gold nano-spheres [171–173] and nano-rods [164], silver nano-spheres and nano-films [48, 50, 174], nano-ellipsoids [163] and nano-prisms [165], and also composite core-shell nano-particles [175]. The complex response of these diverse systems, share some common features that will be described here. This general background will serve us to analyze the results presented in § 9.4.

- The pump pulse drives initially the metal electrons out of equilibrium, creating a *coherent* superposition of the electronic polarization and of the electromagnetic field.

- This collective excitation decays in less than 10 fs [176, 177] into single-electron excitations, leading to a strongly non-thermal distribution with an increase of the occupation of the electron states above the Fermi energy, and a decrease below it (Fig. 9.3) [178].

- The non-thermal distribution persists for several hundreds femtoseconds until e-e scattering processes establish a hot Fermi-Dirac distribution. The timescale of the process is mainly determined by the electrons close to the Fermi level, where the rate of collisions is strongly reduced by the electrostatic screening exerted by the *d*-band electrons.

- As time progresses, the hot electrons equilibrate with the lattice temperature via e-phonon scattering. The characteristic cooling time for the electrons is strongly influenced by the specific electronic structure of the metal [48].
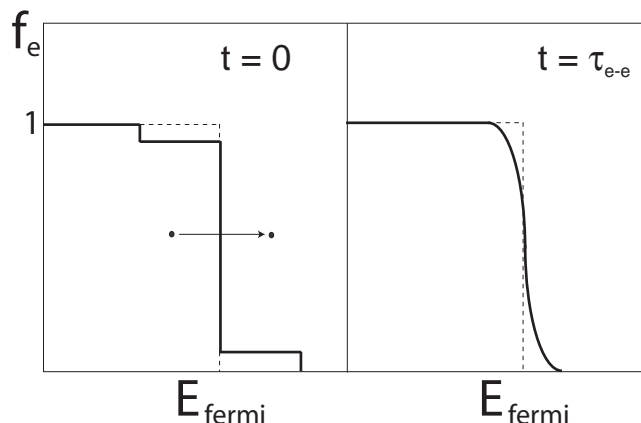
Figure 9.3: Energy dependent electron occupation number during the impulsive laser excitation ($t = 0$), and after the establishment of a hot Fermi-Dirac distribution ($t = \tau_{e-e}$) [45].

- The hot electrons thermalize with the lattice in the first few picoseconds of the dynamics. Before this energy is eventually dissipated to the solvent, the lattice suffers a significant increase in temperature, which causes it to expand. If the timescale for heating is faster than the period of the collective phonon mode that corresponds to the expansion, the mode can be impulsively excited.

- The vibration of the particle damps off.

- The particle cools down, as its thermal energy transfers to the solvent.

We will discuss each process in turn.

9.3.1   Electron - electron scattering

After the initial coherence is lost (≈ 10 fs), the electron excitation can be treated using the single-particle model of free electron absorption: one photon is absorbed by one electron with the assistance of a third particle to conserve energy and momentum [45]. This excitation mechanism leads to a strongly non-thermal distribution with an increase of the occupation of the electron states above the Fermi energy and a decrease below it, as illustrated schematically in Fig. 9.3 [178]. The non-thermal distribution persists for several hundreds femtoseconds, until e-e scattering processes establish a hot Fermi-Dirac distribution. The timescale of this process is mainly determined by the electrons close to the Fermi level, where the rate of collisions is strongly reduced by the electrostatic screening exerted by the d band electrons. Because electrons have a very small heat capacity, increases in the electronic temperature of several thousands K can be easily achieved by ultrafast laser excitation [48].

The changes in the occupation states near the Fermi level result in significant broadening of the surface plasmon band. The induced transmission change can be calculated knowing the exact amount of energy deposited by the laser on the sample, and considering the heat capacity of electrons. The change is determined principally by the imaginary part of the particle dielectric function $\epsilon_2^{\text{inter}}(\omega, T)$, and the expected signal can be calculated substituting this quantity in Eq. 9.2.

The magnitude of the bleach observed in the difference absorption spectra at short times is expected to be proportional to the electronic temperature (i.e. the laser power) [179].

9.3.2 Electron - phonon scattering

The thermalization of electrons with lattice can be monitored by measuring the recovery of the bleach around ω_{SP}, as well as the decay of the transient absorption wings of the surface plasmon band associated to the initial broadening. Low power experiments can be fitted to a single exponential decay. In all the systems studied, the decay rate of the initial bleach shows a linear dependence on the laser power, at least at low intensities. This observation can be rationalized considering a system of two coupled heat equations to describe the evolution of the temperatures of the electrons (T_e) and of the lattice (T_l) [47, 180]. According to this *two-temperature* model, the energy E_0, deposited on the electrons by a laser pulse of temporal width σ, is coupled to the phonon modes in a way that depends directly on their temperature difference:

$$C_e(T_e)\frac{\mathrm{d}T_e}{\mathrm{d}t} = -g(T_e - T_l) + \frac{E_0}{\sqrt{\pi}\sigma}e^{\frac{-t^2}{\sigma^2}} \qquad (9.7)$$

$$C_l\frac{\mathrm{d}T_l}{\mathrm{d}t} = g(T_e - T_l) \ . \qquad (9.8)$$

The electron-phonon coupling constant g is a property of the bulk crystal, and is largely independent of the nanoparticles shape and local electric field [165]. The specific heat of electrons ($C_e(T_e)$), contrary to that of the lattice C_l, is an explicit function of temperature which can be expressed as $C(T_e) = \xi T_e$. The metal-dependent constant ξ varies as a function of the density of electronic states at the Fermi level. Because of this dependence, the effective rate constant for the decay of the electronic temperature corresponds to $g/\xi T_e$, hence it is expected to decrease as the initial electronic temperature (i.e. laser fluence) increases.

9.3.3 Acoustic oscillations

The sudden thermal stress that results from electron thermalization with the lattice makes the particle oscillate about its new equilibrium position, dictated by the increased temperature.

The time-dependent deviation Δx from the equilibrium length of the particle can be described by the differential equation of a damped harmonic oscillation

$$\frac{\mathrm{d}^2}{\mathrm{d}t^2}\Delta x + 2\rho\frac{d}{\mathrm{d}t}\Delta x + \omega_x^2 \Delta x = A\sigma/m \qquad (9.9)$$

with an effective damping ρ. A, m and ω_x are the surface, mass and lowest vibrational eigenfrequency of the particle, respectively. The force driving the oscillations is represented by the stress σ.

Several authors [48, 163, 181] have pointed out that the principal contribution to the particle expansion is coming from the anharmonicity of the heated lattice. However, to reproduce correctly the phase of the oscillations observed experimentally, some authors find it necessary to take into account the stress generated by the hot electron pressure [49], in particular for small particles (radius <10 nm).

The modulation period is observed to be independent of the pump intensity [163], but it was found to be strongly related to the particles size and elastic properties [46].

The oscillations can be followed through their influence on the optical properties of the system (§ 9.6): the peak of the surface plasmon resonance is directly proportional to the plasma frequency ω_p , and hence, through relation 9.5, to the square root of the free electron density $\sqrt{n_e}$. It follows that any increase in the particle volume results in a red shift of ω_{SP} and, conversely, any shrinkage corresponds to a blue shift of the peak. It is worth noting that the aspect ratio of the particle can influence as well the position of the surface plasmon peak (see § 9.1). Extending the theory of Mie to spheroidal objects, it has been shown that the surface plasmon resonance shifts to the red as the major to minor axes ratio increases [41].

Perner *et al.* attributed to this effect, not to the modulations in the electron density, the different oscillation periods observed along the different axes of silver nano-ellipsoids [163].

9.3.4   Decay of the modulations and heat transfer to the solvent

Several mechanisms can be at the origin of the damping of the spectral modulations: coupling to other phonon modes, energy exchange with the environment, dephasing due to the spread in size of the sample, anharmonicity.

Coupling to lower vibrational frequencies can be ruled out, since the observed oscillation frequency is generally associated to the mechanical mode of *lowest frequency*. The transfer of acoustic energy to the surrounding medium was invoked as the principal mechanism of energy loss by Del Fatti *et al.* [182]. Results obtained for silver nano-spheres of different radii indicate that the time constant for damping scales linearly with the particle size, at least in the

5-20 nm radius range. This observation is consistent with an homogeneous, extrinsic damping mechanism.

In a different publication, the decay of the modulations of 25 nm Au nano-spheres was attributed to polydispersivity in the sample [48]. This explanation was justified by the better fit to the experimental data obtained when using an expression accounting for an inhomogeneous process, instead of the simple exponential decay expected for an homogeneous one [2].

The heat transfer to the solvent for gold nano-spheres in aqueous solution was reported to be a strongly non-exponential process [3] characterized by an energy dissipation rate not dependent on the initial temperature of the system, hence on the laser power [173].

In Tab. 9.1 we report the typical timescales of the processes described in this section. These values are just indicative, the actual ones depend strongly on the specific size and material of the nanoparticles, and the characteristics of the surrounding environment.

e-e scattering	e-phonon scattering	Oscillations period	Heat transfer
<0.5 ps	0.5 - 3 ps	1 - 100 ps	10 - 400 ps

Table 9.1: Indicative timescales of the fundamental photophysical processes discussed in § 9.3.

In the following, we will present the experimental results of our original study on the dynamical properties of triangular-shaped silver nano-triangles. The results and the analysis are mostly focussed on the oscillatory dynamics observed on a 100 ps timescale.

9.4 Experimental results

The different timescales associated to the processes described in § 9.3 are analyzed separately in this section, to simplify the description and enforce the parallel with the theoretical background.

Figure 9.4 shows a typical extinction spectrum of the samples measured in the experiment. A comparison with the spectra and TEM images shown in Fig. 9.1 indicates that the sample corresponds to triangular nano-plates of typical 70±15 nm length, and ∼8 nm thickness.

All the multi-wavelength time-resolved scans reported in the following cor-

---

[2]For relatively low size dispersion the signal should decay as e^{-t^2/τ^2}, where τ is proportional to the inverse of the width of the gaussian size distribution [48].

[3]The decay is fitted to a stretched exponential $e^{-(t/\tau)^\beta}$, where the parameter β depends on the particles size [173].

respond to measurements taken using a flow cell of 3 mm thickness. During the experiment, differently from what reported in other recent publications [164, 173], the sample solution was constantly flown through the cell, even for measurements at *low pump power*, to minimize the possibility of any permanent photo-degradation of the sample.
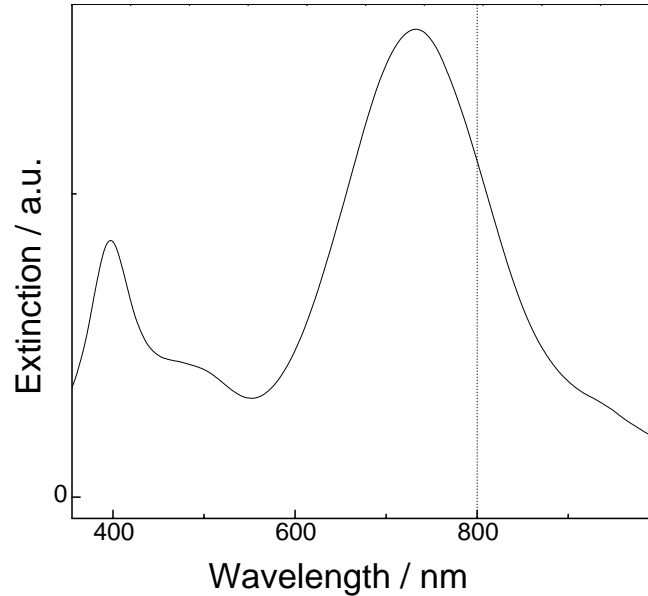
Figure 9.4: Typical extinction spectrum of a solution of silver nanoparticles. The peak at 750 nm corresponds to the surface plasmon resonance of silver nano triangles similar to those shown in the rightmost picture of Fig. 9.1. The peak around 400 nm indicates the presence of a residual fraction of spherical particles present in the original solution.

9.4.1   Electron-electron scattering

Figure 9.5 shows a series of difference spectra measured at short pump-probe time delays. The spectra have been previously corrected for the chirp associated to the white-light pulse, as described in appendix B.

At time-zero we observe a broad bleach feature peaking around 800 nm extending towards the region occupied by the static spectrum of Fig. 9.4. For wavelengths above 840 nm, the character of the difference spectrum changes, as we observe the instantaneous appearance of an additional absorption signal (negative values), typically 5 times less intense than the bleach maximum. During the first 200 fs of dynamics, the bleach increases and the zero crossing between bleach and absorption shifts very fast to the red, consistent with an "instantaneous" broadening of the absorption band, as the pump energy is deposited on the sample.

The dynamics of the difference signals at three selected wavelengths (760, 800 and 840 nm) is shown in Fig. 9.6. Unfortunately, the transient signals before
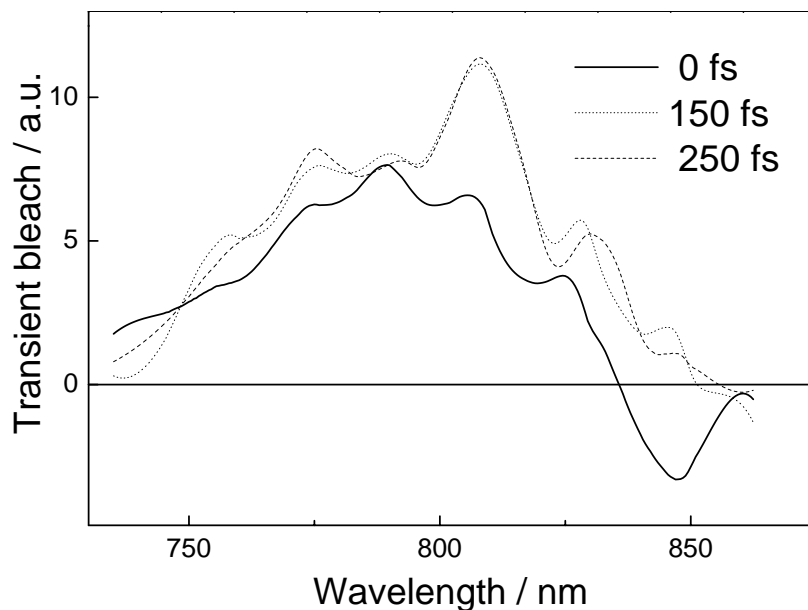
Figure 9.5: Difference spectra measured at pump-probe delays of 0, 150 and 250 fs. The wiggles in the spectra are an artefact due to the difficulty to correct the signal in the spectral region close to 800 nm, which is the wavelength used both to pump the sample and to generate the probe continuum.
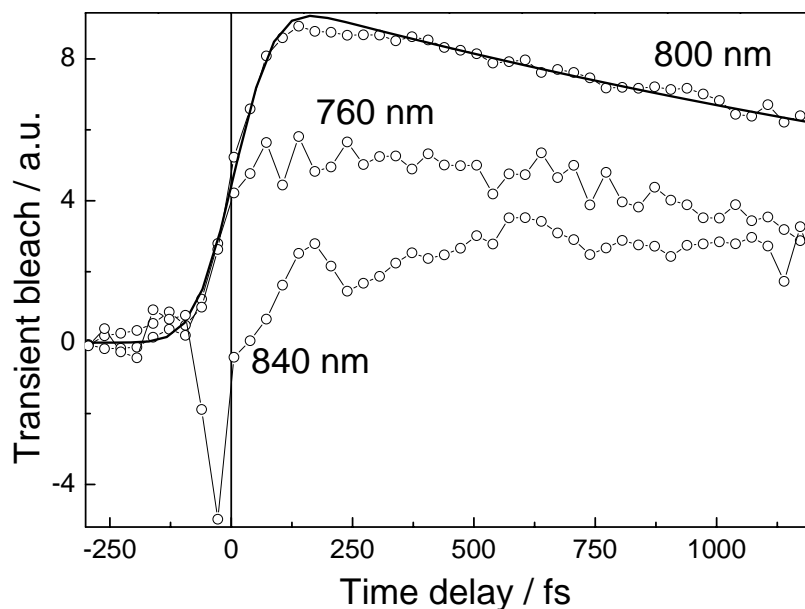
Figure 9.6: **Empty circles.** Subpicosecond dynamics monitored at three different wavelengths (760, 800 and 840 nm). **Thick line.** Fit to the transient at 800 nm with Eq. C.6. The instrumental response corresponds to 150 fs, the exponential decay constant to 2.5 ps.

200 fs are strongly affected by cross-phase modulation [4] limiting the possibility to extract accurate temporal information, in particular in the region of $\lambda >$ 820 nm.

We have fitted the transient at 800 nm, which is manifestly not affected by this problem, with the convolution between a decaying exponential and a gaussian of FWHM equal to the instrumental response of the system (see model function C.6 in appendix C.3). The fit (Fig. 9.6), gives an instrumental response of 150 fs, close to the typical temporal resolution of our set-up in this energy region (120-130 fs), indicating that the rise time of the signal is very likely limited by the resolution. It is worth noting that in Fig. 9.5 the signal above 850 nm remains negative even after the first 200 fs, hence this feature can not be associated to a cross-phase artifact, which would die off in less than 150 fs, and must correspond to an actual additional absorption related to the broadening and red shift of the static band of Fig. 9.4.

The rise time of the bleach contains information about the electron thermalization process illustrated in Fig. 9.3. Measurements at higher temporal resolution have shown that the timescale of the thermalization dynamics of the photoexcited electrons depends on the particle size. A timescale of $\sim$250 fs [45] has been reported for silver nano-spheres of 24 nm diameter, and correspondingly lower for smaller particles. For comparison, the bulk value, measured in silver thin films, is of the order of 350 fs [184].

We note, however, that these values were measured monitoring the absorption changes in the vicinity of the interband transition, where the e-e collisions are strongly reduced by the Coulomb screening of the d-band electrons. On the contrary, the dynamics observed at the surface plasmon resonance, where this screening effect does not play a role, is expected to exhibit an immediate rise as it should directly follow the energy injection in the electron gas [185].

9.4.2   Electron-phonon scattering

Figure 9.7 shows the decays of the initial bleach obtained at different pumping power, along with the fits to the curves obtained through Eq. C.6. The recovery of the bleach is related to the cooling of hot electrons via energy exchange with the crystal ions, as discussed in § 9.3.2.

The observed decay times of the bleach signals and their peak amplitudes scale linearly with the laser power, at least at low intensities, in agreement with Eq. 9.7, and the expression for the heat capacity of the electron gas. Extrapolating the fitted decay constants to zero laser power (inset of Fig. 9.7) we obtain a decay time $\tau_{e-ph} \simeq$ 1.1 ps. This value compares well with those reported in literature ranging from 0.5 to 2 ps for silver nano-particles of several

---

[4]Cross-phase modulation is observed when the refractive index of the sample becomes dependent on the pump intensity. At a given pump-probe delay, different spectral components of the probe pulse are subject to different pump intensities because of the chirp. This introduces a time-dependent modulation of the white light spectrum, since the component overlapping with the pump beam at the maximum intensity is depleted, while the neighboring colors are enhanced [183].
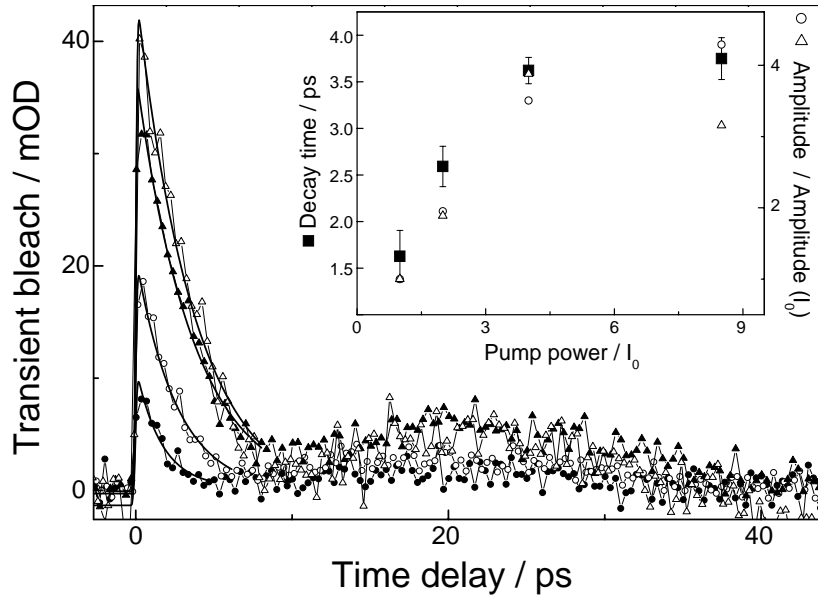
Figure 9.7: Bleach recovery measured at different pump-power settings (I_0, $2I_0$, $4I_0$, $8I_0$). **Continuous lines.** Fits obtained using Eq. C.6 (convolution of the instrumental response with an exponential decay function). **Inset.** Decay times from the fit (**squares**), amplitudes of the peak (**triangles**) and of the bump around 20 ps (**circles**) normalized to their respective values at I_0 pump power. The extrapolation at zero power yields a timescale for the bleach decay of ~ 1.1 ps.
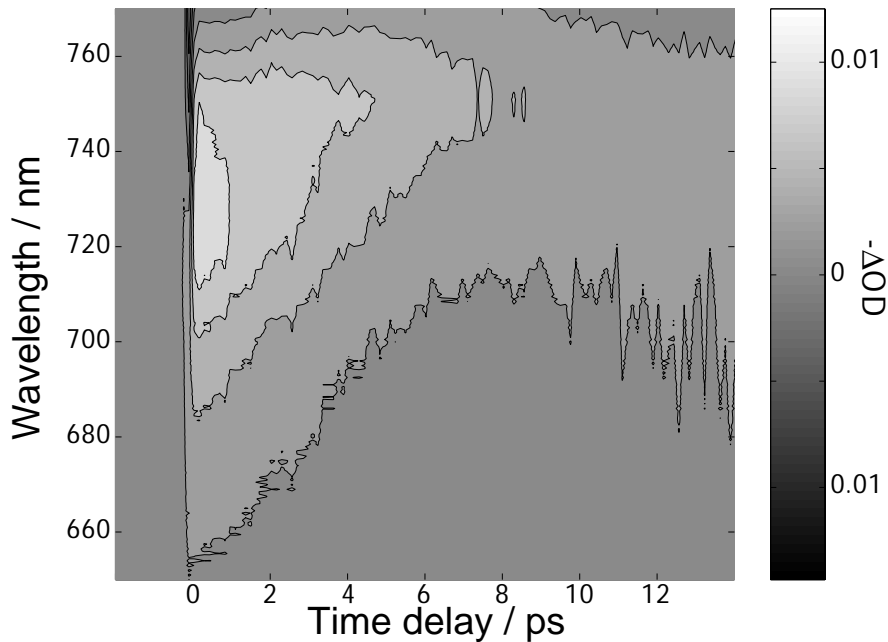
Figure 9.8: Contour plot of the bleach dynamics. One can observe the presence of three contributions to the spectral evolution of the system: a decay of the instantaneous bleach, a red-shift during the first 6 ps and a parallel narrowing of the bleach band. Note that the maximum of the bleach is around 730 nm, because of the different sample and different experimental conditions of this measurement (i.e. the sample solution was not circulating in the flow cell). The dynamics shows features very similar to those observed for samples with the bleach peaking around 800 nm. The dataset has been chosen for clarity, because in this spectral region the white light continuum does not present structures (for comparison see Fig. 9.5).
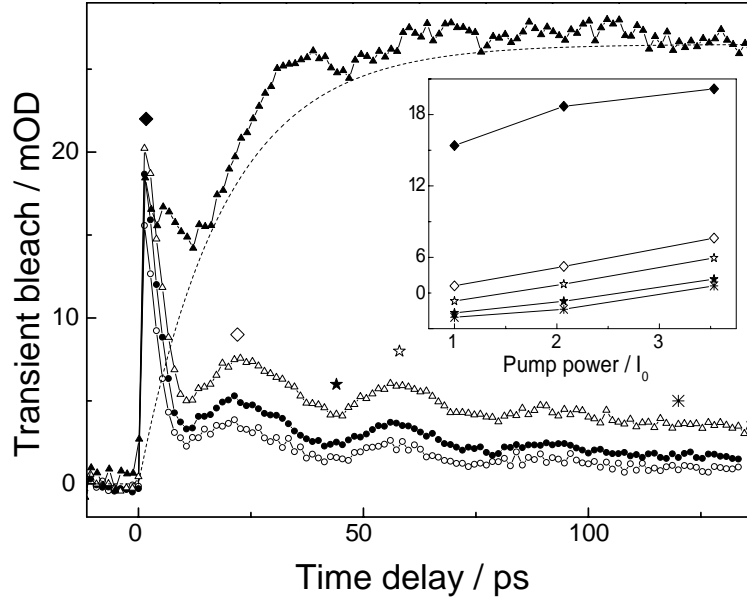
Figure 9.9: Pump power dependence on the acoustic oscillations at I_0, $2\ I_0$, $3.5\ I_0$ and $10\ I_0$ (the latter is associated to a permanent change in the static spectrum of the sample). **Inset.** Amplitudes as a function of pump power of the various features indicated by the symbols in the main plot.

shapes, and in different environments [165, 174, 179, 181]. At the highest pump power ($8\ I_0$) the peak amplitude clearly deviates from the linear regime and the bleach decay is poorly captured by the fitting function (the χ^2 value of the fit results one order of magnitude worse than the others). A deviation from simple exponential decay behavior at high pump power has been observed by several authors [186, 187], and it has been linked to the competition between a transient absorption signal and a transient bleach, respectively corresponding to the broadening of the plasmon band, and to the interband transition which occurs at energy below the Fermi level [180].

The contour plot in Fig. 9.8 shows that, in our case, the evolution of the bleach region during the first 5-7 ps is a combination of three effects: a decay and a red-shift accompanied by a parallel narrowing on the blue side. The first feature corresponds to the thermalization of the electrons with the crystal ions, as already explained. The narrowing and shifting can be interpreted as a faster re-occupation of the lower electronic states below the Fermi level emptied by the pump pulse, hence a faster recovery of the absorption on the blue side (see also Fig. 9.3).

9.4.3   Acoustic oscillations

The subsequent dynamics (10-100 ps) is spectroscopically dominated by the periodic amplitude oscillations of the transient absorption traces shown in Fig. 9.9, that reflect the particle oscillations. We exclude from the analysis the transient corresponding to the maximum pump power (filled triangles), where
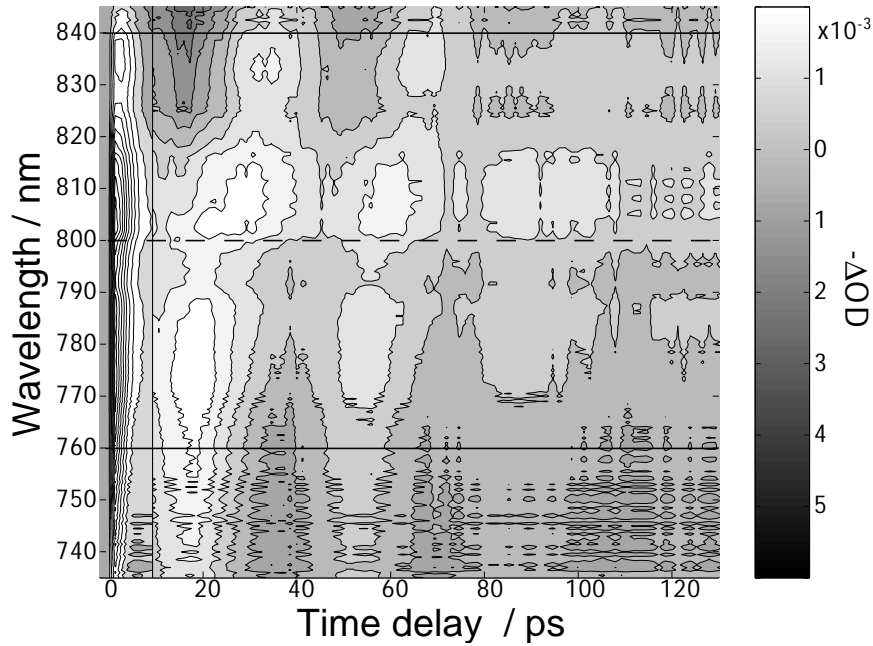
Figure 9.10: Contour plot showing the initial bleach and the acoustic oscillations. Note that the color white corresponds to the highest value of the bleach. **Continuous lines.** Cuts corresponding to the traces plotted in Fig. 9.12.

extensive permanent photodegradation occurs. A comparison of the remaining traces shows that the positions of the amplitude peaks do not change as a function of the laser intensity. The maxima of the first and second oscillations increase linearly with the pump power together with the offset present at very long delays, hence the contrast of the oscillations does not change appreciably. The residual bleach is associated with the increased temperature of the lattice and indicates that the energy deposited by the laser is not completely transferred to the environment on this timescale.
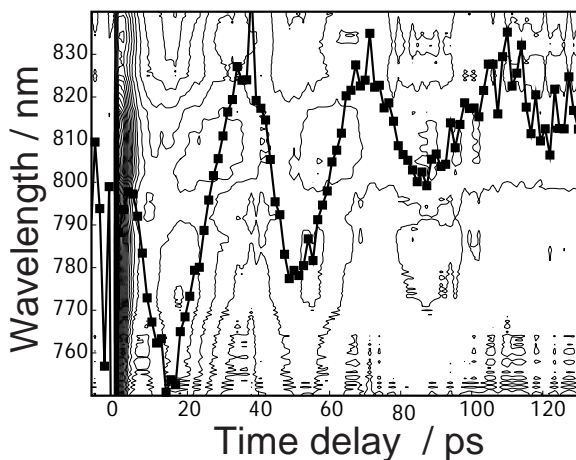
Figure 9.11: First moment of the differential spectrum presented in Fig. 9.10

The amplitude oscillations observed in the single-wavelength traces arise from a periodic shift of the whole surface plasmon resonance around its equilibrium position. The contour plot in Fig. 9.10 illustrates clearly the time and spectral evolution of the process. During the electron thermalization period ($t < 5$ ps) the difference spectrum is dominated by the presence of a major bleach (the additional absorption caused by the instantaneous band broadening lies above 850 nm and is not shown in the plot). For longer delays, the data
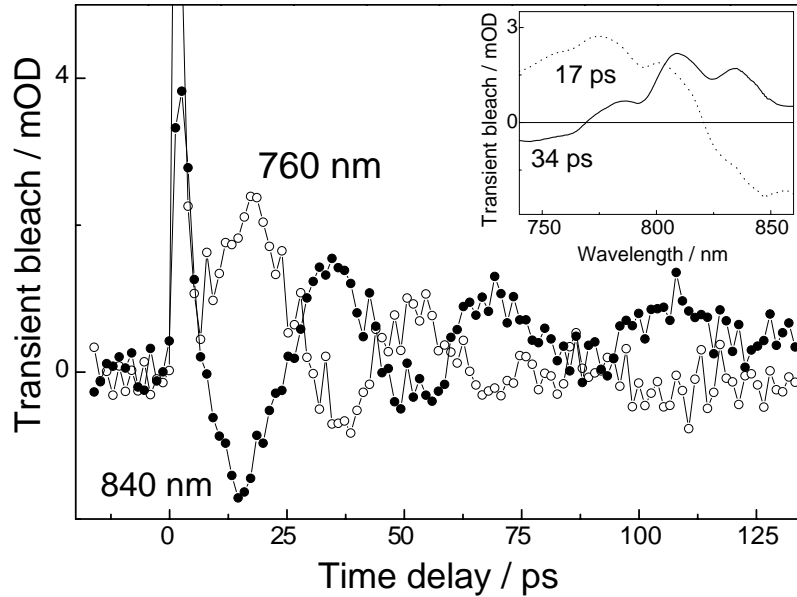
Figure 9.12: Kinetic traces at 760 nm (**empty circles**) and at 840 nm (**filled circles**), symmetric with respect to the equilibrium position of the band. Note that the initial feature is a bleach for both traces, while, after the lattice heating ($t > 5$ ps), the curves are almost perfectly out of phase. **Inset.** Difference spectra corresponding to a delay of 17 ps (**dotted line**) and 34 ps (**continuous line**)

set is characterized by four major oscillations of the bleach band. To illustrate more clearly the spectral behavior of the modulations, in Fig. 9.11 we superimposed to the contour-lines of the data set the first moment of the difference spectra. This quantity reflects the instantaneous center of gravity of the transient bleach, and clearly shows the damping of the oscillations towards an equilibrium position located around 810 nm at long time delays.

Figure 9.12 displays the comparison among the evolution of the transient bleach observed at 760 and 840 nm, along with the difference spectra (in the inset) corresponding to the delays at which the first maximum and minimum in the oscillations occur (17 and 35 ps). The two time-traces are almost perfectly out of phase, indicating that they lie at the opposite sides of the new equilibrium position of the band.

9.5   Data analysis

9.5.1   Preliminary study by SVD decomposition

Our analysis of the dynamics contained in the complex multi-way data set shown in Fig. 9.10, begins with the SVD procedure described in appendix C.1. Our goal is associating specific spectral features to the three kinetic regimes observed in the data set, namely, the immediate bleach and broadening of the

plasmon band, the acoustic oscillations, and the bleach offset persisting at long time delays.

Decomposition and basis rotation. The SVD decomposition returns three principal singular values S_{ii} ($i = 1, 2, 3$) with weights well separated from all the others (see Fig. C.1), hence just three pairs composed by a spectral ($U_i(\lambda)$) and a kinetic ($V_i^T(t)$) basis element are retained for the subsequent analysis. A completely structureless matrix of residuals is obtained subtracting the signal reconstructed using this reduced basis set from the original data set. This is an additional indication that *no fundamental information is neglected* in the procedure. Up to this point, the $U_i(\lambda)$ and $V_i(t)^T$ vectors retained need not to have a specific physical meaning [188]. The next step of the analysis consists in determining the spectrum associated to the acoustic oscillations observed in the original kinetic traces. We follow the procedure described by Ernsting *et al.* [189], which permits to isolate into different kinetic/spectral pairs each periodic component appearing in the data, by optimizing *iteratively* a general rotation matrix R. Briefly, the decomposition of the dataset $A(\lambda, t)$ is re-cast as

$$A(\lambda, t) = U(\lambda)SV(t)^T = U(\lambda)SR^{-1}RV(t)^T \ , \tag{9.10}$$

where the matrix product $R^{-1}R$ corresponds to the identity matrix. The different frequencies eventually present in the data set are identified observing the amplitude Fourier transform of each kinetic trace $V_i(t)^T$. The $V_{\bar{i}}^T$ component associated to the highest spectral density at a given frequency is chosen as a target. Successive rotation operations R_j among $V_{\bar{i}}^T$ and the remaining vectors of the reduced basis, $V_{i \neq \bar{i}}^T$, are performed in order to maximize the Fourier peak in $V_{\bar{i}}^T$. The final kinetic traces are written in compact matrix form as

$$\tilde{V}(t)^T = RV(t)^T \ , \tag{9.11}$$

where $R = R_j...R_2R_1$ represents the resulting generalized rotation. The corresponding spectral amplitudes are given by $\tilde{U}(\lambda) = U(\lambda)SR^{-1}$.

Results of the procedure. For the data set presented in Fig. 9.10, only a single peak shows up in the Fourier amplitudes at 28.5 GHz, corresponding to an oscillation period of ~ 35 ps. The results of the procedure just described are shown in Fig. 9.13, where the transformed $\tilde{V}_i(t)^T$ traces are shown in the top panels together with the corresponding spectral densities in the insets. We observe that:

1. The clear oscillatory pattern shown by the time trace in the top central panel has been obtained maximizing the corresponding peak in the Fourier transform [5]. The associated spectral amplitude (lower panel) is

---

[5]The second peak appearing at slightly lower frequency is just an artifact due to the finite numerical Fourier transform procedure and consequently has no physical meaning.
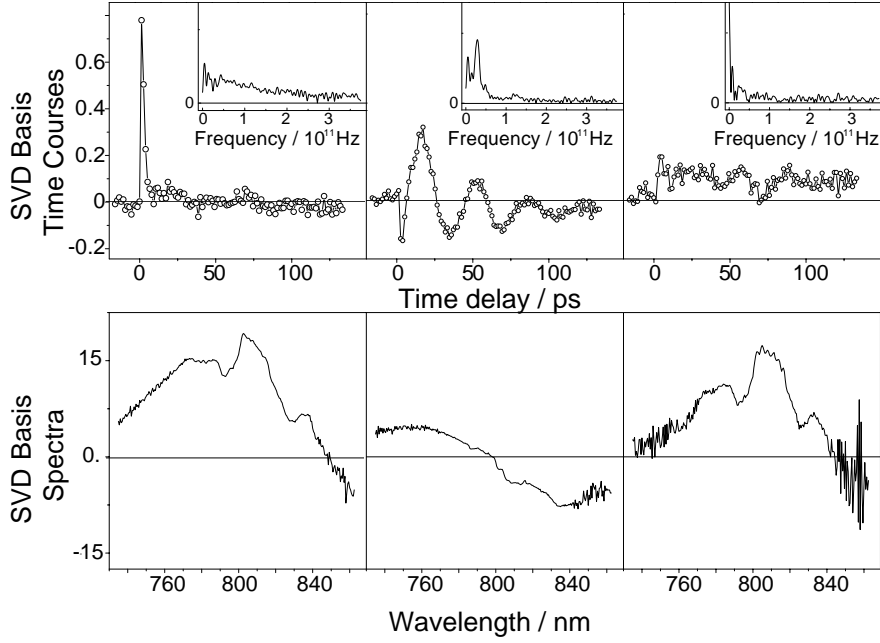
Figure 9.13: Results of the SVD analysis of the acoustic oscillations. **Top row.** Kinetic components with corresponding amplitude Fourier spectra (**insets**). **Bottom row.** Associated spectra. The curves are obtained maximizing the Fourier peak of the component in the second column (~ 35 ps) by successive rotations among the kinetic+spectral pairs. See text for further details.

crossing zero around 797 nm, and has the shape of a positive band derivative. Spectral and kinetic features together indicate that the acoustic oscillations of the system are associated to one single frequency, and take place around an equilibrium position centered around 800 nm, clearly red-shifted from the steady-state peak of the plasmon resonance plotted in Fig. 9.4. Such a shift reflects the change in temperature of the system after the thermalization of the electrons: a similar shift is reported, for example, in Ref. 48.

2. The component in the first column is associated to the electron-phonon coupling dynamics. The instantaneous broadening of the band, discussed in § 9.3.2, can explain the extended bleach and the additional absorption observed above 850 nm (negative values) in the associated difference spectrum. The modulations in the spectrum are an artifact due to the structures appearing in the white light continuum around 800 nm.

3. The third component is characterized by a spectrum less intense on the blue side with respect to the one discussed at point 2. The step-like kinetic trace can be easily related to the permanent offset observed in the data, the negative values above 850 nm indicate that the broadening/shift of the plasmon band is still significant after 120 ps.
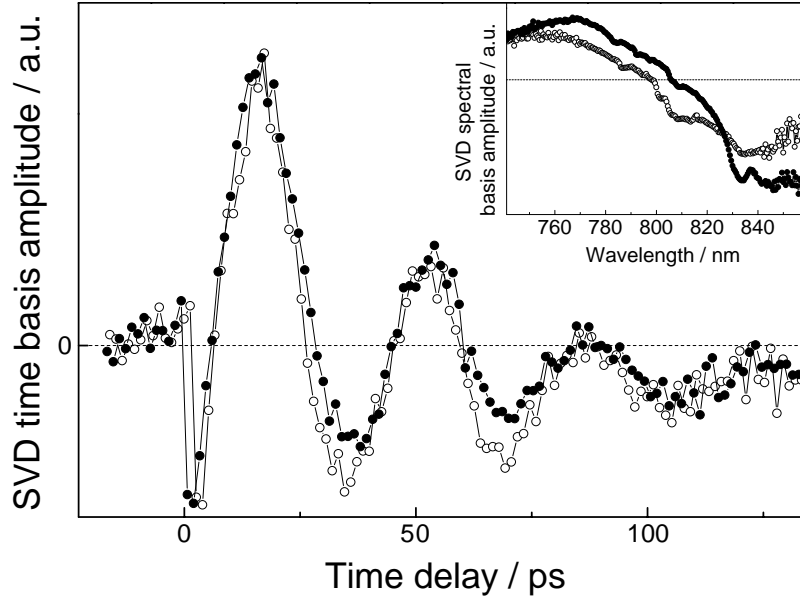
Figure 9.14: Comparison of the oscillatory kinetic component shown in Fig. 9.13 (**open circles**) with an analogous result obtained from a completely independent dataset (**filled circles**). **Inset.** Corresponding spectral components.

A comparison between kinetic and spectral components extracted from different data sets (Fig. 9.14) gives a visual estimate of the quality of the results and the robustness of the analysis. The good agreement, implies that the procedure of spectral maximization is generally applicable and, in particular, that the character of the oscillatory pattern that we extract is reproducible.

Fit with model functions. We have attempted to fit the decay of the oscillating component in Fig. 9.14 through several different analytical functions suggested in literature and summarized in Tab. 9.2.

$$
A\cos\!\left(2\pi\!\left(\tfrac{t}{\tau_{\mathrm{osc}}} + \phi\right)\right) \cdot
\begin{cases}
\exp(-\tfrac{t}{\tau}) & \\
\exp[(-\tfrac{t}{\tau})^2] & {}^{(a)}\\
\exp[(-\tfrac{t}{\tau})^\beta] & {}^{(b)}
\end{cases}
$$

$$
\sum_i A_i \cos\!\left(2\pi\!\left(\tfrac{t}{\tau_i} + \phi\right)\right)
$$

Table 9.2: Model functions used to fit the decay of the oscillations. [a] Ref. 48; [b] Ref. 173.

The best agreement was obtained with the simply exponentially damped cosine function, the result is shown in Fig. 9.15. The phase of the cosine function obtained from this analysis, close to zero, is in good agreement with the assumption that the modulations are triggered by the heating of the lattice, and do not follow directly the energy injection by the pump pulse (§ 9.3.3) [49]. Immediately after the fast thermalization of the hot electrons, the increased particle temperature leads to a new equilibrium position for the particle volume. Hence, the particle finds itself in a strongly compressed configuration,
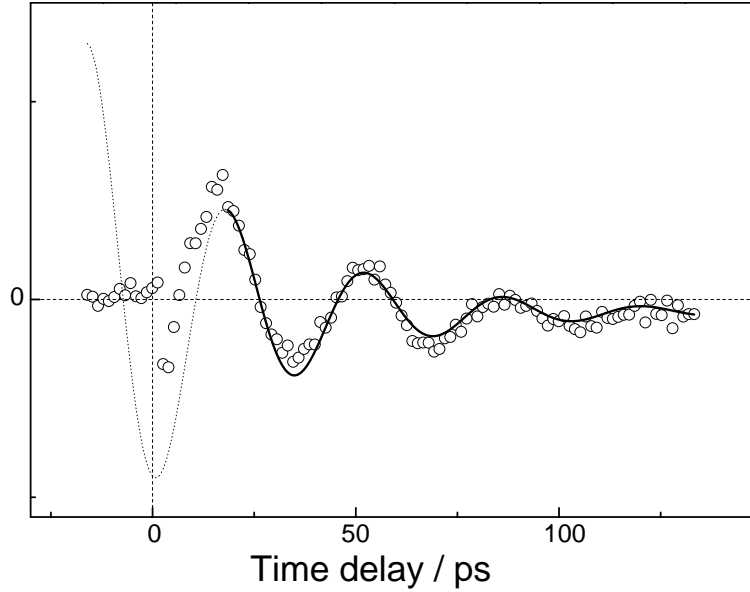
Figure 9.15: Fit to the oscillatory component of Fig. 9.13 using an exponentially damped cosine function. Note that the first minimum of the fitting function takes place around 1.2 ps, which corresponds to the thermalization time of the lattice. The time constant of the damping corresponds to 33 ps.

corresponding to a minimum of the oscillations. We observe that the first minimum of the analytical fitting function occurs at ~ 1.2 ps: this delay corresponds to the typical thermalization time for silver nanoparticles in this size range (§ 9.3.2).

This result points to an indirect excitation mechanism, excluding a direct coupling of the lattice modes with the non thermally equilibrated electrons, consistent with the relatively large lateral dimensions of the particles (70 nm) [49]. On the other hand, it is worth pointing out that this observation, though very likely, was not totally *a priori* obvious, in that the typical thickness of the plates (8 nm) lies in the region where the hot electron pressure *may have* an effect on the phase of the oscillatory dynamics [49]. This result is partially in contrast with the work of Perner *et al.* (silver nano-ellipsoids $\sim$60 nm) where the authors attributed the non-zero phase of the mechanical oscillations to the contribution arising from the high pressure of the hot conduction electrons [163].

9.5.2   Global fitting

The SVD decomposition is a very powerful technique of data analysis, because it gives an immediate feeling of the essential information stored in a multi-way data set. Nevertheless, its rigorous application is limited to specific situations, for example it works best when analyzing the spectral evolution of bands which change amplitude but not their position or width during the dynamics.

A priori, the dynamical evolution shown in Fig. 9.10 could be captured using this approach exclusively if the phase of the oscillations stays constant [6] over all the wavelength range investigated.

The relatively poor quality at short delays of the fit in Fig. 9.15 may be an indication that this is not exactly the case in the present context. Therefore, we decided to perform a more traditional analysis, fitting a series of time-traces obtained averaging slices of 10 nm width covering the whole dataset, as shown in Fig. 9.16. The fitting function chosen to describe the dynamical evolution of the system contains the sum of three distinct contributions:

$$F(t) = \Theta(t) \left\{ A_1 \exp(-\frac{t}{\tau_1}) + A_2 \cos(2\pi(\frac{t}{\tau_{\text{osc}}} + \phi)) \exp(-\frac{t}{\tau_2}) + A_3 \exp(-\frac{t}{\tau_3}) \right\} ,$$
(9.12)

where the symbol $\Theta(t)$ represents the Heavyside function:

$$\Theta(t) = \begin{cases} 0 & t < 0 \\ 1 & t \geq 0 . \end{cases}$$
(9.13)

1. The first term in the sum corresponds to the dynamics associated to the bleach recovery, i.e. the electron-phonon coupling described in § 9.4.1 and § 9.3.2. Hence, we expect the time constant τ_1 to be of the order of 2-3 ps.

2. The second term describes the acoustic oscillations of the system, reflected by the periodic shift of the position of the surface plasmon resonance (§ 9.3.3 and § 9.4.2). In analogy with the fit of Fig. 9.15, the parameter τ_{osc} corresponds to the period of the oscillations, ϕ to their phase, and τ_2 is the timescale for their damping.

3. The last term in Eq. 9.12, corresponding to a slowly decaying exponential, is supposed to reproduce the effects on the differential spectrum of the residual thermal energy present in the system at long time-delays, and its dissipation to the solvent, as discussed in § 9.3.4.

We observe that these three contributions to the model function are analogous to the kinetic traces obtained after the rotation of the SVD components presented in Fig. 9.13.
The results of the different fits, plotted in Fig. 9.16, are fairly good and we can conclude that the essential aspects of the dynamics are captured by the model function. The period of oscillation τ_{osc} , in Fig. 9.17, is essentially constant around the value of 35 ps, while the phase gradually changes from π to

---

[6]A change of phase of any multiple of $\pm\pi$ is also acceptable, as it corresponds to a change of sign of the amplitude.
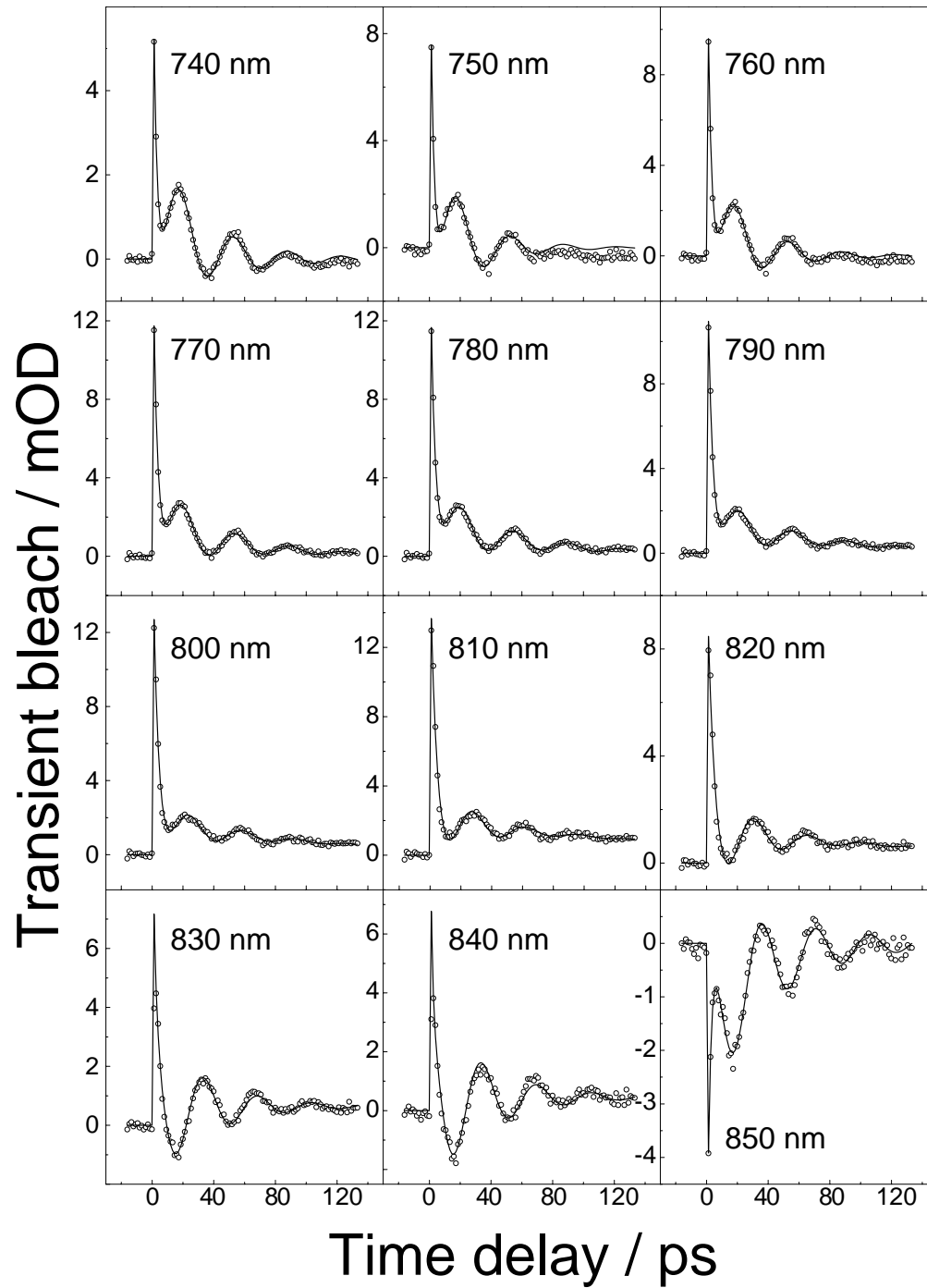
Figure 9.16: Results of the fits obtained with Eq. 9.12 on a series of time-traces calculated averaging slices of 10 nm width.
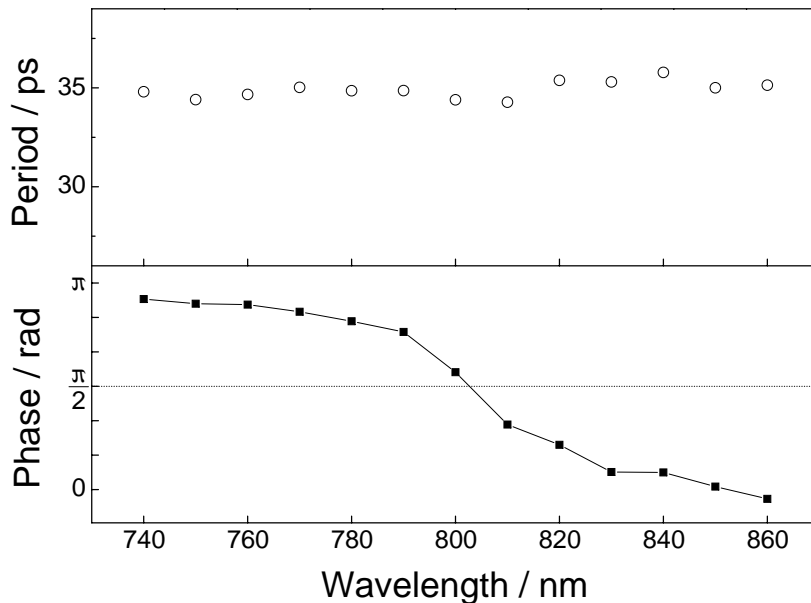
Figure 9.17: **Upper panel.** Periods the oscillations retrieved by fitting time traces at different wavelengths with Eq. 9.12 **Lower panel.** Values of the phase of the oscillations resulting from the same procedure.

0 crossing $\frac{\pi}{2}$ at about 800 nm.

Considering that the period stays the same over the data set, we proceed to refine the fitting approach applying a global procedure (see also § C.2). Basically, we fit simultaneously the entire data set, requiring τ_{osc}, τ_2 and τ_3 to be *global parameters*, independent of the wavelength. The remaining parameters (A_1, A_2, A_3 and τ_1) are left free to vary independently for different temporal traces. The fitting, in this case is done directly on a subset of the raw data (20 traces), with no averaging. The overall agreement of the result is as good as that obtained fitting independently the traces at single wavelength (Fig. 9.16). The values retrieved for the global parameters are reported in Tab. 9.3.

Oscillations period τ_{osc}	Oscillations decay τ_2	Offset decay τ_3
35.4 ps	40	124 ps

Table 9.3: Values of the global parameters after the simultaneous fitting of the time slices of the data set of Fig. 9.10.

The period of the mechanical oscillations is perfectly in agreement with the previous analysis. The timescale (τ_3) of the decay of the step-function, which we associate to the transfer of energy to the solvent surrounding the particle, compares well with those reported for similar measurements on nanoparticles suspended in aqueous solutions [173]. The decay of the mechanical oscillations, τ_2, will be discussed in § 9.5.3 along with the effects of sample inhomogeneity
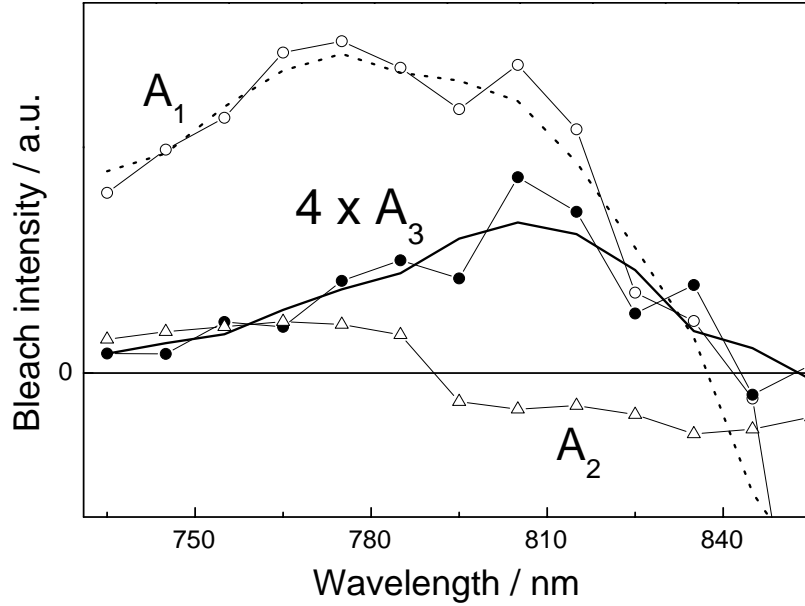
Figure 9.18: Spectral amplitudes associated to the three components in the model function Eq. 9.12. **Empty circles.** $A_1(\lambda)$, amplitude of the initial bleach at different wavelengths. **Empty triangles.** $A_2(\lambda)$, amplitude of the acoustic oscillations. **Filled Circles.** $A_3(\lambda)$, amplitude of the slow decaying step function, note that this line is multiplied by a factor 4 to ease the comparison.

on the dynamics of the system.

The amplitude of the initial bleach, $A_1(\lambda)$, of the oscillations, $A_2(\lambda)$, and that of the long time offset $A_3(\lambda)$ are displayed in Fig. 9.18. These bands are equivalent to the spectra shown in the lower panels of Fig. 9.13. They represent the spectral features associated to each contribution of the model function 9.12. We note that the band associated to A_1 resembles to the experimental difference spectrum at short times (Fig. 9.5), as we would have expected, since this spectrum describes the instantaneous broadening and red-shift of the static band.

Conversely, the intensity of the spectrum characterizing the very late delays, associated to A_3 (9.12), indicates that the initial broadening is almost completely recovered at this stage. Only a weak residual bleach, localized around 810 nm, persists, which is explained by the shift of the surface plasmon resonance caused by the increased lattice temperature of the particles. The interpretation of the spectrum associated with the oscillations follows the one given in § 9.5.1. We observe that, in the present case, the absolute amplitude of the feature is practically constant through all the spectral region; the center of the oscillations, indicated by the sudden change in sign, occurs just before 800 nm.

In hindsight, we may remark that the SVD decomposition was not perfectly appropriate to analyze a data set characterized by an oscillating function, whose phase is gradually changing as a function of the wavelength in a certain spectral region (780-820 nm), in fact each different phase theoretically should be associated to an independent kinetic trace. The plot in Fig. 9.15, even if it shows essentially the correct periodicity of the oscillations, also contains other

contributions, associated to the traces with phases significantly different from $\pm\pi$, which prevent from a satisfactory fitting with the model function.

9.5.3 Inhomogeneous effects

In this section we discuss the results of a model that we developed to simulate the pump-probe signal of the system. In particular, we are interested in understanding the physical origin of the gradual change in phase of the oscillations observed around 800 nm, as reported in Fig. 9.17.

For a perfectly mono-dispersed sample, characterized by nanoparticles of the same size, we expect to observe exclusively two values differing by $\pm\pi$ in the phases of the modulations of the transient absorption intensity, caused by the periodic shifts of the surface plasmon resonance. In other words, the time-resolved traces measured at wavelengths on the red side of the surface plasmon resonance are expected to be out-of-phase with respect to those measured on the blue side (Fig. 9.12). This remark is consistent with the findings in the time-resolved measurements on metallic nano-spheres [48].

The peak position of the surface-plasmon resonance in spherical particles is expected to be largely independent of the radius size, if the dimensions are sufficiently small to neglect the retardation effects on the optical properties of the system (see Eq. 9.2 and note 1) [36]. On the other hand, it has been theoretically and experimentally confirmed that, for non-spherical objects, the position of the plasmon resonance is strongly influenced by the aspect ratio of the particles. In particular, in spheroidal particles the plasmon resonance spectrally shifts to the red as the major to minor axes ratio increases [41]. We may expect, therefore, that the width of the band in Fig. 9.4 bears some inhomogeneous contributions due to the lateral size dispersion of the sample, which corresponds $\sim$10% (Fig. 9.1). It is worth pointing out that the side length dispersion of the plates *is not* accompanied by an equivalent distribution of the particle thickness (Fig. 9.2), hence the aspect ratio of the particles, which is the principal factor determining the position of the band, is supposed to present the same distribution observed in the lateral dimensions.

We have developed a basic model to verify the influence of this effect in the spectral evolution of the system, taking the following assumptions:

1. The spectral position of the surface plasmon resonance varies *linearly* with the size of the particle, within the range of sizes we deal with.

2. The relation between the position of the surface plasmon resonance and the dimension of the particle at point 1 is *absolute*: it holds for particles changing dimensions during the mechanical vibrations, and also for the spectral position of the steady-state surface plasmon band of particles of different dimensions in the sample.

3. The frequency of the mechanical oscillations depends *linearly* on the original dimensions of each particle.

4. The mechanical evolution of the particle size is described by the sum of an exponentially damped cosine function, and an exponentially slowly decaying offset (last two terms in Eq. 9.12).

5. The surface plasmon band is instantaneously red-shifted and broadened after the optical excitation. On a timescale of a few picoseconds the band recovers partially its original position.

6. The surface plasmon band narrows down and undergos a parallel blue-shift on a timescale of hundred picoseconds, because of the gradual energy dissipation to the solvent.

7. The laser pump pulse excites an inhomogeneous distribution of particles with slightly different lateral dimensions but equal thickness. The size distribution characterizing the sample is supposed to be gaussian.

The results of the simulations obtained applying this model are illustrated in Fig. 9.19 as contour lines superimposed to the original dataset of Fig. 9.10. The complete list of parameters used in the calculation is reported in Tab. 9.4. The input parameters describing the different timescales of the process are those obtained by the global fitting procedure described in § 9.5.2.

Bleach decay	Oscill. decay	Therm. decay	Homog. band FWHM	Band broadening	Size change	Inhomog. size distr.
3 ps	40 ps	120 ps	45 nm	8%	1%	8%

Table 9.4: Parameters used for the pump probe simulations. Note that the timescales of the various decays correspond to those obtained by the global fitting procedure.

In light of these results, we observe that the 40 ps timescale associated to the decay of the oscillations does not have an inhomogeneous origin. Indeed, damping of the observed oscillations by dephasing is already accounted for by the inhomogeneous particle population used in the simulation. Therefore, we may conclude that this decay possesses an homogeneous mechanical origin [7]. The maximum size change in the particles has been set to 1%, following the estimate of Perner *et al.* for silver nano-ellipsoids of similar dimensions [163]. It is worth noting that this *is not an absolute estimate*, but this value may vary according to a change in the proportionality constant connecting the position of the surface plasmon resonance and the size of the particle.

We note that the phase behavior of the oscillations is almost perfectly captured by the simulations all the way through the dynamical evolution of the system. The value used for the size-dispersion in the sample (8%) is consistent with the estimate made examining several samples by TEM. The width

---

[7]Nevertheless, we may not *absolutely* exclude that this damping is caused by the inhomogeneous dephasing among particles bearing a similar spectrum, but different mechanical properties, which do not fit in the assumptions of our basic model.
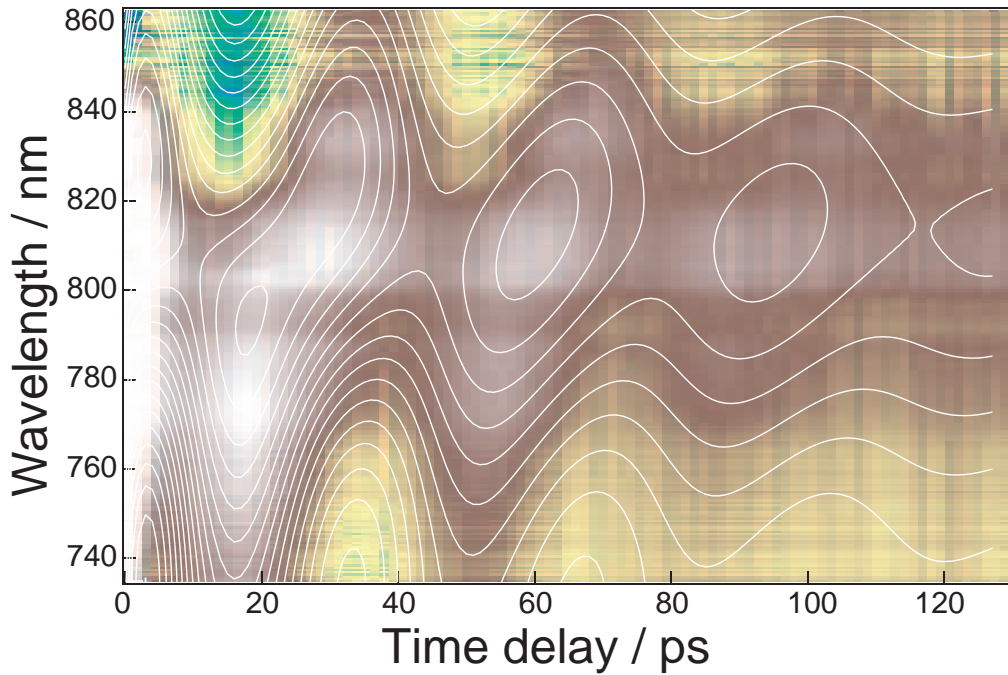
Figure 9.19: Simulations of the pump probe signal calculated including the effect of an inhomogeneous distribution of sizes in the sample. The **contour lines** in white, which are the results of the simulations obtained with the parameters in Tab. 9.3, are superimposed to the transient absorption signal of Fig. 9.10.

of the homogeneous band (45 nm) corresponds to $\sim$60% of the one calculated by Kelly *et al.* for triangular plates of similar aspect ratio [41]. In addition, the overall width of the inhomogeneous band involved in the dynamics, as extracted from the simulations, is in good agreement with the estimate that we could make considering the permanent bleach in the steady state absorption spectrum appearing upon several minutes of sample irradiation at high pump power.

9.6   Mechanical vibrations of a triangular plate

We have used a continuous elastodynamical model to calculate the frequency of mechanical vibration of a triangular plate, and compare it with the value observed for our nanoparticles. Since an exact solution to the problem does not exist, we have sought for an approximate numerical solution, following the guidelines of Cheung *et al.* [51], with a few modifications to their original approach.

9.6.1   Calculation of the vibrations

The strain energy V and kinetic energy T of a freely vibrating elastic body are described by the following integrals:

$$V = \frac{1}{2} \iiint \lambda(\epsilon_x + \epsilon_y + \epsilon_z)^2 + 2\mu(\epsilon_x^2 + \epsilon_y^2 + \epsilon_z^2) +$$
$$+ \mu(\gamma_{xy}^2 + \gamma_{yz}^2 + \gamma_{zx}^2) \, \mathrm{d}x \, \mathrm{d}y \, \mathrm{d}z \ , \tag{9.14}$$

$$T = \frac{\rho}{2} \iiint (\dot{u}^2 + \dot{v}^2 + \dot{w}^2) \, \mathrm{d}x \, \mathrm{d}y \, \mathrm{d}z \ , \tag{9.15}$$

where λ and μ correspond to the Lamé constants and ρ to the density. The symbols ϵ and γ indicate the linear strain-displacement relations, defined through the functions u, v, w and their time-derivatives $\dot{u}$, $\dot{v}$, $\dot{w}$ which describe, respectively, the displacement and the velocity of each point of the body in the x, y and z directions:

$$\epsilon_x = \frac{\partial u}{\partial x} \ , \qquad \epsilon_y = \frac{\partial v}{\partial y} \ , \qquad \epsilon_z = \frac{\partial w}{\partial z} \ , \tag{9.16}$$

$$\gamma_{xy} = \frac{\partial v}{\partial x}\frac{\partial u}{\partial y} \ , \qquad \gamma_{yz} = \frac{\partial w}{\partial y}\frac{\partial v}{\partial z} \ , \qquad \gamma_{zx} = \frac{\partial u}{\partial z}\frac{\partial w}{\partial x} \ . \tag{9.17}$$

For free vibrations of circular angular frequency ω, we can re-cast the displacement functions in the form:

$$u = U(x, y, z)e^{i\omega t} \ , \quad v = V(x, y, z)e^{i\omega t} \ , \quad w = W(x, y, z)e^{i\omega t} \ . \tag{9.18}$$

Defining now the functions $R_{1,2,3}$ as

$$R_1 = (\frac{\partial U}{\partial x} + \frac{\partial V}{\partial y} + \frac{\partial W}{\partial z})^2 \ ,$$
$$R_2 = 2\left[\left(\frac{\partial U}{\partial x}\right)^2 + \left(\frac{\partial V}{\partial y}\right)^2 + \left(\frac{\partial W}{\partial z}\right)^2\right] \ , \tag{9.19}$$
$$R_3 = \left(\frac{\partial U}{\partial y} + \frac{\partial V}{\partial x}\right)^2 + \left(\frac{\partial V}{\partial z} + \frac{\partial W}{\partial y}\right)^2 + \left(\frac{\partial W}{\partial x} + \frac{\partial U}{\partial z}\right)^2 \ ,$$

the maximum strain and kinetic energy of the plate can be described by the following compact expressions:

$$V_{max} = \frac{1}{2} \iiint \lambda R_1 + \mu(R_2 + R_3)\, \mathrm{d}x\, \mathrm{d}y\, \mathrm{d}z \; , \tag{9.20}$$

$$T_{max} = \frac{1}{2}\rho\omega^2 \iiint (U^2 + V^2 + W^2)\, \mathrm{d}x\, \mathrm{d}y\, \mathrm{d}z \; , \tag{9.21}$$

and the Lagrangian energy functional is simply written as

$$L = T_{max} - V_{max} \; . \tag{9.22}$$

At this stage, our query can be envisaged as a variational problem, and the determination of the function minimizing L is realized applying standard procedures. Specifically, the functions U, V, W and R_i are first approximated by finite linear combinations of basis functions F_n (Ritz method). Successively, substituting the approximated expressions in Eq. 9.22, the minimization of the Lagrangian is reduced to a generalized eigenvalue problem, where the coefficients of the expansion on the trial functions F_n represent the eigenvectors, while the eigenvalues are related to the frequencies of the vibrational modes.

As illustrated in Fig. 9.20, the triangular domain is mapped onto a basic cubic domain applying the following transformation:

$$x = \frac{a\xi(1 - \eta)}{4} \; , \qquad y = \frac{a(1 + cos\alpha)(1 + \eta)}{4sin\alpha} \; , \qquad z = \frac{t\zeta}{2} \; . \tag{9.23}$$

This coordinate-transformation is meant to facilitate the procedure and find a well suited basis-set of functions that converge rapidly to the expressions 9.18 and 9.19.

The displacement functions are then approximated by a combination of Chebyshev polynomials F_n on the interval defined by the condition: $\xi, \eta, \zeta \in [-1, 1]$, which represents the volume occupied by the body in the space of the transformed coordinates. For instance, the first displacement function of Eq. 9.18 is developed as:

$$U(\xi, \eta, \zeta) = \sum_{i=1}^{I} \sum_{j=1}^{J} \sum_{k=1}^{K} A_{ijk} F_i(\xi) \tilde{F}_j(\eta) F_k(\zeta) \; , \tag{9.24}$$

and analogous expressions are set up for $V(\xi, \eta, \zeta)$ and $W(\xi, \eta, \zeta)$.
The functions F_n are defined as

$$F_n(\chi) = cos[(n - 1)\arccos(\chi)] \; , \qquad n = 1, 2, ... \tag{9.25}$$

$$\tilde{F}_n(\eta) = (F_n(\eta) - 1) \; , \qquad n \neq 1 \tag{9.26}$$

$$\tilde{F}_1(\eta) = F_1(\eta) \; , \qquad n = 1 \tag{9.27}$$

$\tilde{F}_n$ has been substituted to the original Chebyshev polynomial in the expressions evaluated along the coordinate η in order to avoid singularities that
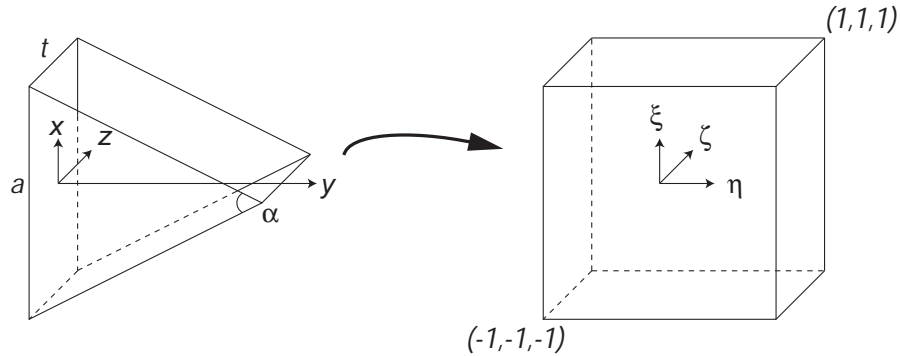
Figure 9.20: Domain transformation from triangular plate to cubic.

prevent the successive numerical integration [8].

The approximated expressions in the form of Eq. 9.24 are finally used to recast the Lagrangian functional in the cubic coordinate system $\{\xi, \eta, \zeta\}$. The minimization of the Lagrangian, at this point, is reduced to the solution of a linear set of eigenfrequency equations, where the terms A_{ijk} (Eq. 9.24) represent the coefficients of the eigenvectors of the system on the basis of the modified Chebyshev polynomials, and carry indications about the symmetry of the vibrational modes. The eigenvalues are associated to the frequency of the corresponding modes.

9.6.2   Comparison with the experimental results

The vibrations of the triangular plate have been calculated using the parameters listed in Tab. 9.5, which includes the values of the macroscopic elastic properties of bulk silver [190].

Young modulus	Poisson ratio	Density	Side length	Thickness
$83 \cdot 10^9$ Pa	0.37	10490 Kg/m^3	70 nm	8 nm

Table 9.5: Parameters used for the calculation of the mechanical vibrations of the silver triangular nano-plates.

---

[8]The analytic integration is numerically approximated using the recursive adaptive Simpson quadrature procedure.

The calculated vibrational periods are reported in Tab. 9.6. Considering the symmetry of the equilateral triangular plates, we labelled the different modes according to their character in the D_{3h} point group [191].

Symmetry	E_1'	E_1'	A_2'	A_1'	E_1'
Period [ps]	60.1	41.2	37.4	34.8	27.6

Table 9.6: Symmetries and periods of the calculated mechanical vibrations. The symmetries are indicated in the D_{3h} point group.

We remark that the period corresponding to the lowest *totally symmetric mode* (A_1') is in fairly good agreement with the periodicity of the oscillations observed in the experiment [9].

The different procedures of data analysis described in § 9.5 indicated that the character of the mechanical oscillations points to an indirect excitation mechanism, mediated by the lattice heating. In this respect, the excitation of a totally symmetric mode is perfectly understandable, because any possible anisotropic distribution of the electrons at the moment of the photo-excitation is completely lost after that the electron-electron and electron-phonon scattering processes have occurred.

A graphical visualization of the mode excited in the experiment is presented in Fig. 9.21.

---

[9]As additional check about the consistency of the parameters used, we calculated that the period of the lowest A_1' mode ranges from 30 to 40 ps, if the side length of the triangles is varied between 60 and 80 nm, while the thickness is kept constant at 8 nm.
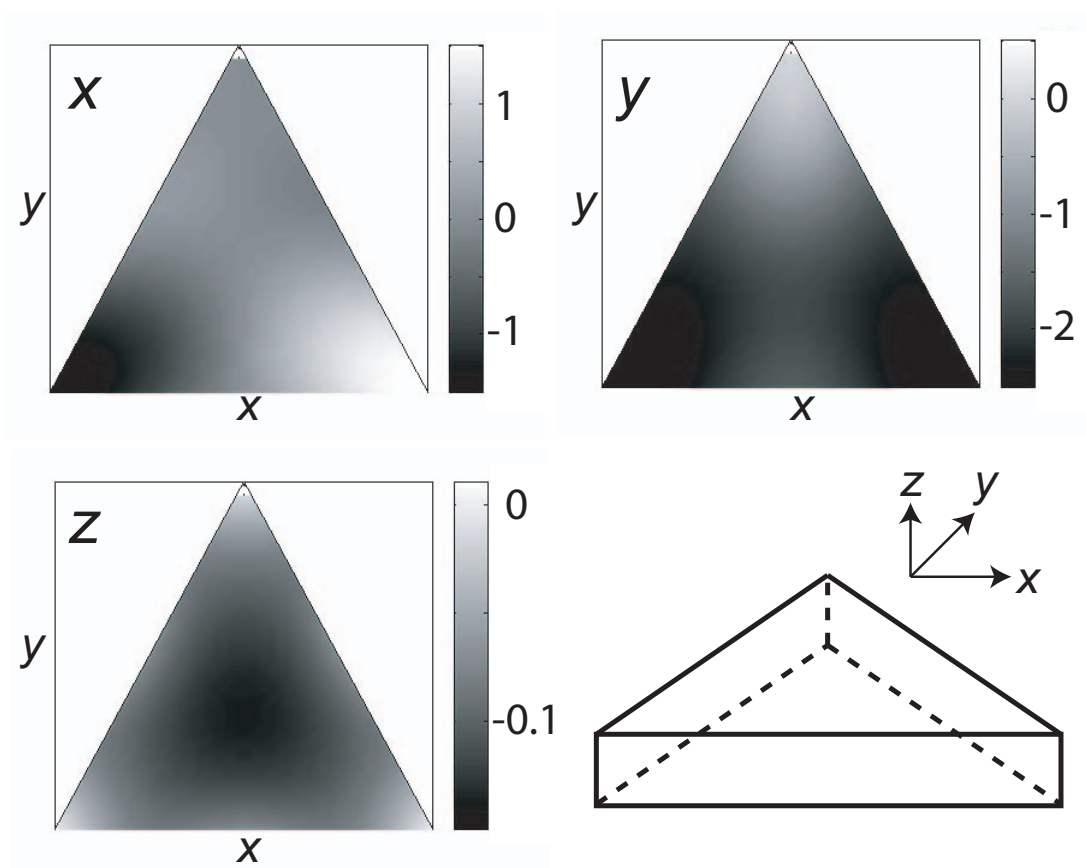
Figure 9.21: Character of the vibrations of the totally symmetric mode (A'_1) of lowest frequency. The contour-plots indicate the relative amplitudes of the vibrations along each axis for the points on the upper surface of the triangular plate.

9.7 Conclusions

This section presents the results of a time-resolved transient-absorption experiment performed on a sample of metallic triangular nano-plates. The particles are synthesized by a novel photo-chemical approach that allows to control their final size and shape by the wavelength of the light used to drive the reaction [44]. The peak position of the plasmon resonance can be tuned in the region of interest (∼800 nm) simply changing the conditions of illumination of the solution during the growth.

The time evolution of the optical properties of the sample was investigated, upon direct intra-band excitation at 800 nm, detecting the absorption changes shown by the sample in the 700-860 nm region using a broad-band continuum probe, with a time-resolution of 130 fs.

At short time-delays, we observed an ultrafast broadening and red-shift of the surface plasmon band, that is attributed to the creation of a hot thermal distribution of electrons in the particles. The transient bleach associated to this process recovers on a timescale of few picoseconds, indicating the thermalization of the electrons with the lattice ions. The decay timescale of this feature depends linearly on the pump-power, as predicted by the two-temperature model (Eq. 9.7). By linear extrapolation, we extracted a value for the electron-phonon scattering time of 1.1 ps.

At longer time delays, we detected four major spectral oscillations of the surface plasmon band, caused by the periodic changes in the particles size triggered by the impulsive heating of the metal lattice.

We used different techniques of global analysis to better characterize, over all the spectral range investigated, the nature of this oscillatory behavior.

At first, we applied an iterative procedure based on successive rotations of the SVD basis, finalized at the maximization of the oscillatory component in a single kinetic-spectral pair. The procedure allowed to isolate three essential dynamical processes and define their spectral character.

Successively, we performed a more traditional analysis by fitting single traces at various wavelengths with an analytical model function derived from the previous SVD analysis.

Finally, we applied a global procedure and fitted *simultaneously* the temporal traces to extract *global* information about the various decay timescales and the exact phase behavior of the oscillations.

All these three complementary analysis indicate that the oscillations take place with a periodicity of 35 ps, and decay mono-exponentially with a time constant of 40 ps. They identify also the presence of a slowly decaying (120 ps) bleach-offset, that we attribute to the raised-temperature of the lattice gradually equilibrating with the solvent.

The presence of cosine-type oscillations showing a phase manifestly different from zero, observed in the time traces at wavelengths around 800 nm, may lead to the erroneous conclusion that there exist some *direct* contributions to the excitation of the acoustic oscillations (i.e. hot electron pressure) [163] that are not expected for particles of this size [49].

We propose a different explanation, that resides on the sample inhomogene-

ity: even relatively low size dispersion in samples of particles of non-spherical symmetry may result in a substantial inhomogeneous broadening of the plasmon resonance. This effect is expected to be more evident than in the case of spherical particles, where the peak position and the width of the band are known to be largely independent of the radius [36].

In order to verify this effect, we developed a simple model, which accounts for the possibility of exciting an inhomogeneous population of particles, to simulate the pump-probe signals. We succeeded in retrieving the phase behavior observed in the experiment using, for describing the particle size evolution, a model function *limited to a purely indirect excitation process*. Within the assumptions of this simple model, the 40 ps exponential damping observed in the oscillations is expected to have an homogeneous, mechanical, origin. In addition, the simulations allowed to *estimate* the homogeneous width of the surface plasmon band of the triangular plates, which results of the order of 45 nm.

Finally, we calculated the vibrational modes of a silver triangular nano-plate within the framework of elastic theory of homogeneous bodies [51]. We found that the period of *the lowest totally symmetric vibrational mode*, calculated for particles of these dimensions and aspect ratio, compares very well with the periodicity observed in the data.

Chapter 10

Visible and infrared study of the cyano complexes of Myoglobin and Hemoglobin I

The following chapter reproduces a recently published paper [52] with some additional contributions and explanations regarding the UV-visible measurements and the data analysis.
The measurements in the mid-IR region have been performed at the University of Zürich by Dr. Jan Helbing.

Heme proteins are widely studied as model systems to understand structure - function relationships and ligand-binding properties. Invertebrate hemoglobins are especially interesting because of their functional ability to bind molecules other than O_2 [192]. *Lucina Pectinata*, for instance, is a clam which contains a unique hemoglobin (HbI) that is involved in H_2S transport. For its food supply this mollusc incorporates a vast population of chemoautotrophic symbiotic bacteria, which must be supplied with the environmental H_2S found in the sediments in which the clam lives. The monomeric HbI, located in the symbiont-harboring gills of *Lucina Pectinata*, reacts with H_2S with an extraordinary affinity [193, 194], and delivers the ligand to the bacteria. However, in contrast to more common ligands like O_2, NO or CO, which bind to ferrous heme proteins (Fe^{II}), hydrogen sulphide binds to Hemoglobin I in its ferric state (Fe^{III}). The X-ray crystal structure of the aquomet complex (see § 10.1.1) has revealed that HbI is structurally very similar to vertebrate
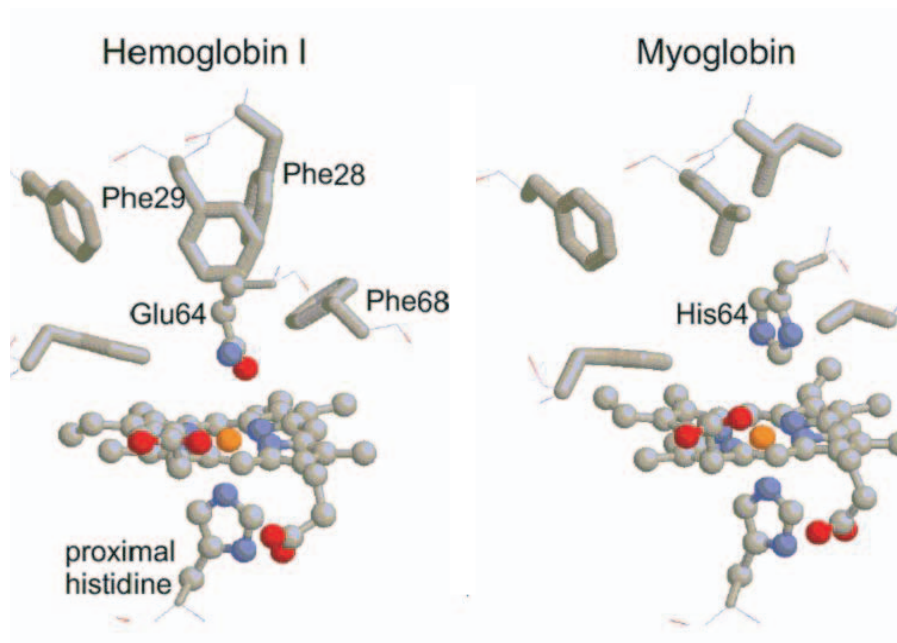
Figure 10.1: Comparison of the heme-pockets of cyanomet HbI from *Lucina Pectinata* and cyanomet (sperm whale) Myoglobin (ligand not shown).

Myoglobin. However, a glutamine residue instead of the typical histidine occupies the distal position 64, and there is an unusual distribution of aromatic residues (Phe29, Phe68, and Phe28) surrounding the heme distal position, as illustrated in Fig. 10.1 [53].

This collaborative study of Hemoglobin I and Myoglobin was initiated to gain better insight into the interaction between the ligand and the heme pocket, by comparing the ultrafast dynamics of ligand dissociation and rebinding in the two proteins.

It has been proposed that the extent of geminate ligand recombination after photolysis is sensitive to the interaction of a ligand with the distal amino acid residues and the possibility of that ligand being trapped within the heme pocket [54, 195]. Since H_2S is an unsuitable ligand for a comparative study, as it only binds to HbI from *Lucina pectinata* [193], we chose the cyanide anion CN^- as ligand, which forms low-spin ferric complexes both with HbI and vertebrate heme proteins [196].

Figure 10.2: Planar configuration of the porphyrin molecule. The symmetry group is D_{4h}.

Ligand dynamics upon femtosecond laser excitation of Hemoglobins and Myoglobins has been intensely studied for almost two decades [54–61] but, owing to their relevance in the respiratory system of vertebrates, most attention has been paid to globins with the iron atom in the ferrous state. Indeed, while

there exists a large amount of information from a variety of experimental studies on the ground state properties of heme proteins in the ferric state, and in particular the CN complex [197–200], little is known about its ultrafast dynamics after laser excitation. On a femtosecond time scale, cyano complexes have only been investigated in an early study on co-operative effects in the binding properties of human hemoglobin [56]. In that study complete ground state recovery within a few picoseconds after laser excitation was observed, but no analysis of possible reaction mechanisms was carried out. More recently, dissociation of NO from ferric Myoglobin was reported [201], which led to the formation of met Myoglobin (see caption of table 10.1) on a millisecond timescale. Two fast time constants in the dynamics (0.7 and 4.6 ps) were attributed to electronic relaxation and cooling of heme [201].

The scarcity of detailed investigations of ferric complexes with high time resolution is especially surprising, as charge transfer processes that involve the central metal atom are commonly invoked to account for ligand photolysis and electronic relaxation of photoexcited metal porphyrins [60, 62]. These should be very sensitive to the oxidation state of the complex under investigation, which calls for a systematic study of the photodynamics of a heme protein with a ferric ground state. To this aim, we carried out the femtosecond pump-probe transient absorption measurements in the 360-600 nm region following Soret band excitation of the HbICN and MbCN (§ 10.3.1). In addition, transient mid-infrared absorption measurements have been performed to monitor directly the dynamics of the CN ligand to Myoglobin. The infrared data, described in § 10.3.2, provides direct information on the recovery of the ligated electronic ground state as well as vibrational cooling, and allow a detailed analysis of the ultrafast dynamics of a ferric heme complex.

10.1 Static spectroscopy

10.1.1 UV-Vis absorption

In the UV-vis region the absorption spectra of heme-proteins are dominated by transitions to the lowest lying electronic states of the porphyrin molecule. Porphyrin, represented in Fig. 10.2, possesses a singlet ground state $|0\rangle$ of A_{1g} symmetry, and two 2-fold degenerate excited singlet states: $|S\rangle = |S_x, S_y\rangle$ and $|Q\rangle = |Q_x, Q_y\rangle$. The so-called Soret band (~ 400 nm) is associated with the strongly allowed $|0\rangle \rightarrow |S\rangle$ transition, while in the 500-600 nm region the much weaker Q-band corresponds to the $|0\rangle \rightarrow |Q\rangle$ transition.

Soret band transitions usually involve little vibrational excitation [202]. Q-band excitations show two separate components associated with vibrationless and vibrational transitions in the case of low-spin (ligated) ferrous hemes. On the contrary, in high-spin 5-coordinated hemes (deoxy species) only one band is observed, corresponding to transitions to vibrationally excited states.
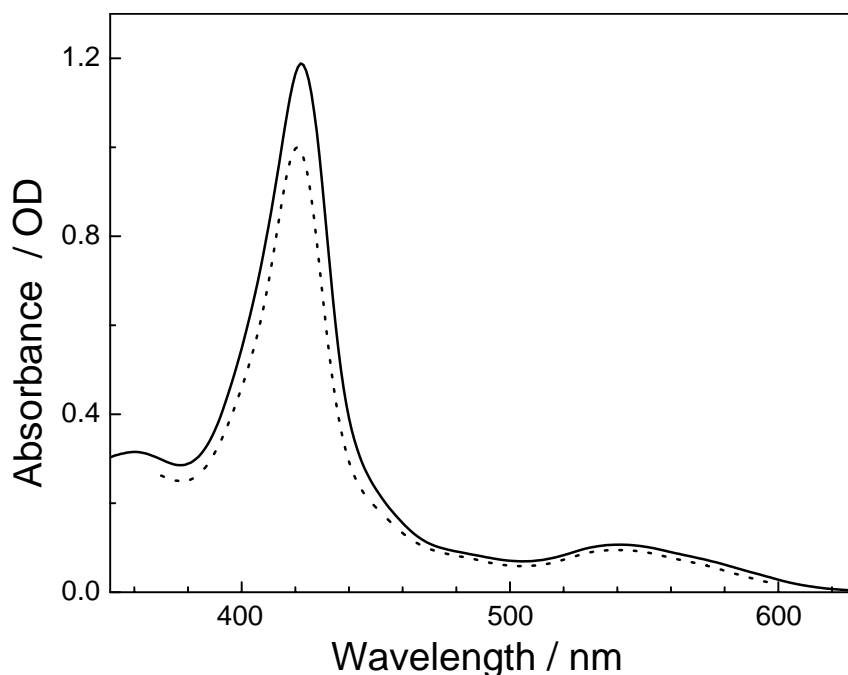
Figure 10.3: Absorption spectra of MbCN (**line**) and HbCN (**dots**). The peak around 420 nm and the weak absorption in the 500-600 nm region correspond to the Soret and Q-band respectively.

Species	Band	Band maximum	ϵ
		[nm]	$[\text{mol l cm}^{-1} \cdot 10^3]$
deoxy HbI	*Soret*	433	119
	Q	557	12.2
cyanomet HbI	*Soret*	421	116
	Q	540	11.3
aquomet HbI	*Soret*	407	178
	Q	502.6	10.2

Table 10.1: Absorption maxima and extinction coefficients of HbI from *Lucina Pectinata* from Ref. 193. The *deoxy* form corresponds to the unligated species in high spin state and 2+ oxidation state. The *aquomet* form corresponds to a high spin complex with the iron atom in the 3+ oxidation state, forming a weak bond with a water molecule. *Cyanomet* HbI is a low spin complex with iron in the 3+ oxidation state.

In general, binding of a ligand or any change in spin and oxidation state of the central iron atom may cause major spectral shifts in the visible absorption region. These modifications are exploited by transient absorption spectroscopy to study in real time the ligand dissociation and recombination process. Table 10.1 shows the absorption maxima and extinction coefficients of HbI from *Lucina Pectinata* in different states and bound to different ligands. Figure 10.3 contains the comparison between the UV-visible absorption spectra of MbCN and HbICN in buffer solution: very similar spectroscopic features characterize both complexes.
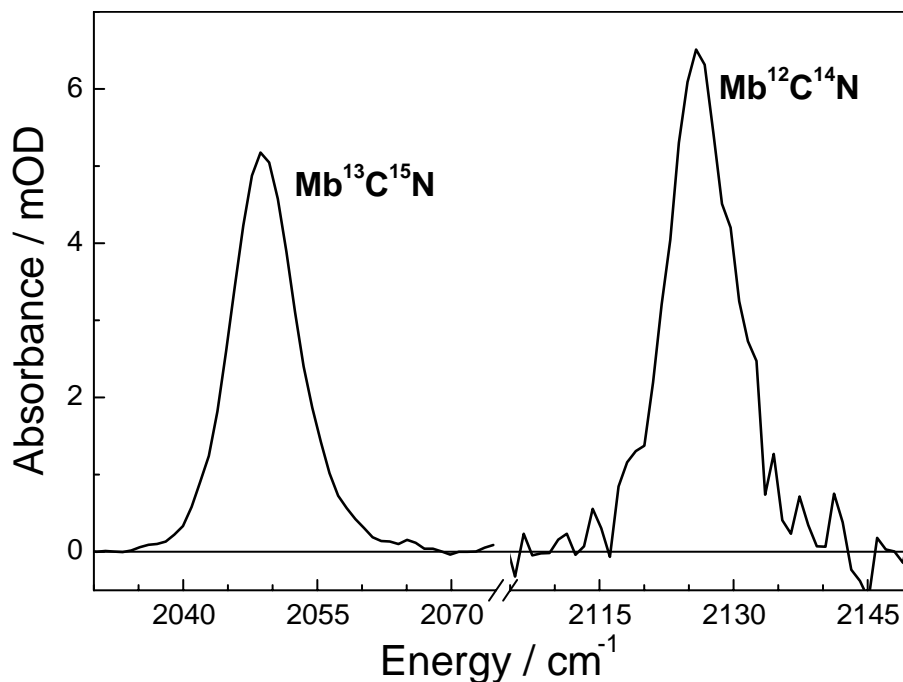
Figure 10.4: FTIR absorption spectra of Mb^{12}C^{14}N (left) and Mb^{13}C^{15}N (right) in deuterated phosphate buffer at pD 7.

10.1.2   Infrared absorption

In Fig. 10.4, we observe that the FTIR absorption spectrum of MbCN in deuterated phosphate buffer consists of a single narrow peak at 2126 cm^{-1}, with a width of 9-10 cm^{-1}.

The use of isotope labelled ^{13}C^{15}N lowers the MbC≡N stretch frequency by 77 cm^{-1} to 2049 cm^{-1}, almost exactly as expected from a reduced mass calculation for CN (2048 cm^{-1}), without significantly changing bandwidth or intensity (Fig. 10.4).

10.2   Experimental

Laser and detection system.   The details of UV-visible experimental set-up are discussed in appendix B.

Samples.   Met Myoglobin from Horse skeletal muscle was purchased from Aldrich and used without further purification. For optical measurements, the protein was dissolved in 0.1 M phosphate buffer solution (pH 7) to a concentration of $\sim$ 100 μM. For IR measurements 10-18 mM solutions were prepared in deuterated phosphate buffer (pD 7). In both cases, the CN complex was formed by adding 2-3 fold excess of potassium cyanide (either ^{12}C^{14}N or the ^{13}C^{15}N isotope).

Lucina pectinata was collected from the shallow mangroves near La Parguera, Puerto Rico. Isolation and purification of HbI from the clam was achieved according to methods described in details in references 194 and 56. The HbI-CN complex was successively prepared by oxidation of oxyHbI with a 10% excess of potassium ferricyanide to obtain ferricHbI and then by adding a slight excess of potassium cyanide. Complex formation was verified periodically by monitoring the UV-VIS spectrum.

UV-vis absorption spectra were also recorded before and after laser measurements to check for sample integrity.

Cells. For the UV-visible measurements the MbCN solution was flown in a closed cycle through a quartz flow cell with 500 μm optical path length. The optical density at the maximum of the Soret band was typically around 0.6 OD. A sealed, 1 mm path-length spinning sample cell made of 2 mm CaF_2 windows was used for HbI (OD 1.2-1.6).

IR measurements were carried out in a flow cell, consisting of two 2 mm thick CaF_2 windows held apart by 50 μm or 100 μm teflon spacers, and protein solution was circulated by a peristaltic pump in a closed circuit especially designed to handle small sample volumes [203].

10.3 Time-resolved experiment

10.3.1 UV-visible

Transient spectra in the Soret and Q-band region of MbCN at different delays after excitation with a 400 nm pump pulse can be seen in Fig. 10.5. For comparison, the inset shows the corresponding spectra recorded for the HbICN complex, which were found to be almost identical. In particular, the signals for both proteins completely decay to zero with the same time constant. Next to the bleach of the Soret band there is an immediate increase in absorption in the 450-500 nm region with a maximum near 480 nm. After only 500 fs this broad feature has almost disappeared again, and the transient spectrum now shows a peak near 440 nm. As this absorption feature grows in, it continuously shifts to shorter wavelengths. At the same time there is a steady decrease in the amplitude of the Soret bleach. The spectra also reveal a blue shift of the local absorption minimum near 540 nm, which is due to the bleaching of the Q-band.

Transients at selected probe wavelengths for MbCN are shown in Fig. 10.6. Positive absorption near 440 nm is largest at a pump-probe delay of 2 ps. At longer delays the transient absorption signal decays on a 4 ps time scale at all wavelengths. This later phase in the dynamics is characterized by an isos-
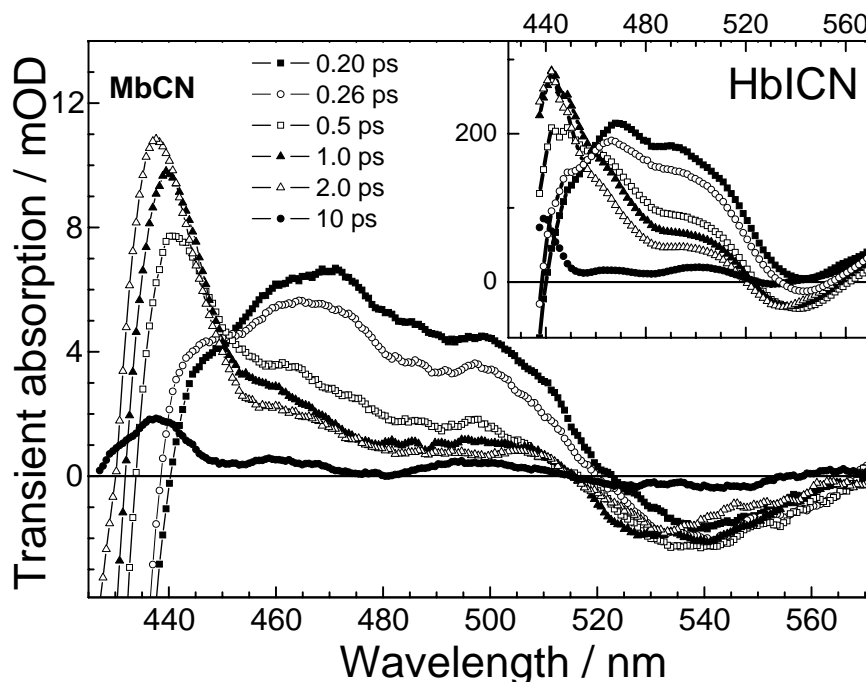
Figure 10.5: Transient absorption signals for probe delays 200 fs, 260 fs, 500 fs, 1 ps, 2 ps, and 10 ps after excitation of MbCN by a 80 fs pump pulse at 400 nm. **Inset.** Same data for the HbICN complex from *Lucina Pectinata*.

bestic point near 430 nm, reflecting the fact, that only minor spectral shifts take place in the Soret region after approximately 4 ps (second trace from top in Fig. 10.6). A transient increase in absorption is also observed to the blue side of the Soret bleach, with a maximum in the transient spectra near 385 nm. At this wavelength the signal is largest at a pump-probe delay of 800 fs, and reaches almost the same maximal amplitude as the signal at 440 nm. It then decays on a 1.5 - 4 ps time scale.

For better comparison with previous work on ferrous systems, we have performed a global fit by applying Singular Value Decomposition (SVD) to the chirp-corrected data and analyzing the basis time traces which correspond to the first largest singular values. These were simultaneously fitted by a linear combination of three exponentials convoluted with a Gaussian function to take into account the finite time resolution. Precise details about this fitting procedure can be found in appendices C.1 and C.2.

The solid lines in Fig. 10.6 show the result of this fit, which yields time constants of 230 fs, 1.3 ps and 3.6 ps. Significantly poorer agreement was found when fitting with only two time constants.

The spectra T_{τ_k} associated with each of the three time constants using Eq. C.5 are shown in Fig. 10.7. The time constants and their wavelength-dependent weight compare well with results obtained for ferrous heme proteins [60], which suggests that the underlying dynamics is very similar for the ferric systems studied here. Note, however, that decay associated spectra only yield physical insight into the dynamics, if the transient spectra consist of state or species associated bands which only change in intensity. An absorption band that
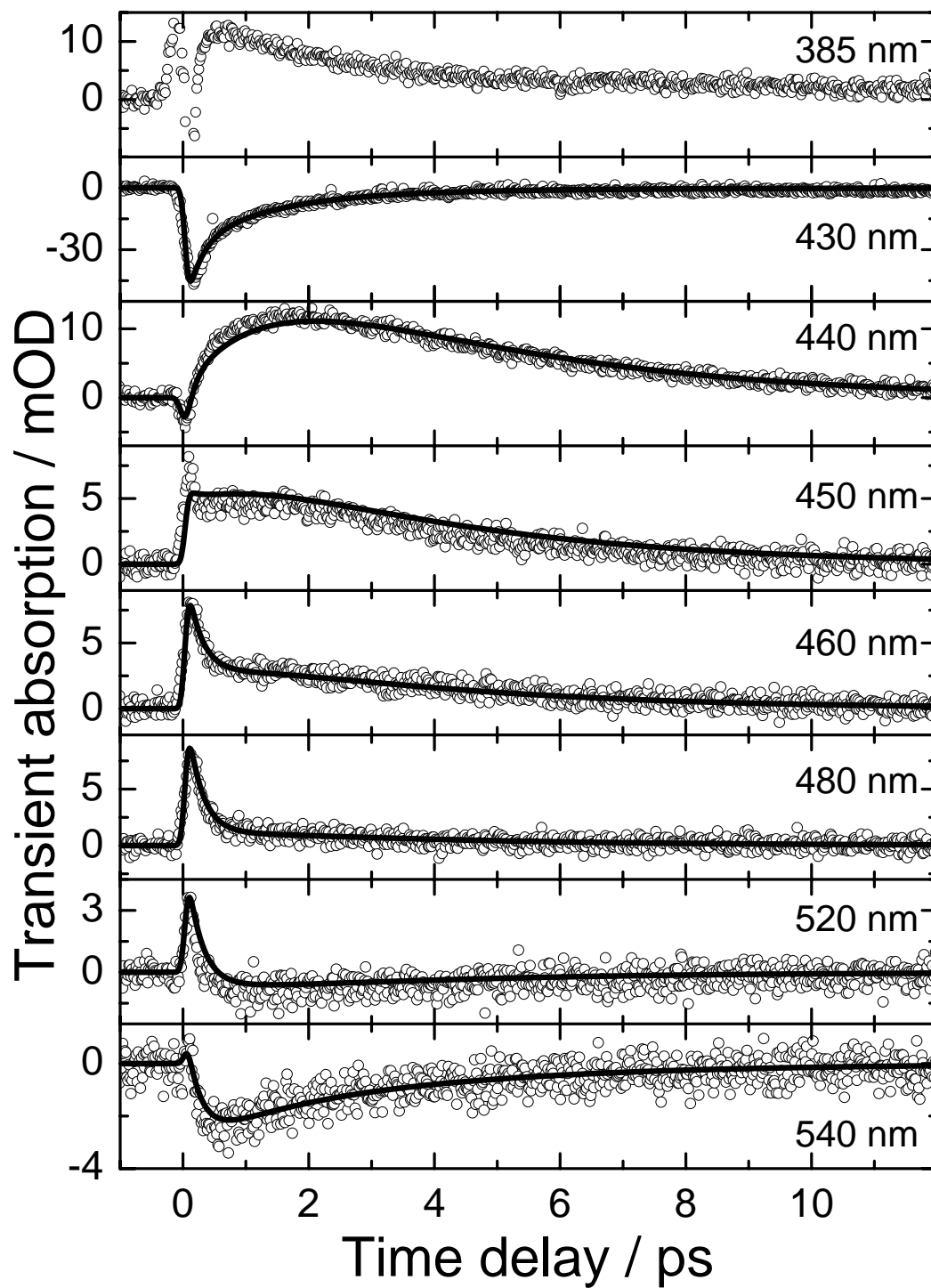
Figure 10.6: **Circles.** Transient absorption changes at different probe wavelengths. **Lines.** Result of global fit with three time constants 230 fs, 1.3 ps and 3.6 ps (see also Eq. C.4). Note the different vertical scales.
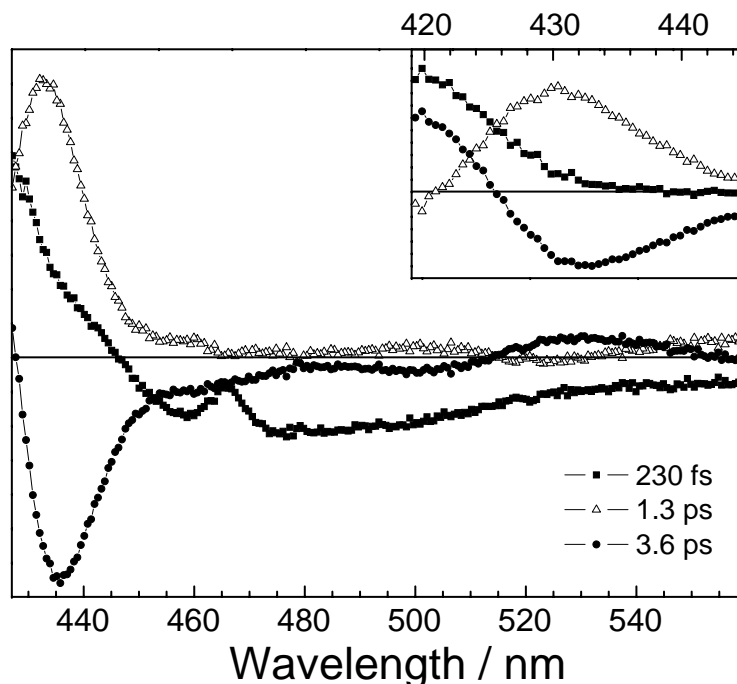
Figure 10.7: Spectral components T_{τ_k} associated with the three time constants 230 fs (**squares**), 1.3 ps (**open triangles**) and 3.6 ps (**circles**), required to fit the transient spectra of MbCN. The dip in the 230 fs spectrum near 465 nm is due to the coherent Raman signal of the H_2O solvent. The inset shows an enlarged view of the Soret band region (data from a more dilute sample).

also changes its shape or spectral position as a function of time is only poorly captured by this analysis.

It has recently been shown, that the transient absorption signal of deoxy Myoglobin can be well reproduced by superposition of the ground state absorption spectrum and a single broadened and red-shifted Soret band which narrows and shifts back to equilibrium with timeconstants of 400 fs and 4 ps respectively [204]. Indeed, already a very simple simulation for MbCN with similar parameters allows to qualitatively capture the main features in our experimental data. Unfortunately, this analysis could not be carried out in full detail here, since different spectral components make up the absorption spectrum of MbCN in the Soret region [199], and their different broadening behavior is not known.

10.3.2   Infrared

Upon UV excitation of the Soret band of CN-ligated Myoglobin, the transient infrared spectra show a strong bleach of the MbC≡N stretch fundamental near 2126 cm^{-1}, as well as two smaller absorption features, one immediately to the red of the bleach, and one red-shifted by approximately 30 cm^{-1}. These are labeled (1) and (2) in Fig. 10.8, respectively.

Band (2), initially centered at 2093 cm^{-1}, is approximately five times weaker
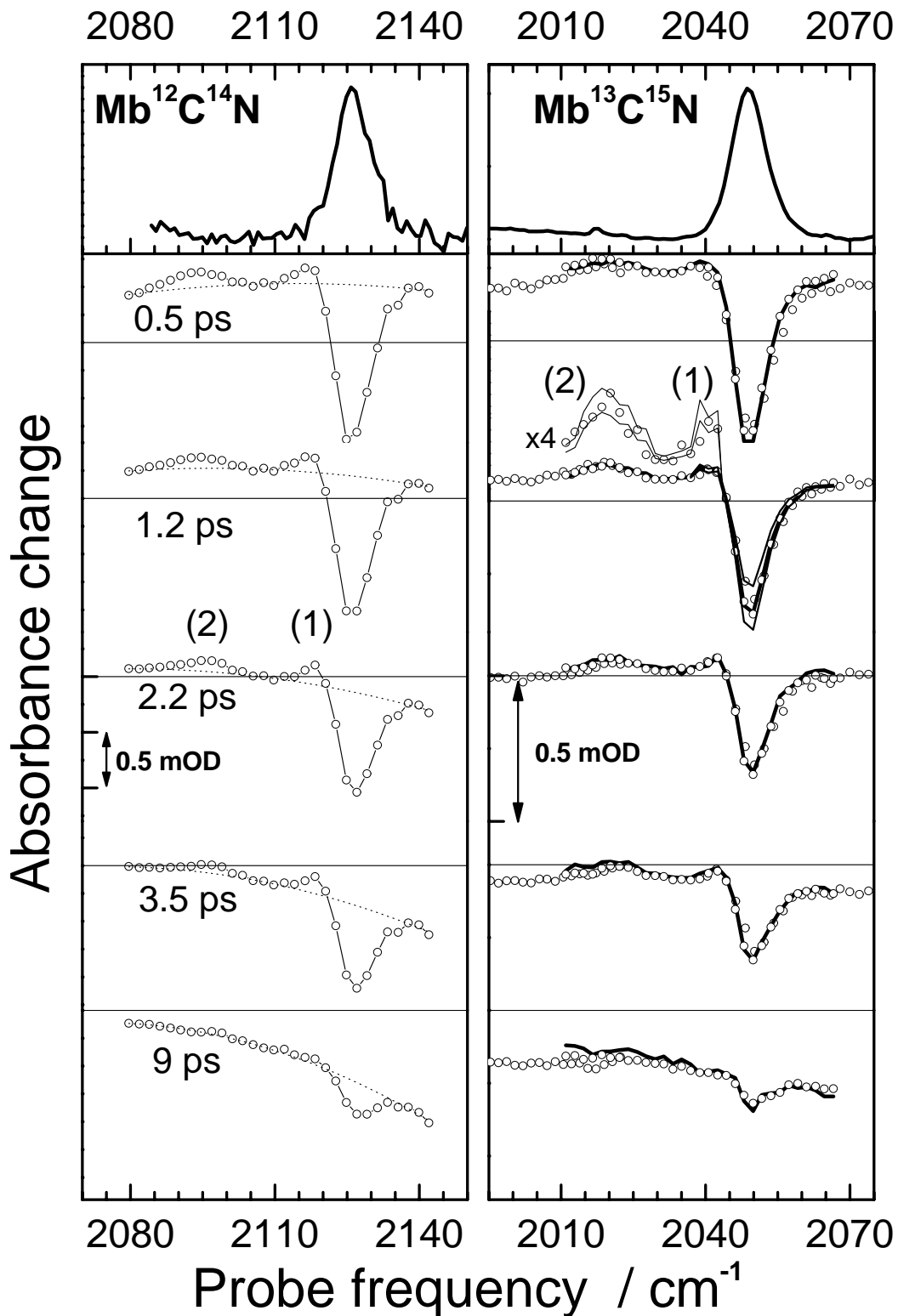
Figure 10.8: **Top.** FTIR absorption spectra as in Fig. 10.4. **Bottom.** corresponding transient absorption signals at different probe delays after excitation of MbCN by a 700 fs pump pulse at 420 nm. The dotted lines show a quadratic fit to the background signal, caused mainly by the rise in solvent temperature. The signals for parallel polarization of pump and probe pulses (Mb^{13}C^{15}N, lines) were multiplied by a factor R=1.5 to superimpose them on the signals for perpendicular polarization (open circles). The lines in the enlarged view ($\times 4$) show the parallel signal multiplied by $R = 1.2$ ($\alpha \approx 40°$) and by $R = 1.7$ ($\alpha \approx 20°$).

than the bleaching signal at 2126 cm^{-1}. It decays with increasing pump-probe delay and its maximum shifts towards larger energies (see also Fig. 10.9). A similar blue shift can also be seen for the minimum of the bleaching signal, which weakens at the same rate as band (2).

The transient absorption signals of MbCN are superimposed on a broad background signal, which is initially positive and caused by cross phase modulation between overlapping pump and probe pulses in the D_2O solvent as well as the CaF_2 windows of the flow cell. At longer pump-probe delays, the background signal becomes negative and tilted towards larger frequencies. It is well known that the infrared absorption bands of liquid water shift towards higher energies with increasing temperatures, giving rise to a negative pump-probe signal at the low energy side of the D_2O stretch vibration. This has been attributed to a weakening of hydrogen bonding, which results in the strengthening of the intramolecular bonds. The time dependence of the background signal thus provides a measure for the transfer of (thermal) energy, originally localized on the porphyrin chromophore, to the solvent. It takes place on a 5-10 ps timescale, which is very similar to what has been previously reported for closely related systems [205].

In order to reduce this background signal, experiments were also carried out using the $^{13}C^{15}N$ isotope as ligand (right hand side of Fig. 10.8). Apart from the shift in CN-stretch frequency, almost identical results were obtained. The small product band at 2020 cm^{-1} is equally red-shifted by 28 cm^{-1} with respect to the fundamental MbC$\equiv$N stretch transition, and is of the same relative strength with respect to the MbCN bleach. No other bands were observed in the 1970-2100 cm^{-1} spectral range.

Transient spectra are difference spectra and can be viewed as the superposition of a negative bleaching component, which is time-independent and has the shape of the absorption spectrum before excitation, and the time-dependent positive absorption of those molecules that have been excited by the pump pulse.

For a better visualization of the temporal evolution it is instructive to eliminate the bleaching component from the transient spectra by adding the FTIR absorption spectrum with the same scaling factor for all time delays [1]. The resulting pump-probe spectra contain only positive signals, which reflect the time-dependent absorption of those molecules that have absorbed a UV photon (Fig. 10.9a). The return of excited molecules to the (electronic and/or vibrational) ground state now appears as a growth of the fundamental MbC$\equiv$N stretch absorption band. It can be seen that at early time delays this band (labelled 1') does not appear at 2126 cm^{-1}, but is shifted to smaller energies, with a considerably larger width. It is this shift and broadening of the MbC$\equiv$N stretch transition, that leads to the positive signal (1) in the transient spectra of Fig. 10.8.

---

[1]The scaling factor was determined by fitting the FTIR spectrum to the 0.5 ps signal in the 2130-2145 (2050-2065) cm^{-1} spectral range (blue wing of the main bleach. This yields the smallest possible value that eliminates negative contributions from the signal after background subtraction. The ground state population derived from Fig. 10.9 is therefore associated with relatively large error bars and may be underestimated.
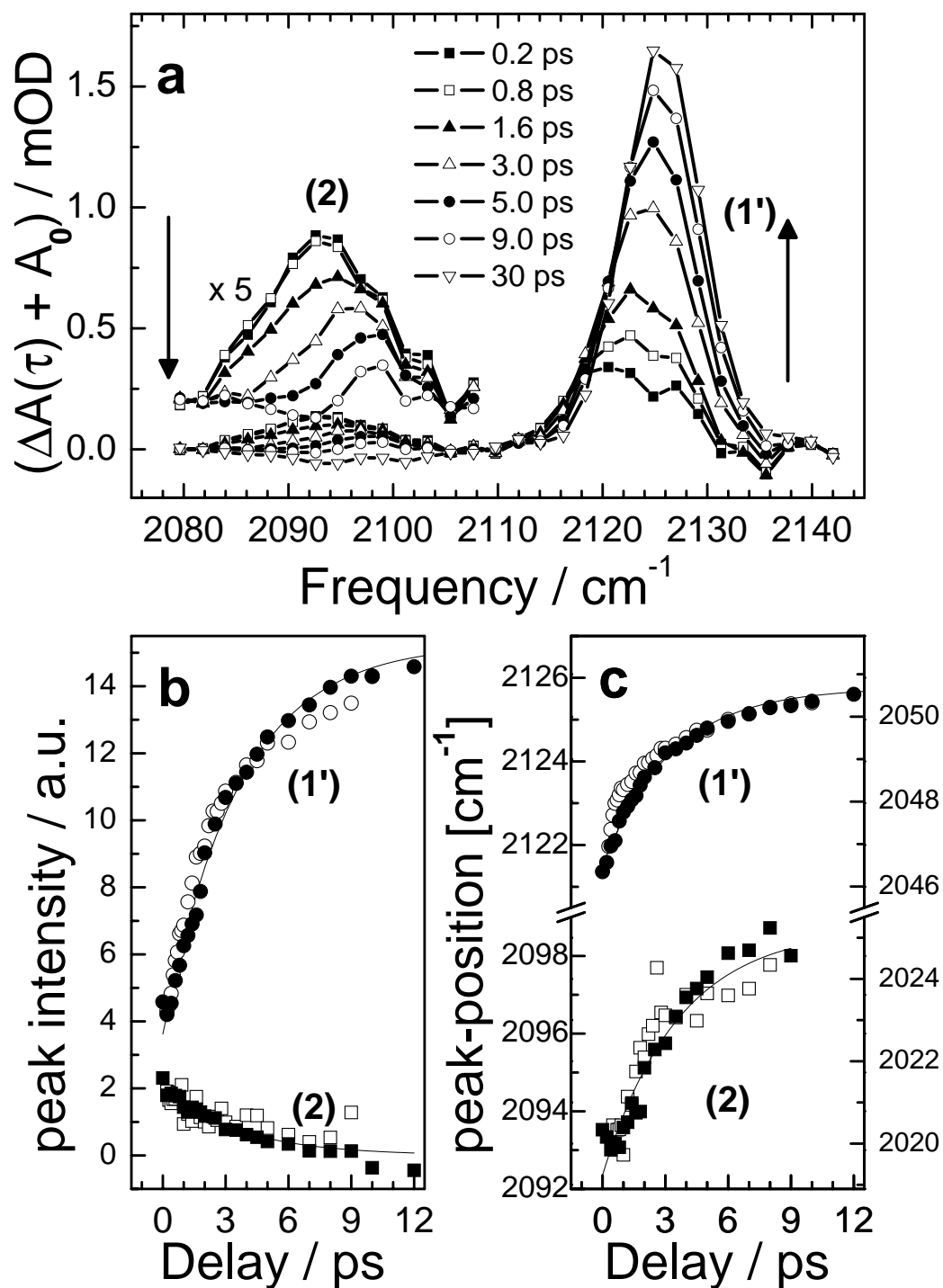
Figure 10.9: **a)** Transient absorption signals of $Mb^{12}C^{14}N$, with the bleaching component eliminated by adding the same scaled FTIR absorption spectrum A_0, and subtracting the second order polynomial fit to the background (dotted lines in Fig. 10.8) from all spectra. The intensities and peak positions of the bands labelled **(1)** and **(2)** where determined by fitting gaussian lineshapes and are shown in **b)** and **c)** respectively. The solid lines are exponentials with a fixed 3.6 ps time constant.

The time-dependent intensities (area) and central frequencies of the two bands in Fig. 10.9a were extracted by least square fitting with gaussian lineshapes, and are shown as a function of pump-probe delay in Fig. 10.9b and c. The decay of band (2) and the recovery of the fundamental MbC≡N stretch absorption occur exactly in parallel and can be well reproduced by an exponential function with the 3.6 ps time constant obtained from the fit of the visible data (solid lines in Fig. 10.9b). Very similar exponential dynamics are found for the position of the corresponding band maxima (Fig. 10.9c). Both undergo a blue-shift of approximately 4 cm^{-1} on the same 3-4 ps timescale.

Anisotropy Finally, the signal anisotropy was determined from the quasi simultaneous measurement of the transient absorption changes with parallel and perpendicularly polarized pump and probe laser pulses. At all pump-probe delays the same scaling factor of 1.5 ± 0.2 is needed to completely overlap the spectra recorded with parallel and perpendicular polarizations (solid lines in Fig. 10.8). The anisotropy is thus identical for all bands in the transient absorption spectra, and does not change with time.

For a plane-polarized pump transition (the Soret transition is doubly degenerate) and a linearly polarized probe transition, the angle α between the C≡N axis and the normal to the heme plane is related to the polarization ratio via [206]:

$$R = \frac{\Delta A_\perp}{\Delta A_\parallel} = \frac{4 - \sin^2 \alpha}{2 + 2\sin^2 \alpha} \ . \tag{10.1}$$

The observed value of $R = 1.5 \pm 0.2$ corresponds to an angle of $30 \pm 8°$. This value (which is an upper limit since possible saturation of the transition and imperfect polarizers tend to lower the observed anisotropy) can be compared with results of NMR studies, which measured a $\approx 15°$ tilt of the Fe-C≡N unit with respect to the heme normal [207] and polarized infrared absorption measurements on Mb single crystals, which yielded a tilt of 21-22° [208].

10.4 Discussion

In the following we first assign the transient mid-infrared absorption bands, and show that they provide information on both vibrational cooling and relaxation of electronic excitation of the heme. We then discuss the optical response in the Soret and Q-band region in direct comparison with previous studies of ferrous heme proteins.

10.4.1   Assignment of the transient infrared absorption bands

Two positive absorption features are present in the transient infrared spectra in the 2000 - 2200 cm^{-1} region. The band labeled (1) in Fig. 10.8, immediately next to the bleaching signal of the equilibrium MbC≡N stretch fundamental is a typical signature of an increased vibrational temperature in the molecule, which shifts the C≡N transition to lower frequencies. This frequency shift can be understood as the result of thermal (or non-thermal) excitation of low frequency modes of the heme (or protein), which anharmonically couple to the C≡N stretch vibration [209]. *The small red-shift associated with band (1) can therefore be viewed as an indicator of the temperature of CN-ligated molecules in the electronic ground state.*
This is better seen in Fig. 10.9, where the bleaching signal of equilibrium MbCN species has been subtracted. From the intensity of band (1′) in this figure, we can directly read off the fraction of molecules which have returned to the CN-ligated electronic ground state (trace (1′) in Fig. 10.9b). It appears that within the time resolution of our experiment at least 25% of the initially excited molecules are CN-bound and electronically relaxed, but vibrationally hot. The full return of the signal to the equilibrium spectrum then takes place with a 3-4 ps time constant and involves both population relaxation, as reflected by the changes in signal intensity, and heme cooling, i.e. the de-excitation of the anharmonically coupled low-frequency modes that are responsible for the observed frequency shift of the CN stretch vibration. The timescale of vibrational cooling of heme in MbCN is thus very similar to the 3 ± 1 ps deduced from time-resolved anti-Stokes Raman measurements upon photolysis of MbCO [210].

Information about the nature of population relaxation is provided by the second transient absorption band (labeled (2) in Fig. 10.8). It appears approximately 30 cm^{-1} to the red of the equilibrium MbC≡N stretch fundamental, very close to the spectral position of the HC≡N vibration in aqueous solution. Since the absorbance of the C≡N stretch band of free CN$^-$, HCN or DCN is also 3-5 times weaker than that of heme-bound CN [211], spectral position and low intensity of band (2) may suggest that it arises from ligand dissociation. However, two observations speak against the assignment of band (2) to fully photodissociated CN$^-$ ligands:

1. The signal anisotropy, which is constant in time and identical for product bands and bleach, shows that the CN angle relative to the heme plane does not change significantly [2].

2. The time-dependent frequency shift of band (2) implies coupling to the thermally excited low-frequency modes of the heme, that is very similar

---

[2]Signal to noise at delays shorter than 4 ps is high enough to exclude differences in angle of more than 20°

to the coupling responsible for the spectral shifts of band ($1'$).

Thus, *CN associated with band (2) cannot be moving freely inside the heme pocket* and must still be in close contact with the macrocycle. This leaves two possible assignments, which are discussed separately: Band (2) could either represent the C≡N stretch fundamental in a more loosely bound, electronically excited state, or it could be due to the $v = 1 \rightarrow v = 2$ transition of heme-bound ligands that have become vibrationally excited in the photoprocess.

Vibrational Excitation of the C≡N stretch.   The possibility that band (2) is a result of the excitation of one quantum of C≡N stretch is suggested by the observation that the 28 cm^{-1} frequency shift with respect to the bleaching signal is very similar to the anharmonicity of the CN$^-$ stretch vibration in water [3]. In addition, this assignment would nicely explain why the maxima of band (1) and (2) in Fig. 10.9 blue-shift by nearly the same amount and in parallel during heme-cooling. However, in the case of vibronic excitation, the negative signal from the $0 \rightarrow 1$ transition (bleach and stimulated emission) should have the same intensity as the $1 \rightarrow 2$ absorption band. In contrast, band (2) is approximately five times weaker than the bleaching signal, and this intensity ratio is maintained at all time delays. As a result, the molecules with one quantum of excitation in the C≡N stretch can only represent a small fraction of the excited species (excitation to higher vibrational levels was not observed). The main fraction of excited molecules would have to be invisible in the mid-infrared spectrum before they return to the CN-ligated electronic ground state on a 3-4 ps time scale.

In Fig. 10.10a we show a relatively simple kinetic scheme, that would be able to account for these observations. Before becoming observable again in the 2000-2200 cm^{-1} region of the mid-infrared spectrum, excited molecules could populate a state $|e\rangle$, characterized either by a very broad and/or strongly frequency shifted distribution of C≡N stretch frequencies with a very weak extinction coefficient. The decay of state $|e\rangle$ would lead to population of the CN-ligated electronic ground state with rate constants constrained by the observation that decay of band (2) (i.e. the $v = 1$ vibrationally excited state in this scheme) and the recovery of the MbC≡N stretch fundamental take place on the same time scale of 3-4 ps [4].

The "IR-invisible" state $|e\rangle$ in this scheme would most likely be a *photolyzed state*: ligands that are able to rotate almost freely in the heme pocket may be characterized by a strongly broadened absorption band [213, 214]. Furthermore, the large amount of energy required for the vibrational excitation of CN

---

[3]The $v = 1 \rightarrow v = 2$ transition of $^{13}C^{15}N^-$ in D$_2$O is 26 cm^{-1} lower in energy than the $v = 0 \rightarrow v = 1$ fundamental [212]

[4]The decay of $|e\rangle$ may lead to the simultaneous population of both the CN v=1 and v=0 levels in the ligated electronic ground state. The experimental time constants can then be reproduced by setting $k_{e0} + k_{e1} \approx (3.6\,\text{ps})^{-1}$ and assuming much faster vibrational relaxation ($k_{10} > k_{e1}$). A fine tuning of the individual rates also allows one to obtain the correct signal intensities.
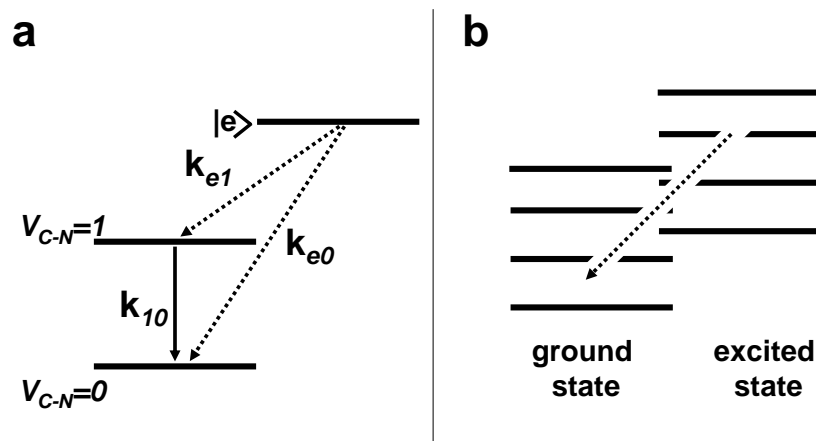
Figure 10.10: Two alternative kinetic models to account for the transient absorption changes in the C≡N stretch region. **Left.** The lower two levels represent MbCN in the electronic ground state with no or one quantum of excitation in the CN stretch mode. They are populated by the decay of an excited or unligated state $|e\rangle$ with no detectable infrared absorption in the spectral region investigated. **Right.** The red-shifted IR band (2) is due to a more weakly bound excited state, which may also be vibrationally hot (indicated by the stack of horizontal lines). Electronic relaxation and vibrational cooling take place on the same timescale.

implies an impulsive process that can realistically only be expected as a direct result of photo excitation (C=O has been observed in the v=1 state after photolysis from Myoglobin [213]), but not during the decay of an electronically excited state on a 3-4 ps timescale. Thus vibrational excitation would already have to exist in state $|e\rangle$, where it should be relatively long-lived. Upon return to the (ligated) ground state, on the other hand, vibrational excitation would have to decay rapidly (significantly faster than the lifetime of $|e\rangle$), as would be feasible following a free-to-bound transition.

As a result, ligand dissociation and subsequent recombination on a 3-4 ps timescale would appear as a consequence of an assignment of band (2) to the $v = 1 \rightarrow v = 2$ transition of heme-bound CN^- [5]. A positive transient absorption signal at 385 nm has been associated with the formation of an unligated ferric heme [204], and this feature in our UV-vis data may be viewed as supporting ligand dissociation (see below). On the other hand, we also observe that the dynamics of HbICN and MbCN are almost identical. This would not be expected, if photodissociated CN^- ligands were fully exposed to the two very different heme-pocket environments. We therefore also consider an alternative interpretation of the infrared spectra, which does not rely on the formation of an "IR-invisible" unligated state.

---

[5]In order to critically test such an assignment, we hope to soon be able to measure the anharmonicity and vibrational relaxation time T_1 of the MbC≡N stretch vibration directly by infrared pump-probe spectroscopy. The proposed mechanism is only possible if the v=1 life time of heme-bound CN^- was dramatically shortened (to ≈ 1 ps or less) with respect to the 30-120 ps observed in H_2O and D_2O [212].

Bond-weakening due to electronic excitation of heme. Although the CN molecule giving rise to band (2) may not be freely moving inside the heme pocket, its weakness (relative to the bleaching signal) and spectral position may nevertheless be due to a substantial weakening of its binding to heme. In ferrous globins the ligand stretch frequency is usually found to decrease upon binding, which is often explained by transfer of electron density from the iron d_π-orbitals (d_{xz}, d_{yz}) to the antibonding π^* orbitals of the ligand (π-backbonding). However, back-bonding is only very weak in $Fe^{II}CN$ complexes that exhibit a C≡N stretch frequency only slightly below the value for free CN^- [6]. The π-interaction between ligand and heme must be even weaker in ground state ferric CN complexes, where one expects the Fe^{III}-CN bond to be mainly due to σ donation from the molecular orbitals of CN^- [197]. Thus, transient band (2) may correspond to a C≡N stretch transition, which derives its spectral position and low oscillator strength from a weakening of the heme iron's ability to act as a σ acceptor. This would be possible in an electronically excited complex with an electron configuration that strongly influences the C≡N bond. It has recently been argued that the (d, d) excited states of heme, characterized by a ground state porphyrin with an excited iron d-electron configuration may become (thermally) populated during the relaxation of photoexcited globins [60]. A modified d-electron configuration (for example additional electron density in the d_{z^2} orbital, which may be lowered in energy as a result of an increasing Fe-CN distance) could indeed weaken the σ-bonding interaction. If we assign band (2) to an electronically excited state, heme cooling appears to be independent of electronic excitation. Indeed, d-electron excitations of the heme iron require only relatively little energy [215], and the vibrational temperature is not expected to be very different in the ground state and a (d, d) excited state. More surprising is the observation, that changes in population and shifts in the band frequencies (cooling) also take place on the same timescale (see right scheme in Fig. 10.10). While this could be coincidental, low frequency heme modes, that anharmonically couple to the CN-vibration, could be excited during the decay of the electronically excited state (or ligand recombination after photodissociation), which may then become the rate limiting step for the full thermalization of the ground state heme.

In summary, a small red-shift of the C≡N stretch vibration is observed for molecules that return to the ligated electronic ground state of MbCN after Soret excitation. This is explained by anharmonic coupling of low frequency modes of the heme with excess vibrational energy, and provides a direct measure of the time scale (3-4 ps) for vibrational energy relaxation. The time evolution of this signal also reveals a quasi-instantaneous return of approximately one quarter of the excited molecules to the ligated electronic ground state (with CN in the vibrational ground state), and a slower relaxation of the remaining species, again with a 3-4 ps time constant. The second transient absorption band, red-shifted by approximately 30 cm^{-1} from the bleaching signal could

---

[6]2058 cm^{-1} in ferrous $^{12}C^{14}N$ and 1988 cm^{-1} in ferrous $^{13}C^{15}N$ complexes of *Scapharca inaequivalvis* Hemoglobin [198]

be assigned to heme-bound CN that has become vibrationally excited, under a mechanism which would imply ligand dissociation. Alternatively band (2) could be the signature of a more weakly bound, electronically excited state of the heme, possibly characterized by a non-equilibrium population in the iron *d*-orbitals.

10.4.2   Transient signals in the Soret and Q-band region

The most important observations in the UV-visible spectra are:

1. The photoinduced dynamics is independent of the specific distal protein environments of Mb and HbI.

2. Spectral features and timescales in the response of the ferric cyanide complexes are strikingly similar to results of previous measurements on globins in the ferrous state.

The transient absorption spectra of ferrous heme complexes like MbCO, MbNO, MbO$_2$ or the unligated deoxy form of the protein were initially interpreted in terms of two independent photocycles [56].
In one photocycle ligand-photolysis leads to the formation of the unligated deoxy species in the ground state. The unligated ground state is populated via an excited state intermediate, often called Hb$_\mathrm{I}^*$. This intermediate is characterized by a short-lived (300 fs) transient absorption feature peaking at 480 nm, which is superimposed on the ground state bleaching signal in the transient spectra at very early time delays. The ligand may then rebind to the deoxy species (geminate recombination).
A second photocycle was proposed to account for the fast reformation of the ground state ligated complexes, observed within 2-3 ps after photoexcitation for ligands like oxygen and nitric oxide. A five-coordinated intermediate state (called Hb$_\mathrm{II}^*$), with the spectral characteristics of a red-shifted Soret band, was held responsible for ultrafast rebinding in this photocycle [56]. While this pioneering work did not evaluate the influence of vibrational energy relaxation on the transient absorption data, molecular dynamics simulations [216, 217], time-resolved Raman [55, 210, 218] and infrared measurements [205] all point to the importance of heme cooling after photoexcitation, which takes place on the same timescale as fast ligand dynamics (< 10 ps), and may have a strong effect on electronic spectra in the Soret and Q-band region.
Many works in the past decade have been dedicated to a clarification of these effects: by monitoring the near-infrared heme-to-iron charge transfer band III in deoxy Myoglobin Lim *et al.* deduced an electronic ground state recovery in 3.4 ± 0.4 ps and an exponential cooling of heme in 6.2 ± 0.5 ps [58]. A reinterpretation of the transient absorption data in the Soret region has recently been given in the context of absolute quantum yield measurements for ligand photo-dissociation of Myoglobin, which was found to be 100% for MbCO, 50%

for MbNO and only 28% for MbO$_2$ [61]. It was proposed that the molecules which remain six-coordinated immediately return to the vibrationally hot electronic ground state, characterized by a broadened and red-shifted Soret absorption band. Vibrational cooling on a femtosecond to picosecond timescale then accounts for the spectral dynamics previously associated with the decay of Hb$_I^*$ and Hb$_{II}^*$ [204]. A careful analysis of the optical response of deoxy Myoglobin in the Q-band region also led to the conclusion that vibrational cooling of heme is the main determinant for spectral evolution on the picosecond time scale [195].

A somewhat different view was put forward in work by Franzen *et al.* [60]. Although recognizing that the Soret absorption band may strongly broaden and shift to longer wavelengths at elevated temperatures, the authors concluded that the size of the experimentally observed red-shifts could not be reproduced by considering vibrational excitation of a ground state heme alone. Instead, Hb$_{II}^*$ was assigned to a porphyrin ground state with a thermally excited d-electron configuration (see above). In the same paper it was postulated, that the short-lived excited state Hb$_I^*$ forms independent of ligand in all ferrous heme complexes and is a signature of an iron-to-porphyrin charge transfer state. The charge transfer process, which would leave the iron in the oxidation state (III), is believed to be closely linked to the mechanism of ligand photolysis [60].

Sub-picosecond dynamics. The broad, short-lived transient absorption signal in our data on ferric MbCN strongly remind of the spectral signature associated with Hb$_I^*$ in ferrous systems. In addition, our global analysis yields a very similar ultrafast time constant of 230 fs (compared to 250 ± 80 fs in MbCO [60]). During the first picosecond after UV-excitation, there appears to be a quasi isosbestic point at 450 nm, separating the signal decay at long wavelengths from the rise of the antibleach immediately to the red of the Soret (Fig. 10.5). This may support the view, that this ultrafast dynamics involves population transfer between distinct electronic states, although we note that a narrowing and shifting Soret band (due to vibrational cooling in the electronic ground state) can also produce such a spectral feature. Relaxation of the initially excited state should occur on a similar ultrafast timescale. Unfortunately, stimulated emission is not a strong observable as for example in chlorophylls [219], but excited state absorption from intermediate electronic states may nevertheless contribute to the broad fast-decaying signal. *In a protein with a ferric heme iron, however, the assignment of an electronically excited state to an iron-to-ligand charge transfer state encounters some difficulties.* The electron transferred to the porphyrin cannot originate from an iron d-orbital as postulated in [60], but would have to be provided from outside the heme. In this case the short timescales involved seem to limit the choice of possible electron donors to either the proximal histidine or the CN$^-$ ligand. The proximal histidine has been considered to be involved in heme reduction [220]. Transfer of an electron from the CN$^-$ ligand to the heme may be more likely, since the Fe-CN bond in the ground state already involves par-

tial ligand to iron charge transfer. However, full transfer of an electron would result in a CN radical with a much stronger oscillator strength for the C≡N stretch transition. Our mid-infrared data provides no hint to the formation of such a species, which should have been easy to detect. Thus the presence of a Hb_I^*-like signal in the transient spectra of a ferric complex creates some doubt on its association with a porphyrin anion. Indeed, it has been pointed out that the 400-500 nm region is rather ill-suited for the identification of excited states in metal porphyrin complexes [221], and a very detailed investigation of the near-infrared region will be necessary to clarify this point.

Picosecond dynamics. At least after delay times longer than 0.5 ps the transient signal carries all the characteristics of a spectrally narrowing and blue-shifting product absorption band. Spectral narrowing can explain the initial increase of the positive absorption signal near 440 nm, while the increasing overlap with the ground state bleach may contribute to its subsequent decay and cause the continuous blue-shift of the zero-crossing between Soret bleach and photo-induced absorption. The interpretation of this kind of spectral evolution in terms of vibrational energy relaxation in a hot heme was first given by Rodriguez and Holten [222]. Although vibrational cooling in that work was observed in a (d, d) excited state of 4-coordinated Ni-porphyrins, it has frequently been pointed out that similar signals in ferrous heme complexes may be due to red-shifted Soret absorption of vibrationally hot molecules that are already in the electronic ground state [58, 59, 201, 204]. Here, the mid-infrared measurements help to carry out a differentiated analysis of the transient spectra in the Soret region for the ferric cyano complexes.

The time-dependent energy shift of the MbC≡N stretch vibration clearly shows that hot, ligated ground state molecules are present already very early in the dynamics and that they cool down on a 3-4 ps time scale. Ultrafast electronic ground state recovery is also indicated by the observation of the ground state Fe-His vibrational mode of ferrous MbNO at 220 cm^{-1} without measurable phase lag in femtosecond coherence measurements [223, 224]. Cooling in the electronic ground state is consistent with a red-shifted Soret absorption band, which gradually approaches the equilibrium position. In addition, however, the two possible assignments for the small, second IR absorption band implies the existence of either an electronically excited, or a dissociated state on the same time scale.

In the case of ligand dissociation, the transient spectra in the Soret region should also reflect the formation of a 5-coordinated, unligated ferric heme. The absorption spectrum of such a species, a rather broad band with a maximum at 394 nm, has recently been reported [201]. We do, indeed, observe a relatively large positive signal to the blue of the ground state Soret bleaching which decays on the required timescale and which could be attributed to an unligated heme (or a very weakly bound complex). However, similar blue-shifted transient absorption signals (although usually smaller) are observed in ferrous systems as well, and we cannot exclude that the signal in the 380 nm region is due to a strongly broadened Soret absorption of a vibrationally hot

but ligated heme in the electronic ground state.

If electronic excitation is the origin of the weak transient IR band, this may or may not influence the spectra in the Soret region. Near-infrared measurements on deoxy Myoglobin have identified an electronically excited state with a 1 ps lifetime and an absorption maximum at 830 nm [58]. On the other hand, excited states of (d, d) character in metal porphyrins give rise to red-shifted Soret and Q-absorption bands [221] due the interaction of the non-equilibrium d-electron configuration with the porphyrin π-orbitals. Thus, as proposed by Franzen *et al.* for ferrous complexes [60], the transient absorption feature near 440 nm in MbCN and HbICN could in part be due to a distorted Soret transition. Indeed, the decay of the signal at 440 nm and of the C$\equiv$N stretch bleaching signal at 2126 cm^{-1}, which provides a measure for the return of molecules to the ligated electronic and vibrational (CN) ground state, take place exactly in parallel.

In this context it is interesting to recall an earlier hypothesis [225], which links the ultrafast relaxation of the porphyrin $\pi \rightarrow \pi^*$ excitation to the simultaneous promotion of electrons from d_π to d_{z^2} or $d_{x^2-y^2}$ to d_{z^2}. Such a modification of the electron density in the heme iron d-orbitals, apart from perturbing the porphyrin absorption, may also be responsible for the weakening of the iron ligand bond, both in ferrous and in ferric complexes.

10.5 Conclusions

Combined time-resolved UV-visible and infrared measurements of MbCN and HbICN from *Lucina pectinata* have been carried out and allow a detailed analysis of the photoinduced dynamics in ferric heme complexes. The UV-visible response of the cyanide complexes is independent of the specific distal protein environments despite the fact that Hemoglobin I from *Lucina Pectinata* possesses a larger number of polar side chains than Myoglobin which would be expected to alter the dynamic behavior of a charged ligand.

At very early times, the transient spectra reveal a broad absorption feature, similar to the one associated with Hb$_I^*$ in ferrous systems. This calls for a reconsideration of a recent assignment of Hb$_I^*$ to an iron-to-porphyrin CT state [60]. It can only be maintained if either the CN$^-$ ligand or the proximal histidine are invoked as electron donors in the ferric systems.

Approximately one quarter of the molecules return to the (hot) ligated electronic ground state already within the time resolution of the IR experiment (500 fs), as evidenced by the corresponding MbC$\equiv$N stretch transition. Full recovery of the ligated electronic and vibrational ground state then takes place with a 3-4 ps time constant, which dominates the decay of both IR and UV-vis spectra at longer time delays. This is very similar to the value reported for deoxy Myoglobin [58], and much faster than for any other six-coordinated heme complex investigated so far. The infrared measurements allow for two alter-

native interpretations for the underlying mechanism. In the first case, the IR
spectra would monitor the population of heme-bound ligands with and without
vibrational excitation of the CN-stretch, and imply ligand dissociation with a
quantum efficiency of approximately 75%. Complete recombination would then
take place with a 3.6 ps time constant. Alternatively, the Fe-CN bond may
only be weakened in an electronically excited state, possibly of (d, d)-character,
leading to a down-shift of the C≡N stretch frequency. In this case, the dom-
inant 3.6 ps time constant corresponds to the excited state decay. Although
the dissociation hypothesis, that is based on a number of critical assumptions,
cannot be ruled out completely, we prefer the latter interpretation, given the
insensitivity of the transient response to the heme pocket environment.

Excited state relaxation or, alternatively, recombination is accompanied by the
vibrational cooling of a hot heme. This is evidenced by shifts of the infrared
band maxima, and takes place on the same timescale as the population decay
(3-4 ps). As a result, vibrational cooling *and* population dynamics accompany
the spectral dynamics in the Soret region. Indeed, our data suggests that both
processes may be linked by energy release upon electronic decay or recombi-
nation and should not be considered separately.

Given the similarity of the photodynamics of the ferric heme proteins inves-
tigated here, and observations made on ferrous globins, we believe that our
findings are not specific to the ferric systems. The special property of the
cyano complexes is rather, that they provide a very sensitive local probe (in
form of the CN ligand) which allows to monitor independently the population
and cooling dynamics of a 6-coordinated heme embedded in a protein.

Summary and outlook

In this work we investigated dynamical processes in three different condensed phase systems: solid hydrogen, silver nano-triangles, and heme proteins. The dynamics is in all cases triggered impulsively by the electronic photo-excitation of the sample, while the schemes used to follow the subsequent evolution are tailored on the nature of the system. In the hydrogen experiment, we detect the depletion of the fluorescence from the Rydberg A state of NO, for silver and heme proteins, we measure transient changes of the absorption spectrum.

The results obtained on solid hydrogen clearly show the presence of three characteristic timescales in the lattice relaxation, which we interpret in the framework of a bubble model. The first two (subpicosecond) timescales are associated with the *radial expansion* of the shells of H_2 molecules surrounding the dopant. In the very early stage, in particular, the dynamics involves *exclusively* the first shell of lattice neighbors around the impurity, which expands freely, without interacting with the rest of the crystal. Successively, as the perturbation propagates outwards, the interaction with further shells slows down the expansion, which finally ends after 800 fs. The third timescale is associated with a much slower (10 ps) local re-organization of the crystal around the excited center. We also measure a weak recurrence in the fluorescence depletion signal at long time delays, which we interpret as an elastic response of the medium, in analogy with similar features reported for doped solid neon and argon. We do not observe differences in the ultrafast dynamics in solid normal and para hydrogen, which justifies neglecting all internal degrees of freedom of the host molecules, in our simplified bubble model.
We have also investigated the structural relaxation using classical molecular dynamics simulations. These calculations reproduce very well the principal static and dynamic properties observed in the experiment. In particular, they identify and characterize the three timescales of the dynamics. The calculations show a rapid dissipation of the excess energy at short times, in line with the bubble-model interpretation of the experiment; they also confirm that the quantum nature of the host plays no role during the initial ultrafast step of the relaxation.

The second system investigated consists of triangular silver nanoplates, prepared with a novel photo-chemical technique developed in our laboratory [44]. This technique allows to control the size, shape and optical response of the

particles, by varying the color of the light used to drive their growth. We have focused our spectroscopic investigation on the size oscillations of the particles triggered by the impulsive heating of the metal lattice. The period of oscillation that we measure compares very well with the theoretical value, calculated with a classical elastodynamic model. The phase of the oscillations, with respect to the trigger pulse, contains information on the excitation process and the size homogeneity of the sample. To disentangle these two effects, we have developed a model, that accounts for the size distribution of the particles. In this way we succeed in reproducing our experimental measurement, both spectrally and temporally. The results indicate that (1) the excitation process is purely thermal and does not have any contribution from electron pressure, and (2) for non-spherical particles, even a relatively low size-dispersion may affect significatively the character of the phase in the oscillations. The same calculation yields also an estimate for the homogeneous width of the surface plasmon band of the particles, and suggests that the two decay constants observed in the dynamics are related to energy dissipation to the solvent, and not to inhomogeneous effects (de-phasing).

In the third part of the work, we have reported the results of a *comparative study* on ligand dynamics of two ferric heme complexes: CN-bound Myoglobin and Hemoglobin I, performed with broad-band UV-visible spectroscopy.
The UV-visible response is very similar in the two systems, and, therefore, independent from the specific distal protein environment. The transient spectral features, observed at short times, are similar to those reported for ferrous systems. This finding calls for a critical reconsideration of their common assignment to a metal-to-porphyrin charge transfer state. A complementary set of infrared measurements [7] indicates that upon photo-excitation of the porphyrin, the Fe-CN bond is weakened but likely not broken, and that no complete dissociation of the ligand takes place, in agreement with the insensitivity of the transient visible response to the heme pocket environment. Finally, we remark that vibrational cooling and population dynamics accompany the spectral evolution in the Soret region, and cannot be considered as separate processes. We believe that our findings are general and not limited to ferric systems.

---

[7]Performed in the framework of a collaboration with Dr. Jan Helbing at the University of Zürich [52].

This report gives a few examples of the immense potential of time-resolved spectroscopy to address diverse dynamical phenomena in a wide range of condensed phase systems. It illustrates how, on a sub-picosecond timescale, the conventional distinction between physics, chemistry and biology becomes more fuzzy, and the very same technique, set-up (and Ph.D student!) can be used to address issues that, at first sight, have little in common with one another. In addition, this versatility leads to the fruitful exchange of methods between different fields of research: for example, the global techniques applied to analyze the data on silver nanoparticles are commonly used by the bio-physics community to interpret the complex transient spectra measured on biological samples [60, 189].

Each of the investigations presented in this thesis answers important questions and raises new ones, opening the possibility for future developments.

Clarifying the exact mechanisms of energy re-distributions in solid hydrogens and, in particular, the nature of the weak recurrence observed at long-time delays is an important challenge for future investigations. The comparison of the present results with similar experiments in solid ortho-deuterium and in liquid hydrogens, performed with a comparable time-resolution, may help understanding quantitatively how temperature, mass and structure of the surrounding environment influence the local relaxation.
We believe that the present work can stimulate the development of simulations of *dynamical processes in quantum systems*, based on a rigorous approach, which are still lacking at present. In this respect, our study allows to compare with simulations both *equilibrium* and *dynamical* features [8]. Therefore, it provides a natural starting point to develop new computational approaches from the existing ones [28, 29, 31, 32].

The characterization of the silver nanoparticles should be completed looking in more details at short time delays, where both the electron-electron and the electron-phonon scattering processes take place. This goal can be achieved with the use of a different pump-probe scheme, based on the output of two non-collinear optical parametric oscillators [226]. Such an experiment will also be appropriate to verify the possible presence of mechanical oscillations at short times, associated with vibrational modes of higher frequency [164], that may not have been detected in the present study.
Characterizing the particles optical response is a prerequisite for a diverse number of applications that we can envisage for these particles. The field enhancement localized at the tips may be exploited by fixing one particle on the tip of an apertureless near-field microscope, leading to a considerable improvement of the spatial resolution of the apparatus. The same property can be used to increase the efficiency of resonance energy transfer between a nanoparticle attached at the tip, and the neighboring molecules on a substrate, with many fascinating implications and possible developments [227–229].
The control over the spectral position of the surface plasmon resonance of the particles, simply by varying the illumination conditions during their growth,

---

[8]Static absorption / emission spectra and time-resolved transients.

allows to synthesize nano-probes that are optically "tunable" in the visible and near-infrared region. One could also envisage to activate their surface, and attach them to proteins, in a way that they could act as ultrafast local heating sources, that can be optically excited to trigger, for instance, protein-folding reactions.

In the heme proteins experiment, I believe that the key-point resides on its very concept: the photo-dynamics in complex systems like the biological ones is too rich to be analyzed without comparative studies, that allow to separate the various contributions to the experimental signal. Moreover, the possibility to study in parallel how two independent observables of the system (the electronic levels of the porphyrin and the vibrations of the ligand) respond to the same perturbation, makes the assignments of the spectroscopic features more sound and reliable. I think that such a broad approach is particulary effective for investigating the complexity of large bio-systems.

Appendix A

Probe power dependence in the fluorescence depletion transients

During the time-resolved measurements described in Chap. 6, particular care was taken to check the linearity in the probe power of the depletion signals. A typical series of depletion scans obtained varying the probe intensity I_0 over more than one order of magnitude is presented in Fig. A.1. The scans corresponding to I_0 and 2.5 I_0 are linear in the probe, while the third one clearly is not, pointing to a saturation of the depletion process. In the right panel of Fig. A.1, the traces corresponding to 36 I_0 and 2.5 I_0 have been normalized at their peak value, and plotted on top of each other. We observe a relatively lower depletion level of the plateau in the case of the linear transient (2.5 I_0). This 10% difference in the relative level at 1 - 2 ps delay should be compared with the plots in Fig. 6.7. In that series, the initial peak is the feature growing with respect to the flat plateau as the probe power is increased. This behavior can be explained considering the position of the probe windows corresponding to the two series (Fig. 6.4). The 1280 nm wavelength is sampling the early stages of the dynamics, while the 1160 nm probe samples directly the relaxed configuration of the bubble. If we increase the power of the probe pulse, the tails of the gaussian observation windows may become intense enough to deplete the wavepacket, even when the latter happens to be in regions far from their center. Therefore, while the signal probed by the central part of the window gets easily saturated, the contributions from the tails keep on growing even at higher probe intensities, and eventually modify the shapes of the transients. This characteristic behavior is reported in Fig. A.2, which shows a comparison of the depletion levels for two wavelengths sampling the beginning of the dynamics (1300 and 1280 nm), and a third probe wavelength (1185 nm) sampling

167
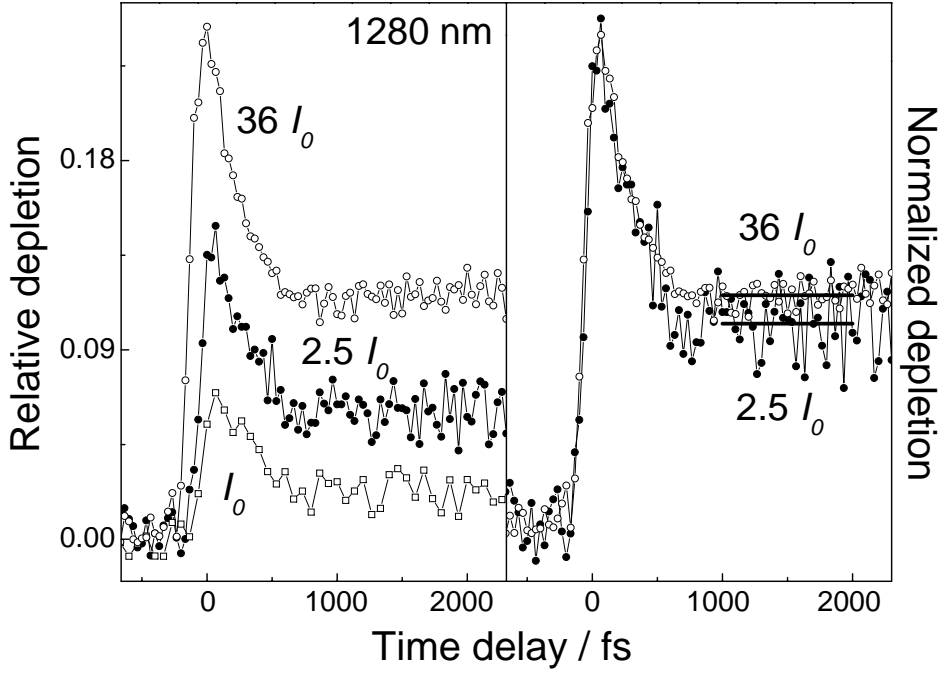
Figure A.1: Effect of probe beam intensity on the signal shape at 1280 nm. **Right.** Depletion signals corresponding to probe intensities 2.5 I_0 and 36 I_0 normalized at the peak value. **Thick lines.** Average value of the plateau for the two different probe intensities (2.5 I_0 and 36 I_0).

the final configuration of the system (Fig. 6.4). The plotted quantities correspond to the depletion level measured at the maximum of the short-time peak, and at a delay of 3 ps, normalized to the corresponding weakest value of the series. The probe intensities are calculated correcting the average ADC counts recorded for each different scan by the response curve of the IR photodiode. The values of the peaks (open triangles) in the transient at 1300 nm deviates from the linearity around 200 probe counts, while the long time level increases almost linearly up to 400 counts. At the opposite extreme, we note that in the 1185 nm plot, even if both quantities deviate very early from the linearity, the relative intensity of the peak increases with respect to the long time depletion even for high probe counts. Finally, an absolute comparison of the saturation behavior observed for several different probes is shown in Fig. A.3. The blue transients deviate from the linear regime at very low probe intensities. In the saturation regime, they reach depletion levels as high as 60%. The transients probed by the redmost wavelengths deviate from linearity at much higher probe intensities, and exhibit an overall weaker depletion level.

The explanation of the saturation of the process resides in the experimental conditions. With a simple calculation, we can compute the number of excited centers in the sample. We assume a crystal thickness of 70 μm, a pump focal spot of about 40 μm, and a concentration of NO molecules with respect to the H_2 molecules of $\sim 10^{-3}$ (upper estimate). Supposing now that the impurities occupy exclusively substitutional sites [35], we can predict that in the volume excited by the laser there are about $2.6 \cdot 10^{12}$ NO molecules. Considering a typ-
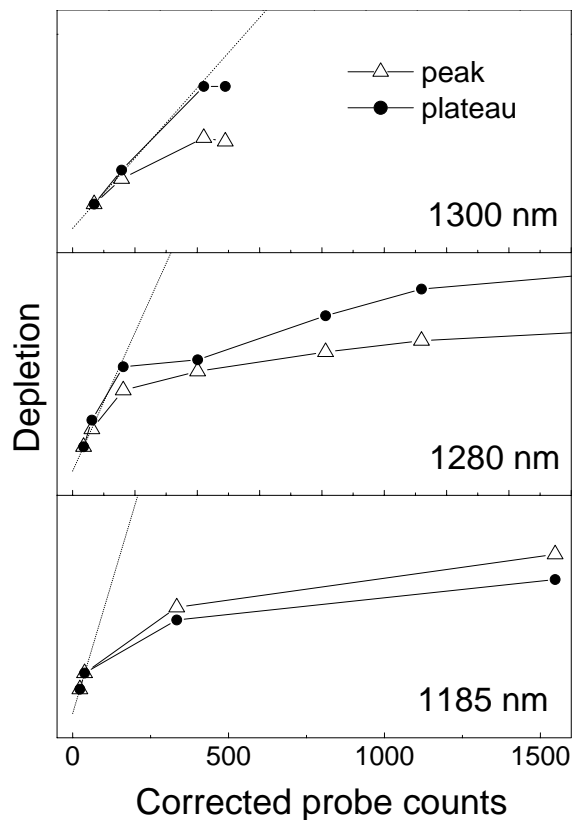
Figure A.2: Different saturation properties of the depletion corresponding to the peak at short time delay (**triangles**) and the plateau signal measured at 2 ps delay (**filled circles**) for different probe wavelengths. The quantities have been normalized to the first value of each series.
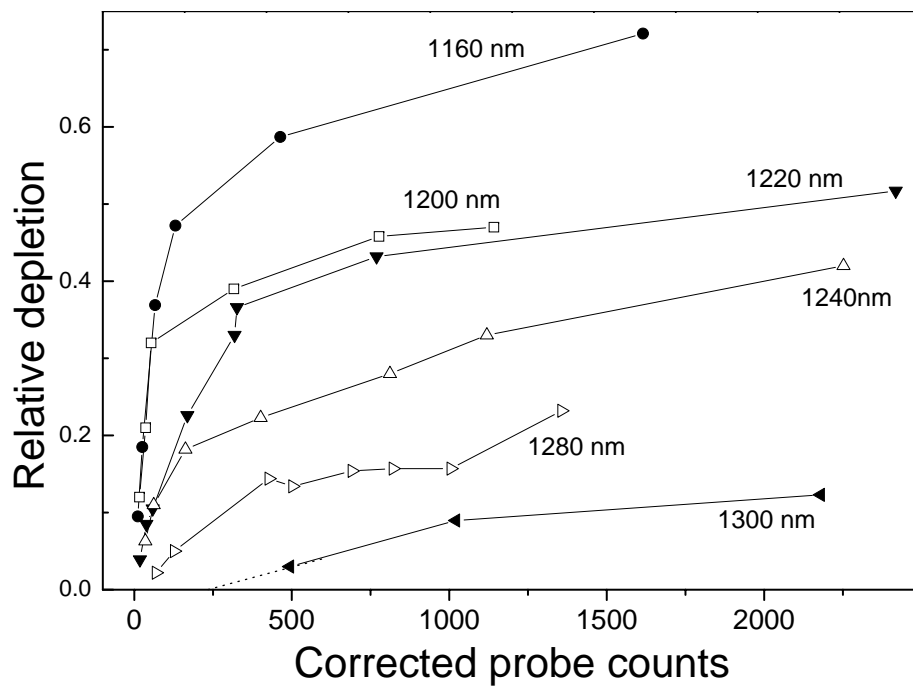
Figure A.3: Probe saturation curves at different probe wavelengths. The probe counts at different wavelengths are corrected by the photodiode response curve.

ical excitation energy of 1 μJ at 400 nm, and a probe energy of 0.1 μJ at 1200 nm, we count $2 \cdot 10^{12}$ pump and $6 \cdot 10^{11}$ probe photons, respectively. Taking into account that the excitation is a non-resonant two photon transition, likely just a small fraction of the pump photons will meet the conditions for excitation (§ 4.2.1), and therefore the probe photons will easily saturate the transitions to the C and D states already at much lower probe intensities.
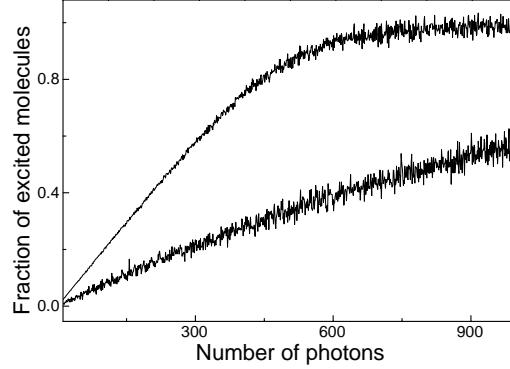
Figure A.4: Monte Carlo simulations of the saturation of the transients. In the simulations the number of molecules that can be depleted is set to 20 times less than the available probe photons. The upper curve is calculated considering a probability to deplete a molecule transferring the A state population to C and D 10 times greater than in the case of the lower curve. The relative difference in the cross sections of the two curves is estimated from the intensities of the depletion signals in the linear regime of probe energies shown in Fig. A.3.

The depletion probability as a function of the probe photons has been estimated developing a very basic *zero-dimensional* Monte Carlo model. We consider that each photon has a given probability pr to excite a molecule. The probability $p_{\bar{n}}$ to excite the $\bar{n}^{\text{th}}$ molecule in the focal spot depends on the number of molecules that the photon encounters before reaching it:

$$p_{\bar{n}} = (1 - \sum_{n=1}^{\bar{n}-1} p_n) \cdot pr \ . \tag{A.1}$$

Consequently, the first probe photon has a probability $P_1 = \sum_{n=1}^{N} p_n$ to deplete one of the N excited molecules of the sample. If the first photon succeeds in depleting a molecule, the following one has a decreased total probability, $P_2 = \sum_{n=1}^{N-1} p_n$. And so forth for all the successive photons.

The curves displayed in Fig. A.4 correspond to the results of this simple calculation in the case that the number of molecules that can be depleted (N) is 20 times smaller than the number of available probe photons. The upper curve corresponds to a probability of depletion pr 10 times greater than in the case of the lower curve. This relative difference in the cross sections associated to the two curves is estimated from the intensities of the depletion signals in the linear regime of probe energies, shown in Fig. A.3. The traces in the figure can account for the qualitative differences in the probe saturation properties at different wavelengths (Fig. A.3).

Appendix B

Transient absorption spectroscopy

The technical aspects shared by the experiments described in Chap. 9 and 10 are discussed in this short appendix.

Multi-wavelength transient absorption is a very versatile tool to investigate dynamical processes, its unique drawback resides in the fact that the large amount of information that can be simultaneously gathered contains many different contributions, which is not always straightforward to isolate.

After that the pump pulse has induced some changes in the sample, the intensity of a spectrally large probe beam is monitored as a function of the wavelength, and of the time-delay with respect to the pump pulse. The transmission of the probe can be modulated by different competing processes, including: ground state bleaching, stimulated emission and excited state absorption. Each of these processes has a sign (induces a positive or negative variation in the transmission of the probe beam) and a peculiar time-dependence. A complete understanding of the dynamics of a system can be normally achieved exclusively applying global techniques of analysis to the multidimensional data sets measured in the experiment.

B.1   Experimental

Probe pulse generation.   The broad-band probe pulses were produced by focusing a small portion of 800 nm light into a 2 mm thick CaF_2 window to generate white light continuum with a low wavelength cutoff near 390 nm. In the heme proteins experiment, measurements in the 360 - 400 nm region were
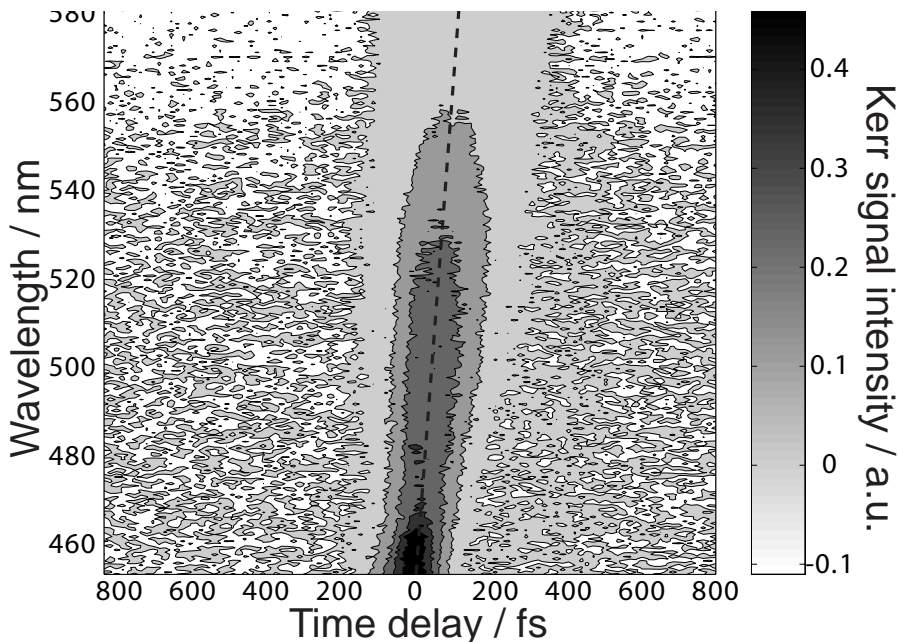
Figure B.1: Contour plot of the Kerr signal obtained in pure water. **Dotted line.** Linear interpolation, corresponding to 1.25 fs/nm, used to determine the white light chirp of the set-up and correct the time-resolved spectra.

carried out with white light produced from frequency-doubled 400 nm laser pulses.

The white-light was focused onto the sample using *all-reflective optics*, and the chirp inside the sample cell was determined by measuring the laser-induced Kerr signal of the solvent, as reported in Fig. B.1. In the bluemost spectral region investigated (380 - 450 nm), the chirp was typically of the order of ∼1.3 fs/nm and close to linear [1]. Around 800 nm the effect was considerably less present, given the weaker group velocity dispersion for pulses in the near-IR region.

White light detection.   White-light pulses are generated by non linear processes in the radiation-matter interaction [126], hence the resulting shot-to-shot intensity fluctuations are considerably more important than those of the laser source. For probing changes in the absorption below 10^{-3} ΔOD is mandatory to correct each white-light shot with a reference pulse.

To this end, as illustrated in Fig. B.2, the probe pulse train was split into two branches of equal intensity by a beam-splitter, and guided along two parallel optical paths. One branch (*probe*) was overlapped with the pump pulse in the sample cell. The second one (*reference*) was vertically displaced by 1 cm and transmitted through the sample in a different position. Both beams were then focussed onto the entrance slit of a monochromator (CHROMEX, 250IS) and

---

[1]The substitution of lenses and other refractive components with all-reflective optics, i.e. aluminum coated parabolic mirrors, greatly reduced the chirp on the probe pulses. For comparison, white light pulses generated on the same laser system and focussed on the sample by a conventional lens were associated to a chirp of the order of 12 fs/nm [230].

dispersed along two parallel planes by a 600 grooves/nm grating blazed at 750 nm. On the image plane at the exit of the monochromator, the two spectra where reflected on a vertical plane by the opposite sides of a prism, and finally detected by two silicon photodiode arrays (HAMAMATSU, S3901-256Q), as illustrated in the enlarged detail in Fig. B.2.

The detection was made on a single shot basis, synchronizing the diode arrays start-signal with the trigger from the regenerative amplifier. Contrary to the scheme of the fluorescence depletion experiment, the synchronized chopper, operating at half of the amplifier repetition rate, was placed in the optical path of the pump beam. The data from the diode arrays were transferred to a personal computer via a fast acquisition card (NATIONAL INSTRUMENTS, SCB-68).

Signal calculation   The transient absorption signal $A_\tau(\lambda)$ at a given pump-probe time-delay τ was calculated as

$$A_\tau(\lambda) = -\log_{10}\left(\frac{I(\lambda) - I_0(\lambda)}{I_R(\lambda) - I_{R0}(\lambda)}\right)_{\text{pmp}} + \log_{10}\left(\frac{I(\lambda) - I_0(\lambda)}{I_R(\lambda) - I_{R0}(\lambda)}\right)_{\text{unpmp}} . \quad \text{(B.1)}$$

In the expression, $I(\lambda)$ and $I_R(\lambda)$ correspond to the spectral intensities detected by the probe and reference diode array, the index 0 indicates the background measurement recorded with both probe and reference beams blocked at the beginning of each time-scan for every channel, and the subscript *pmp* and *unpmp* indicate the presence or not of the pump pulse on the sample. Typically, each data point was calculated as the average of 1000-2000 shots over 3-4 successive scans. With these figures, the sensitivity of the measurement was typically of the order of 10^{-4} ΔOD. The intensity of the pump beam was recorded as well on a single shot basis, using the same scheme and acquisition electronics described for the fluorescence depletion experiment in § 4.3.2. Nevertheless, the data presented in this work were not corrected for the shot-to-shot fluctuations of the pump pulse.

Pump beam

800 nm   800 / 400 nm

Delay line

Diaphragm
Short f lens
Shaded filter
CaF_2 plate

Phase-locked
chopper 500Hz

Reference

Probe

White light

Beam
splitter

Diode array

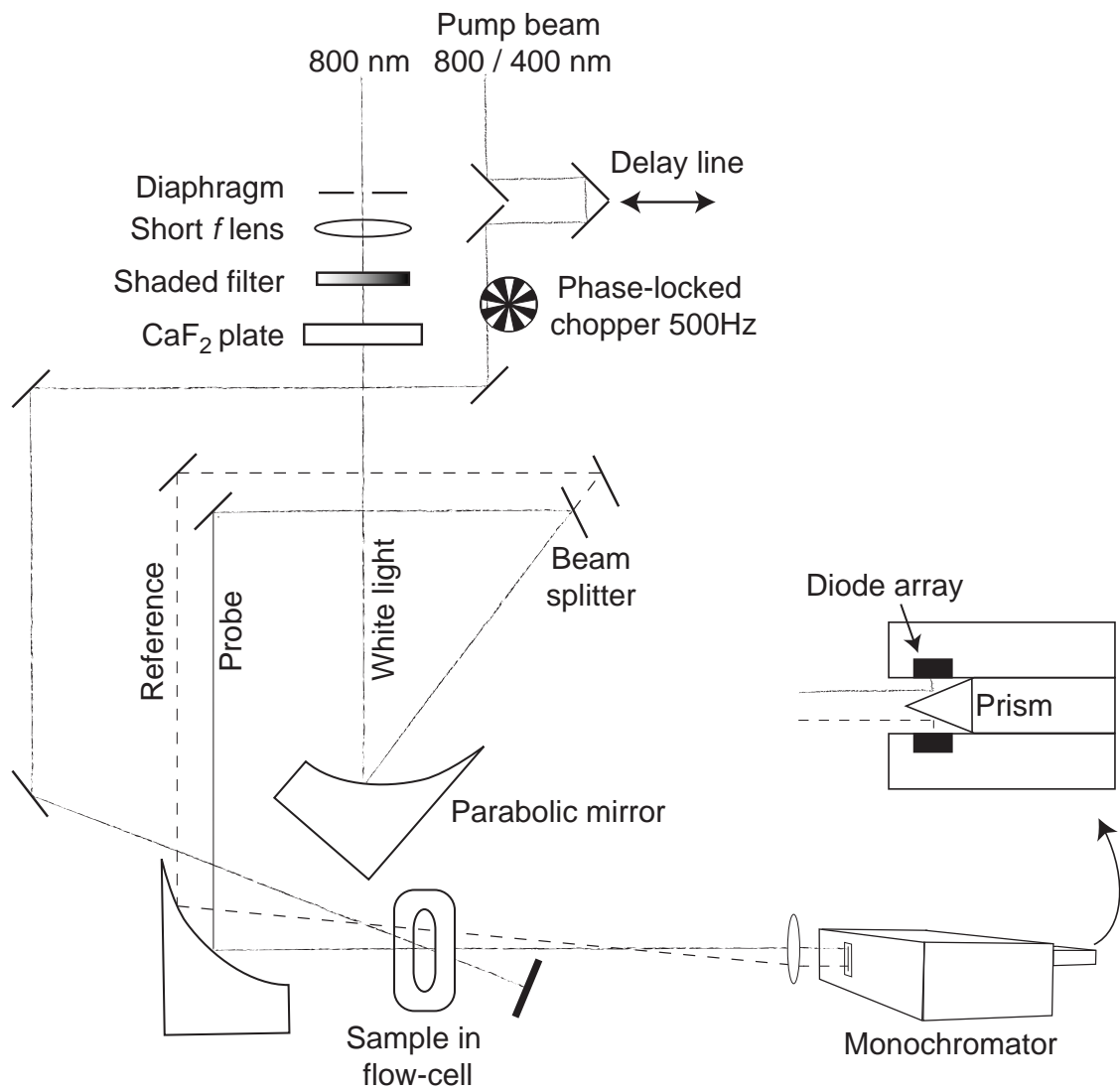Prism

Parabolic mirror

Sample in
flow-cell

Monochromator

Figure B.2: Schematic view of the transient absorption set-up.

Appendix C

Global analysis of multiway data

The term global analysis refers to a simultaneous analysis of all measurements contained in a multiway dataset. Time-resolved transient-absorption spectra are a typical example of two-way measurements, where the two ways (i.e. independent variables) correspond to wavelength, and time-delay between pump and probe.

In the present work, the dimensions of a typical experimental scan were of the order of 256×300 data points. The use of global techniques on data sets of these dimensions can be very useful, allowing, for instance, to separate information from stochastic noise, and to verify different dynamical scenarios by simultaneous fitting of all the data.

C.1 Singular value decomposition

Singular value decomposition (SVD) is a procedure deeply rooted in the theory of linear algebra, which represents, in first instance, a technique to determine the *rank* of matrix corrupted by random noise. Additionally, it results a powerful tool for data reduction and noise suppression [188]. In this respect, it can be applied when a non linear least-square global fit to the data is needed, in order to reduce the dimensionality of the data, and save computational resources.

Suppose that the $m \times n$ matrix $A(\lambda_i, t_j)$ contains the transient absorption data as a function of a discrete set of wavelengths λ_i and time-delays t_j. Assuming additive noise, A can be represented by the sum

$$A = \tilde{A} + \Xi \, , \tag{C.1}$$
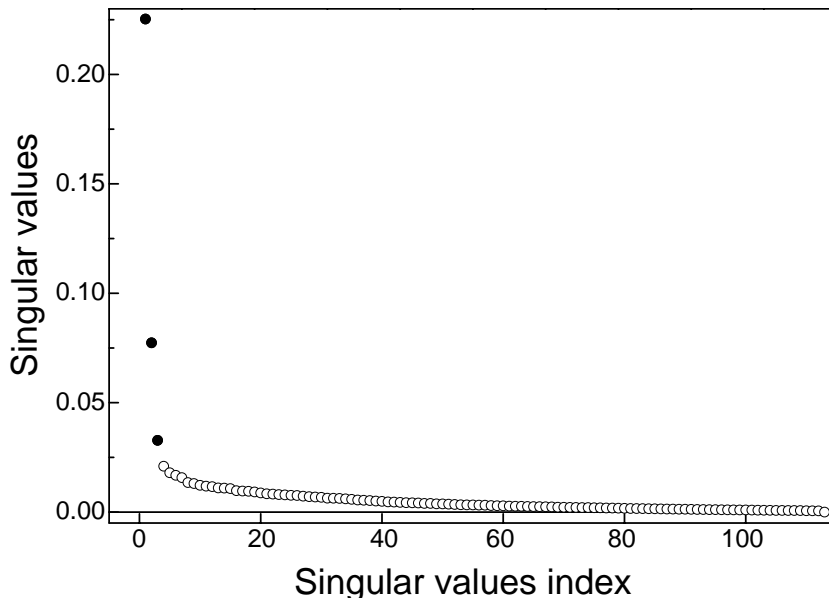
Figure C.1: **Circles.** Singular values obtained applying the decomposition of Eq. C.2 on the dataset presented in Fig. 9.10. **Filled circles.** Significant components retained for the analysis.

the first element contains the information about the spectral evolution of the system, while Ξ denotes a normally distributed stochastic disturbance with zero mean [1]. The SVD approach consists in decomposing A into the product of three matrices

$$A = USV^T .\tag{C.2}$$

U and V are orthogonal matrices of dimensions $m \times m$ and $n \times n$, respectively. Their columns contain the left and right singular vectors. Limiting ourselves to the case of transient absorption data, we can identify the columns of U as basis spectra, and the rows of V^T as basis time courses [60]. The diagonal elements of the $m \times n$ matrix S are the singular values $s_i = S_{ii}$. They correspond to the square roots of the eigenvalues of the second moment matrices $A^T A$ or AA^T, sorted in descending order [231].

A typical outcome of the transformation C.2 is presented in Fig. C.1, which displays the singular values extracted from the data set in Fig. 9.10. We clearly identify the first three values as distinct from the rest. They are supposed to be associated to the most prominent spectral and kinetic information of the data set.

In the case of a completely noise-free matrix, characterized by n *linearly independent* components, we expect the number of non-zero singular values to be equal to the rank of the matrix n: $s_1 \geq s_2 \geq ... \geq s_n \geq s_{n+1} = 0$. In the presence of noise, the singular values and the singular vector pairs $\{U_i, V_j^T\}$ result perturbed. *Assuming that the noise is small in comparison to the signal,* we can still discriminate between the singular vector pairs carrying dynamical information on the system, and those associated to noise. The number of the linearly independent significant components, in fact, can be determined from

---

[1]Note that possible systematic errors are not included in this description

the number of singular values which differ appreciably from the noise.

Calling $s_{\bar{i}}$ the greatest singular value associated to the noise [2], a linear algebra theorem ensures that the perturbation is negligible for all the vectors pairs with label $i < \bar{i}$, such that $s_i - s_{i+1} \gg s_{\bar{i}}$ [232].

It should be noted that the basis spectra U_i and time courses V_i^T identified by this procedure in general are not associated to any specific species or dynamics. The physical information of interest should be extracted constructing linear combinations of these orthogonal vectors through appropriate kinetic models, as described in § C.2.

As already mentioned, the SVD can be used as a tool for data reduction and suppression of the random noise. The original dataset can be projected upon the significant subset of the singular vectors setting $s_i = 0$ for $i \geq \bar{i}$ in Eq. C.2. Particular care should be taken when applying this procedure, in fact it can result in a loss of information in the case that $s_i - s_{i+1} \simeq s_{\bar{i}}$. An useful check is to ensure that the matrix of the residuals, obtained subtracting the projection from the original dataset, is structureless, eventually controlling the distribution of the singular values of this matrix [233]. For time-resolved data, the presence of any feature out of the noise statistics around time zero in a trace V_i^T is an unambiguous indication that significant information are carried by this component, and thus it can not be neglected.

C.2   Global fitting

As mentioned in the preceding section, the vector pairs from the SVD analysis *a priori* do not carry any specific physical information about the evolution of the system. However, we can test specific kinetic models on this reduced set and, eventually, obtain meaningful linear combinations of these elements. If we suppose, for example, that the kinetic response of a system can adequately be described by the sum of K functions (see § C.3):

$$\sum_{k=1}^{K} f_k \ , \tag{C.3}$$

we can try to fit *simultaneously* all the N significant time-courses V_i^T retained from the SVD analysis, applying a standard algorithm for the minimization of the χ^2 value. The coefficients $c_{i,k}$, obtained by the fitting,

$$V_i^T \simeq \sum_{k=1}^{K} c_{i,k} f_k \ , \tag{C.4}$$

can be used to calculate the spectra T_k associated to the different kinetic components present in the dynamics:

$$T_k = \sum_{i=1}^{N} s_i c_{i,k} U_i \ . \tag{C.5}$$

---

[2] The value of $s_{\bar{i}}$ can be considered as un upper bound for the perturbation [188].

These spectra show the amplitude of each kinetic component playing a *visible* role in the evolution of the system. An example of this analysis is shown in Fig. 10.7, and in the related discussion. It should be noted that alternative algorithms have recently appeared in literature, for example the variable projection algorithm, which allows to apply the global fitting procedure to very large *unreduced* dataset [188].

C.3   Model functions

Time-resolved transient absorption-traces spectra are usually fitted by a sum of K exponential functions convoluted with the instrument response function of the system, $R(t)$. This latter is represented by a gaussian of FWHM Δ. Its convolution with a decaying exponential is an analytical expression in the form:

$$e^{-\alpha_k t} \bigoplus R(t) = \frac{1}{2} e^{-\alpha_k t} e^{\alpha_k (\mu + \alpha_k \frac{\tilde{\Delta}^2}{2})} \left[1 + \mathrm{erf} \left(\frac{t - \left(\mu + \alpha_k \tilde{\Delta}^2 \right)}{\sqrt{2}\tilde{\Delta}} \right) \right] \, , \qquad \text{(C.6)}$$

where $\tilde{\Delta} = \Delta(2\sqrt{2})$ and the parameters α_k, μ represent, respectively, the decay rate and the distance from the origin [188].

Bibliography

[1] K. Murakami, H. C. Gerritsen, H. Vanbrug, F. Bijkerk, F. W. Saris, and M. J. Vanderwiel. Pulsed-laser irradiated silicon studied by time-resolved x-ray absorption (90-300 ev). *Physical Review Letters*, 56(6):655–658, 1986.

[2] M. Nisoli, S. DeSilvestri, O. Svelto, R. Scholz, R. Fanciulli, V. Pellegrini, F. Beltram, and F. Bassani. Single-electron subpicosecond coherent dynamics in kbr f centers. *Physical Review Letters*, 77(16):3463–3466, 1996.

[3] T. Shibata, S. Iwai, T. Tokizaki, K. Tanimura, A. Nakamura, and N. Itoh. Femtosecond spectroscopic studies of the lattice-relaxation initiated by interacting electron-hole pairs under relaxation in alkali-halides. *Physical Review B*, 49(18):13255–13258, 1994.

[4] T. Tokizaki, T. Makimura, H. Akiyama, A. Nakamura, K. Tanimura, and N. Itoh. Femtosecond cascade-excitation spectroscopy for nonradiative de-excitation and lattice-relaxation of the self-trapped exciton in nacl. *Physical Review Letters*, 67(19):2701–2704, 1991.

[5] G. Zimmerer. *Excited-state spectroscopy in solids*. Soc. Italiana di Fisica, Bologna - Italy, 1987.

[6] E. M. Bringa and R. E. Johnson. Electronic sputtering of solid o-2. *Surface Science*, 451(1-3):108–115, 2000.

[7] A. H. Zewail. Femtochemistry: Atomic-scale dynamics of the chemical bond using ultrafast lasers - (nobel lecture). *Angewandte Chemie-International Edition*, 39(15):2587–2631, 2000.

[8] A. Douhal and J. Santamaria. *Femtochemistry and Femtobiology V*. World Scientific, Singapore, 2001.

[9] M.M Martin and J.T. Hynes. *Femtochemistry and Femtobiology VI*. Elsevier, Amsterdam, The Netherlands, 2004.

[10] I. Norman and G. Porter. Trapped atoms and radicals in a glass cage. *Nature*, 174(4428):508–509, 1954.

[11] W. Kaiser. *Science*, 233:1276, 1986.

[12] A. H. Zewail. Chemistry at the uncertainty limit. *Angewandte Chemie-International Edition*, 40(23):4371–+, 2001.

[13] M.L. Klein and J.A. Venables. *Rare gas solids*. Academic Press, London, 1977.

[14] I. F. Silvera. The solid molecular hydrogens in the condensed phase - fundamentals and static properties. *Reviews of Modern Physics*, 52(2):393–452, 1980.

[15] J. van Kranendonk. *Solid Hydrogen*. Plenum Press, New York, 1983.

[16] B.I. Verkin. *Handbook of properties of condensed phases of hydrogen and oxygen*. Hemisphere Publishing, New York, 1991.

[17] P.C. Souers. *Hydrogen Properties for Fusion Energy*. University of California Press, Berkley and Los Angels, California U.S.A., 1986.

[18] F. Stienkemeier, F. Meier, A. Hagele, H. O. Lutz, E. Schreiber, C. P. Schulz, and I. V. Hertel. Coherence and relaxation in potassium-doped helium droplets studied by femtosecond pump-probe spectroscopy. *Physical Review Letters*, 83(12):2320–2323, 1999.

[19] A. V. Benderskii, J. Eloranta, R. Zadoyan, and V. A. Apkarian. A direct interrogation of superfluidity on molecular scales. *Journal of Chemical Physics*, 117(3):1201–1213, 2002.

[20] F. Vigliotti, L. Bonacina, and M. Chergui. Structural dynamics in quantum solids. ii. real-time probing of the electronic bubble formation in solid hydrogens. *Journal of Chemical Physics*, 116(11):4553–4562, 2002.

[21] S. Tam, M. Macler, M. E. DeRose, and M. E. Fajardo. Electronic spectroscopy of b atoms and b-2 molecules isolated in para-h-2, normal-d-2, ne, ar, kr, and xe matrices. *Journal of Chemical Physics*, 113(20):9067–9078, 2000.

[22] C. Callegari, J. Higgins, F. Stienkemeier, and G. Scoles. Beam depletion spectroscopy of alkali atoms (li, na, k) attached to highly quantum clusters. *Journal of Physical Chemistry A*, 102(1):95–101, 1998.

[23] T. Momose, H. Hoshina, N. Sogoshi, H. Katsuki, T. Wakabayashi, and T. Shida. Tunneling chemical reactions in solid parahydrogen: A case of cd3+h-2 -¿ cd3h+h at 5 k. *Journal of Chemical Physics*, 108(17):7334–7338, 1998.

[24] T. Momose, M. Miki, T. Wakabayashi, T. Shida, M. C. Chan, S. S. Lee, and T. Oka. Infrared spectroscopic study of rovibrational states of methane trapped in parahydrogen crystal. *Journal of Chemical Physics*, 107(19):7707–7716, 1997.

[25] T. Momose, H. Katsuki, H. Hoshina, N. Sogoshi, T. Wakabayashi, and T. Shida. High-resolution laser spectroscopy of methane clusters trapped in solid parahydrogen. *Journal of Chemical Physics*, 107(19):7717–7720, 1997.

[26] M. E. Fajardo. Matrix-isolation spectroscopy of metal atoms generated by laser ablation .2. the li/ne, li/d2, and li/h2 systems. *Journal of Chemical Physics*, 98(1):110–118, 1993.

[27] A. V. Danilychev, V. E. Bondybey, V. A. Apkarian, S. Tanaka, H. Kajihara, and S. Koda. Photodynamics in oxygen doped solid deuterium. *Journal of Chemical Physics*, 103(10):4292–4299, 1995.

[28] Y. M. Ma, T. Cui, and G. T. Zou. Effects of pressure on the trapping site structures and absorption spectra of li in solid h-2: A path integral monte carlo study. *Journal of Chemical Physics*, 114(7):3092–3104, 2001.

[29] J. R. Krumrine, S. M. Jang, M. H. Alexander, and G. A. Voth. Quantum molecular dynamics and spectral simulation of a boron impurity in solid para-hydrogen. *Journal of Chemical Physics*, 113(20):9079–9089, 2000.

[30] Z. Li and V. A. Apkarian. Impurity rotations in quantum versus classical solids: O-2 in solid hydrogens. *Journal of Chemical Physics*, 107(5):1544–1550, 1997.

[31] E. Cheng and K. B. Whaley. Theoretical calculations of zero-temperature absorption spectra of li in solid h-2. *Journal of Chemical Physics*, 104(9):3155–3175, 1996.

[32] D. Scharf, G. J. Martyna, D. H. Li, G. A. Voth, and M. L. Klein. Nature of lithium trapping sites in the quantum solids para-hydrogen and ortho-deuterium. *Journal of Chemical Physics*, 99(11):9013–9020, 1993.

[33] M. E. Fajardo. Limitations on stored energy densities in systems of separated ionic species. *Journal of Propulsion and Power*, 8(1):30, 1992.

[34] R. Zadoyan, J. Almy, and V. A. Apkarian. Lattice dynamics from the 'eyes' of the chromophore - real-time studies of i-2 isolated in rare gas matrices. *Faraday Discussions*, (108):255–269, 1997.

[35] F. Vigliotti, M. Chergui, M. Dickgiesser, and N. Schwentner. Rydberg states in quantum crystals no in solid h-2. *Faraday Discussions*, (108):139–159, 1997.

[36] U. Kreibig and L. Genzel. Optical-absorption of small metallic particles. *Surface Science*, 156(JUN):678–700, 1985.

[37] A. D. McFarland and R. P. Van Duyne. Single silver nanoparticles as real-time optical sensors with zeptomole sensitivity. *Nano Letters*, 3(8):1057–1062, 2003.

[38] J. C. Riboh, A. J. Haes, A. D. McFarland, C. R. Yonzon, and R. P. Van Duyne. A nanoscale optical biosensor: Real-time immunoassay in physiological buffer enabled by improved nanoparticle adhesion. *Journal of Physical Chemistry B*, 107(8):1772–1780, 2003.

[39] J. P. Kottmann, O. J. F. Martin, D. R. Smith, and S. Schultz. Field polarization and polarization charge distributions in plasmon resonant nanoparticles. *New Journal of Physics*, 2:271–279, 2000.

[40] J. P. Kottmann, O. J. F. Martin, D. R. Smith, and S. Schultz. Dramatic localized electromagnetic enhancement in plasmon resonant nanowires. *Chemical Physics Letters*, 341(1-2):1–6, 2001.

[41] K. L. Kelly, E. Coronado, L. L. Zhao, and G. C. Schatz. The optical properties of metal nanoparticles: The influence of size, shape, and dielectric environment. *Journal of Physical Chemistry B*, 107(3):668–677, 2003.

[42] J. P. Kottmann, O. J. F. Martin, D. R. Smith, and S. Schultz. Non-regularly shaped plasmon resonant nanoparticle as localized light source for near-field microscopy. *Journal of Microscopy-Oxford*, 202:60–65, 2001.

[43] T. Kalkbrenner, M. Ramstein, J. Mlynek, and V. Sandoghdar. A single gold particle as a probe for apertureless scanning near-field optical microscopy. *Journal of Microscopy-Oxford*, 202:72–76, 2001.

[44] A. Callegari, D. Tonti, and M. Chergui. Photochemically grown silver nanoparticles with wavelength-controlled size and shape. *Nano Letters*, 3(11):1565–1568, 2003.

[45] C. Voisin, D. Christofilos, P. A. Loukakos, N. Del Fatti, F. Vallee, J. Lerme, M. Gaudry, E. Cottancin, M. Pellarin, and M. Broyer. Ultrafast electron-electron scattering and energy exchanges in noble-metal nanoparticles. *Physical Review B*, 69(19):–, 2004.

[46] J. H. Hodak, A. Henglein, and G. V. Hartland. Photophysics of nanometer sized metal particles: Electron-phonon coupling and coherent excitation of breathing vibrational modes. *Journal of Physical Chemistry B*, 104(43):9954–9965, 2000.

[47] R. H. M. Groeneveld, R. Sprik, and A. Lagendijk. Femtosecond spectroscopy of electron-electron and electron-phonon energy relaxation in ag and an. *Physical Review B*, 51(17):11433–11445, 1995.

[48] G. V. Hartland. Coherent vibrational motion in metal particles: Determination of the vibrational amplitude and excitation mechanism. *Journal of Chemical Physics*, 116(18):8048–8055, 2002.

[49] C. Voisin, N. Del Fatti, D. Christofilos, and F. Vallee. Time-resolved investigation of the vibrational dynamics of metal nanoparticles. *Applied Surface Science*, 164:131–139, 2000.

[50] N. Del Fatti, S. Tzortzakis, C. Voisin, C. Flytzanis, and F. Vallee. Time resolved investigation of coherent acoustic mode oscillations in silver nanoparticles. *Physica B*, 263:54–56, 1999.

[51] Y. K. Cheung and D. Zhou. Three-dimensional vibration analysis of can-
     tilevered and completely free isosceles triangular plates. *International Jour-
     nal of Solids and Structures*, 39(3):673–687, 2002.

[52] J. Helbing, L. Bonacina, R. Pietri, J. Bredenbeck, P. Hamm, F. van Mourik,
     F. Chaussard, A. Gonzalez-Gonzalez, M. Chergui, C. Ramos-Alvarez,
     C. Ruiz, and J. Lopez-Garriga. Time-resolved visible and infrared study of
     the cyano complexes of myoglobin and of hemoglobin i from lucina pecti-
     nata. *Biophysical Journal*, 87(3):1881–1891, 2004.

[53] M. Rizzi, J. B. Wittenberg, A. Coda, M. Fasano, P. Ascenzi, and M. Bolognesi.
     Structure of the sulfide-reactive hemoglobin from the clam lucina-pectinata
     - crystallographic analysis at 1.5-angstrom resolution. *Journal of Molecular
     Biology*, 244(1):86–99, 1994.

[54] J. L. Martin and M. Vos. Femtosecond measurements of geminate recombina-
     tion in heme proteins. *Methods in Enzyology*, 232:418, 1994.

[55] J. W. Petrich, J. L. Martin, D. Houde, C. Poyart, and A. Orszag. Time-
     resolved raman-spectroscopy with subpicosecond resolution - vibrational
     cooling and delocalization of strain-energy in photodissociated (carbon-
     monoxy)hemoglobin. *Biochemistry*, 26(24):7914–7923, 1987.

[56] J. W. Petrich, C. Poyart, and J. L. Martin. Photophysics and reactivity of
     heme-proteins - a femtosecond absorption study of hemoglobin, myoglobin,
     and protoheme. *Biochemistry*, 27(11):4049–4060, 1988.

[57] M. Lim, T. A. Jackson, and P. A. Anfinrud. Binding of co to myoglobin
     from a heme pocket docking site to form nearly linear fe-c-o. *Science*,
     269(5226):962–966, 1995.

[58] M. H. Lim, T. A. Jackson, and P. A. Anfinrud. Femtosecond near-ir absorbance
     study of photoexcited myoglobin: Dynamics of electronic and thermal re-
     laxation. *Journal of Physical Chemistry*, 100(29):12043–12051, 1996.

[59] Y. Kholodenko, M. Volk, E. Gooding, and R. M. Hochstrasser. Energy dissi-
     pation and relaxation processes in deoxy myoglobin after photoexcitation
     in the soret region. *Chemical Physics*, 259(1):71–87, 2000.

[60] S. Franzen, L. Kiger, C. Poyart, and J. L. Martin. Heme photolysis occurs by
     ultrafast excited state metal-to-ring charge transfer. *Biophysical Journal*,
     80(5):2372–2385, 2001.

[61] X. Ye, A. Demidov, and P. M. Champion. Measurements of the photodissocia-
     tion quantum yields of mbno and mbo(2) and the vibrational relaxation of
     the six-coordinate heme species. *Journal of the American Chemical Society*,
     124(20):5914–5924, 2002.

[62] B. Steiger, J. S. Baskin, F. C. Anson, and A. H. Zewail. Femtosecond dynamics
     of dioxygen - picket-fence cobalt porphyrins: Ultrafast release of o-2 and

the nature of dative bonding. *Angewandte Chemie-International Edition*, 39(1):257–+, 2000.

[63] C. Kittel. *Introduction to solid state physics*. Wiley, New York, 7th edition, 1996.

[64] V.G. Manzhelli and Y.A. Freiman. *Physics of Cryocrystals*. AIP Press, Woodbury, New York, 1997.

[65] I. N. Krupskii, A. I. Prokhvatilov, and G. I. Shcherbakov. X-ray studies of solid n-h-2. *Fizika Nizkikh Temperatur*, 9(8):858–864, 1983.

[66] M. Roger, J. H. Hetherington, and J. M. Delrieu. Magnetism in solid he-3. *Reviews of Modern Physics*, 55(1):1–64, 1983.

[67] S. Grebenev, B. Sartakov, J. P. Toennies, and A. F. Vilesov. Evidence for superfluidity in para-hydrogen clusters inside helium-4 droplets at 0.15 kelvin. *Science*, 289(5484):1532–1535, 2000.

[68] D. Colognesi, M. Celli, and M. Zoppi. Density of phonon states in solid parahydrogen from inelastic neutron scattering. *Journal of Chemical Physics*, 120(12):5657–5663, 2004.

[69] P. J. Berkhout and I. F. Silvera. Mixing of rotational states, breakdown of independent polarizability approximation and renormalized interactions in solid hydrogens under pressure. *Communications on Physics*, 2(4):109–114, 1977.

[70] G.K. White. *Experimental Techniques in Low-Temperature Physics*. Clarendon Press, Oxford, U.K., 1968.

[71] F. Vigliotti and M. Chergui. Lineshape analysis of impurity rydberg transitions in van der waals solids: derivation of intermolecular potentials. *Chemical Physics Letters*, 296(3-4):316–322, 1998.

[72] M. Lax. The franck-condon principle and its applications to crystals. *The Journal of Chemical Physics*, 20(11):1752, 1952.

[73] T.H. Keil. Shape of impurity absorption bands in solids. *Physical Review*, 140(2A):601, 1965.

[74] R.C. O'Rourke. Absorption of light by trapped electrons. *Physical Review*, 91(2):265, 1953.

[75] M. Chergui, N. Schwentner, and V. Chandrasekharan. Rydberg fluorescence of no trapped in rare-gas matrices. *Journal of Chemical Physics*, 89(3):1277–1284, 1988.

[76] F. Vigliotti. *Photoinduced structural dynamics in solid hydrogens and solid neon*. PhD thesis, 2000.

[77] K.K. Rebane. *Impurity spectra of solids*. Plenum Press, New York, N.Y. U.S.A., 1970.

[78] C. Cohen-Tannoudji, B. Diu, and F. Laloë. *Quantum mechanics*. Wiley, New York, 1977.

[79] M. J. Weber. Multiphonon relaxation of rare-earth ions in yttrium orthoaluminate. *Physical Review B*, 8(1):54–64, 1973.

[80] A. Nitzan, S. Mukamel, and J. Jortner. Energy-gap law for vibrational-relaxation of a molecule in a dense medium. *Journal of Chemical Physics*, 63(1):200–207, 1975.

[81] M. Chergui, R. Schriever, and N. Schwentner. Electronic and vibrational-relaxation in rydberg and valence states of no in ne matrices. *Journal of Chemical Physics*, 89(12):7083–7093, 1988.

[82] F. Vigliotti, G. Zerza, M. Chergui, and J. Rubayo-Soneira. Lifetime lengthening of molecular rydberg states in the condensed phase. *Journal of Chemical Physics*, 109(9):3508–3517, 1998.

[83] E. Miescher and K.P. Huber. volume 3 of *International Review of Science - Physical Chemistry - 2*. Butterworths, London, 1976.

[84] H.M. Stevens. *J. Geophys. Res.*, 100:14735, 1995.

[85] G. Herzberg. *Molecular Spectra and Molecular Structure. I. Spectra of Diatomic Molecules*. Krieger Publishing Company, Malbar, Florida, 2nd edition, 1950.

[86] T.F. Gallagher. *Rydberg atoms*. Cambridge University Press, Cambridge, 1994.

[87] K. Kaufmann, C. Nager, and M. Jungen. Rydberg states and quantum defects of the no molecule. *Chemical Physics*, 95(3):385–390, 1985.

[88] M. Chergui, N. Schwentner, and W. Bohmer. Rydberg states of no trapped in rare-gas matrices. *Journal of Chemical Physics*, 85(5):2472–2482, 1986.

[89] J. Eloranta, K. Vaskonen, H. Hakkanen, T. Kiljunen, and H. Kunttu. 193 nm photodynamics of no in rare gas matrices: Fluorescence, thermoluminescence, and photodissociation. *Journal of Chemical Physics*, 109(18):7784–7792, 1998.

[90] F. Vigliotti and M. Chergui. Rydberg states in the condensed phase studied by fluorescence depletion spectroscopy. *European Physical Journal D*, 10(3):379–390, 2000.

[91] F. Vigliotti, A. Cavina, C. Bressler, B. Lang, and M. Chergui. Structural dynamics in quantum solids. i. steady-state spectroscopy of the electronic bubble in solid hydrogens. *Journal of Chemical Physics*, 116(11):4542–4552, 2002.

[92] H. Zacharias, J. B. Halpern, and K. H. Welge. 2-photon excitation of no (a sigma-2+-upsilon'=0,1,2) and radiation lifetime and quenching measurements. *Chemical Physics Letters*, 43(1):41–44, 1976.

[93] W. Groth, D. Kley, and U. Schurat. *J. Quant. Spectrosc. Radiat. Transfer.*, 11:1475, 1981.

[94] R. Gallusser and K. Dressler. Multistate vibronic coupling between the excited 2-pi-states of the no molecule. *Journal of Chemical Physics*, 76(9):4311–4327, 1982.

[95] M. Chergui. Structural dynamics in quantum solids. *Comptes Rendus De L Academie Des Sciences Serie Iv Physique Astrophysique*, 2(10):1453–1467, 2001.

[96] M. Großand F. Spiegelmann. A pseudopotential study of molecular spectroscopy in rare gas matrices: absorption of no in argon. *European Physical Journal D*, 4(2):219–224, 1998.

[97] W. S. Dennis, E. Durbin, Fitzsimm.Wa, O. Heybey, and G. K. Walters. Spectroscopic identification of excited atomic and molecular states in electron-bombarded liquid helium. *Physical Review Letters*, 23(19):1083, 1969.

[98] A. Fujisaki, K. Sano, T. Kinoshita, Y. Takahashi, and T. Yabuzaki. Implantation of neutral atoms into liquid-helium by laser sputtering. *Physical Review Letters*, 71(7):1039–1042, 1993.

[99] Y. Takahashi, K. Sano, T. Kinoshita, and T. Yabuzaki. Spectroscopy of alkali atoms and molecules in superfluid-helium. *Physical Review Letters*, 71(7):1035–1038, 1993.

[100] T. Kinoshita, K. Fukuda, and T. Yabuzaki. Doubly shaped d-2 excitation spectra of cs and rb atoms in superfluid helium due to a quadrupole bubble surface oscillation. *Physical Review B*, 54(9):6600–6607, 1996.

[101] T. Kinoshita, K. Fukuda, Y. Takahashi, and T. Yabuzaki. Optical-properties of impurity atoms in pressurized superfluid-helium. *Zeitschrift Fur Physik B-Condensed Matter*, 98(3):387–390, 1995.

[102] T. Kinoshita, K. Fukuda, Y. Takahashi, and T. Yabuzaki. Optical-properties of alkali-metal atoms in pressurized liquid-helium. *Physical Review A*, 52(4):2707–2716, 1995.

[103] M. Arndt, R. Dziewior, S. Kanorsky, A. Weis, and T. W. Hansch. Implantation and spectroscopy of metal atoms in solid helium. *Zeitschrift Fur Physik B-Condensed Matter*, 98(3):377–381, 1995.

[104] A. V. Benderskii, R. Zadoyan, N. Schwentner, and V. A. Apkarian. Photodynamics in superfluid helium: Femtosecond laser-induced ionization, charge recombination, and preparation of molecular rydberg states. *Journal of Chemical Physics*, 110(3):1542–1557, 1999.

[105] Q. Hui, J. L. Persson, J. H. M. Beijersbergen, and M. Takami. Spectroscopy and dynamics of neutral atoms in superfluid-helium. *Zeitschrift Fur Physik B-Condensed Matter*, 98(3):353–357, 1995.

[106] H. Bauer, M. Beau, B. Friedl, C. Marchand, K. Miltner, and H. J. Reyher. Laser spectroscopy of alkaline-earth atoms in he-ii. *Physics Letters A*, 146(3):134–140, 1990.

[107] S. I. Kanorsky, M. Arndt, R. Dziewior, A. Weis, and T. W. Hansch. Optical spectroscopy of atoms trapped in solid helium. *Physical Review B*, 49(5):3645–3647, 1994.

[108] S. I. Kanorsky, M. Arndt, R. Dziewior, A. Weis, and T. W. Hansch. Pressure shift and broadening of the resonance line of barium atoms in liquid-helium. *Physical Review B*, 50(9):6296–6302, 1994.

[109] N. Schwentner, E.E. Koch, and J. Jortner. *Electronic excitations of condensed rare gases.* Springer, Berlin, 1985.

[110] S. P. Walch and W. A. Goddard. Dipole-moments and electric-field gradients for correlated wavefunctions of no - x pi-2, a sigma-2(+), and d sigma-2(+) states. *Chemical Physics Letters*, 33(1):18–24, 1975.

[111] M. T. PortellaOberli, C. Jeannin, and M. Chergui. Ultrafast dynamics of rydberg states in the condensed phase. *Chemical Physics Letters*, 259(5-6):475–481, 1996.

[112] F. Vigliotti, L. Bonacina, and M. Chergui. Ultrafast structural dynamics in electronically excited solid neon. i. real-time probing of the electronic bubble formation. *Physical Review B*, 67(11):–, 2003.

[113] G. Rojas-Lorenzo, J. Rubayo-Soneira, F. Vigliotti, and M. Chergui. Ultrafast structural dynamics in electronically excited solid neon. ii. molecular-dynamics simulations of the electronic bubble formation. *Physical Review B*, 67(11):–, 2003.

[114] M.B. Robin. *Higher excited states of polyatomic molecules.* Academic, New York, 1974.

[115] R. L. Brooks, S. K. Bose, J. L. Hunt, J. R. Macdonald, J. D. Poll, and J. C. Waddington. Electron bubbles, small-polaron holes, and charge-induced effects in solid deuterium. *Physical Review B*, 32(4):2478–2488, 1985.

[116] S. K. Bose and J. D. Poll. Complex-formation in solid deuterium in the presence of d-3(+) ion. *Canadian Journal of Physics*, 65(1):67–75, 1987.

[117] J. Eloranta, N. Schwentner, and V. A. Apkarian. Structure and energetics of he-2* bubble-states in superfluid he-4. *Journal of Chemical Physics*, 116(10):4039–4053, 2002.

[118] J.C. Diels and W. Rudolph. *Ultrashort laser pulse phenomena.* Optics and Photonics. Academic Press, London, 1996.

[119] M Göppert-Mayer. *Ann. Phys.*, 9:273, 1931.

[120] W. Denk, J. H. Strickler, and W. W. Webb. 2-photon laser scanning fluorescence microscopy. *Science*, 248(4951):73–76, 1990.

[121] J. Burris, T. J. Mcgee, and T. J. Mcilrath. A 2-photon absorption cross-section measurement in nitric-oxide. *Chemical Physics Letters*, 101(6):588–592, 1983.

[122] J. Burris and T. J. Mcilrath. Experimental-method for the determination of 2-photon cross-sections using 4-wave mixing. *Journal of the Optical Society of America B-Optical Physics*, 2(8):1307–1312, 1985.

[123] C. Jeannin. *Etude en temps reel de deformations photoinduites dans l'argon et l'hydrogene solides.* PhD thesis, 1999.

[124] N. S. Sullivan, D. Zhou, and C. M. Edwards. Precise and efficient insitu ortho-hydrogen para-hydrogen converter. *Cryogenics*, 30(8):734–735, 1990.

[125] A. M. Juarez, D. Cubric, and G. C. King. A compact catalytic converter for the production of para-hydrogen. *Measurement Science and Technology*, 13(5):N52–N55, 2002.

[126] W. Demtröder. *Laser Spectroscopy.* Springer-Verlag, Berlin, 2nd edition, 1996.

[127] J. H. Eggert, E. Karmon, R. J. Hemley, H. K. Mao, and A. F. Goncharov. Pressure-enhanced ortho-para conversion in solid hydrogen up to 58 gpa. *Proceedings of the National Academy of Sciences of the United States of America*, 96(22):12269–12272, 1999.

[128] M. Chergui, N. Schwentner, and A. Tramer. Spectroscopy of the no molecule in n2 and mixed n2/kr matrices. *Chemical Physics Letters*, 201(1-4):187–193, 1993.

[129] C. Jeannin, M. T. PortellaOberli, S. Jimenez, F. Vigliotti, B. Lang, and M. Chergui. Femtosecond dynamics of electronic 'bubbles' in solid argon: viewing the inertial response and the bath coherences. *Chemical Physics Letters*, 316:51, 2000.

[130] R. P. Feynman and A.R. Hibbs. *Quantum mechanics and path integrals.* Mc Graw-Hill, New York, 1965.

[131] D. H. Li and G. A. Voth. A path integral einstein model for characterizing the equilibrium states of low-temperature solids. *Journal of Chemical Physics*, 96(7):5340–5353, 1992.

[132] H. Saito, H. Nagao, K. Nishikawa, and K. Kinugawa. Molecular collective dynamics in solid para-hydrogen and ortho-deuterium: The parrinello-rahman-type path integral centroid molecular dynamics approach. *Journal of Chemical Physics*, 119(2):953–963, 2003.

[133] J. S. Cao and G. A. Voth. The formulation of quantum-statistical mechanics based on the feynman path centroid density .1. equilibrium properties. *Journal of Chemical Physics*, 100(7):5093–5105, 1994.

[134] S. Jang and G. A. Voth. Path integral centroid variables and the formulation of their exact real time dynamics. *Journal of Chemical Physics*, 111(6):2357–2370, 1999.

[135] J. S. Cao and G. A. Voth. The formulation of quantum-statistical mechanics based on the feynman path centroid density .2. dynamical properties. *Journal of Chemical Physics*, 100(7):5106–5117, 1994.

[136] M. Sterling, Z. Li, and V. A. Apkarian. Simulations of quantum crystals by classical dynamics. *Journal of Chemical Physics*, 103(13):5679–5683, 1995.

[137] W. M. C. Foulkes, L. Mitas, R. J. Needs, and G. Rajagopal. Quantum monte carlo simulations of solids. *Reviews of Modern Physics*, 73(1):33–83, 2001.

[138] M.P. Allen and D.J. Tildesley. *Computer simulations of liquids*. Claredon Press, London, 1992.

[139] L. Verlet. Computer experiments on classical fluids .i. thermodynamical properties of lennard-jones molecules. *Physical Review*, 159(1):98, 1967.

[140] I. F. Silvera and V. V. Goldman. Isotropic inter-molecular potential for h-2 and d-2 in solid and gas phases. *Journal of Chemical Physics*, 69(9):4209–4213, 1978.

[141] H. Thuis, S. Stolte, and J. Reuss. Investigation of the angle dependent part of the inter-molecular potential of no inert gas systems using crossed molecular-beams. *Chemical Physics*, 43(3):351–364, 1979.

[142] H. M. Lin, M. Seaver, K. Y. Tang, A. E. W. Knight, and C. S. Parmenter. Role of inter-molecular potential well depths in collision-induced state changes. *Journal of Chemical Physics*, 70(12):5442–5457, 1979.

[143] M. Celli, D. Colognesi, and M. Zoppi. Experimental determination of the translational kinetic energy of liquid and solid hydrogen. *European Physical Journal B*, 14(2):239–244, 2000.

[144] J. P. Bergsma, P. H. Berens, K. R. Wilson, D. R. Fredkin, and E. J. Heller. Electronic-spectra from molecular-dynamics - a simple approach. *Journal of Physical Chemistry*, 88(3):612–619, 1984.

[145] P. Larregaray, A. Cavina, and M. Chergui. Ultrafast solvent response upon a change of the solute size in non-polar supercritical fluids. *Chemical Physics*, accepted.

[146] Special issue on ions and atoms in superfluid helium. *Z.Phys.*, 98, 1995.

[147] S. Jimenez, M. Chergui, G. Rojas-Lorenzo, and J. Rubayo-Soneira. The medium response to an impulsive redistribution of charge in solid argon: Molecular dynamics simulations and normal mode analysis. *Journal of Chemical Physics*, 114(12):5264–5272, 2001.

[148] S.W. Lovesey. *Theory of neutron scattering from condensed matter*, volume 1. Claredon Press, London, 1984.

[149] C. Andreani, P. Cipriani, D. Colognesi, and E. Pace. Single-particle dynamics in fluid hydrogen and deuterium. *Journal of Physics-Condensed Matter*, 12(8A):A139–A145, 2000.

[150] R. Bersohn and A. H. Zewail. Time-dependent absorption of fragments during dissociation. *Berichte Der Bunsen-Gesellschaft-Physical Chemistry Chemical Physics*, 92(3):373–378, 1988.

[151] F. Vigliotti, E. Sarraf, M. Chergui, and R. Scholz. Dynamics of electronic "bubble" formation in solid hydrogen: A classical model calculation based on fluid dynamics. *Physical Review Letters*, 83(12):2355–2358, 1999.

[152] I. Rips. Cavitation model of electron solvation dynamics: Effect of energy dissipation. *Journal of Chemical Physics*, 106(7):2702–2711, 1997.

[153] M. Berg. Viscoelastic continuum model of nonpolar solvation. 1. implications for multiple time scales in liquid dynamics. *Journal of Physical Chemistry A*, 102(1):17–30, 1998.

[154] M. A. Berg and H. W. Hubble. A viscoelastic continuum model of non-polar solvation. ii. vibrational dephasing in moderate to high-viscosity liquids and glasses. *Chemical Physics*, 233(2-3):257–266, 1998.

[155] M. A. Berg. A viscoelastic continuum model of nonpolar solvation. iii. electron solvation and nonlinear coupling effects. *Journal of Chemical Physics*, 110(17):8577–8588, 1999.

[156] M. Berg. Comparison of a viscoelastic theory of solvation dynamics to time-resolved experiments in a nonpolar solution. *Chemical Physics Letters*, 228(4-5):317–322, 1994.

[157] S. Jimenez, A. Pasquarello, R. Car, and M. Chergui. Dynamics of structural relaxation upon rydberg excitation of an impurity in an ar crystal. *Chemical Physics*, 233(2-3):343–352, 1998.

[158] V. L. Ginzburg and A. A. Sobyanin. Can liquid molecular-hydrogen be superfluid. *Jetp Letters-Ussr*, 15(6):242, 1972.

[159] E. Babaev, A. Sudbo, and N. W. Ashcroft. A superconductor to superfluid phase transition in liquid metallic hydrogen. *Nature*, 431(7009):666–668, 2004.

[160] M. E. Fajardo. Personal communication. 2004.

[161] Z. Li, R. Zadoyan, V. A. Apkarian, and C. C. Martens. Femtosecond many-body dynamics of caging - experiment and simulation of i-2 photodissociation-recombination in solid ar. *Journal of Physical Chemistry*, 99(19):7453–7465, 1995.

[162] R. Zadoyan, M. Sterling, and V. A. Apkarian. Dynamical spectroscopy of many-body interactions coherent vibrations and predissociation of i-2(b) in solid kr. *Journal of the Chemical Society-Faraday Transactions*, 92(11):1821–1829, 1996.

[163] M. Perner, S. Gresillon, J. Marz, G. von Plessen, J. Feldmann, J. Porstendorfer, K. J. Berg, and G. Berg. Observation of hot-electron pressure in the vibration dynamics of metal nanoparticles. *Physical Review Letters*, 85(4):792–795, 2000.

[164] M. Hu, X. Wang, G. V. Hartland, P. Mulvaney, J. P. Juste, and J. E. Sader. Vibrational response of nanorods to ultrafast laser induced heating: Theoretical and experimental analysis. *Journal of the American Chemical Society*, 125(48):14925–14933, 2003.

[165] N. Okada, Y. Hamanaka, A. Nakamura, I. Pastoriza-Santos, and L.M. Liz-Marzan. Linear and nonlinear optical reesponse of silver nanoprisms: Local electric fields of dipole and quadrupole plasmon resonances. *Journal of Physical Chemistry*, 108(26):8751, 2004.

[166] U. Kreibig and M. Vollmer. *Optical properties of metal clusters*. Springer-Verlag, Berlin, 1995.

[167] G. Mie. 25:377, 1908.

[168] N.W. Ashcroft and N.D. Mermin. *Solid State Physics*. Harcourt, Orlando, 1976.

[169] R. Rosei, C. H. Culp, and J. H. Weaver. Temperature modulation of optical-transitions involving fermi-surface in ag - experimental. *Physical Review B*, 10(2):484–489, 1974.

[170] R. Rosei. Temperature modulation of optical-transitions involving fermi-surface in ag - theory. *Physical Review B*, 10(2):474–483, 1974.

[171] J. H. Hodak, I. Martini, and G. V. Hartland. Observation of acoustic quantum beats in nanometer sized au particles. *Journal of Chemical Physics*, 108(22):9210–9213, 1998.

[172] Y. Hamanaka, J. Kuwabata, I. Tanahashi, S. Omi, and A. Nakamura. Ultrafast electron relaxation via breathing vibration of gold nanocrystals embedded in a dielectric medium. *Physical Review B*, 6310(10):art. no.–104302, 2001.

[173] M. Hu and G. V. Hartland. Heat dissipation for au particles in aqueous solution: Relaxation time versus size. *Journal of Physical Chemistry B*, 106(28):7029–7033, 2002.

[174] Y. Hamanaka, N. Hayashi, A. Nakamura, and S. Omi. Ultrafast relaxation dynamics of electrons in silver nanocrystals embedded in glass. *Journal of Luminescence*, 76-7:221–225, 1998.

[175] J. E. Sader, G. V. Hartland, and P. Mulvaney. Theory of acoustic breathing modes of core-shell nanoparticles. *Journal of Physical Chemistry B*, 106(6):1399–1402, 2002.

[176] B. Lamprecht, J. R. Krenn, A. Leitner, and F. R. Aussenegg. Resonant and off-resonant light-driven plasmons in metal nanoparticles studied by femtosecond-resolution third-harmonic generation. *Physical Review Letters*, 83(21):4421–4424, 1999.

[177] T. Vartanyan, M. Simon, and F. Trager. Femtosecond optical second harmonic generation by metal clusters: The influence of inhomogeneous line broadening on the dephasing time of surface plasmon excitation. *Applied Physics B-Lasers and Optics*, 68(3):425–431, 1999.

[178] C. K. Sun, F. Vallee, L. H. Acioli, E. P. Ippen, and J. G. Fujimoto. Femtosecond-tunable measurement of electron thermalization in gold. *Physical Review B*, 50(20):15337–15348, 1994.

[179] J. H. Hodak, I. Martini, and G. V. Hartland. Spectroscopy and dynamics of nanometer-sized noble metal particles. *Journal of Physical Chemistry B*, 102(36):6958–6967, 1998.

[180] J. Hodak, I. Martini, and G. V. Hartland. Ultrafast study of electron-phonon coupling in colloidal gold particles. *Chemical Physics Letters*, 284(1-2):135–141, 1998.

[181] N. Del Fatti, C. Voisin, D. Christofilos, F. Vallee, and C. Flytzanis. Acoustic vibration of metal films and nanoparticles. *Journal of Physical Chemistry A*, 104(18):4321–4326, 2000.

[182] N. Del Fatti, C. Voisin, F. Chevy, F. Vallee, and C. Flytzanis. Coherent acoustic mode oscillation and damping in silver nanoparticles. *Journal of Chemical Physics*, 110(23):11484–11487, 1999.

[183] K. Ekvall, P. van der Meulen, C. Dhollande, L. E. Berg, S. Pommeret, R. Naskrecki, and J. C. Mialocq. Cross phase modulation artifact in liquid phase transient absorption spectroscopy. *Journal of Applied Physics*, 87(5):2340–2352, 2000.

[184] N. Del Fatti, C. Voisin, M. Achermann, S. Tzortzakis, D. Christofilos, and F. Vallee. Nonequilibrium electron dynamics in noble metals. *Physical Review B*, 61(24):16956–16966, 2000.

[185] N. Del Fatti, R. Bouffanais, F. Vallee, and C. Flytzanis. Nonequilibrium electron interactions in metal films. *Physical Review Letters*, 81(4):922–925, 1998.

[186] R. W. Schoenlein, W. Z. Lin, J. G. Fujimoto, and G. L. Eesley. Femtosecond studies of nonequilibrium electronic processes in metals. *Physical Review Letters*, 58(16):1680–1683, 1987.

[187] J. Y. Bigot, J. C. Merle, O. Cregut, and A. Daunois. Electron dynamics in copper metallic nanoparticles probed with femtosecond optical pulses. *Physical Review Letters*, 75(25):4702–4705, 1995.

[188] I.H.M. van Stokkum, D.S. Larsen, and R. van Grondelle. Global and target analysis of time-resolved spectra. *Biochimica et Biophysica Acta*, 1657:82, 2004.

[189] N. P. Ernsting, S. A. Kovalenko, T. Senyushkina, J. Saam, and V. Farztdinov. Wave-packet-assisted decomposition of femtosecond transient ultraviolet-visible absorption spectra: Application to excited-state intramolecular proton transfer in solution. *Journal of Physical Chemistry A*, 105(14):3443–3453, 2001.

[190] *Handbook of Chemistry and Physics.* CRC Press, Boca Raton, Florida, 70th edition, 1989.

[191] D.C. Harris and N.D. Bertolucci. *Symmetry and spectroscopy.* Oxford University Press, New York, 1982.

[192] N.M. Terwilliger. Functional adaptations of oxygen-transport proteins. *Journal of Experimental Biology*, 201:1085, 1998.

[193] D. W. Kraus and J. B. Wittenberg. Hemoglobins of the lucina-pectinata bacteria symbiosis .1. molecular-properties, kinetics and equilibria of reactions with ligands. *Journal of Biological Chemistry*, 265(27):16043–16053, 1990.

[194] J. B. Wittenberg and D. W. Kraus. *Hemoglobins of eukaryote / procaryote symbiodes.* Springer, New York, 1991.

[195] Y. Kholodenko, E. A. Gooding, Y. Dou, M. Ikeda-Saito, and R. M. Hochstrasser. Heme protein dynamics revealed by geminate nitric oxide recombination in mutants of iron and cobalt myoglobin. *Biochemistry*, 38(18):5918–5924, 1999.

[196] J. Cerda, Y. Echevaria, E. Morales, and J.L. Garriga. Resonance raman studies of the heme-ligand active site of hemoglobin i from lucina pectinata. *Biospectroscopy*, 4:311, 1999.

[197] S. Yoshikawa, D. H. Okeeffe, and W. S. Caughey. Investigations of cyanide as an infrared probe of hemeprotein ligand-binding sites. *Journal of Biological Chemistry*, 260(6):3518–3528, 1985.

[198] A. Boffi, E. Chiancone, S. Takahashi, and D. L. Rousseau. Stereochemistry of the fe(ii)- and fe(iii)-cyanide complexes of the homodimeric scapharca inaequivalvis hemoglobin. a resonance raman and ftir study. *Biochemistry*, 36(15):4505–4509, 1997.

[199] R. Schweitzer-Stenner, A. Cupane, M. Leone, C. Lemke, J. Schott, and W. Dreybrodt. Anharmonic protein motions and heme deformations in myoglobin cyanide probed by absorption and resonance raman spectroscopy. *Journal of Physical Chemistry B*, 104(19):4754–4764, 2000.

[200] T. K. Das, M. Couture, M. Guertin, and D. L. Rousseau. Distal interactions in the cyanide complex of ferric chlamydomonas hemoglobin. *Journal of Physical Chemistry B*, 104(46):10750–10756, 2000.

[201] W. X. Cao, J. F. Christian, P. M. Champion, F. Rosca, and J. T. Sage. Water penetration and binding to ferric myoglobin. *Biochemistry*, 40(19):5728–5737, 2001.

[202] R. M. Esquerra, R. A. Goldbeck, D. B. Kim-Shapiro, and D. S. Kliger. Spectroscopic evidence for nanosecond protein relaxation after photodissociation of myoglobin-co. *Biochemistry*, 37(50):17527–17536, 1998.

[203] J. Bredenbeck and P. Hamm. Versatile small volume closed-cycle flow cell system for transient spectroscopy at high repetition rates. *Review of Scientific Instruments*, 74(6):3188–3189, 2003.

[204] X. Ye, A. Demidov, F. Rosca, W. Wang, A. Kumar, D. Ionascu, L. Zhu, D. Barrick, D. Wharton, and P.M. Champion. Investigations of heme protein absorption line shapes, vibrational relaxation, and resonance raman scattering on ultrafast time scales. *Journal Physical Chemistry A*, 107:8156, 2003.

[205] T. Lian, Y. Kholodenko, S. Gnanakaran, and R. M. Hochstrasser. Ir probe of solvent responses in solvation process. *Abstracts of Papers of the American Chemical Society*, 207:138–Phys, 1994.

[206] J. N. Moore, P. A. Hansen, and R. M. Hochstrasser. Iron carbonyl bond geometries of carboxymyoglobin and carboxyhemoglobin in solution determined by picosecond time-resolved infrared-spectroscopy. *Proceedings of the National Academy of Sciences of the United States of America*, 85(14):5062–5066, 1988.

[207] K. Rajarathnam, G. N. Lamar, M. L. Chiu, and S. G. Sligar. Determination of the orientation of the magnetic axes of the cyano-metmb complexes of point mutants of myoglobin by solution h-1-nmr - influence of his e7 -] gly and arg cd3 -] gly substitutions. *Journal of the American Chemical Society*, 114(23):9048–9058, 1992.

[208] J. T. Sage. Infrared crystallography: Structural refinement through spectroscopy. *Applied Spectroscopy*, 51(4):568–573, 1997.

[209] P. Hamm, S. M. Ohline, and W. Zinth. Vibrational cooling after ultrafast photoisomerization of azobenzene measured by femtosecond infrared spectroscopy. *Journal of Chemical Physics*, 106(2):519–529, 1997.

[210] Y. Mizutani and T. Kitagawa. Direct observation of cooling of heme upon photodissociation of carbonmonoxy myoglobin. *Science*, 278(5337):443–446, 1997.

[211] K. S. Reddy, T. Yonetani, A. Tsuneshige, B. Chance, B. Kushkuley, S. S. Stavrov, and J. M. Vanderkooi. Infrared spectroscopy of the cyanide complex of iron(ii) myoglobin and comparison with complexes of microperoxidase and hemoglobin. *Biochemistry*, 35(17):5562–5570, 1996.

[212] P. Hamm, M. Lim, and R. M. Hochstrasser. Vibrational energy relaxation of the cyanide ion in water. *Journal of Chemical Physics*, 107(24):10523–10531, 1997.

[213] M. H. Lim, T. A. Jackson, and P. A. Anfinrud. Midinfrared vibrational-spectrum of co after photodissociation from heme evidence for a ligand docking site in the heme pocket of hemoglobin and myoglobin. *Journal of Chemical Physics*, 102(11):4355–4366, 1995.

[214] J. M. Kriegl, F. K. Forster, and G. U. Nienhaus. Charge recombination and protein dynamics in bacterial photosynthetic reaction centers entrapped in a sol-gel matrix. *Biophysical Journal*, 85(3):1851–1870, 2003.

[215] M. Gouterman. *Optical spectra and electronic structure of porphyrins and related rings.*, volume 3. Academic Press, New York, 1978.

[216] E. R. Henry, W. A. Eaton, and R. M. Hochstrasser. Molecular-dynamics simulations of cooling in laser-excited heme-proteins. *Proceedings of the National Academy of Sciences of the United States of America*, 83(23):8982–8986, 1986.

[217] D. E. Sagnella, J. E. Straub, and D. Thirumalai. Time scales and pathways for kinetic energy relaxation in solvated proteins: Application to carbon-monoxy myoglobin. *Journal of Chemical Physics*, 113(17):7702–7711, 2000.

[218] Y. Mizutani and T. Kitagawa. Vibrational energy relaxation of metalloporphyrins in a condensed phase probed by time-resolved resonance raman spectroscopy. *Bulletin of the Chemical Society of Japan*, 75(4):623–639, 2002.

[219] H. M. Visser, O. J. G. Somsen, F. Vanmourik, S. Lin, I. H. M. Vanstokkum, and R. Vangrondelle. Direct observation of subpicosecond equilibration of excitation-energy in the light-harvesting antenna of rhodospirillum-rubrum. *Biophysical Journal*, 69(3):1083–1099, 1995.

[220] S. Sato, K. Kamogawa, K. Aoyagi, and T. Kitagawa. Time-resolved resonance raman investigation of the photoreduction of iron octaethylporphyrin complexes by using the quasi-simultaneous pump probe measurement technique. *Journal of Physical Chemistry*, 96(26):10676–10681, 1992.

[221] J. Rodriguez, C. Kirmaier, and D. Holten. Optical-properties of metal-loporphyrin excited-states. *Journal of the American Chemical Society*, 111(17):6500–6506, 1989.

[222] J. Rodriguez and D. Holten. Ultrafast vibrational dynamics of a photoexcited metalloporphyrin. *Journal of Chemical Physics*, 91(6):3525–3531, 1989.

[223] F. Rosca, A. T. N. Kumar, X. Ye, T. Sjodin, A. A. Demidov, and P. M. Champion. Investigations of coherent vibrational oscillations in myoglobin. *Journal of Physical Chemistry A*, 104(18):4280–4290, 2000.

[224] A. T. N. Kumar, F. Rosca, A. Widom, and P. M. Champion. Investigations of ultrafast nuclear response induced by resonant and nonresonant laser pulses. *Journal of Chemical Physics*, 114(15):6795–6815, 2001.

[225] A. Waleh and G. H. Loew. Quantum-mechanical studies of the photo-dissociation of carbonylheme complexes. *Journal of the American Chemical Society*, 104(9):2346–2351, 1982.

[226] E. Riedle, M. Beutter, S. Lochbrunner, J. Piel, S. Schenkl, S. Sporlein, and W. Zinth. Generation of 10 to 50 fs pulses tunable through all of the visible and the nir. *Applied Physics B-Lasers and Optics*, 71(3):457–465, 2000.

[227] G. T. Shubeita, S. K. Sekatskii, M. Chergui, G. Dietler, and V. S. Letokhov. Investigation of nanolocal fluorescence resonance energy transfer for scanning probe microscopy. *Applied Physics Letters*, 74(23):3453–3455, 1999.

[228] S. K. Sekatskii, G. T. Shubeita, M. Chergui, G. Dietler, B. N. Mironov, D. A. Lapshin, and V. S. Letokhov. Towards the fluorescence resonance energy transfer (fret) scanning near-field optical microscopy: Investigation of nanolocal fret processes and fret probe microscope. *Journal of Experimental and Theoretical Physics*, 90(5):769–777, 2000.

[229] S. K. Sekatskii, M. Chergui, and G. Dietler. Coherent fluorescence resonance energy transfer: Construction of nonlocal multiparticle entangled states and quantum computing. *Europhysics Letters*, 63(1):21–27, 2003.

[230] J. Helbing. *Solvation and photo-induced dynamics in rare gas matrices and ferric heme proteins*. PhD thesis, Universit de Lausanne, 2001.

[231] R. Bonneau, J. Wirz, and A. D. Zuberbuhler. Methods for the analysis of transient absorbance data. *Pure and Applied Chemistry*, 69(5):979–992, 1997.

[232] G.H. Golub and C.F. van Loan. *Matrix Computations*. Johns Hopkins University Press, Baltimore, 2nd edition, 1990.

[233] I.H.M. van Stokkum. Personal communication, 2004.

Curriculum vitae

Name:	*Luigi Bonacina*
Date, place of birth:	*30.06.1973, Milano*
Nationality:	*Italian*
Address:	*Laboratoire de spectroscopie ultrarapide*
	ISIC - SB
	Swiss Federal Institute of Technology Lausanne
	BSP, CH-1015
	tel: +41-21-6930452
	fax: +41-21-6930422
	e-mail: luigi.bonacina@epfl.ch

Education

2000-2004
Ph.D thesis on "Ultrafast structural dynamics in electronically excited many-body systems" under the supervision of Prof. M. Chergui

November 1999
Degree in physics (Laurea) 110/110 Magna cum laude

1998-1999
Laurea thesis on "Dynamics of Micromaser driven by an external coherent field" under the supervision of Prof. F. Casagrande

1992-1999
Studies in physics at the Universitá Statale degli Studi di Milano

June 1992
High school diploma (Maturitá Classica) 60/60

Teaching and working experience

2000-2003

- *Teaching assistant for the course of Molecular Physics (Prof. S. Haacke)*

- *Teaching assistant for the course of General Physics for Medicine and Forensic Science (Prof. M. Chergui)*

- *Teaching assistant for the 2nd year laboratory for physics students*

1999-2000

- *High school teacher of physics and mathematics*

1995-1999

- *Private tuition of physics and mathematics for high school and undergraduate students*

Publications

- J.Helbing, L.Bonacina, R.Pietri, J.Bredenbeck, P.Hamm, F.van Mourik, F.Chaussard, A.Gonzalez-Gonzalez,M.Chergui, C.Ramos-Alvarez, C.Ruiz, J.Lopez-Garriga **Time-resolved visible and infrared study of the cyano complexes of myoglobin and of hemoglobin I from Lucina pectinata** *Biophysical Journal*, **87**, 1881-1891 (2004)

- F.Vigliotti, L.Bonacina, M.Chergui **Ultrafast structural dynamics in electronically excited solid neon. I. Real-time probing of the electronic bubble formation** *Physical Review B*, **67**, 31, art.11519 (2003)

- F.Vigliotti, L.Bonacina, M.Chergui, G.Rojas-Lorenzo, J.Rubayo-Soneira **Ultrafast expansion and vibrational coherences of electronic 'Bubbles' in solid neon** *Chemical Physics Letters*, **362**, 31-38 (2002)

- F.Vigliotti, L.Bonacina, M.Chergui **Structural dynamics in quantum solids. II. Real-time probing of the electronic bubble formation in solid hydrogens** *Journal of Chemical Physics*, **116**, 4553-4562 (2002)

- L.Bonacina, F.Casagrande, A.Lulli **Dynamics of a coherently driven micromaser by the Monte Carlo wavefunction approach** *Journal of Optics B-Quantum and Semiclassical Optics*, **2**, 490-496 (2000)

Conference seminars

- **Invited talk:** *Ultrafast Structural Dynamics in Solid Hydrogen*
  5th International Conference - Low Temperature Chemistry (LTC5), Berlin-Dahlem, September 7-10, 2004

- **Oral contribution:** *Structural Dynamics in Quantum Solids*
  Swiss Physical Society Meeting, Lausanne, February 28 - March 1, 2002

Poster presentations

- L.Bonacina, P.Larregaray, M.Chergui *Ultrafast dynamics of non-polar solvation in solid para-hydrogen*
  2nd International Conference - From Solid State to Biophysics, Cavtat-Dubrovnik, June 26 - July 2, 2004

- L.Bonacina et al. *Time-Resolved UV-Vis and Infrared Study of the cyano complexes of Myoglobin and Hemoglobin I from Lucina Pectinata*
  Swiss Chemical Society Meeting, Lausanne, October 9, 2003

- L.Bonacina, F.Vigliotti, M.Chergui *Ultrafast Expansion and vibrational Coherences of electronic "Bubbles" in solid Neon*
  1st International Conference - From Solid State to Biophysics, Cavtat-Dubrovnik, June 13-19, 2002

- L.Bonacina, F.Vigliotti, M.Chergui *Structural Dynamics in Quantum Solids*
  12th International Conference - Ultrafast Processes in Spectroscopy, Florence, November 1, 2001

- L.Bonacina, F.Vigliotti, M.Chergui *Structural Dynamics in Quantum Solids*
  5th International Conference - Femtochemistry, Toledo, September 2-6, 2001

- L.Bonacina, F.Vigliotti, M.Chergui *Femtosecond Structural Dynamics in Solid Neon and Solid Hydrogens*
  Euro Conference Matrix 2001, Szklarska Poreba, July 7-13, 2001

Acknowledgements

I would like to express my gratitude to Prof. Majed Chergui, who accepted me in the group in June 2000. Majed has been a constant and passionate scientific guide, and it is his merit if during these years my enthusiasm for physics and for doing science has constantly grown.

I am very thankful to Prof. Giacinto Scoles and Prof. Fabrice Vallée, who accepted to travel a long journey to Lausanne for my exam. I am also grateful to the experts from EPFL, Prof. Olivier Martin and Dr. Marcel Drabbels, and to the president of the commission, Prof. Harald Brune, for their interest in my work.

This thesis is the result of a collective effort of many people, that collaborated directly with me or prepared the necessary groundwork in the past. Without Dr. Frank van Mourik my life in the lab would have been different, his help with laser systems and electronics was essential. I am grateful to him, because he taught me that taking things apart can be very insightful, as long as we are able to put them back together.

Dr. Pascal Larregaray is, first of all, a great friend of mine with whom I spent some of the best moments of my Ph.D experience. Its collaboration in the development of the simulations of structural relaxation in solid hydrogen, was precious and insightful. I would like to acknowledge also the work of Dr. Franco Vigliotti, who started the study on hydrogen crystals few years before I arrived.

I got involved in the experiment on silver nanoparticles almost by chance, as Dr. Andrea Callegari came one evening to the lab with one of his samples asking me to take just a quick look. Collaborating with him was a priceless scientific experience and also good fun, as everybody who is familiar with him knows. Camilla Bonati helped me with the calculations of the mechanical vibrations of the triangular plates, working hard to keep the schedule of my thesis: grazie!